UNIVERSITY OF SOUTHAMPTON

FACULTY OF ENGINEERING AND APPLIED SCIENCE

CIVIL AND ENVIRONMENTAL ENGINEERING DEPARTMENT

CALIBRATION OF PENETROMETERS AND INTERPRETATION OF PRESSUREMETERS IN SAND

by

MORTEZA ZOHRABI

B.Sc. (Honours), M.Sc.

Thesis submitted for the degree of

Doctor of Philosophy

July 1993

This thesis is dedicated to my wife
whose support and encouragement made
the work possible.

ABSTRACT

UNIVERSITY OF SOUTHAMPTON

DOCTOR OF PHILOSOPHY

CALIBRATION OF PENETROMETERS AND INTERPRETATION OF PRESSUREMETERS IN SAND

by Morteza Zohrabi

Extensive Cone Penetration Tests have been performed in large scale calibration chambers over the past 20 years under two distinct [constant stress (BC1) and mean zero lateral strain(BC3)] lateral boundary conditions. The investigation has shown that such tests on dense sand are affected by the size of the chamber. In an attempt to achieve a more natural boundary behaviour, the boundaries of a large scale calibration chamber (on loan from NGI) were modified to correspond to the the stiffness indicated by full length expanding cylinder tests for both NC and OC soils. The outer boundary in these tests was controlled to simulate soil expanding to infinity by forcing it to follow the same stress-strain behaviour as given at an earlier stage of the test by the expansion of the inner cavity. This gave an opportunity to analyse the distribution of stress with radius as well as with time. The soil was assumed to yield plastically in response to the extreme principal stresses - initially in a vertical plane and then, with more expansion, in the horizontal plane. The results show that although plastic dilation was appreciable at higher shear strains it was largely (and sometimes more than) nullified in the chamber as a whole by elastic compression accompanying the higher stresses.

A series of CPT's in dense Hokksund sand were performed in the modified chamber. The results showed that for a 2 bar NC test BC1 underestimated cone resistance by 12 % but that a BC3 test matched the measured values under an infinite boundary test. The cone resistance of OC samples under either BC1 or BC3 needed to be increased by 7 %. Similar correction factors were also deduced for the sleeve friction. The CPT results also indicated a relationship which (at least in theory) predicted the possibility of obtaining the necessary information regarding the stress state of the soil from a single CPT.

The results of the expansion tests were then used to predict the normal stresses at the penetrometer and thus the sleeve friction. The results matched the corresponding CPT results surprisingly well.

In an attempt to model the soil behaviour during penetration, a solution was developed for a spheroidal cavity expansion in a transversely isotropic elastic medium. This was then used in conjunction with the expansion test results to obtain an elastic/plastic solution for the sleeve friction and for the distribution of lateral stress as a function of radius and depth for semi-infinite penetration. The resulting predictions at the outer soil boundary are compared with the values deduced from the strain gauge measurements. Realising that the former includes the effects of theoretical stresses from beyond the chamber top and bottom boundaries, the comparison is reasonably good.

ACKNOWLEDGEMENTS

The author wishes to thank his supervisor Mr. R. M. Harkness for his continuous supervision throughout the research programme.

The author is deeply grateful to Mr. T. Lunne of the Norwegian Geotechnical Institute for the opportunity to work on their calibration chamber.

Many thanks are also due to the technical staff of the Civil Engineering Department for their help in performing the tests, in particular, Mr. Malcolm Booth and Mr. Mark Foster for their technical assistance with the Chamber and the latter also for his indispensable help with the computer plots.

The author is indebted to his father for the financial support and continuous encouragement.

Finally, the author wishes to thank all of those who have contributed to the production of this thesis.

CONTENTS

PRINCIPAL ABBREVIATIONS AND NOTATIONS

a radius of the penetrometer

b radius of the calibration chamber

B base width of the cone

BC boundary condition

B.M. bending moment

c cohesion

CC calibration chamber

C_{ij} elastic stiffness constants

CPT cone penetration test

CPTU undrained cone penetration test

CRB County Roads Board of Victoria

D depth of wedge or cone

d_c cone diameter

D_c chamber diameter

D/B relative depth

DMT Marchetti's dilatometer test

D_r relative density

e void ratio

E horizontal Young's modulus

E' vertical Young's modulus

EBV elastic body wave

ENEL-CRIS Ente Nazionale per l'Energia Elettrica - Centro Ricerche Idrauliche e Strutturali, Milano (Italy)

E_s Young's modulus for steel

ESP effective stress path

f_s sleeve friction

f_s/q_c friction ratio

G horizontal shear modulus

G' shear modulus due to effect of vertical stress on horizontal strain

HS Hokksund sand

IB infinite boundary

I_r rigidity index

I_R relative dilatancy index

I_{rr} reduced rigidity index

ISMES Istituto Sperimentale su Modelli e Strutture, Bergamo (Italy)

K_o coefficient of earth pressure at rest

K_o^{NC} K_o at the last stage of loading

K_o^{OC} K_o at the last stage of the unloading

M constrained modulus

NC normally consolidated

NGI Norwegian Geotechnical Institute

N_c, N_q & N_{γ_q} bearing capacity factors

$N_{\phi'}$ stress obliquity = $(1 + \sin\phi')/(1 - \sin\phi')$

$N_{\psi'}$ strain obliquity = $(1 + \sin\psi')/(1 - \sin\psi')$

OC over-consolidated

OCR over-consolidation ratio

P_a reference pressure (normally equal to 1 kg/cm^2)

P_i internal pressure

P_u ultimate pressure of the expanding cavity

q_c cone resistance

r radius of the soil within chamber

s wall thickness of rigid wall chamber

s' $= 1/2\ (\sigma'_1 + \sigma'_3)$

S slope of the cavity pressure vs. cavity strain in the log-log cycles

SBR self-boring pressuremeter

SPT standard pressuremeter test

SU Southampton university

t $= 1/2\ (\sigma'_1 - \sigma'_3)$

TS Ticino sand

α proportion of the vertical doublet in the development of the anisotropic spheroidal cavity expansion

β the ratio of the radius to the height of the spheroid (r/z)

δ friction angle between soil and steel

Δ percent volumetric strain $\equiv \varepsilon_v$

ε_r radial strain

ε_θ circumferential strain

ε_z vertical strain

γ unit weight of the soil

γ_c shape factor due to cohesion

γ_q shape factor due to friction

ψ dilation angle

Ψ state parameter

μ & λ Lame's constants

λ empirical shape factor = $1 + \tan\phi'_s$

λ_{ss} slope of the steady-state line

ω distributed load over circular beam

ν Poisson's ratio in the horizontal plane

ν' Poisson's ratio for effect of vertical stress on horizontal strain

ϕ' angle of internal friction

ϕ'_{cv} constant volume friction angle

ϕ'_p peak friction angle

ϕ'_s secant friction angle in the plastic zone

ρ ratio of the horizontal to the vertical Young's modulus

σ' effective confining stress

σ_h horizontal stress

σ_m mean stress

σ_r radial stress

σ_θ circumferential (hoop) stress

$\Sigma\varepsilon_\gamma$ cumulative shear strain

$\Sigma\varepsilon_v$ cumulative volumetric strain

ζ_v volume change factor

ζ_{γ_q} shape factor

CHAPTER 1

INTRODUCTION

In-situ measurement techniques such as the cone penetration test (CPT) are indirect methods of subsurface soil exploration where information is obtained without the need to obtain representative soil samples. The results do not rely on the successful retrieval of undisturbed samples and measurements are taken under actual field conditions instead of the synthetic environment of the laboratory.

CPT has played an important part in both onshore and offshore soil investigations. Many cone penetrometers are in use, and even though they adhere more or less to the European standards, they may give different results due to instrumentation and probe soil interaction effects (Campanella and Robertson, 1981, 1982). This means that soil parameters interpreted from cone penetration tests may be different depending on the type of cone penetrometer and the laboratory or field conditions under which they are used. Hence, repeatability of results obtained using an electrical cone and the procedure related to the accuracy of these results become important.

Being a faster and simpler test than other in-situ tests, CPT's adaptation for common use in site investigation has accelerated in the last decade. However, in all the applications of CPT data the soil parameters, properties and characteristics could only be arrived at indirectly. The method of inference is commonly developed by either direct calibration, empirical correlations or assumed theoretical relationships.

Sometimes these approaches may not take account of sufficient variables. It is essential, therefore, that a sound theoretical basis

be developed and verified against data from accurate and reproducible experiments in which soil properties are controlled and actual penetration mechanisms observed. Cone resistance is determined by several factors which cannot, at present, be incorporated in a single formula that relates the CPT values to soil properties. A brief review of the previous theoretical as well as the experimental work on penetration mechanisms is given in Chapter 2.

There are two approaches that are commonly used to interpret CPT data in sand:

The first approach is the direct one that aims at correlating the measured cone stresses (cone tip resistance, q_c, and sleeve friction, f_s) with measured performance of foundations without the need to evaluate any soil parameters. For example, the measured bearing capacity of a shallow pile might be expressed as a function of q_c. This approach leads to empirical methods in which the quality of the result is strictly linked to the number and quality of the case histories upon which the approach has been established.

The second approach is to use large scale calibration chambers in order to make penetration tests in samples of known sand at predesigned densities. The latter are obtained through special pluviation techniques which depend on the rate of pouring and drop of the sand particles. The pluviated sample is then compressed to the desired stress level and the penetrometer pushed into the sample while its cone stresses are measured. Small scale laboratory tests are often required to obtain the conventional engineering properties of the tested sand and the measured penetration stresses and small scale test properties are then correlated so that the latter may be deduced from field values of the former and used in design. This approach, although basically more sound and rational than the direct one, suffers in that a theoretical support requires the solutions for very complex boundary value problems that are rarely feasible for the CPT (Jamiolkowski et al., 1988). Despite this, the indirect approach has been used in the past 15 years by performing comprehensive calibration chamber (CC)

tests on numerous silica sands of varying crushability with the aim of validating and improving the existing correlations between the cone stresses and engineering parameters for a wide range of soil types and conditions.

In this regard, a large calibration chamber has been on loan from the Norwegian Geotechnical Institute (NGI) to Southampton University for the past decade. It holds a cylindrical sample of sand 1.2 m diameter by 1.5 m high with sides and base having independent, flexible, constant pressure support whilst the rigid top has a central hole through which a full scale penetrometer ($10cm^2$ in cross-section) may be passed and forced into the soil mass.

An initial Southampton project, supported by NGI and SERC, comprised a total of 73 successful loading and penetration tests in Hokksund sand [SU series] and involved both full scale and half scale penetrometers to include the study of scale effects. These tests were performed under two distinct lateral boundary conditions: one constant pressure [denoted by BC1] and the other zero mean lateral strain [denoted by BC3] with stress histories ranging from normally consolidated (NC) to very overconsolidated (OC) and all at various soil densities. An analysis of the results of the SU series, as well as those of comparable tests in Norway and Italy, is given in Chapter 3 in order to investigate existing techniques for the interpretation of CPT data on sand.

The results of the analysis show that calibration chamber tests on dense Hokksund sand are affected by the size of the chamber and thus raise questions about the validity of the obtained experimental results. Extensive research by NGI and others together with the findings in Chapter 3 has shown that the chamber-to-cone diameter ratio should be higher than an estimated 50 [the NGI chamber's is only about 34 when using the standard cone] if boundary and size effects [sometimes also called the scale effects] are to be eliminated. Cone stresses have been shown to be underestimated in both BC1 and BC3 cases and the effect is believed to be linked, mainly, to the influence

of the lateral boundary on the calibration chamber specimens.

The use of chambers having dimensions sufficiently large to avoid the chamber size effects for dense samples has met limitations in the cost effectiveness of research programs. Some researchers have suggested the implementation of a computer controlled feedback at the radial boundary of the specimen to simulate the stress which will occur at the same radius for a hypothetical cylinder of soil having infinite radius. This would be useful if a clear understanding of the penetration mechanism existed and has been partially successful in the testing of pressuremeters in sand by assuming a plane strain type of expansion. It has been found difficult to extend the analysis to the effects of chamber size on the CPT results as the variation with depth makes any numerical analysis very complex and requires a description of soil behaviour in 3-D which is practically impossible to measure directly.

Having recognised this fact, researchers have tried to quantify the scale effect by introducing some correction factors to the measured cone resistance values depending on the stress level and the stress history of the sample. Hence, Chapter 4 focuses on the effects of boundary conditions and chamber size from various perspectives.

The present research program seeks to model a more natural boundary behaviour and this, ideally, would have required the implementation of a variable stiffness boundary for testing soils of different stiffnesses. Such a design was, however, beyond the available resources and a basically constant stiffness boundary was, therefore, adopted and thus limited the range of soil stiffness conditions that could be studied.

Since the boundary stiffness effect is most noticeable in very dense sand, the required stiffness for the modified chamber needed to be determined for the test sand (Hokksund sand) at one stress under NC conditions and another under a given over-consolidation ratio (OCR) (to give the same lateral stiffness) and chosen to match similar stress

conditions in tests under the previously setup boundary configurations (i.e., BC1 and BC3). The boundary strains produced during CPT would be beyond the elastic range of a simple thin walled, steel, confining cylinder and the boundary stiffness was, therefore, modelled by using a radial compression layer using natural rubber strips placed at certain spacings and covered with a thick layer of solid rubber (which distributed the load and filled out the annulus between the flexible sample membrane and the inner wall of the chamber). The design of the new boundary stiffness required an extensive preliminary research program which included the development of a full-length, axially placed, expanding cylinder designed to expand in three, approximately equal length sections, in plane strain expansion. The development of this expanding cylinder together with a complete testing program under various boundary conditions including a true infinite field condition is given in Chapter 5 and Appendix I. The results of the expansion tests were then used to develop a new method of analysing pressuremeter tests in sand. A theoretical approach based on the cylindrical cavity expansion in an elastic Mohr-Coulomb plastic material is given in Appendix II.

A major part of the new instrumentation included the placing of the designed rubber strips vertically together with the installation of a great number of strain gauges at different levels of the lateral boundary and the provision of enclosed pockets in the base and top of the chamber to measure or control the stresses and strains at different locations. Chapter 6 and Appendix III, respectively, summarise the calibration chamber's old and new features and the strain gauge installations.

Having modified the calibration chamber for the new boundary stiffness control and obtained the corresponding operating stress conditions, a series of cone penetration tests [named CP series] were conducted. Additional tests that did not conform to the designed boundary stiffness were also performed on both dense and medium dense samples under different stress levels and stress histories [originally intended for a contract to NGI in collaboration with STATOIL] in order

to determine the effect/usefulness of the designed boundary under different stress and density conditions. The analysis and the interpretation of the CPT data under the new boundary conditions with regards to the evaluation of engineering parameters as well as the confirmation and/or modification of the previous empirical correlations [as presented in Chapters 3 and 4] are given in Chapter 7. This also includes the boundary stresses as measured by the strain gauges during penetration together with those obtained from the theoretical analysis under similar confining stress conditions.

From the measurements of the lateral strain gauges it was realised that the calibration chamber might deform due to variation in the sand density giving a non-uniform stress around the boundary at any given depth. The effects of such a phenomenon on the resulting soil stresses have been discussed in Appendix IV.

Gross simplifications needed to be made in current theories concerning the mechanisms of expansion and penetration. Moreover, interpretation and assessment of particular output data, despite separate cone and sleeve measurements, seems to give guidance only to a single soil property. To achieve any realistic advance in theory or interpretation the detailed distribution of both stresses and strains in the material surrounding the penetrometers is needed. Clearly, this cannot be obtained directly, but can be reasonably deduced from the boundary stresses and strains for the plane-strain expanding cylinder. The results of such an analysis could then be used, together with the stresses and strains on the boundaries of penetrometer tests during penetration, to interpret the local stress/strain behaviour (as a function of radius, height, and degree of penetration) of the latter tests. To understand the mechanisms involved during both pressuremeter expansion and penetration testing, a mathematical model was developed for a transversely-isotropic material subject to an integrated series of cavity expansions. The elastic constants necessary for the model were obtained from the results of the expanding cylinder tests and of special triaxial tests in the calibration chamber (CC) as well as further small scale tests [see Appendix V]. This theoretical model and

its development are discussed in detail in Chapter 8. Appendix IV introduces a more direct approach to the expansion of cylindrical cavities in purely anisotropic elastic media and compares the results with those of the model.

In Chapter 9, first, a unique relationship between the expanding cylinder and the cone penetration test results is formulated. Then the components of the theoretical CPT model are combined for the different testing conditions used in the expanding cylinder test analysis. The obtained lateral pressure distributions at the outer soil boundary are compared with those deduced by the strain gauge measurements.

Chapter 10, finally, gives the conclusion of the research program together with future suggestions regarding the use of penetrometers and calibration chambers for further research.

CHAPTER 2

REVIEW OF PREVIOUS THEORETICAL AND EXPERIMENTAL WORK ON PENETRATION

2.1 Introduction

The cone penetration test (CPT) has been in common use since the 1930's primarily to determine layer sequence and thickness as well as the lateral extent of different layers. Initially, a mechanical cone was used and soon it was realised that the results could be related to the bearing capacity and shear resistance of the deeper sand layers on which piles were founded.

In the late 1960's, the CPT was greatly improved by the introduction of the electrical penetrometer (De Ruiter and Richards, 1983) which has permitted continuous measurements of cone resistance, q_c, and sleeve friction, f_s. This penetrometer has now become the major tool for offshore soil investigations and offers an almost exclusive capability for obtaining reliable information on the shear strength and deformation properties of soil deposits in deep water. The new generation of penetrometers could be remotely controlled, with automatic data acquisition. There are developments to include measurements of permeability, seismic activity, moisture content and soil resistivity.

The standard cone penetrometer in the CPT testing is 35.7 mm in diameter (10 cm^2) with a 60° apex angle which is pushed into the ground at a constant rate (usually 2 cm/sec). The penetration resistance at the tip of the cone as well as the friction along a 150 cm^2 sleeve placed behind the cone are measured. The work required to advance the penetrometer is interpreted as a measure of the soil strength so that a record of the variation of resistance to penetration with depth can provide both qualitative and quantitative information on the soil profile.

A historical background of penetration testing is given by Sanglerat (1972) and more recent state-of-the-art reports have been documented in ESOPT I (1974), CPTE (1981), ESOPT II (1982), and ISOPT I (1988), and equipment and procedure standards in ASTM D3441 (1979).

Cone penetration test results have been used qualitatively for soil classification, stratigraphy, type and variability by Sanglaret (1972), Schmertmann (1975), Dayal and Allen (1975), Baligh et al. (1980), Douglas and Olsen (1981), Jones and Rust (1982), Robertson and Campanella (1983), Senneset and Janbu (1984), Robertson et al. (1986), and Campanella and Robertson (1988).

In quantitative analysis, the following areas have used the CPT data:

1. Assessing mechanical properties of soils in-situ, e.g. strength, deformability, permeability and pore pressure prediction: Plantema (1957), Meigh and Nixon (1961), Rodin (1961), Begemann (1965), ESOPT I (1974), Schmertmann (1975), Torstensson (1977, 1982), Wissa et al. (1975), Mitchell and Lunne (1978), ESOPT II (1982), Keaveny (1985), and ISOPT I (1988).

2. Estimating pile length, capacity, settlement, and drivability: Kerisel (1961), De Beer (1967), and Schmertmann (1975).

3. Estimating bearing capacity, settlement, and safety factor for shallow foundations: Schmertmann (1970), Mitchell and Gardner (1975).

4. Assessing liquefaction potential of soils: Marchetti (1982).

A brief review of theoretical evaluations of the CPT data will be given in this chapter supplemented by a discussion of experimental techniques relating to the penetration mechanism. Studies of such theories and deformation patterns will give the background to the interpretation of previous CPT data from a calibration chamber and the principle of penetrometer calibration.

2.2. Theoretical Evaluation of Cone Resistance

In view of the complexity of the problem, it is perhaps unrealistic to seek a single formula to account for all factors which influence the mechanism of penetration. Numerous empirical and theoretical approximations already exist each with certain limitations which cause difficulties in their application.

The deduction of soil strength from the results of a cone penetration test is essentially a deep foundation bearing capacity problem in reverse. A measure of the ultimate bearing capacity of the sand (i.e., the tip resistance, q_c,) is known, a failure mechanism is assumed, and from this an estimate of the soil strength mobilised along the assumed failure surface is made. Theoretical failure mechanisms and/or empirical correlations based on field or laboratory data obtained under controlled conditions are used.

Cone resistance evaluations have been made by adopting certain computation procedures based on the classical theory of plasticity of a rigid-plastic body or on the theory of expanding cavities in an elastic-perfectly plastic material; this latter has allowed one to take into account, in an approximate way, the influence of the soil deformability in both elastic and plastic zones on the computed q_c values (Vesic, 1975; Al-Awkati, 1975).

Among the available computation procedures, several bearing capacity theories (e.g., Durgunoglu and Mitchell, 1973, 1975), cylindrical and spherical cavity expansion theories (Vesic, 1975, 1977), and recently the modified cavity expansion approach (Keaveny, 1985 and Mitchell and Keaveny, 1986) have been used to evaluate the cone resistance.

2.2.1. Limit Equilibrium Method - Bearing Capacity Theories

The limit equilibrium method is concerned with incipient failure under conditions of plane strain. This was originally applied to obtain the bearing capacity of piles and shallow footings for which mechanisms of collapse consisting of slip planes were assumed.

Most of the bearing capacity theories represent extensions of the classical work by Prandtl (1921) and Reissner (1924), whose solutions were applied to bearing capacity of deep foundations first by Caquot (1934) and Buisman (1935). These are illustrated in Fig. 2.1.

One of the solutions that somewhat differs in approach from all the others is that by Skempton, Yassin, and Gibson (1953), as shown in Figure 2.1.d. Their analysis is based on the work by Bishop, Hill, and Mott (1945), who had first presented a special case of expansion of a cavity inside a solid.

All the solutions for q_c are in the following general form:

$$q_c = c \cdot N_c \cdot \gamma_c + \sigma'_{vf} \cdot N_q \cdot \gamma_q \qquad (2)$$

where σ'_{vf} is failure effective vertical stress at the level of the foundation base, and N_c and N_q are bearing capacity factors with γ_c and γ_q being shape factors. The bearing capacity factors are given in the form

$$N_c = (N_q - 1) \cdot \cot\phi' \qquad (3)$$

and $$\gamma_c = (\gamma_q - 1/N_q) \; / \; (1 - 1/N_q) \qquad (4)$$

So, only N_q and γ_q are independent quantities. A single factor N_q^* is normally used for circular or square bearing areas such that

$$N_q^* = N_q \cdot \gamma_q \qquad (5)$$

Fig. 2.2 shows the values of bearing capacity factor N_q^* for deep circular or square footings, as obtained by different solutions. As evident from this Figure, there are appreciable differences in proposed N_q^* values, even if solutions based on slip lines extending back to the shaft are excluded. Among the latter(Fig. 2.1.b), Meyerhof (1961) presented data relating the bearing capacity of rough and smooth cones and wedges of deep piles to the depth. The measure of roughness was the ratio of the angle of friction between the cone and soil to the friction angle of the soil (δ/ϕ').

Another theory developed along similar lines is that of Janbu and Senneset (1974) but with a slight difference (Fig. 2.3). The theory was based on experimental results and on back calculation of values of bearing capacity factor, N_q, from plate loading tests. The experiments indicated that the failure mechanism did not extend back to the shaft

and was of quite limited extent, terminating on a plane at an angle (generally 15°) below the horizontal. This effect was attributed to the compressibility of the soil. It also incorporates a failure criterion in terms of an attraction, a, where $a = c \cdot \cot\phi'$, which must be estimated in practice from the q_c versus depth curve (Parkin, 1988). This parameter was included because the sand was believed to have a strength envelope which was linear but which did not pass through the origin.

The formula for cone resistance is

$$q_c = N_q \cdot (P' + a) - a \qquad (6)$$

where P' is effective overburden pressure, and

$$N_q = \tan^2 (\pi/4 + \phi'/2) \exp [(\pi - 2\beta)\tan \phi'] \qquad (7)$$

Although this theory is for plane strain only, and does not incorporate a lateral stress like the majority of other bearing capacity theories, it appears to work well in practice. Janbu and Senneset give a recommended range (also by Lunne and Christophersen, 1983; Chapman and Donald, 1981).

Durganuglu and Mitchell (1973, 1975) presented a bearing capacity equation based on the results of experiments on shallow footings. The mechanism generated for deeper foundations was suggested to have the form given in Fig. 2.4., with the assumption of general shear failure having to be used in order to obtain the solutions from the theory. This contradicts experimental results but, interestingly, the theory gives good results when used to predict the bearing capacity at large relative depths (Treadwell, 1976). They proposed the following expression for the evaluation of cone resistance in sand:

$$q_c = \gamma \cdot B \cdot N_{\gamma_q} \cdot \zeta_{\gamma_q} \qquad (8)$$

where γ is the unit weight of sand; B the base width of cone; N_{γ_q} the bearing capacity factor; and ζ_{γ_q} the shape factor.

This theory has the advantage of incorporating the lateral stress, only through the coefficient of earth pressure, K_o.

N_{γ_q} is a function of the soil friction, ϕ', base roughness (δ/ϕ'), relative depth of penetrometer (D/B), K, and wedge or cone apex angle. This factor, according to the authors, may be overestimated at depths greater than critical D/B (the depth just enough to contain the full failure mode), which means most practical situations. However, the fact that the failure mechanism was based on the results of tests at relatively shallow depths should not be overlooked (Last, 1982).

The bearing capacity relationship proposed by Durganuglu and Mitchell is able to match, in an approximate way, the variations of q_c with depth only if necessary consideration is given to the problem of the variation of the friction angle with depth (Durganuglu and Mitchell, 1975). In order to get agreement between measured and computed q_c values, it is necessary to allow for a decrease of the angle of friction in the plastic zone with increasing cone resistance, a phenomenon which reflects the non-linearity of the strength envelope.

The effect of apex angle on the variation of slip-line field geometry was included using finite difference approximation solutions (Nowatzki and Karafaith, 1972). Figs. 2.5 and 2.6 show the output from such an analysis for six different apex angles and the same base diameter. The results show a contraction of the radial shear zone with the decrease in cone angle. The active, passive, and radial shear zones all have curvilinear boundaries because of the three-dimensional nature of the problem and is clearly different from the classical Prandtl solution for weightless soil which involves logarithmic spirals in the radial shear zone. The analysis assumed a slip-line field which ends at the base level and in so doing ignored the shear strength of the

overburden. There was also no consideration for the effects of dilation and it does not represent deep penetration.

2.2.2. Cavity Expansion Theory

Results from cone penetration tests have shown that large plastic deformations of the soil medium occur in the immediate vicinity of the probe while smaller elastic deformations exist over a wide region beyond this plastic zone (Addo, 1983). This theory is concerned with the expansion of either a spherical or cylindrical cavity in an infinite medium (Gibson, 1952; Vesic, 1965; Chadwick, 1959; and Gibson and Anderson, 1961) and since its early development many authors have attempted to improve it by including more realistic soil properties (Ladanyi, 1963; Vesic, 1972, 1975, 1977; Baligh, 1976; and Baldi et al., 1982). Schmertmann (1975) reported on the work of Al-Awkati in determining ϕ' from pressuremeter test data, in which the effect of volume change in the soil was considered. Hughes et al (1977) also accounted for volume change in sand by assuming that the sand fails with constant ratio of principal stresses. The dilatant behaviour of the sand was modelled by a linear volumetric stress- strain relationship.

The cone resistance is given by:

$$q_c = q \cdot N_q^* \qquad (9)$$

where

$q = [(1+2 \cdot K_o)/3] \cdot \sigma_v'$ = initial octahedral normal effective stress

σ_v' = vertical effective stress

N_q^* = bearing capacity factor

This also takes into account the stiffness and compressibility of the soil by using a reduced rigidity index, I_{rr}, defined by

$$I_{rr} = \zeta_v \cdot \frac{E}{2(1+\nu)(c+q\cdot\tan\phi)} = \zeta_v \cdot I_r = \frac{I_r}{(1+\Delta\cdot Ir)} \qquad (10)$$

where ζ_v = Volume change factor incorporating the average volumetric strain in the plastic zone

E = Young's modulus = $2G(1+\nu)$

G = shear modulus

ν = Poisson's ratio

I_r = rigidity index.

Vesic originally proposed the use of the initial tangent Young's modulus to calculate rigidity index, but a much better correlation between calibration chamber measurements and theoretical cone resistance has been obtained by using the secant modulus at a deviatoric stress level of 50% (E_{50}) of that required to cause failure in a triaxial test (Keaveny, 1985).

Vesic's approach based on the theory of the cylindrical expanding cavity can also be used to obtain the following approximate formula for q_c when cohesionless materials with curved strength envelopes are considered (Baldi et al., 1981):

$$q_c = P_u \cdot \lambda \cdot \left[1 + \tan\left(\frac{\pi}{4} + \frac{\phi_s}{2}\right) \cdot \tan(\phi_s)\right] \cdot \exp\left(\pi/2 - \phi_s\right) \qquad (11)$$

where P_u = ultimate pressure of the expanding cavity in an elasto-plastic infinite medium,

λ = empirical shape factor = $1+\tan\phi_s$ (Vesic, 1974), and

ϕ_s = secant angle of friction related to the average effective stress at failure in the plastic zone.

The corresponding equation for the spherical expanding cavity is (Vesic, 1977)

$$q_c = \frac{P_u}{1 + \sin\phi_s} \cdot \tan^2\left(\frac{\pi}{4} + \frac{\phi_s}{2}\right) \cdot \exp\left[\left(\pi/2 - \phi_s\right) \cdot \tan\phi\right] \qquad (12)$$

where P_u is the same pressure as before but for a spherical cavity.

Given strength envelope, Young's modulus, and volumetric strain relationships, P_u values have been evaluated using the theory proposed by Baligh (1975)- a non-linear strength envelope theory- by means of the computer programme EXPAND developed at the Civil Engineering Department of Massachussetts Institute of Technology. Comparison of the results from Vesic's expansion theory and from calibration chamber tests (Baldi et al., 1981) shows that, in the case of dense and very dense sands, computed q_c values are in reasonable agreement with those measured in the calibration chamber. Generally, one observes that a spherical cavity approach matches the experimental values better at shallow depths, while cylindrical cavity theory gives better results for greater depths. Also, the agreement between measured and computed q_c values is better for CC tests performed under BC1 (σ'_v = constant and σ'_h = constant). For tests under BC3 (σ'_v = constant and $\Delta\varepsilon_h$, change in lateral strain = 0), measured q_c is slightly higher due to the increase of the radial stress during penetration, a phenomenon which becomes pronounced with increasing D_r.

In the case of medium-dense sand, all measured q_c values fall on or slightly below the lower limits of the computed q_c values (in conjunction with soil parameters from drained-triaxial tests).

The application of Vesic's theory, however, will require some knowledge or assumption of the volumetric strain in the plastic zone and its effect on the measured cone resistance. Analysis of several sands by Mitchell and Keaveny (1986) showed most to exhibit dilatant behaviour during triaxial deformation (i.e., Δ was negative, meaning that Δ is assumed to be zero due to Vesic's formulation, thus making

reduced rigidity index equal to rigidity index). Under these circumstances and with the theory being unable to formulate the dilating behaviour of the yielding soil around the expanding cavity, the influence of ε_v on q_c is neglected. The assumption of $\Delta=0$ has been shown, however, to have little effect on the results of the tested sands.

On the other hand, positive (compressive) volumetric strain during shear will have a significant effect on the reduced rigidity index. A decrease in reduced rigidity index for a given ϕ' causes a decrease in the bearing capacity factor (Vesic, 1975, 1977).

Measurements of volume change around an advancing miniature probe within a triaxial specimen were made by Miura et al. (1984) and were found to be comparable to that measured in a triaxial extension test. More importantly, dilatancy did not develop around the advancing probe until the sand had a relative density of more than 75%. Thus, it might be reasonable to assume that volumetric shear strain is equal to zero during cone penetration into sands that are dilatant in triaxial compression tests.

2.3. In-Situ Evaluation of Deformation Characteristics

Available in-situ techniques for the evaluation of deformation characteristics of soils can be classified in the following three categories (Baldi et al., 1988):

i. When all strained soil elements follow a very similar effective stress path (ESP), deformation modulus can be calculated from theory, e.g. self-boring pressuremeter (SBP) and elastic body waves (EBV).

ii. When strained soils follow different ESP's, an average equivalent modulus of deformation of semi-empirical nature is

computed from simplified assumptions, e.g. plate loading test.

iii. When penetration testing (SPT, CPT, DMT, etc.) induces large straining of the surrounding soil, only purely empirical correlations with deformation moduli are possible.

This classification of the in-situ tests suggests that correlations between penetration resistance and deformation characteristics of soils are far from fulfilling the basic requirements suggested by Wroth (1984, 1988), which are

- Physical appreciation of why correlation is expected to work;
- Theoretical background, however simplified or idealised;

and further by an additional requirement (Baldi et al., 1988):

- Validated by large scale laboratory tests and prototype performance.

One may argue that the links between penetration resistance and deformation characteristics of sand are certainly not very strong and therefore, with few exceptions, are of purely empirical nature.

2.3.1. Displacement Measurement Techniques within Sand Samples

It has always been of interest to be able to obtain detailed experimental information regarding displacements and strains within a granular medium subjected to penetration by a probe. The techniques have been very limited, especially for deep penetration. Some qualitative measures of soil failure modes and deformation patterns were provided by the use of layered coated sand. Layers of coloured sand were mixed with cement. After the test, water was allowed into the mix and the mix was left to set. The set mix was then sectioned for examination. Such a method was never adequate for quantitative analysis. In another case, an inductance type gauge was used to record soil movement around foundations. Such gauges did not gain support in

that they were relatively large and caused disturbances of the soil during installation.

A successful method for measuring plane-strain soil deformation was developed by Butterfield et al., (1970). A pair of photographic plates taken at the start and the end of a displacement increment were used in a stereo photogrammetric technique. The method is generally cheap and can be used for very detailed examination and measurements, provided highly accurate photographic equipment is used. It is particularly good if the deformation mechanism is in the form of relative body displacements.

An alternative method to derive such strain data is by radiographic techniques using discrete lead markers. The pioneer of such study was Roscoe at Cambridge University in the early sixties. Addo (1983) used this technique together with the stereo photographic method as a qualitative back up in some tests to study details of sand movements in a plane strain condition, and, in particular, to search for thin slip surfaces which could not easily be differentiated by X-ray methods. The transmitted X-ray beam out of the medium is usually detected by photographic means to reveal a scatter shadow of the latent internal structure. The strains were measured by inserting a regular grid matrix of lead shot into the middle of the sand medium. When the sand is irradiated from the front, only the X-rays which transverse the sand sample can produce an image on radiographic film positioned at the back of the sample. Radiographs taken at different stages of the test can then be compared using two radiographs at a time. By superposition, the relative movements of the positions from the images of each shot are measured. From the measured displacements, strains can be measured. It is also possible to determine the dilational behaviour of the sand which is proportional to the apparent exposure of the resultant radiographic negatives.

The penetration mechanism of a more realistic three-dimensional axisymmetric problem using X-ray analysis was studied by Chen (1986). He managed to prepare suitable test samples with lead shot in a vertical plane along the radius of the sample. He obtained experimental measurements of the displacements around a cone penetrometer in a cylindrical sample in three-dimensions.

Addo's experiments had shown that the small absolute values of volumetric strain in the elastic zone are cumulatively significant because the extent of this region is large. Hence, Chen combined Last's (1982) solution for an expanding spherical cavity, in which plastic and elastic volume changes in the plastic zone were treated separately and no volume changes were accounted for in the elastic zone, so that all elastic and plastic volume changes could be accounted for simultaneously. The results of his study are given in the following section.

Baligh (1984) developed a closed form solution for a probe penetrating an incompressible homogeneous isotropic material initially subjected to an isotropic state of stress. A spherical cavity is allowed to expand at a specific volumetric rate in this material as the material flows past. He found that directly beneath the probe (Fig. 2.7), the direct simple shear strains (obtained through a procedure of integration) are relatively small and such that the major principal strain acts in the vertical direction. In zones II and III the direct simple shear strains and those associated with cylindrical cavity expansion (i.e., a mode of failure associated with a pressuremeter test) rapidly increases at similar rates. In zone IV the major principal strain is that associated with the condition imposed during a pressuremeter test (plane strain condition).

2.3.2. Deformation Patterns around an Advancing Cone

There have been numerous arguments about deformation patterns around and under advancing probes and cones in sand. From a review of the past studies of the failure mechanisms associated with static penetration, including Vesic (1963, 1967), Robinsky and Morrison, 1964), Durgunoglu and Mitchell (1975) and Keaveny (1985) several conclusions can be drawn concerning a probe (such as thin rods or steel balls) penetrating soil or a soil simulant:

1. A zone approximating the shape of a wedge is found beneath the pile extending downwards and outwards from the edge of the pile point. This wedge is conically shaped for circular probes and wedge shaped for rectangular probes (Figs. 2.8 and 2.9). The soil within the above mentioned wedge is highly compressed in that it is subjected to high confining stresses relative to the initial confining stress of the soil and predominantly two-directional horizontal expansion takes place away from the pile point, accompanied by radial downward translation. Subsequently it has a higher stiffness than the surrounding soil.

2. For rectangular shaped probes (i.e. strip footing), in relatively incompressible soils with a penetration depth to probe diameter ratio (D/B) of less than about 10, a distinct general shear surface , i.e., a slip line of a radial shear zone, emanates from the tip of the wedge to the ground surface (Figs. 2.9 and 2.10). These slip lines can be closely approximated by a logarithmic spiral.

3. For circular shaped probes (i.e., piles and penetrometers) at D/B values equal to and greater than 1, no distinct shear surface has been observed beyond the immediate vicinity of the tip in any soil. This implies that in dense, and also loose, sands a punching shear or at best a local shear mechanism occurs around an advancing penetrometer (Figs. 2.8 to 2.11).

4. A deep probe, therefore, regardless of its diameter or the shape, strength, or rigidity index of the soil it is penetrating, appears to fail the soil in the same manner, i.e., in a punching shear mechanism under the conical tip.

a. Experimental Studies by Chong (1983, 1988)

Chong (1983, 1988) performed a series of CPT on sand with different densities and measured density changes and deformation patterns. During sample preparation, thermocouple needle probes were embedded in the sand to measure the density changes around the penetrometer and on the shaft immediately above the cone at different stages of the penetration.

The probe contained a constantan heater wire and a copper constantan thermocouple located at midheight of the tubing and was filled with silicon oil. The probes detect changes in thermal conductivity in the sand due to the changes in the density. The thermal conductivity was calculated based on a line heat source theory by measuring the temperature at the centre of the probe at different times.

The results showed that the sand close to the shaft of the penetrometer had undergone considerable loosening as a result of penetration (Fig. 2.12 - zone 1). The decrease is maximum at a relative depth of 8 (Fig. 2.13) and then followed by a lesser decrease in density with increasing penetration depth.

In the areas surrounding the penetrometer, loosening occurred for the dense sand in the form of 'V' shape and for the medium dense sand in the form of an irregularly outlined 'U' shape (Fig. 2.12- zone 2). Further away from the penetrometer, densification had generally occurred, with some randomly scattered areas of slight loosening

(Fig. 2.12 - zone 3). In the zone immediately beneath the cone tip, loosening occured for dense sand while densification occured for looser sands (Fig. 2.12 - zone 4).

Density changes were used to calculate the volumetric strain values throughout the sample. These strains immediately behind the cone vary greatly from dilation at the penetrometer surface to compression some distance away. The volumetric strains, as a function of the relative radial distance from the axis of the penetrometer are shown in Fig. 2.14.

The volumetric strain data were used as inputs to the spherical cavity expansion theory of Vesic (1972) in order to compute cone resistance values. This theory was used for a blunt cone with a modification factor to account for a rough cone with 60^{o} apex angle [the radius of the perceived hemisphere beneath the cone tip (at the end of the cavity expansion) being equal to the radius of the penetrometer].

Fig. 2.15 shows the computed and measured q_c values. For medium dense sands the computed cone resistance, using an average of the volumetric strain at a relative radial distance of 7, was lower than the measured cone resistance. In the case of dense sands, the computed cone resistance, taking the volumetric strain to be zero and ignoring dilations at the cone tip and base, agreed fairly well with the measured ones.

b. Experimental Studies by Addo (1983)

Addo (1983) performed X-ray studies of a plane-strain wedge penetration under four different boundary conditions in relation to soil density and stress level giving the following results:

The displacement field in loose sands showed no distinct particle movement. The same pattern seemed to occur equally in dense sand as well, except for the large extent of the major movement in the latter case. In general, the deformations around the penetrometer were similar irrespective of the boundary conditions. Close to the probe, soil was pushed downwards and then outwards on both sides of the tip. The effect became apparent further away. Outside the immediate surrounding of the probe, the favoured direction of particle movement was controlled by the disposition of the flexible boundary. As might, perhaps, have been expected, the all-rigid test and all-flexible test results showed most similarity while the other boundary condition tests (side-flexible base-rigid test and side-rigid base-flexible) results were the most contrasting. Typical patterns of displacement fields which propagated ahead of the tip are shown in Figs. 2.16 and 2.17 under BC1 and BC3. These showed that the direction of the dominant movement was towards the flexible boundary.

The penetration mechanism can also be observed from the volumetric strain data, as shown typically in Figs. 2.18 and 2.19 for loose and dense sands under BC1 and BC3. It was believed that the penetration process took place with soil elements undergoing a complex loading and unloading path. The loading initiated compaction well ahead of the probe with dilation being started by the high shear strain in the near vicinity of the tip followed finally by some recompression mainly behind the tip adjacent to the shaft. In loose sand, the material is found to be compressed along the shaft, (as also found by Robinsky and Morrison, 1964) whereas in dense sand, the material along the shaft has been loosened (as seen from Chong's study). The above figures also show that the zones of dilation are localised around the tip in loose sand whereas in dense sand dilation is apparent along the shaft as well with finger-like zones extending horizontally. This consistent pattern could suggest that a block mechanistic mode may tend to develop with zones of discontinuous slipping.

Based on the above results, Addo (1983) proposed a mechanism for deep penetration (Figs. 2.20). The volumetric strain data suggested dilatant rupture lines which are shear bands separating block zones. The envelope which enclosed the instantaneously failing zones and the area previously failed are shown in a simplified smoothened form in Fig. 2.21c. The exact extent of the precompressed zone, below the failed bulb at the tip varied with the test boundary conditions and was believed to vary with soil density. The stress-strain response of the different zones is indicated in Fig. 2.21d. The block mechanism of Fig. 2.20a is similar to the local, steady-state, shear mechanism proposed by Last (1982) whereby zone R represents a sustained cavity around the shaft and the radial compression zone corresponds to a cavity at the tip. Zone T is the region through which the cavity at the tip, probably, spherical, degenerates into a cylindrical cavity around the shaft. Beyond the critical depth, the size of the cavity around the probe would not be expected to increase significantly and hence penetration into an infinite medium is believed to become a steady-state process.

c. Experimental Studies by Mahmoud (1985)

Mahmoud studied the effect of different penetration probe shapes on the kinematics of plane strain soil deformation in a rigid rectangular tank 1.0m x 1.0m x 0.4m (length x height x width). The ratio of the tank length, where deformation patterns are studied, to the 20mm dia. cone with parallel sided shaft is 50. [Calibration chamber tests, as discussed in the next two chapters, will show that this ratio needs to be maintained in order for the penetration results not to be affected by the boundary conditions].

The penetrometers were buried in the sand before the test, and, therefore, pull-out tests were done rather than actual penetration ones. Only the results of his studies on parallel sided shaft penetrometers are, briefly, described below:

Typical displacement patterns for dense sand, for shallow penetration (D/B = 3.5) and deep penetration (D/B = 20), are shown in Figs. 2.22 and 2.23, respectively. In shallow penetration the particle movement directly adjacent to the tip remains horizontally outward but, further out from the probe, the material is pushed outward and upward. In deep penetration, on the other hand, the material around the tip is pushed laterally outward and downward. Above the probe tip, the particles seem to move outward and slightly upward near the surface. Davidson et al. (1981) reported the same phenomenon occuring in CPT's on dense sand (Fig. 2.24).

d. Experimental Studies by Chen (1986)

Finally, in this section, a summary of Chen's three-dimensional X-ray analysis of the displacement patterns during CPT under different boundary condition is discussed. His aim was to use the displacement data to see whether or not the displacement vectors radiated from one fixed point [i.e., based on theories of continuum which assume homogeneous behaviour, e.g. expanding cavity theories]. He also checked the data against block mechanisms of various forms [e.g. limit equilibrium and bearing capacity methods] such as those of Addo (1983) and Last (1982).

A more qualitative comparison was made by studying the lateral and vertical components of the displacement vectors. Fig. 2.25 shows the lateral component for 'all-flexible' and 'all-rigid' dense and loose tests. The most obvious trend from these diagrams is that the bulb of significant displacement is much larger in the dense tests. The only difference, however, observed between the all-flexible and all-rigid tests is that the absolute displacements are slightly more restricted in the all-rigid cases.

The results of mixed boundary tests (Fig. 2.26) confirmed the findings of Addo (1983) where the zone of major movements was towards the flexible boundaries.

Density and boundary effects can also be observed from the shear strain plots, obtained from the displacement data, for different stresses (Fig. 2.27). The general trend is that the region appears to be larger in the dense tests, the contrast being very severe in the all-rigid tests. The size of the zones seem to be the same for loose tests regardless of the ambient stress level in the all-flexible tests (a and b). There is also a marked tendency for fingers of plastic zones to form in the dense test (most intense in the all-flexible cases), which is believed to be the result of the low imposed lateral stress. The zones of plastic deformation in the all-rigid tests appear to reach opposite extremes. Hence, the plastic bulb in the loose test is smaller than for the all-flexible cases, while in the dense tests it is significantly larger.

Based on these observations, Chen developed an analytical model based on the expansion of a spherical cavity in a Mohr-Coulomb material which allowed elastic volume changes in the elastic zone and elastic as well as plastic volume changes in the plastic zone. The analytical data obtained from considering three boundary conditions were then compared with the experimental data. There appeared to be a mismatch between theoretical and experimental results which was believed to be caused mainly by incorporating the enormous expansion required for the build-up of the cavity pressure; thus giving theoretical displacements not relevant to those in the near vicinity of the tip.

2.4. Review of Procedures to Calibrate Penetrometers in Sand

Interpretation of cone penetration tests is normally based on empirical correlations between the measured cone stresses (namely cone resistance and/or sleeve resistance) and soil properties that may be

used in geotechnical analyses.

In the case of cohesive soils, the most obvious way to calibrate is to perform field vane tests or to recover undisturbed samples for standard laboratory testing, allowing CPT outputs to be compared with field results via theory.

In sands, however, there is a real difficulty in relating cone stresses to design parameters. Firstly, there is no equivalent of the field vane tests for sands to determine an in-situ strength parameter directly. Secondly, laboratory testing of undisturbed samples of most sands is difficult and does not provide an alternative approach as it does for clays. Two approaches to cone penetration testing are, therefore, currently in use for the interpretation of results.

The first approach is to correlate the measured cone stresses directly with measured performance. For example, the measured ultimate bearing capacity of a pile may be expressed as a function of the measured q_c value. It is noted that a sound understanding of the behaviour of the CPT and the foundation design problem is still required if this methodology is to be useful.

The alternative approach to CPT interpretation in sands is to use large-scale laboratory calibration chamber (CC) tests. A sample of known material at a known density is prepared in the chamber and then subjected to the desired stress level. The cone is pushed into the sample and the cone tip resistance and the sleeve friction determined. Laboratory tests (usually triaxial tests) are then carried out to determine the engineering properties of the sample in the chamber. The cone stresses can then be related either directly to the engineering properties (such as friction angle, ϕ') or can be related to relative density with the engineering properties in turn being defined as a function of relative density. This approach will be adopted in this section.

2.4.1. Cone Resistance versus Relative Density - Stress Level

Many attempts have been made to calibrate penetrometers through measured cone stresses. These have been correlated to other parameters over limited ranges.

In sands, it is almost universal practice to correlate cone results against relative density, D_r. Work in large scale calibration chambers (Veismanis, 1974; Harmon, 1976; Parkin et al., 1980; Baldi et al., 1981; Chapman and Donald, 1981; Villet and Mitchell, 1981; Bellotti et al., 1985) has provided numerous correlations of cone resistance with relative density. Most of these works have also shown that no single unique relationship exists between relative density, in-situ effective stress, and cone resistance for all sands, because factors such as soil compressibility also influence cone resistance. Schmertmann's (1978) results of tests on a highly compressible sand, Baldi et al.'s (1982) on a moderately compressible sand, and those of incompressible sands (Villet and Mitchell, 1981), respectively, have shown that compressible sands result in lower cone resistances at both loose and dense states than do less compressible sands.

Tumay (1976) analysed the variance of the results of a large number of CC tests performed at the University of Florida and showed that relative density and effective stress are the most important variables influencing cone resistance, while less important factors are stress history, sand type (valid only for predominantly quartz sands), boundary conditions, and moisture level.

Schmertmann (1976) and Harman (1976) analysed several different correlations of cone resistance with relative density and stress level to find the best fit of CC data. Schmertmann then suggested the following relationship for NC sands

$$q_c = C_o \, \sigma'^{C_1}_v \exp (C_2 \cdot D_r/100) \qquad (13)$$

where C_o, C_1, and C_2 are experimental coefficients, and q_c and σ'_v are in kg/cm^2.

Bellotti et al. (1985) found that in OC samples alone, or in combination with the NC ones, q_c is best related to relative density through either horizontal or mean stress. Based on regression analyses carried out on the CC experimental data, they generalised Eqn. (13) for all stress histories and suggested a range of C_2 values for both Hokksund and Ticino sands [0.53 to 0.57 and 0.54 to 0.73, respectively]. Parkin (1988) believes that this generalised relationship which uses a vertical stress for NC samples and a lateral or mean stress for OC samples (or NC + OC samples) does not differentiate whether the coefficient of earth pressure at rest, K_o, is greater or less than one, or whether σ'_h is changing as in a BC3 test. These factors, in his opinion, would naturally influence the degree of dependency of q_c on the stress level used.

In an attempt to account for the OC samples, Schmertmann (1978b) recommended the following equation, based on CC test results, for calculating an equivalent NC cone resistance from the OC samples:

$$\left(q_{c_{OC}} / q_{c_{NC}}\right) = 1 + 0.75 \left(K_o^{OC} / K_o^{NC} - 1\right) \qquad (14)$$

Also

$$K_o^{OC} / K_o^{NC} = (OCR)^{0.42} \qquad (15)$$

Lunne and Christophersen (1983) updated Eqn. (13) to account for the boundary effects, and suggested a 30% increase to the Schmertmann curves for very dense samples.

In an attempt to estimate sand deformability on the basis of CPT data, Lancellotta (1983), however, developed a correlation between D_r and q_c through σ'_v from a regression analysis on five different sands. This correlation, as given in Fig. 2.28, is applicable to NC, uncemented, unaged, sands in which quartz minerals are predominant. The correlation is not, however, directly applicable to OC sand deposits for which no unique relationship exists between D_r and q_c through σ'_v [Schmertmann (1976) and Baldi et al. (1983 and 1985)].

Lancellotta's relationship through effective stress is also thought to be influenced by grain size and minerological composition, structure, and crushability of the test material (Baldi et al., 1981).

In conclusion, it is necessary to point out that the relationships discussed so far suffer at present from some uncertainties linked with the fact that they have all been established on freshly deposited sands. The tendency to infer σ'_h and/or OCR from the results of the penetration tests is quite recent. The insertion of the penetrometer into the sand changes the geostatic stress conditions drastically, so that the horizontal stress surrounding the penetrometer increases to a value above the K_o stress. The change in these stresses depends on relative density and effective confining stresses. In dense soil, the σ'_h may, however, tend to decrease with time due to relaxation. This soil-penetrometer interaction illustrates the difficulties faced when soil parameters, describing the initial state, are inferred from any kind of penetration tests.

2.4.2. Cone Resistance - State parameter

Extensive testing on a Canadian sand (Been and Jefferies, 1985; Been et al., 1987) has shown that the bulk characteristics of sands are not sufficient to characterise mechanical behaviour of granular materials (see also Lee, 1965; Lade, 1972). Confining pressure, in particular, modifies the material behaviour of sands: if tested at

sufficiently high confining pressure, a dense sand will behave similarly to loose sand at lower confining pressure. Therefore, properties of sands cannot be expressed in terms of relative density alone and a description of stress level must also be included.

In this regard a sand, tested with several silt contents and under very different combinations of void ratio and mean effective stress, will behave similarly if there is an equal initial proximity to the steady state, defined by a state parameter (Fig. 2.29) [Been and Jefferies, 1985]. The physical state of the soil is represented in void ratio–log stress space. A reference state is defined in order to quantify the state of a soil, the steady state line providing the reference state for sands and the void ratio distance from this line, Ψ, the state parameter. It is claimed that Ψ can be used to describe much of the behaviour of granular materials over a wide range of stress levels and relative densities, and that this emphasises the fact that it is the combination of these conditions that is physically relevant to the description of granular material.

Calibration chamber test programmes do provide a valid and useful data base for the interpretation of the state parameter for a tested sand. But, it is unrealistic to carry out CC tests on every sand or natural sand deposit. By utilising the state parameter concept many sand properties, in particular failure parameters commonly used in bearing capacity analyses, normalise very well with respect to Ψ. The relationship between normalised cone resistance and the state parameter for different sands has been evaluated (Been et al., 1987 and 1988). This relationship is illustrated in Fig. 2.30. In the evaluation of Ψ from q_c, a knowledge of the in-situ stresses and the value of λ_{ss}, which is the slope of the steady- state line in e-log p' space, is necessary. Laboratory tests are, therefore, required to determine λ_{ss} (Castro, 1969; Casagrande, 1975; Poulos, 1981; Castro and Poulos, 1977).

Having obtained the steady state line for Hokksund sand [i.e., $\lambda_{ss} = 0.056$], Been et al. (1986) used the void ratio and stress conditions of each CPT test result from CC in order to calculate Ψ and, hence, obtain a relationship between q_c and Ψ in the form

$$\frac{q_c - \sigma'_m}{\sigma_m} = k \cdot \text{EXP}(-m\Psi) \qquad (16)$$

From the graphs provided by Been et al., the constants k and m were deduced, approximately, as 25.8 and 11.3, respectively.

2.4.3. Overconsolidation Ratio (OCR)

The influence of overconsolidation on a cohesionless soil can be divided into two factors. The first one is the strain hardening of the material produced by the accumulated plastic strain. The second one is the increase in σ'_h for a given level of σ'_v, or $K_o^{OC} > K_o^{NC}$. Work by Mesri and Castro (1987) shows that this last factor is linked with mechanical overconsolidation only [in clay K_o increases with aging] while the plastic hardening of the soil appears as a consequence of all types of preconsolidation mechanisms, i.e. aging, cementation, stress history induced by earthquakes and wind loading, etc.

Large scale (CC) laboratory tests have shown that penetration resistances are influenced by the current level of σ'_h and remain insensitive to the effect of the accumulated plastic strain as is the case with deformation moduli.

2.4.4. Deformation Characteristics of Sands

The deformation characteristics of sands are defined using the laws of continuum mechanics, with the soil behaving as a linear isotropic material. However, experimental evidence suggests that a linear elastic cross anisotropic model becomes more realistic (Wroth

and Houlsby, 1985).

It is generally accepted that the deformation characteristics of a given soil depends on the stress and strain history of the soil, including the current level of the mean effective stress, the induced level of the shear strain, the effective stress path (which reflects both anisotropy and plasticity) and, finally, on a time factor, e.g. for phenomena like aging and creep in shear (Jamiolkowski et al., 1985). Therefore, the safe use of correlations between cone resistance and soil moduli, from a qualitative point of view, depends on the skill of the engineer to account for the factors mentioned above.

Sand stiffness can be described by various parameters including Young's modulus, E, Shear modulus, G, and Constrained modulus, M, which are related via Poisson's ratio, ν, (at least at first loading). Of these, M, measured in a K_o situation as in the calibration chamber, is the one most directly relevant to structural settlements [M is defined as the tangent modulus evaluated considering the increments of vertical stress and strain during the final load increment (for NC samples) and as the tangent modulus evaluated considering the changes of the vertical stress and strain during the last stage of the unloading process (for OC samples)] . E and ν are normally obtained from drained triaxial tests and G is derived from pressuremeter tests.

a. Constrained Modulus, M

Due to the complexity of the penetration process, there is no generally applicable analytical solution available to correlate cone resistance to constrained modulus. Instead, many empirical correlations have been proposed for a range of predominantly quartz sands which take the form $M = \alpha \cdot q_c$ where the factor α is generally recommended in the range of 1.5-4.0 (Mitchell and Gardner, 1975), the smaller α values being used when q_c exceeds a certain limit. Considerable confusion appears to exist as to whether or not this relationship should remain

constant with depth. Vesic (1970) proposed this factor to be a function of the relative density in the form $\alpha = 2(1 + D_r^2)$. Dahlberg (1974) found α to increase with q_c based on M values obtained from screw plate tests for precompressed sand.

The constrained modulus is considered to vary, nearly, with the square root of stress (Janbu, 1963). Baldi et al. (1986) has included other parameters such as OCR and D_r. On the other hand, M has also been expressed as a function of cone resistance. Senneset et al. (1982) considers M to be a function of the square root of net resistance $(q_c - \gamma \cdot h)$, applicable to all stress levels and OCR. This conflicts with Baldi et al.'s (1986) suggestion that M/q_c is a function of σ', OCR, and D_r. Based on field and laboratory results, a linear relationship was found between M and q_c by Lunne and Christoffersen (1983).

b. Shear Modulus, G

Based on extensive laboratory work (Seed and Idriss, 1970; Hardin and Drnevich, 1972), correlations have been developed for sands between cone resistance and the dynamic shear modulus, G [obtained from resonant column tests (RCT) and in-situ tests using elastic body wave (EBV) propagation tests]. Having found such correlations, it should be possible to estimate the shear modulus at any strain level using some reduction curves developed by Seed and Idriss (1970). Byrne and Eldridge (1982) suggest that the initial tangent modulus under static loading condition is about 1/5 the dynamic modulus. This includes the combined effect of strain level and repeated loading.

As mentioned earlier, Baldi et al. (1986, 1988) believe that q_c bears a more fundamental relationship to G than to M or E as G is little affected by stress and strain history (borne out by the large number of experimental data that show G for cohesionless soils is influenced very little by the stress and the strain history of the sand). For a given cohesionless soil this modulus is mostly a function

of the following variables (Yu and Richart, 1984):

$$G = f\ (D_r,\ \sigma'_a,\ \sigma'_b) \qquad (17)$$

where:

σ'_a = effective stress acting in the direction of seismic wave propagation, and

σ'_b = effective stress acting in the direction of soil particle motion.

It is noted that G/q_c depends strongly on D_r but only moderately on the stress. Parkin (1988) believes that the product $(D_r/100)\cdot(G/q_c)$ varies relatively little over the range of study (3.0 to 5.5).

In an attempt to model the penetration mechanism, Greeuw et al. (1988) obtained the following relationship for shear modulus as a function of relative density from triaxial tests in a cylindrical 1.9 m diameter chamber:

$$G\ [MPa] = G_o \left(\frac{\sigma'_m}{P_a} \right)^{0.5} \cdot D_r^{\alpha} \qquad (18)$$

with σ'_m, being the isotropic pressure = $\frac{1}{3}\left(1 + 2\ K_o\right)\ \sigma'_v$

and P_a, a reference stress = 1 kg/cm²

The measured shear moduli for a dry uniform fine sand (Oosterschelde) ranged from 29 to 370 MPa. He points out that even apparently identical samples gave a variation in G of more than a factor 2.

Cone resistance has been plotted against dynamic shear modulus for Ticino sand (TS) using the CC test data (Baldi et al., 1986), resonant column tests (Lo Presti, 1987) obtained on pluvially deposited TS with the field data of cross-hole tests and CPTU's performed on medium to fine Po River silica sand (Baldi et al., 1988) [Fig. 2.31].

2.4.5. Prediction of Sand Strength

In coarse grained soils where penetration takes place under drained conditions, the penetration test results are used to evaluate the drained shear strength expressed as the friction angle, ϕ'. It is generally a normal practice to determine the friction angle, once the relative density is agreed upon, either by triaxial tests or some empirical correlations. There has been a tendency, lately, to estimate friction angle directly, without reference to relative density. This can be done via a bearing capacity factor, N_q, in the form $q_c = P_o.N_q$ (Koumoto, 1988) in which P_o is considered to be a function of overburden pressure at the cone base. Bearing capacity factor, in turn, is a function of ϕ'. Robertson and Campanella (1983) reviewed a series of calibration chamber test results in order to compare the measured cone resistance with measured friction angle from drained triaxial tests, which were performed at confining stresses approximately equal to K_o condition. The result of this study is shown on Fig. 2.32. Based on the average relationship obtained from this figure, a design chart was then proposed by Robertson and Campanella for estimation of friction angle from cone resistance for given vertical stresses (Fig. 2.33).

The methods generally used for the determination of sand strength can be divided into three categories:

(a) those based on bearing capacity theories [such as Durgunoglu and Mitchell (D & M) (1973, 1975) and Janbu and Senesset (1974)];

(b) those based on cavity expansion theories [Vesic (1975, 1977), Keaveny (1985) and Mitchell and Keaveny (1986)]; and

(c) an empirical method proposed by Been et al. (1985) based on the state parameter, Ψ.

In the analysis of several sands, Mitchell and Keaveny (1986) obtained similar sand strength values using the D & M bearing capacity, (a), and the state parameter, (c), methods. Being based on a theory that takes no account of the compressibility, the D & M method underpredicts the actual peak triaxial friction angle by up to 15% - for Hokksund sand the underprediction is more than 5°.

The prediction of peak triaxial friction angle made using the Vesic's expanding cavity theory show good agreement with the measured values (Mitchell and Keaveny, 1986). The method originally developed was modified by using Young's Modulus corresponding to 50% of the deviatoric stress at failure rather than the initial tangent modulus (Keaveny, 1985). Cavity expansion theories which can account for nonlinearity in the strength envelope and soil compressibility, however, require a knowledge of additional soil parameters, such as K_o, ε_v, and G, and makes their use in practice difficult.

The state parameter approach of Been et al. (1985, 1986) appears to be useful for evaluating ϕ' but may not be able to account for the environmental factors (aging, cementation, and fabric) that have a dominant influence on the in-situ state (K_o) and stiffness. A summary of the approach proposed by Been et al. (1986) and modified by Jamiolkowski and Robertson (1988) is shown in Fig. 2.30.

The shear strength of sands is related to the dilation rate at failure which in turn depends on the relative density, mean effective stress level and soil compressibility. These factors are reflected in Rowe's stress-dilatancy theory (Rowe, 1971) which has recently received a simple but conceptually sound formulation by Bolton (1984, 1986).

Bolton (1986) has shown that the peak secant friction angle (ϕ'_s) of many sands can be estimated from the empirical expression

$$\phi'_s = \phi'_{cv} + 3I_R \qquad (19)$$

where ϕ'_{cv} is the friction angle at constant volume and I_R is a relative dilatancy index given by:

$$I_R = D_r\ (Q - \ln p'_f) - 1 \qquad (20)$$

D_r being the relative density, P'_f the mean effective stress at failure (in Kpa) and Q a constant depending on the compressibility and mineralogy of the sand. Bolton (1986) suggested a general value of Q = 10 for most silica sands.

Fig. 2.34 shows the results of triaxial tests on Hokksund sand to evaluate Bolton's formulation. Although Hokksund sand is a predominantly silica sand Bolton's formulation underpredicts ϕ'_s by about 2° to 3°.

Bolton's formulation represents a useful tool for evaluating ϕ'_s from cone resistance. A method that uses Bolton's formulation to derive ϕ'_s was proposed by Jamiolkowski et al. (1988). Fig. 2.35 shows a comparison between measured ϕ'_s from triaxial results and the predicted values from CPT-q_c using Bolton's formulation and the method suggested by Jamiolkowski et al. (1988).

2.5. Conclusion

Some of the interpretation methods discussed throughout section 2.4 will be analysed and checked against the data obtained from a series of large scale calibration chamber tests on Hokksund sand at Southampton University for a range of relative densities, stress levels and stress histories in the next chapter.

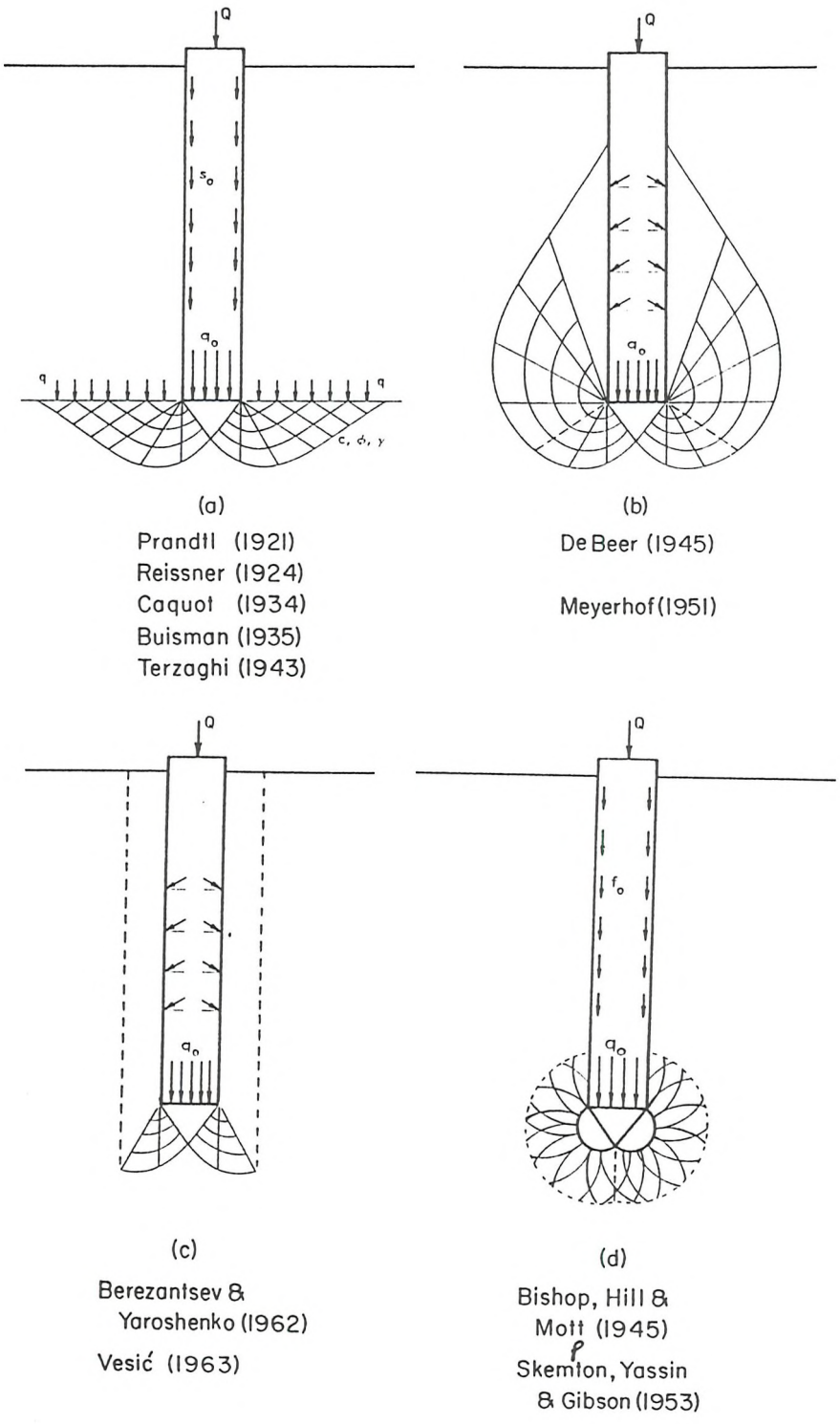

Fig. 2.1 Different assumed failure patterns under deep foundations (Vesic, 1963)

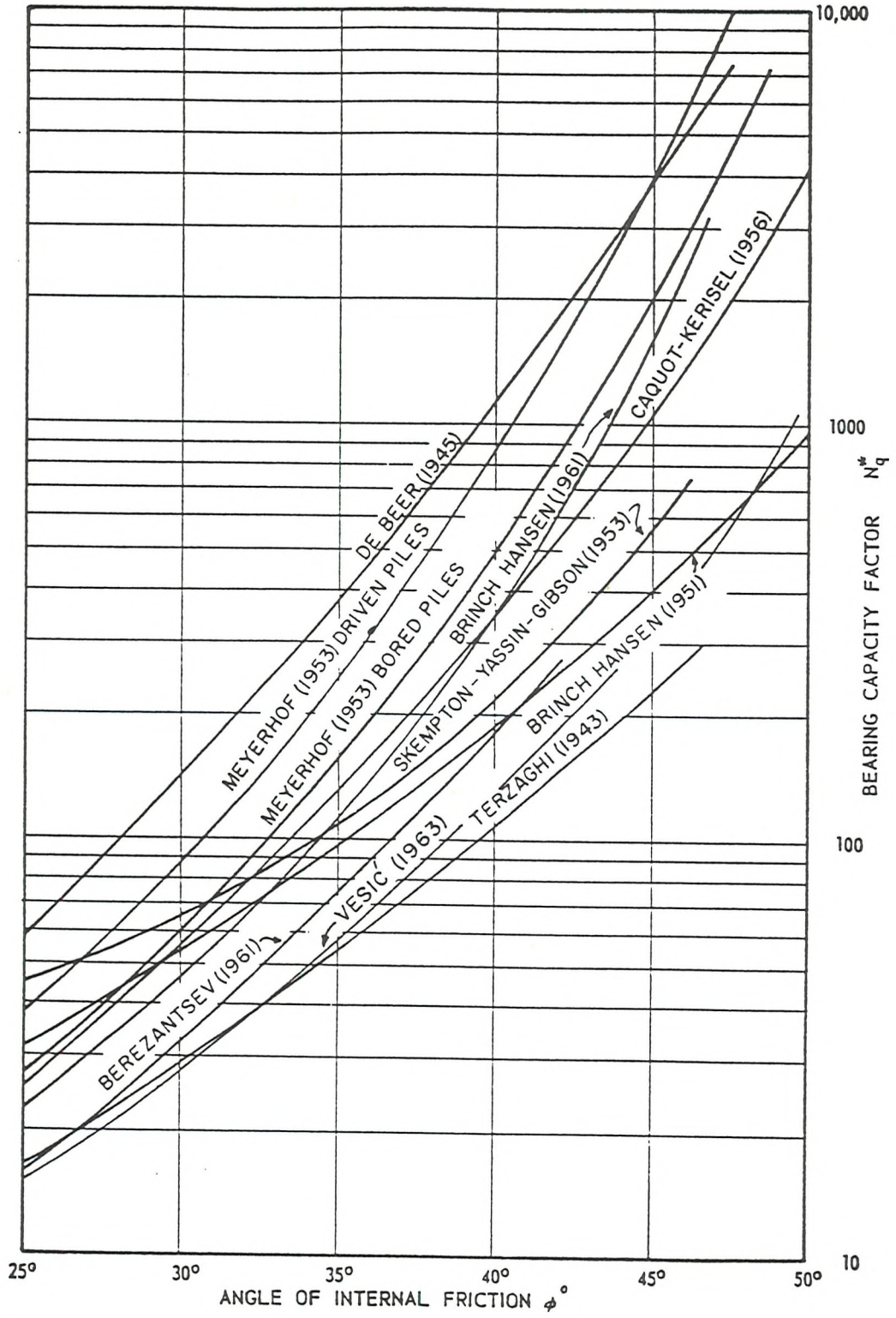

FIG. 2.2 Bearing capacity factor for circular deep foundations (Vesic, 1963 and Mitchell and Keaveny, 1986)

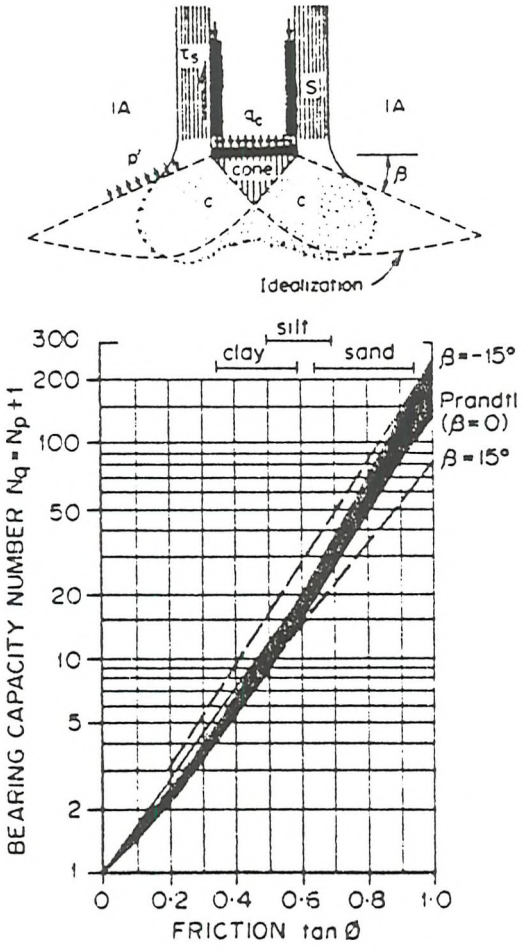

Fig. 2.3 Failure pattern and Bearing Capacity Number proposed by Janbu and Senneset (1974)

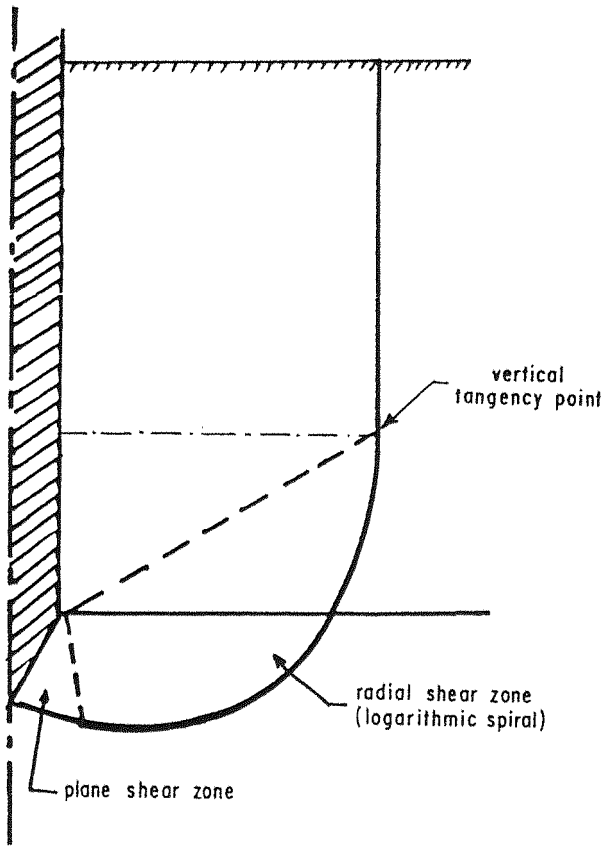

FIG. 2.4 Failure mechanism proposed by Durganuglu and Mitchell (1975)

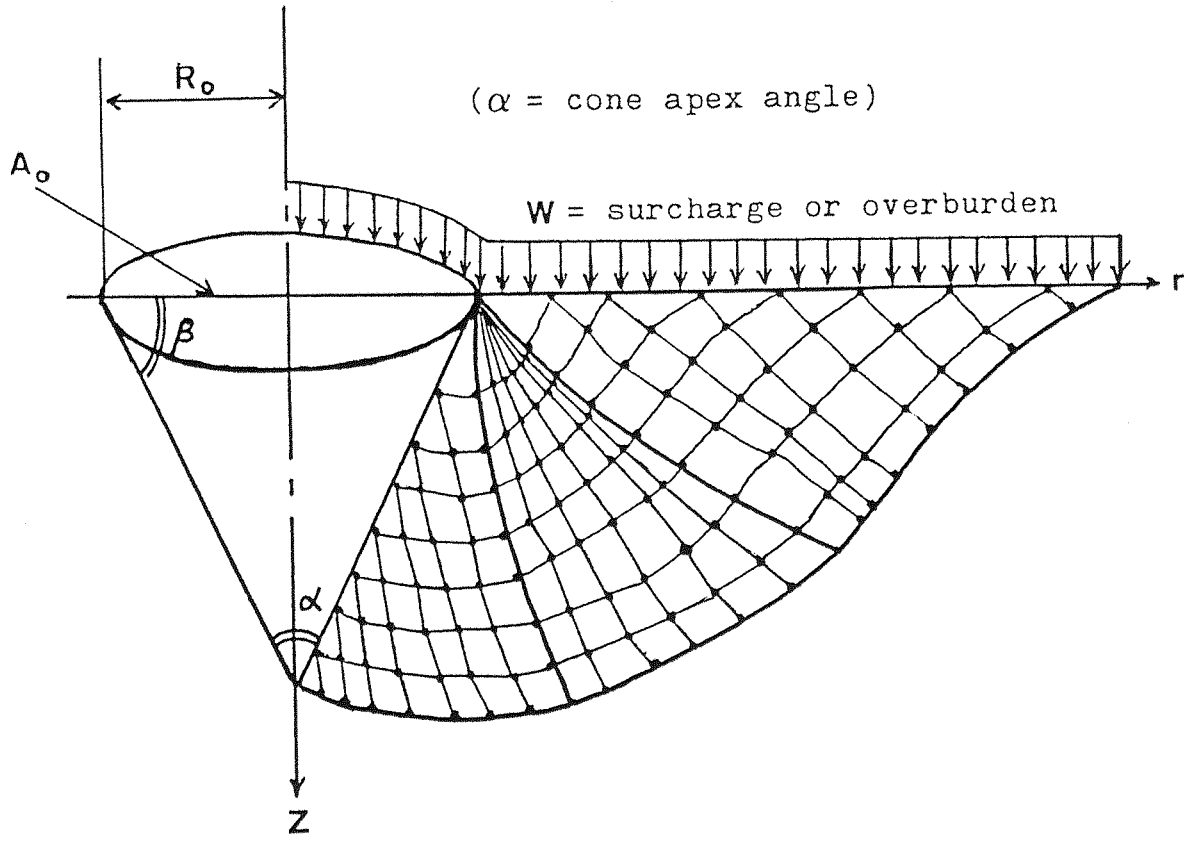

Fig. 2.5 Geometry for cone indentation problem proposed by Nowatski and Karafaith (1972)

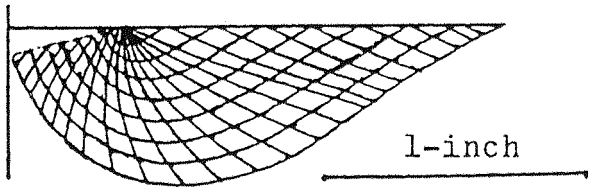

$\alpha = 150^{o}$

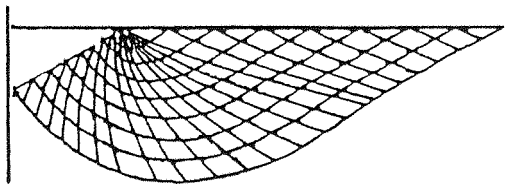

$\alpha = 120^{o}$

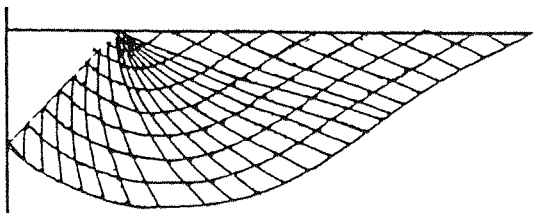

$\alpha = 90^{o}$

α = apex angle

Fig. 2.6 Slipline fields for cones penetrating ideal soil proposed by Nowatski and Karafaith (1972)

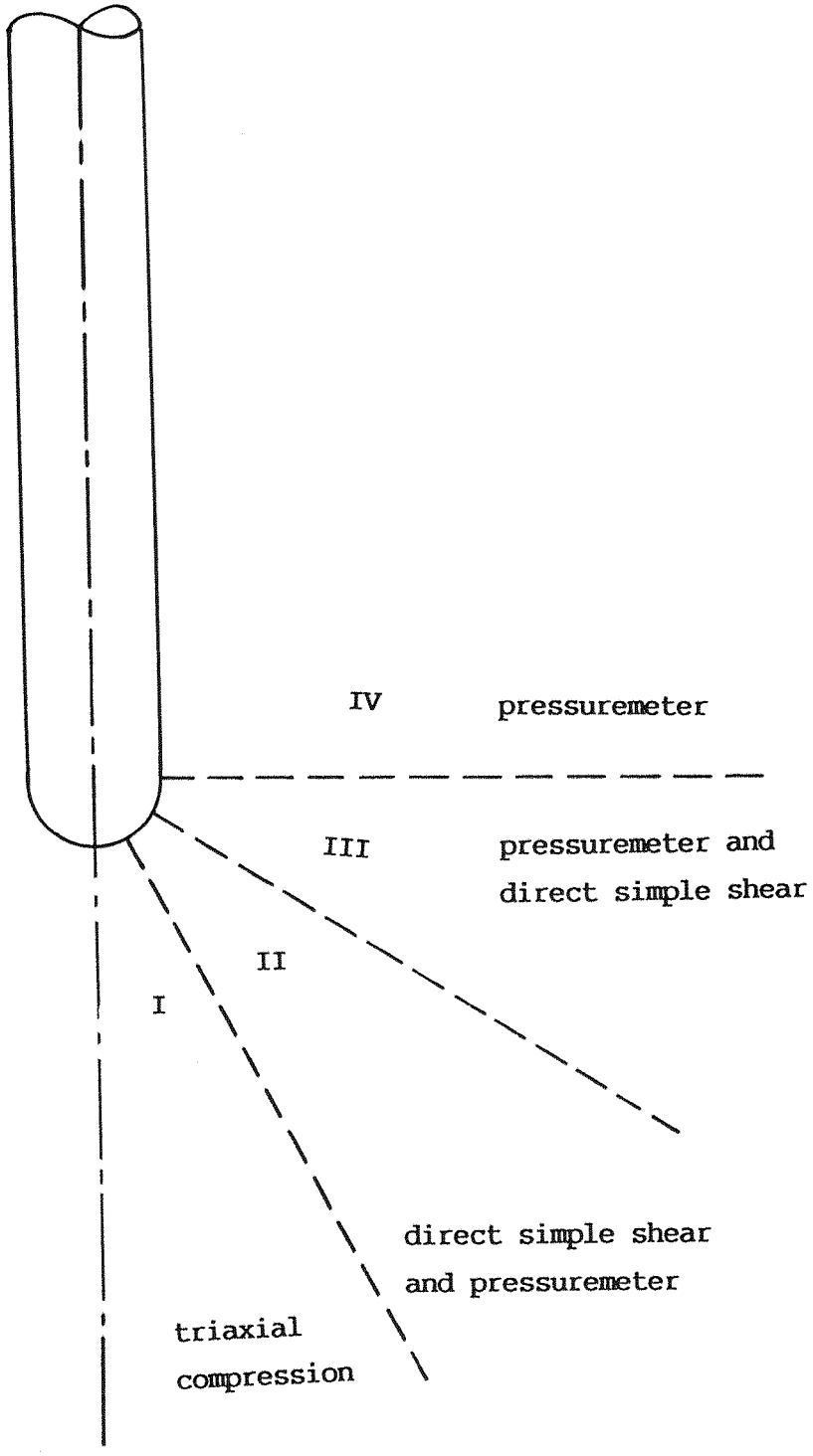

Fig. 2.7 Predominant failure modes around an advancing probe proposed by Baligh (1984)

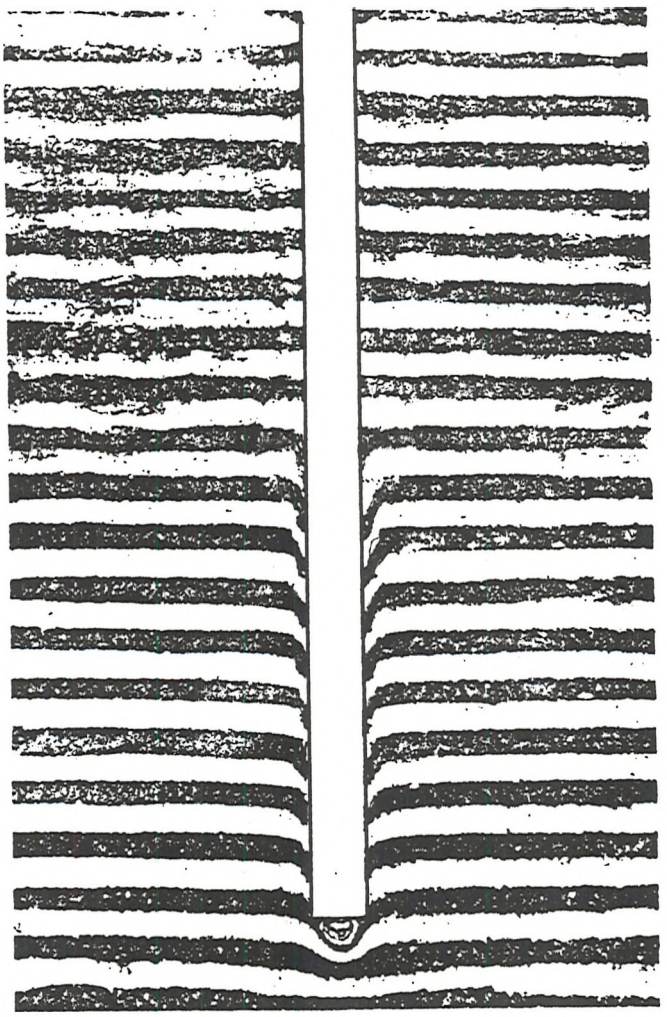

Fig. 2.8 Shear pattern under a circular foundation placed at greater depth in very dense sand (Vesic, 1963)

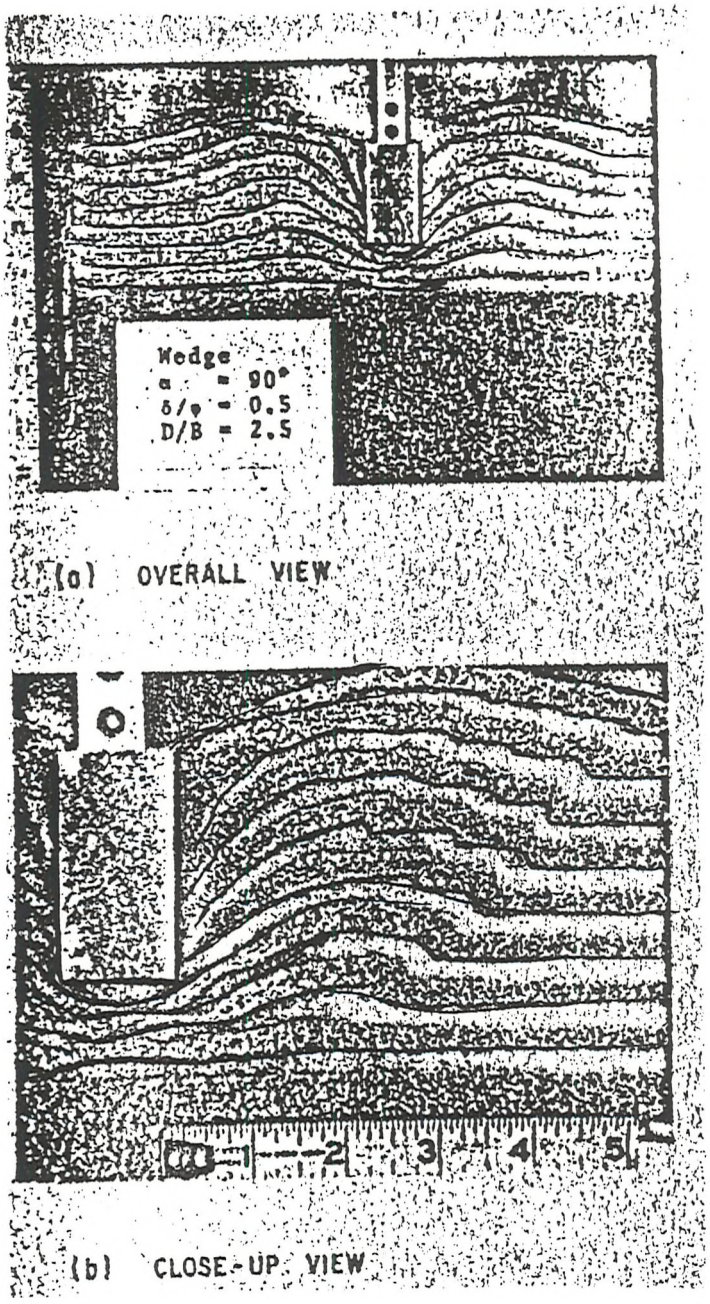

Fig. 2.9 Shear pattern under shallow strip footing model (Durgunoglu and Mitchell, 1973)

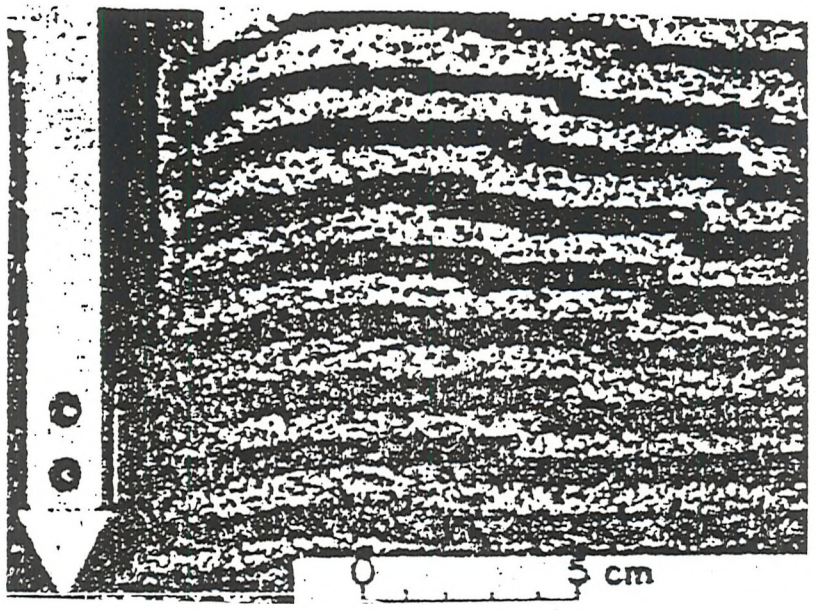

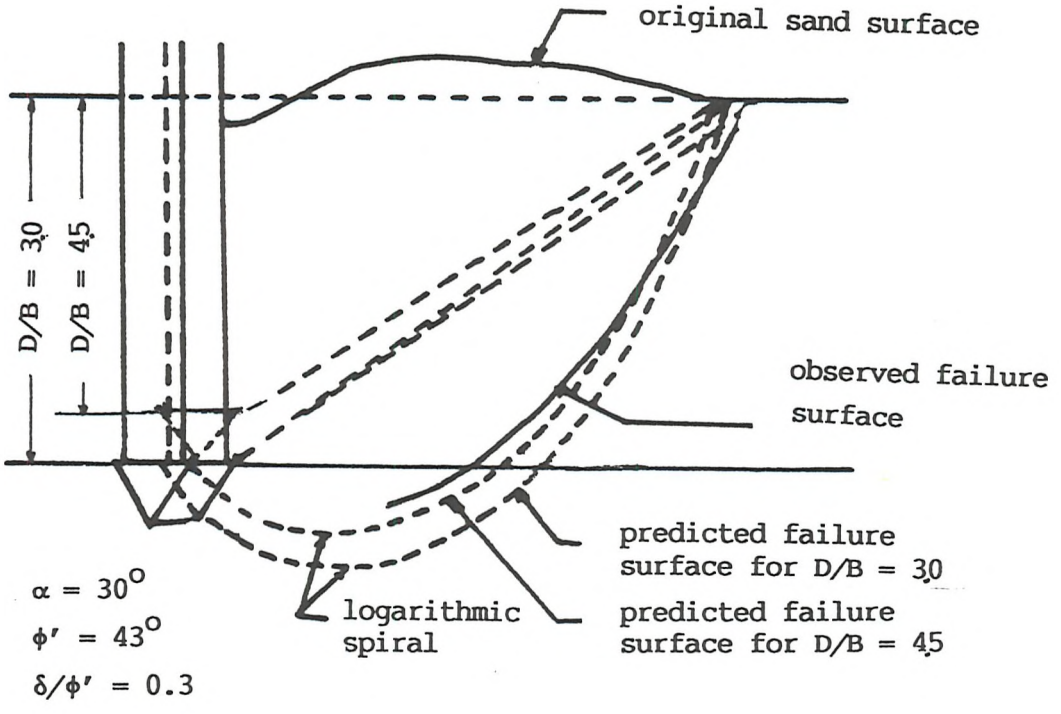

Fig. 2.10 Comparison of observed and predicted failure surfaces - Wedge Penetration, Using D & M Theory (Durgunoglu and Mitchell, 1975)

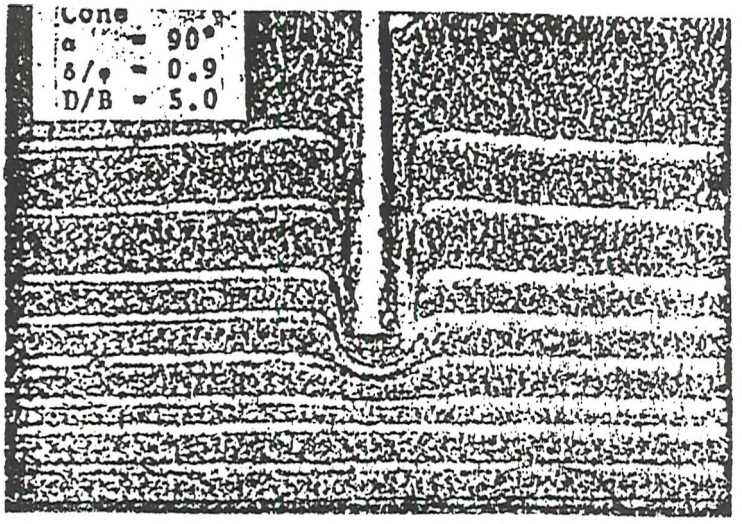

(a)

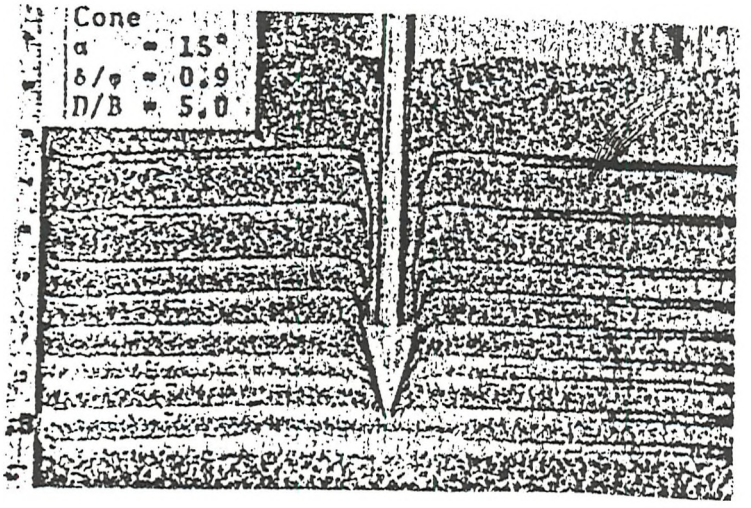

(b)

Fig. 2.11 Observed shear patterns of shallow cylindrical probes in medium dense sand, D_r = 60%, (a) blunt end; (b) 30^o apex angle (Durgunoglu and Mitchell, 1973)

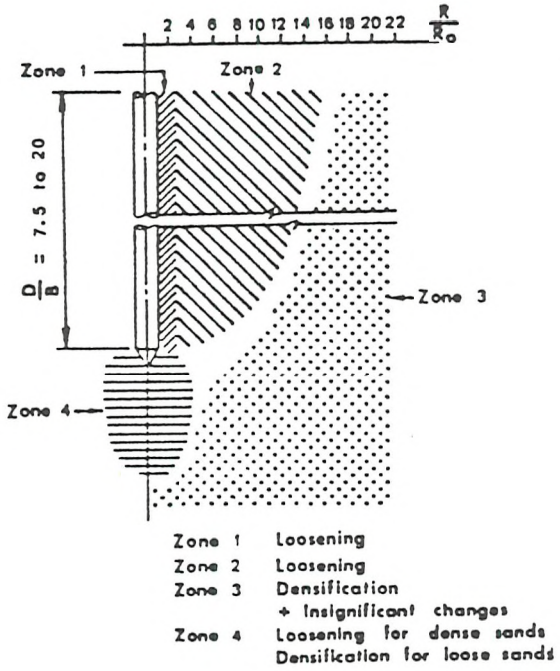

Fig. 2.12 Zones of density changes around cone penetrometer (Chong, 1983)

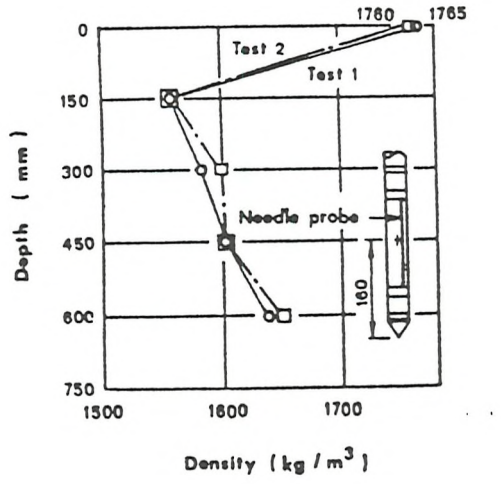

Fig. 2.13 Density of sand at surface of penetrometer vs. depth (Chong, 1983)

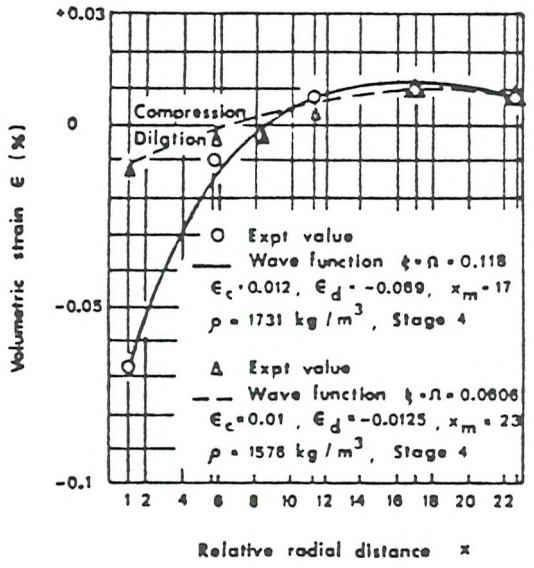

Fig. 2.14 Volumetric strain vs. relative radial distance from penetrometer axis (Chong, 1983)

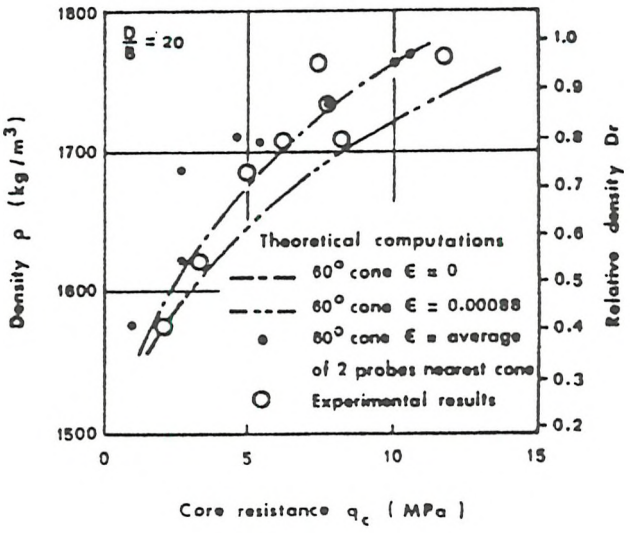

Fig. 2.15 Measured and computed cone resistance vs. initial density of sand (Chong, 1983)

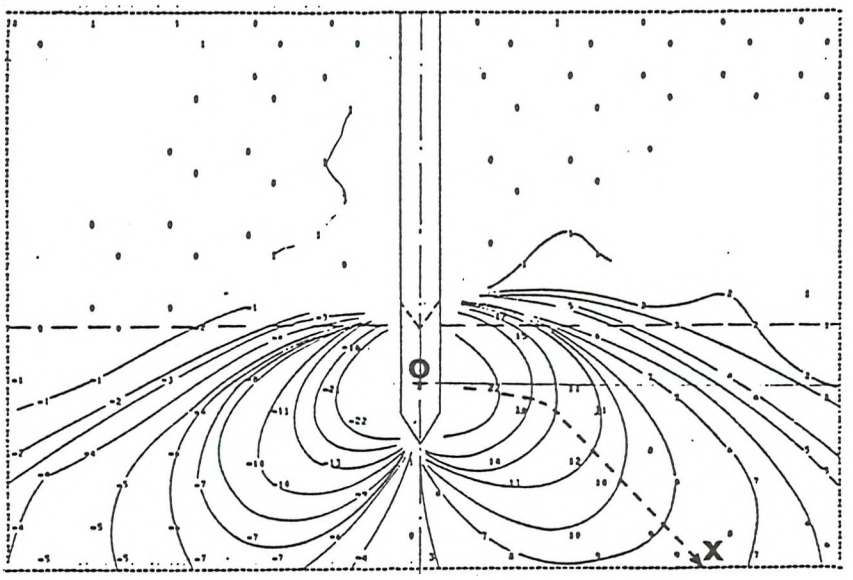

Displacement of Probe from (80 to 110)mm

(a) Lateral (X) Displacements in tenths of 1mm.

(b) Vertical (Y) Displacements in tenths of 1mm.

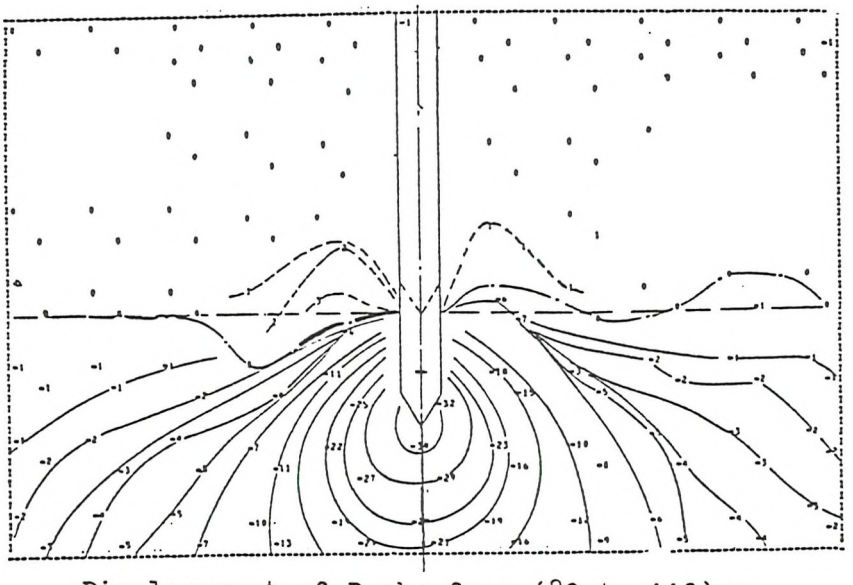

Displacement of Probe from (80 to 110)mm

Fig. 2.16 Lateral and vertical components of resultant local displacements, BC1 series (Addo, 1983)

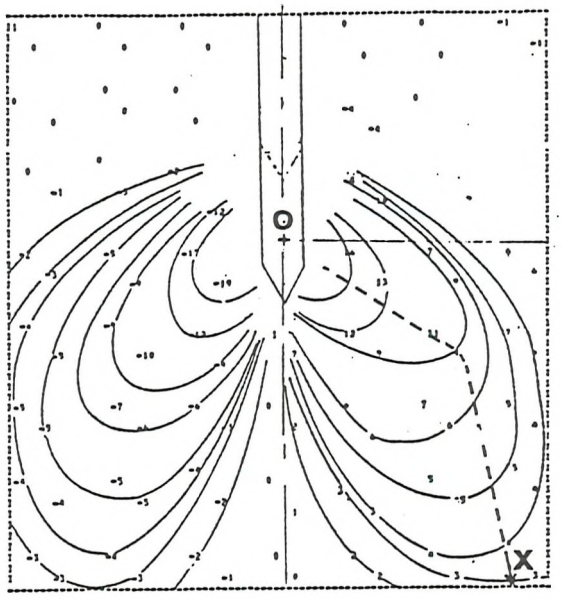

Displ. of Probe from (60 to 80)mm

(a) Lateral (X) Displacements in tenths of 1mm

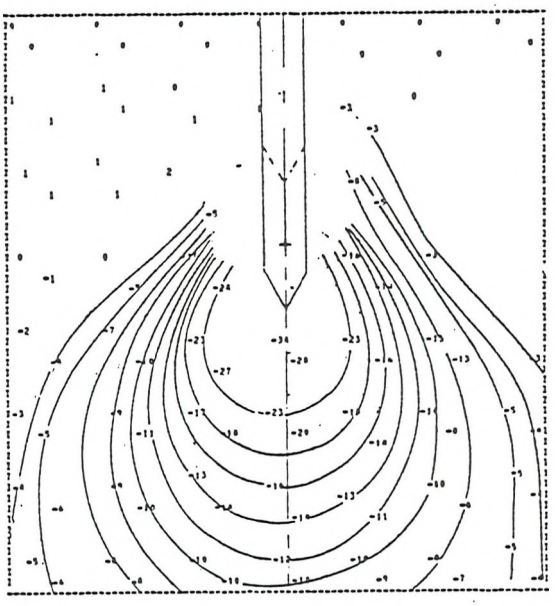

Displ. of Probe from (60 to 80)mm

(b) Vertical (Y) Displacements in tenths of 1mm

Fig. 2.17 Lateral and vertical components of resultant local displacements, BC3 series (Addo, 1983)

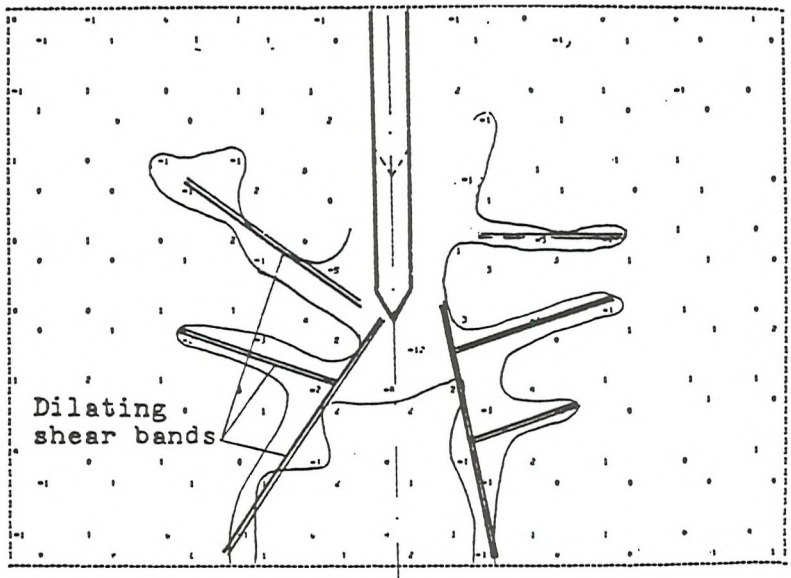

Fig. 2.18 Volumetric strains around the penetrometer, BC1 Series, e_o = 0.73, loose samples (Addo, 1983)

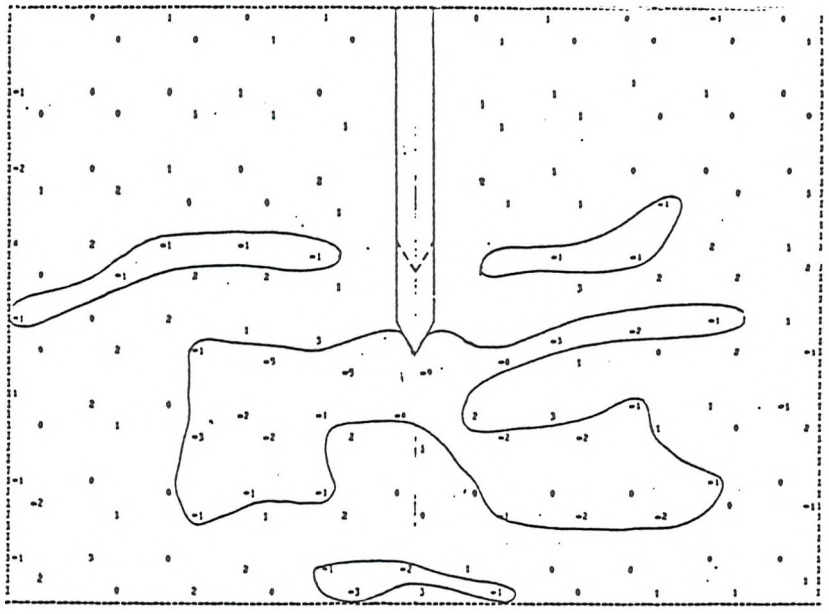

Fig. 2.19 Volumetric strains around the penetrometer, BC3 Series, e_o = 0.53, dense samples (Addo, 1983)

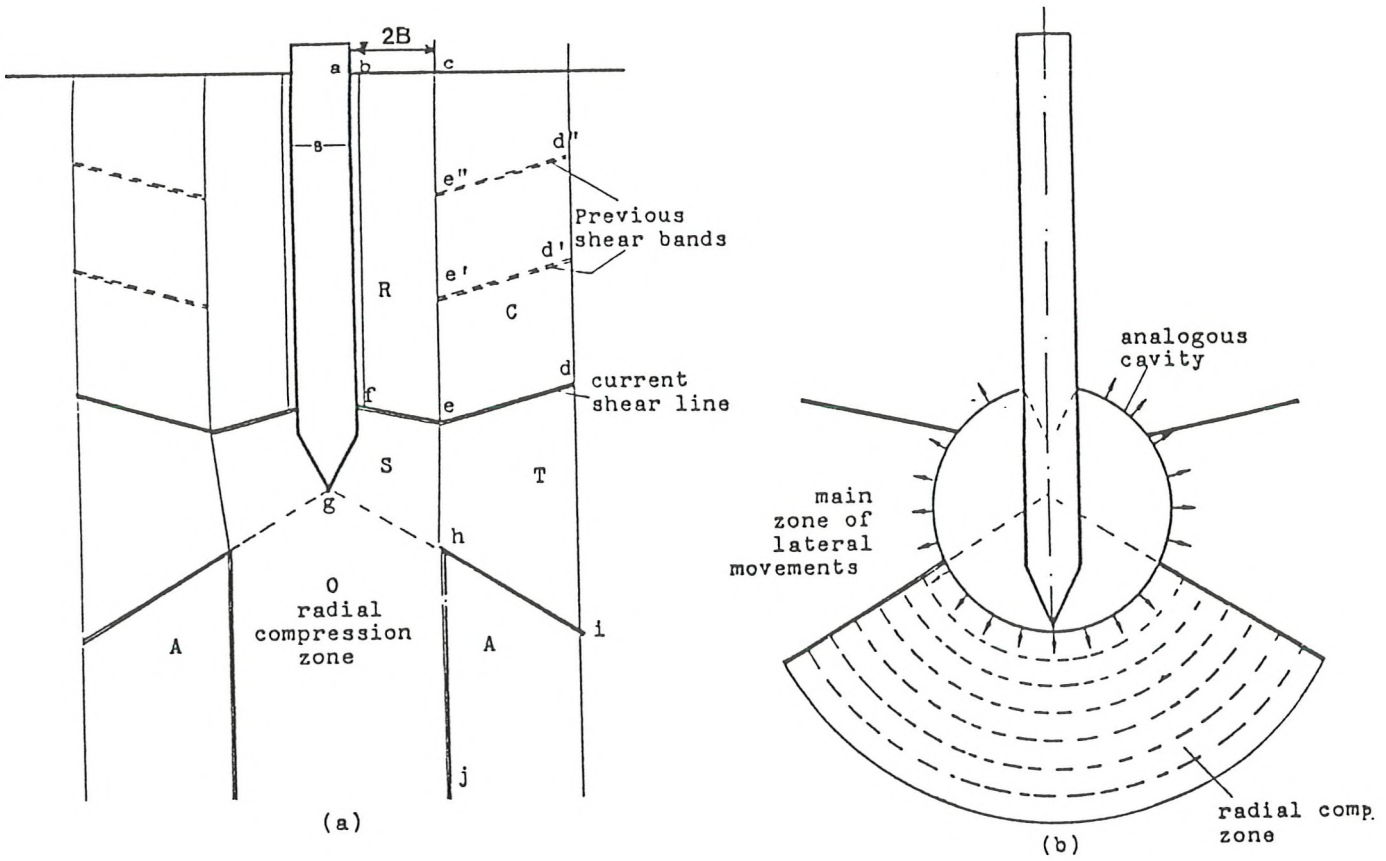

Fig. 2.20 Proposed Mechanisms of Deep Penetration (Addo, 1983)

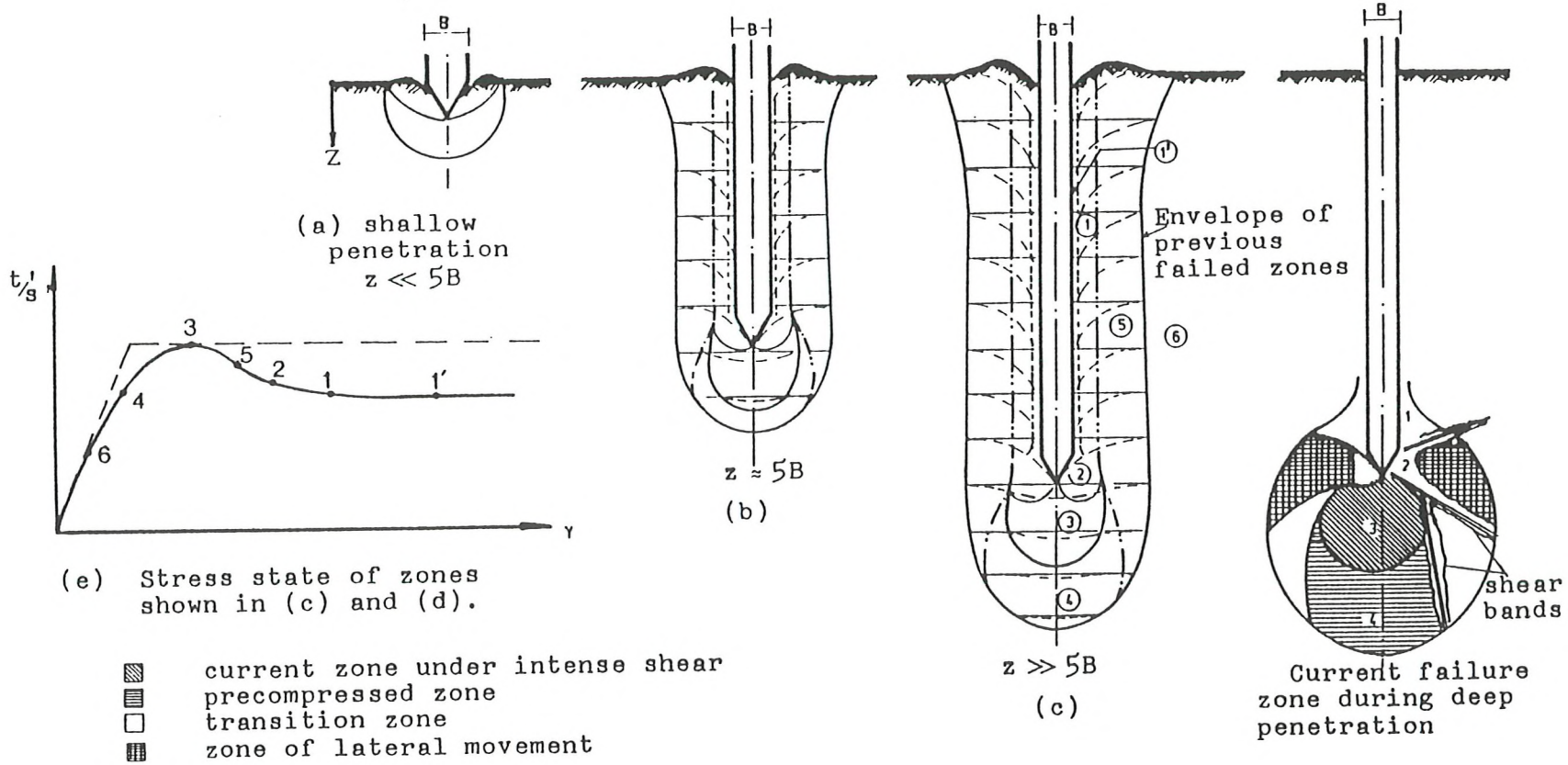

Fig. 2.21 Development of the proposed mechanism of penetration and the various zones of deformation (Addo, 1983)

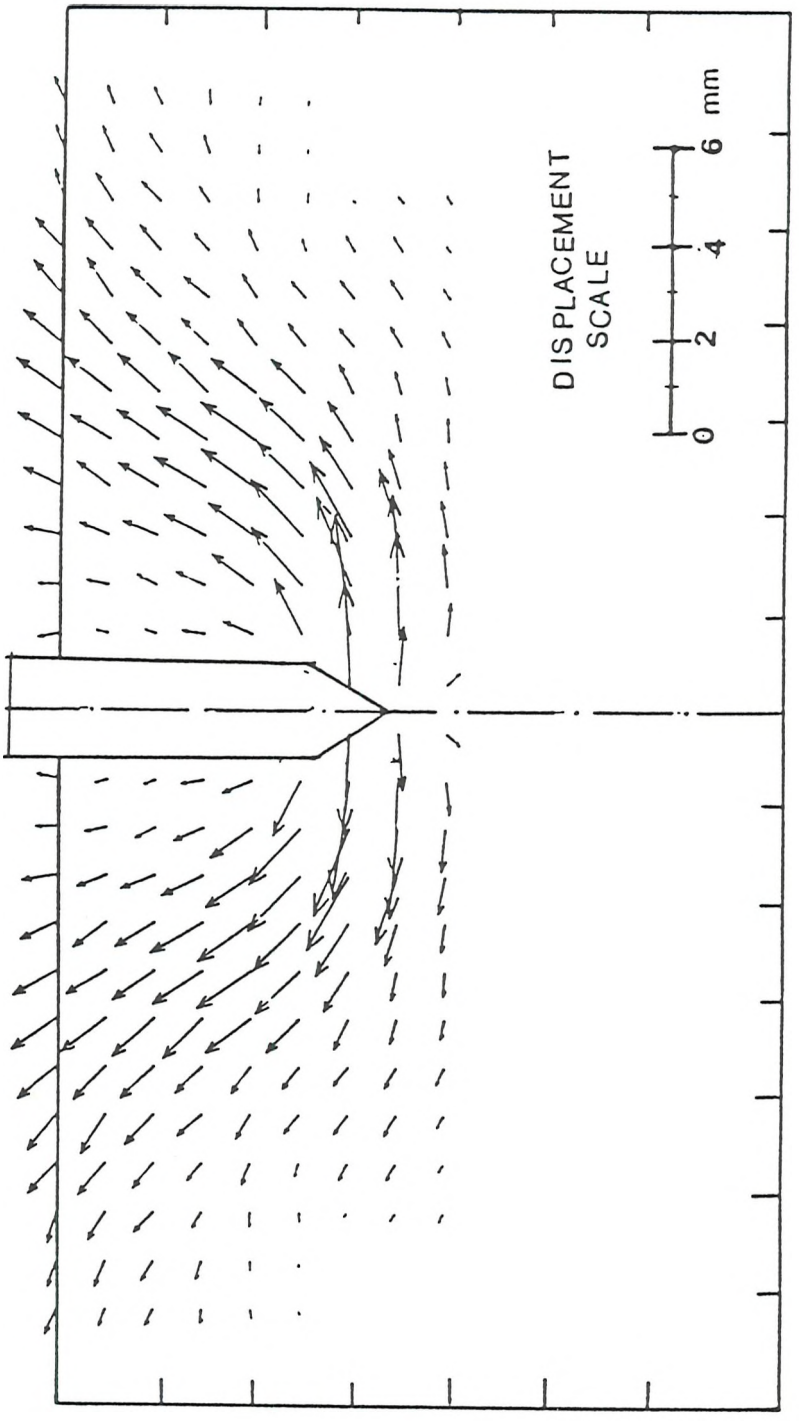

Fig. 2.22 Displacement resultant vectors, D/B = 3.5, dense sample, e_o = 0.52 (Mahmood, 1985)

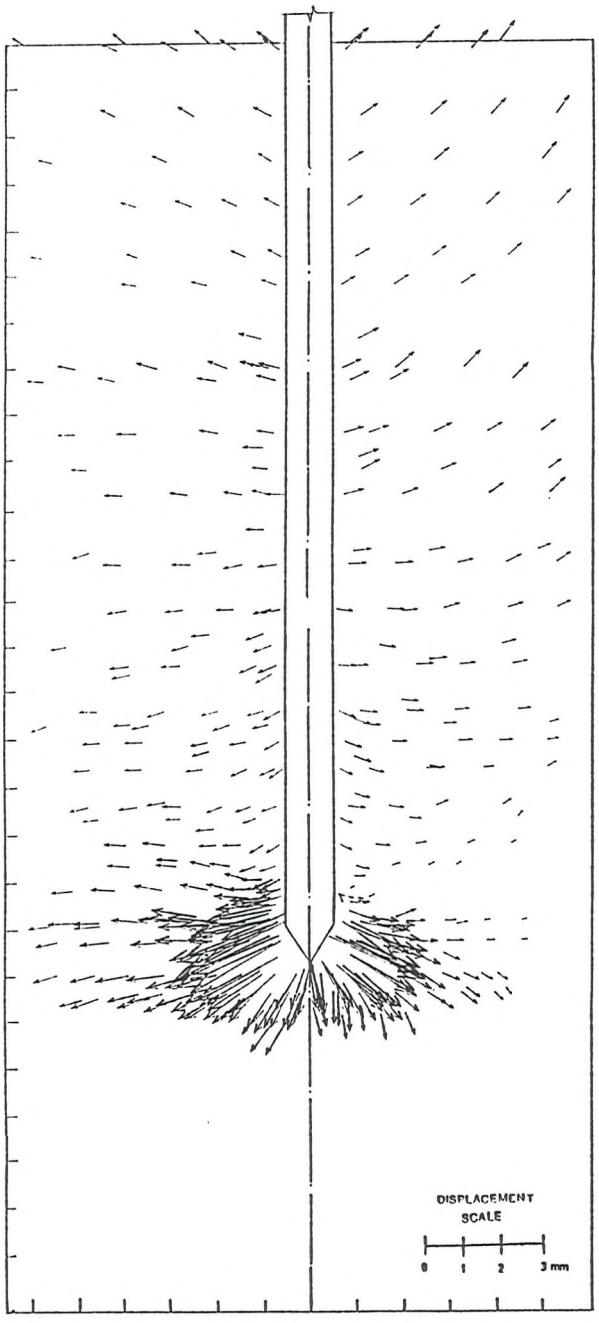

Fig. 2.23 Displacement resultant vectors, D/B = 20.0, dense sample, e_o = 0.52 (Mahmood, 1985)

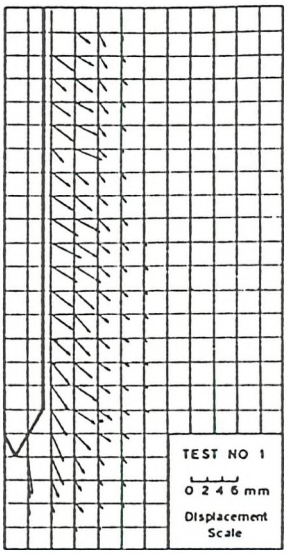

(a) LOOSE SAND

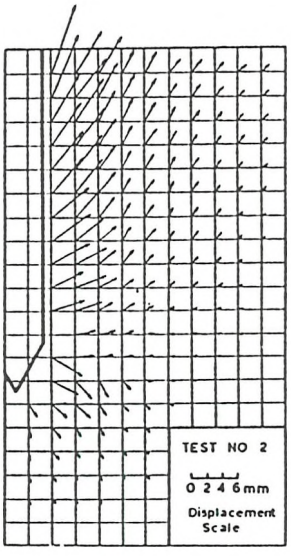

(b) DENSE SAND

Fig. 2.24 Displacement resultant vectors, (a) loose sand; (b) dense sand (Davidson et al., 1981)

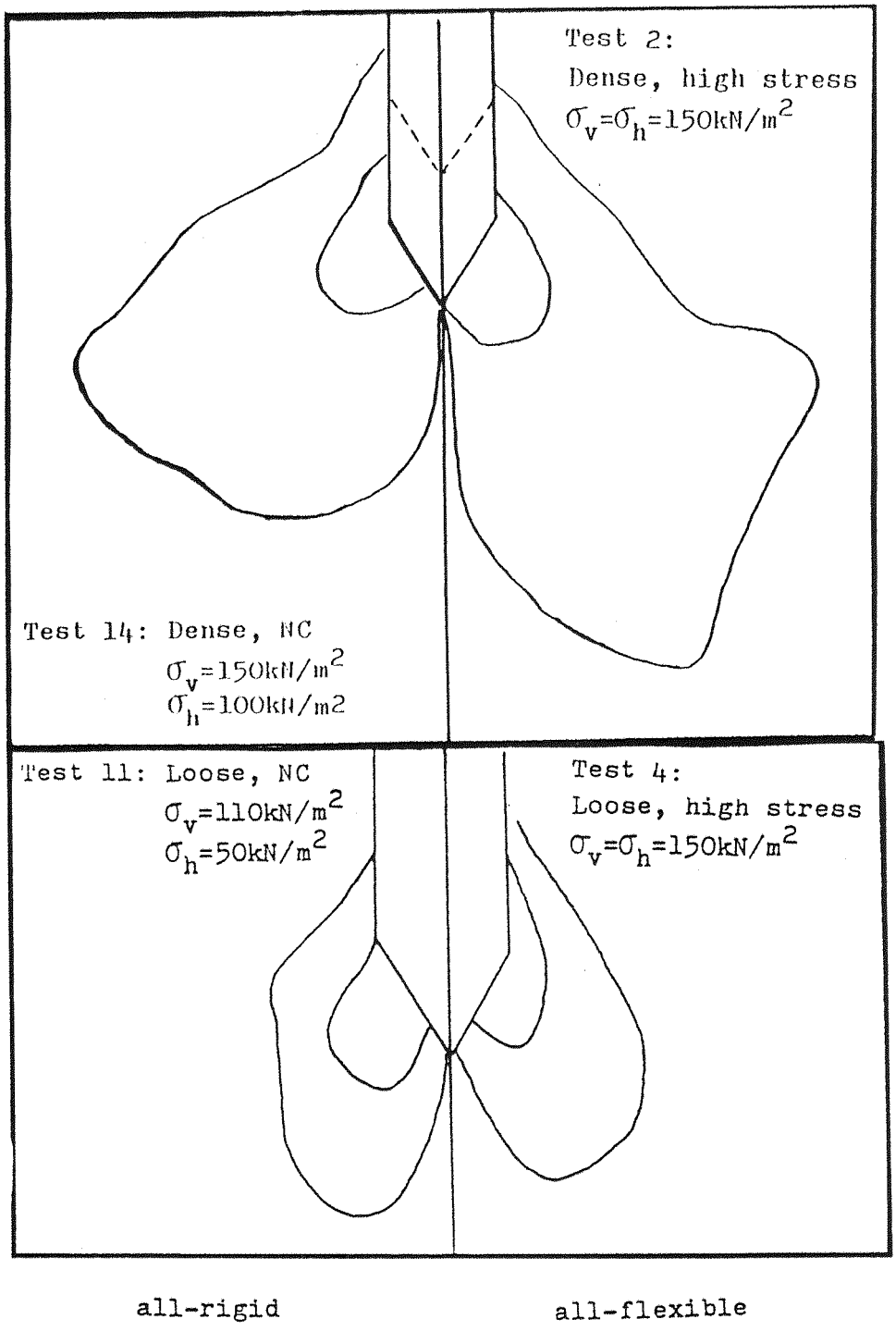

Fig. 2.25 Lateral component contours of NC and OC dense and loose samples of sand ['all-rigid' vs. 'all-flexible'] (Chen, 1986)

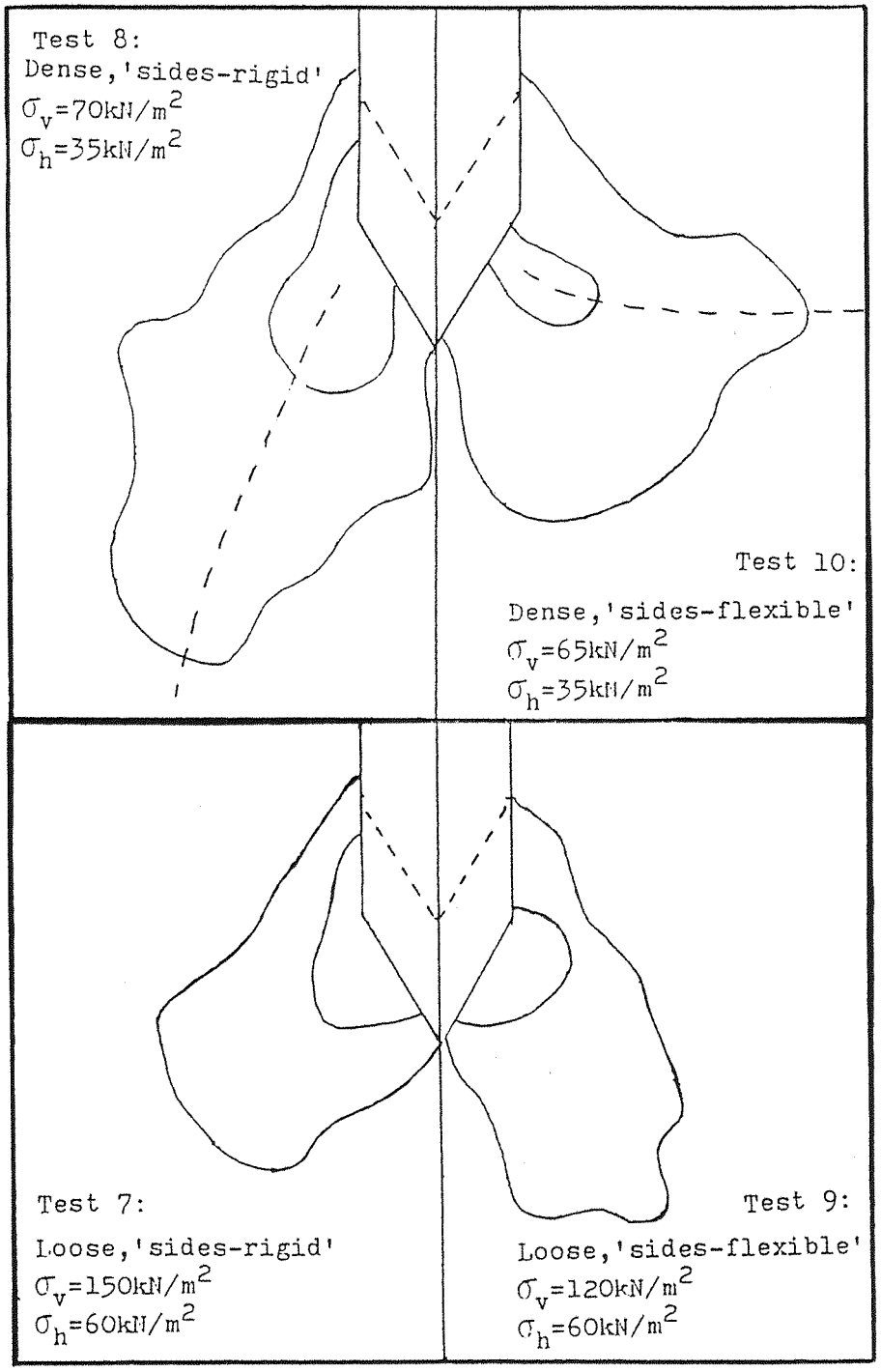

Fig. 2.26 Lateral component contours of NC and OC dense and loose samples of sand [mixed-boundary tests] (Chen, 1986)

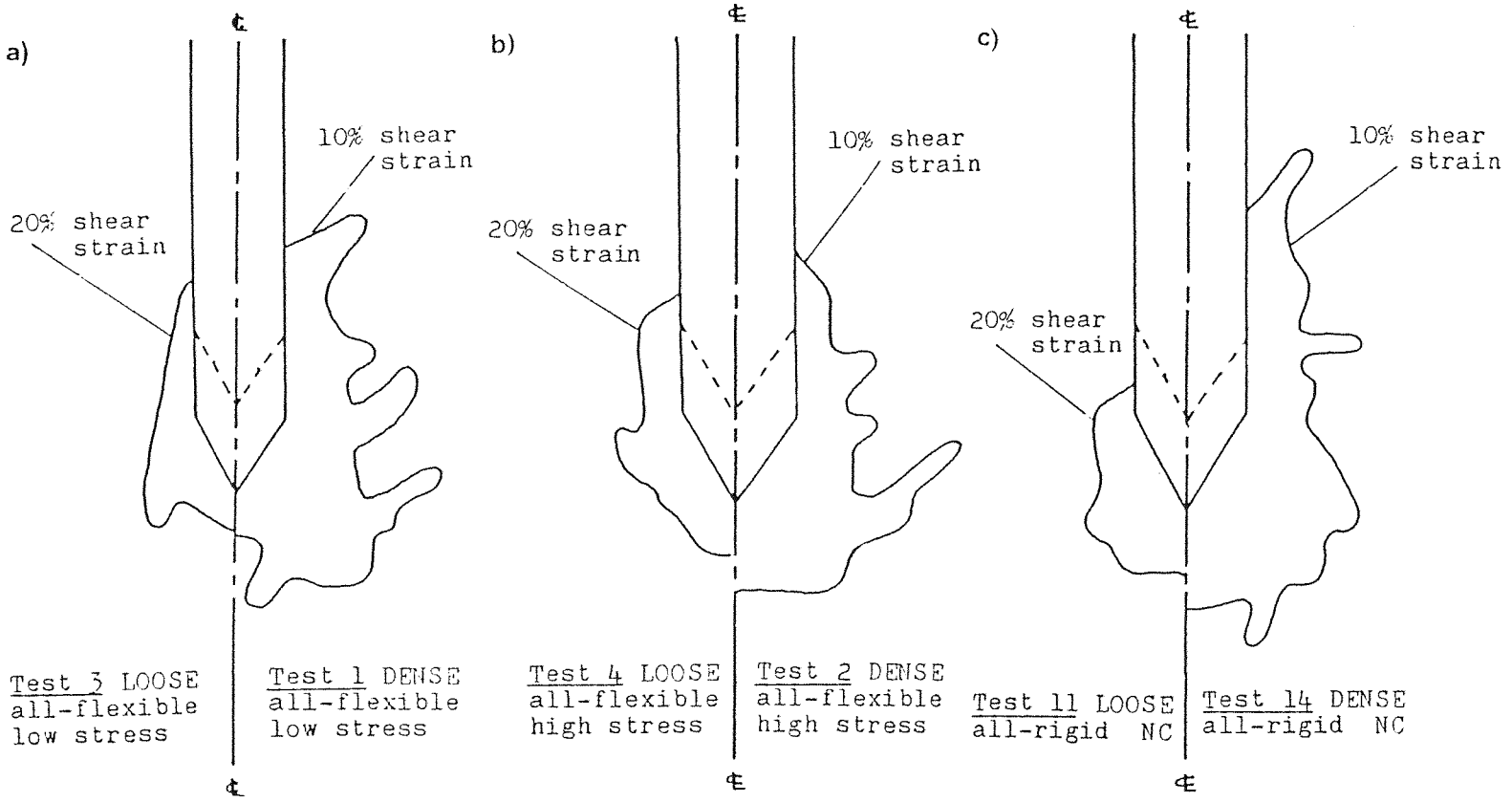

Fig. 2.27 Comparative shear strain plots (Chen, 1986)

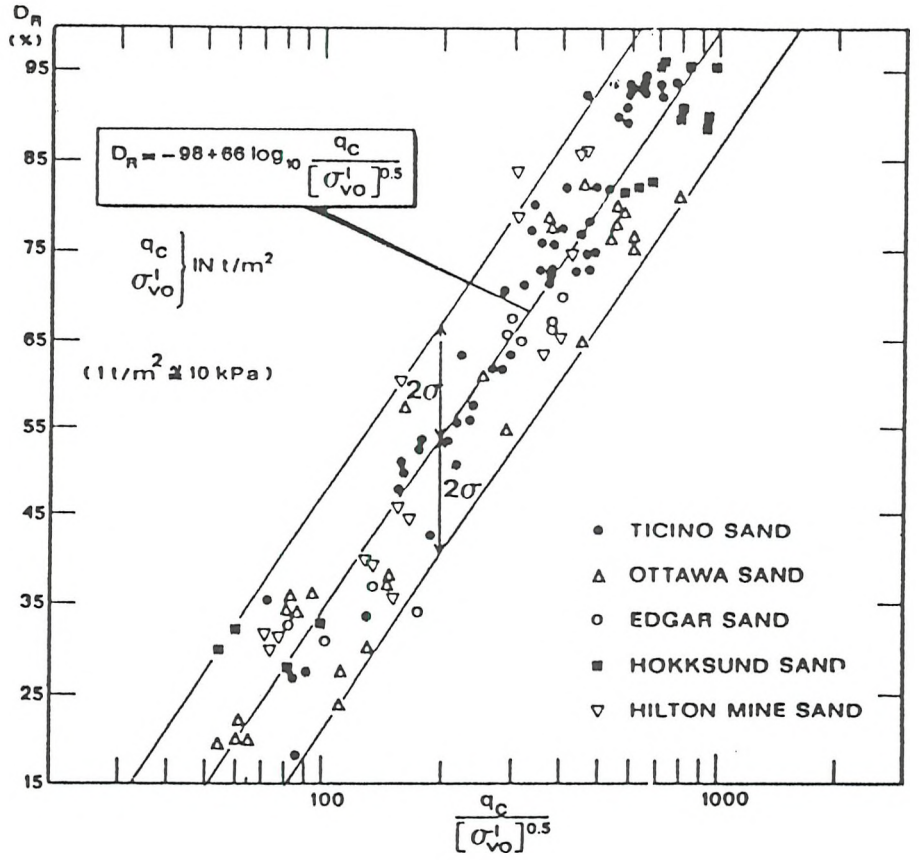

Fig. 2.28 Correlation between D_r and q_c through σ'_v (Lancellotta, 1983)

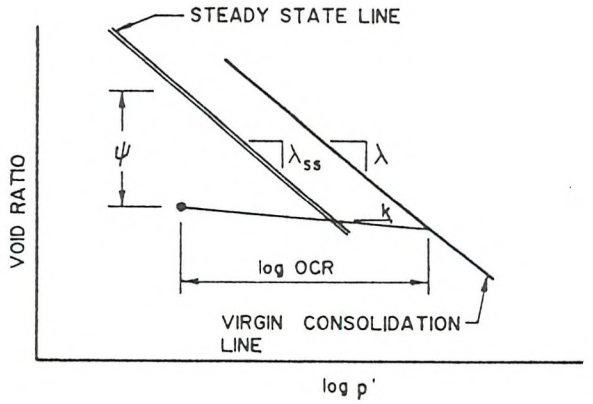

Fig. 2.29 Definition of State parameter for sands (Ψ) and clays (log OCR) (Been et al., 1987)

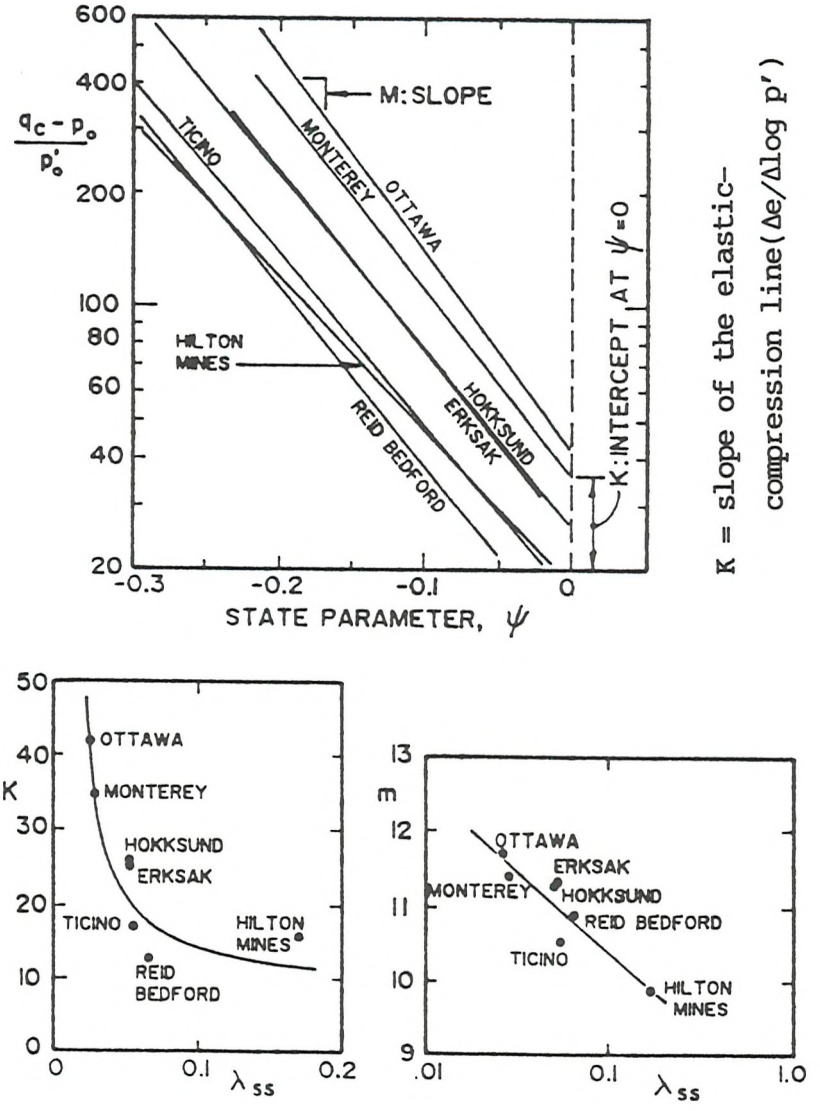

Fig. 2.30 CPT interpretation for sands in terms of Ψ and λ_{ss} (Been et al., 1988)

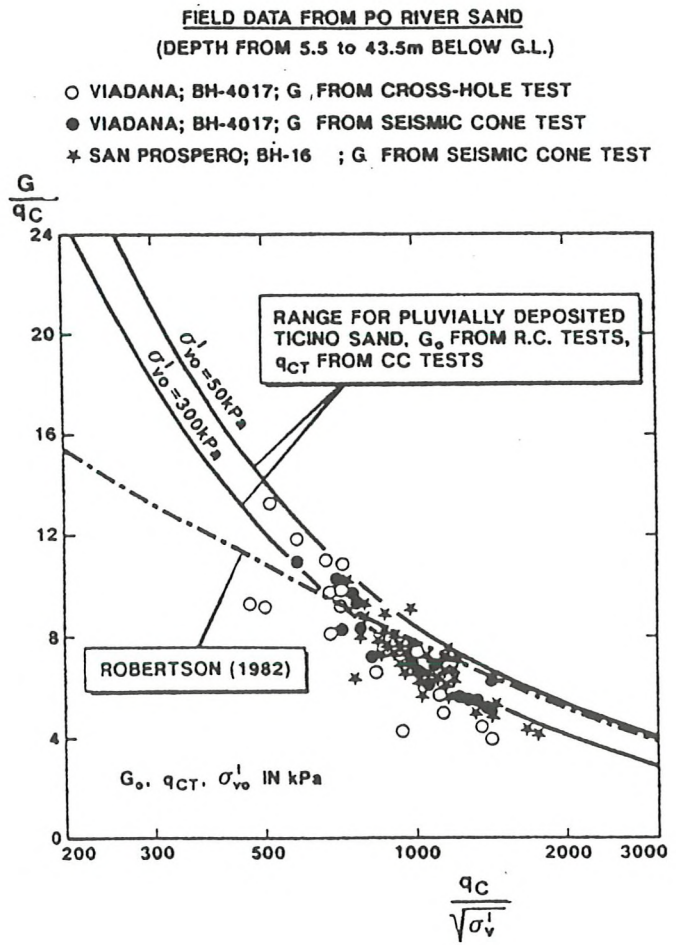

Fig. 2.31 q_c versus G correlation for predominantly quartz NC and OC sands (Baldi et al., 1988)

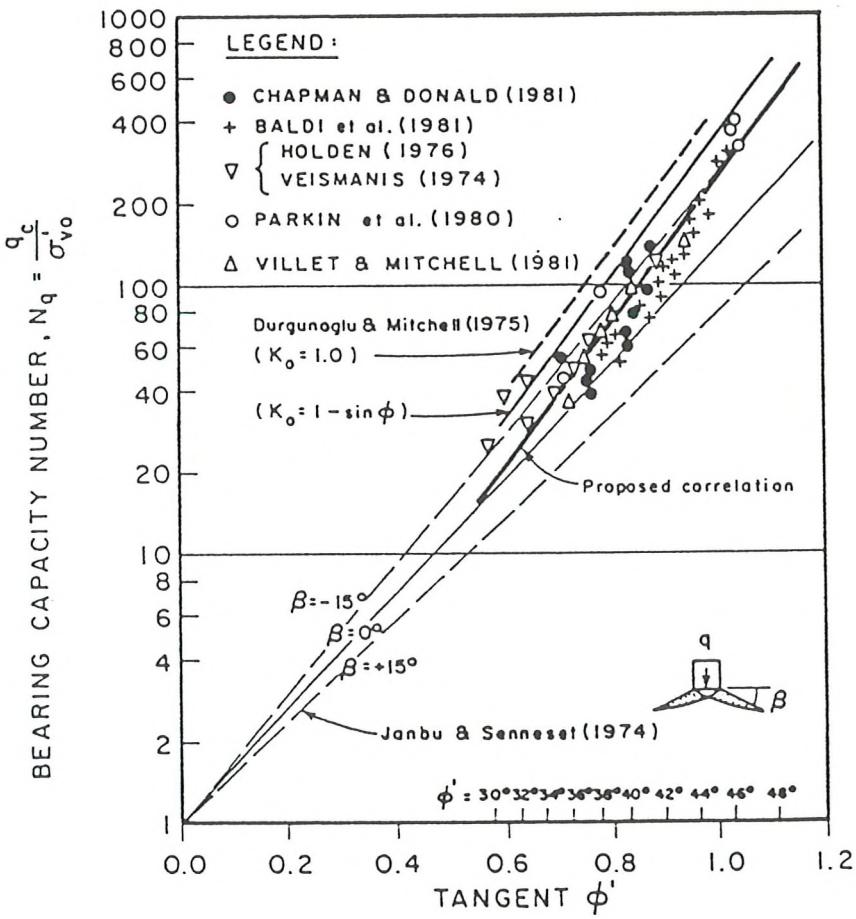

Fig. 2.32 Relationship between Bearing Capacity Number and peak friction angle from large CC tests (Robertson and Campanella, 1983)

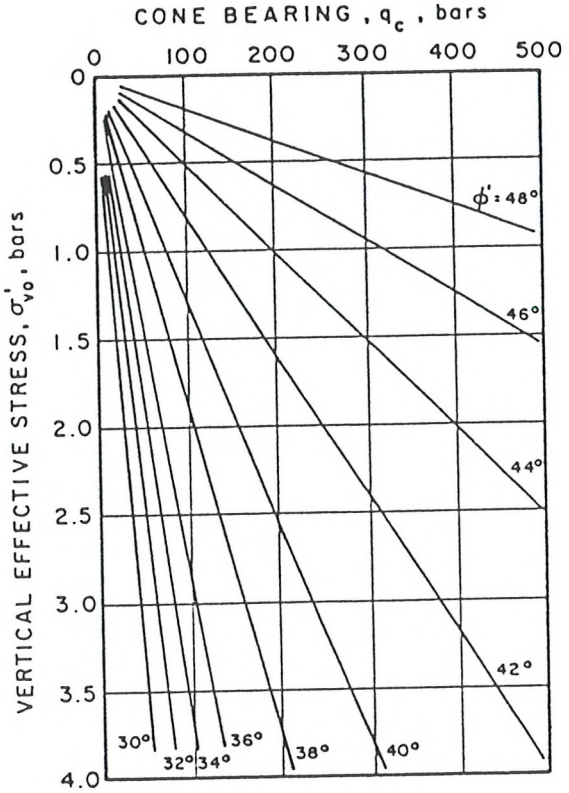

Fig. 2.33 Proposed relationship between cone resistance and peak friction angle for uncemented, quartz sands (Robertson and Campanella, 1983)

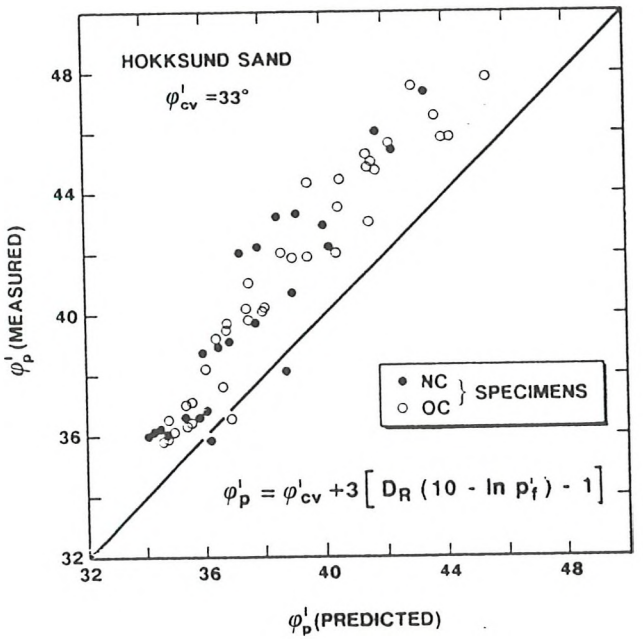

Fig. 2.34 Validation of Bolton's (1984) dilatancy theory (Jamiolkowski and Robertson, 1988)

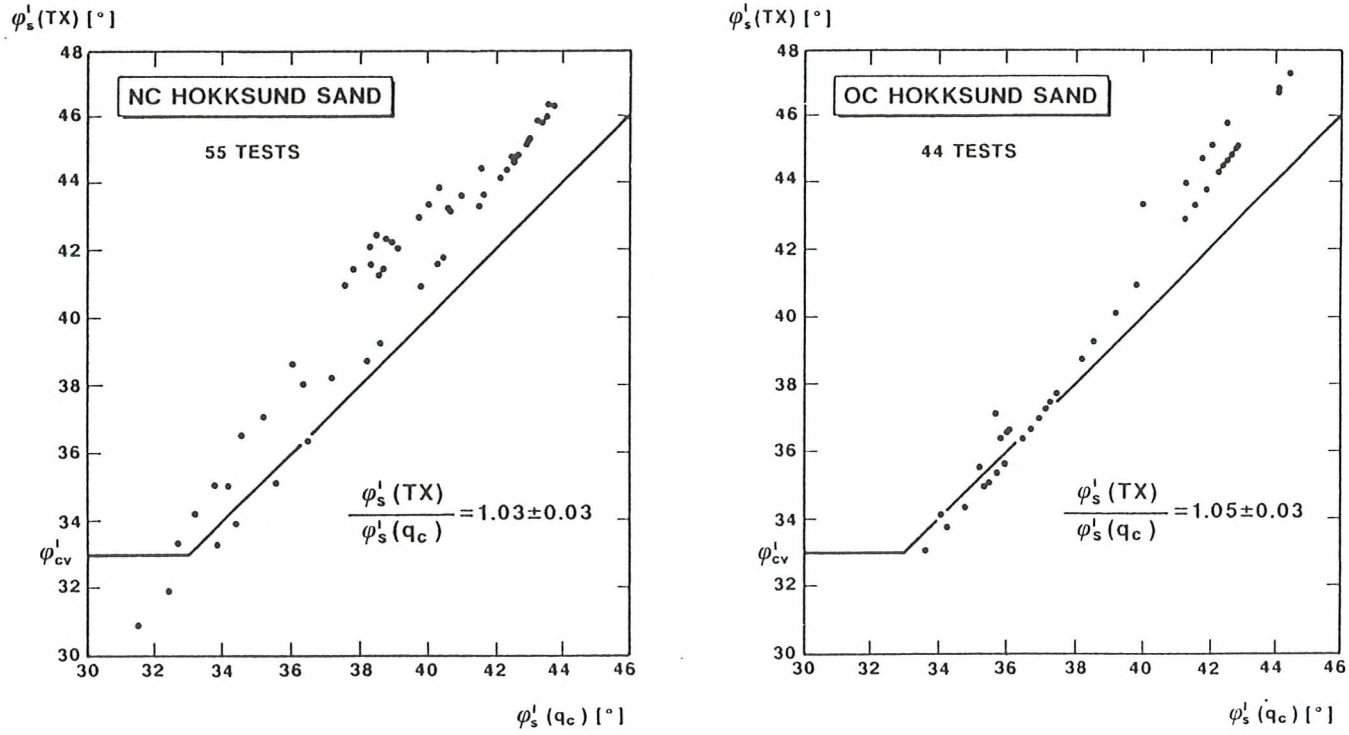

Fig. 2.35 Evaluation of ϕ'_s from CPT (q_c) for Hokksund sand using Bolton's stress-dilatancy theory (Jamiolkowski and Robertson, 1988)

CHAPTER 3

Analysis and Interpretation of Previous Southampton CPT Results and Related Tests on Hokksund Sand

3.1. Introduction

The last section of Chapter 2 gave an extensive review of the procedures that are commonly used today to calibrate penetrometers and evaluate engineering parameters in sand. The objective of this chapter is to check some of the empirical correlations for Hokksund sand tested previously in a large scale calibration chamber at Southampton (SU series).

The SU series included a total of 73 loading and penetration tests that covered a wide range of initial stress levels (0.5 to 4.0 Kg/cm^2) under two distinct lateral boundary conditions: one constant pressure (BC1) and the other zero mean lateral strain (BC3). These tests covered a variety of stress histories ranging from normally consolidated to an overconsolidation ratio of 8 with relative densities ranging from very loose state (D_r = 20%) to very dense (D_r > 95%). Both standard 10 cm^2 and half scale [5 cm^2] penetrometers were used to study the chamber size effects on the produced results. In conjunction with the results of other tests using non-standard cone sizes in different chambers, a range of diameter ratios can provide information that would lead to quantifying this effect. The wide range of stresses covered in this series provided data which was lacking from the more limited NGI and Italian (ENEL-CRIS) series. Hence, the deficiency in data and the gap between techniques of interpretation and the results of limited CC tests, as noted from the results of extensive work by NGI, might have very well been filled. The results of these tests have been summarised in graphical format by Last et al. (1987).

Of the 73 tests, 12 were limited to the pre-loading phase - extended to provide further stiffness data as very large-scale triaxial tests. All the tests provided K_o consolidation data (some with rebound as well) whilst 3 explored isotropic loading prior to penetration [though not considered in the present analysis]. Results for the NC tests are given in Table 3.1, whilst those for overconsolidation are given in Table 3.2. These are supplemented by the NGI and Italian results as given in Tables 3.3 and 3.4. The information given in these tables are for both loading and penetration phases. The loading phase data includes density, vertical confining stress, K_o, OCR and the vertical stiffness as constrained modulus, M. The penetration data only includes the cone resistance, q_c, and sleeve friction, f_s, though many of the Italian and NGI published results only give the cone resistance.

It is hoped that the results of this analysis in conjunction with further tests in the modified chamber will give a clearer understanding of the scale [size] effects that are present in CPT testing in conventional fluid control boundary chambers.

As a normal procedure for calibrating penetrometers, the cone stresses - cone resistance and sleeve friction - are related to different soil parameters.

3.2. Evaluation of Engineering parameters in Hokksund sand

3.2.1. Coefficients of Earth Pressure at Rest

During the consolidation phase of the sand samples, the vertical and horizontal stresses are continuously measured; therefore reliable values of coefficients of earth pressure at rest, K_o, for first loading (K_o^{NC}) and rebound (K_o^{OC}) can be determined. Figs. 3.1a and 3.1b show the variation of K_o versus effective vertical stress for selected loose and dense samples rebound at various stresses. K_o^{NC} refers to the end of the loading stage (the maximum load reached in each test); K_o^{OC}, on the other hand, refers to the end of the rebound stage.

As far as K_o^{NC} is concerned, the experimental data show the following:

- for a given range of relative densities, the K_o^{NC} at the end of the consolidation stage seems to be independent of vertical stress past an applied vertical stress of 0.5 kg/cm^2.

- K_o^{NC} tends to decrease as D_r increases. The observed variation between them can be approximated by the following empirical relationship (Bellotti et al., 1985)

$$K_o^{NC} = K_{o\ min}^{NC} + \lambda\ D_r^{\omega} \qquad (1)$$

During unloading, the variation of the principal stress ratio is very different and appears to be a function of the applied stress. The slope of the elastic rebound of the unloading curve (i.e., K_{oe} as will be used in the derivation of the five elastic constants for an anisotropic model) does appear to be a function of the maximum past vertical pressure as shown in the above figures for both dense and loose samples. The K_{oe} values at any common vertical pressure is the same for both loose and dense samples despite the difference in their K_o^{NC} values prior to rebound.

As far as over-consolidated samples are concerned, the observed variation of K_o^{OC} with OCR can be approximated quite well by the empirical relationship proposed by Schmidt (1966) and Alpan (1967) to compute an equivalent K_o^{OC} from K_o^{NC} :

$$\frac{K_o^{OC}}{K_o^{NC}} = (OCR)^{\beta} \qquad (2)$$

Based on a series of calibration chamber tests, Schmertmann (1975) recommended a value of $\beta = 0.42$ for Hokksund Sand. The experimental values of β, although quite scattered, increase as D_r increases.

3.2.2. Cone Resistance - Relative density

In order to obtain the in-situ relative density from the measured cone resistance, it is convenient to express $D_r = f(q_c, \sigma')$ in the form originally suggested by Schmertmann (1976) as:

$$D_r = 1 / C2 \ln \left(\frac{q_c}{C0 \cdot \sigma'^{C1}} \right) \qquad (3)$$

in which C0, C1, and C2 are the experimental coefficients and σ' is an effective stress which may be vertical, horizontal or a combination of both stresses.

In NC sands, the cone resistance - relative density relationship is best related through effective vertical stress, whereas in OC or for both NC and OC samples taken together, it has been found that a better comparison is obtained using the effective horizontal stress or the effective mean stress comparison between experimental and theoretical results. An analysis of the dense sand results has shown that at lower confining stresses ($\sigma'_h < 0.75$ Kg/cm^2) [Fig. 3.2] experimental q_c values are slightly higher than those obtained by using the above relationship, but testing under high stresses, CC results are lower than the calculated values. Such relationships are not linear, suggesting some crushing of sand grains at higher densities (Schmertmann, 1978b; Holden, 1976; Veismanis, 1974). However, it must be pointed out that if one accepts the validity of the theory of the expanding cavity for modelling the cone resistance of materials with curved envelopes, it is then possible to justify the non-linearity between q_c and σ'_v even in the case of a sand that does not crush (Baligh, 1976).

A regression analysis made on the results of the SU test series indicated that the accuracy of relating q_c to D_r through the mean stress, σ'_m, and OCR is better than the same through σ'_m alone as shown in the following equation.

$$q_c = C0\ p_o \left(\frac{\sigma'_m}{p_o}\right)^{C1} (OCR)^{C3}\ EXP\ (C2 \cdot D_r) \qquad (4)$$

where: C0, C1, C2 and C3 = experimental coefficients

p_o = reference stress (= 1 kg/cm²)

It is noted that q_c values were corrected for the chamber size effects through the procedure given by Lunne and Christophersen (1983). [They suggested that the NC values of q_c under BC1 and BC3 should be increased by 25 and 7 %, respectively, whilst the same for the OC tests should be increased by 24 % under both BC1 and BC3]. The experimental coefficients of Eqns. (3) and (4) together with those of Baldi et al. (1986) (which includes some earlier results of SU and Italian and Norwegian results) are shown in Table 3.5. It shows that the q_c values corrected by the Baldi et al. (1986) procedure [see Chapter 4] seem to give a better fit than those obtained using Lunne and Christophersen (1983) correction factors.

The accuracy of relating cone resistance to overconsolidation can be confirmed in another way by considering both the vertical and horizontal stresses in the $q_c - D_r$ relationship. The SU results showed that both the OC cone resistance and more importantly sleeve friction are more sensitive to σ'_h than to the σ'_v. The regression analysis of the test data fitted to the following empirical equation allows the separation of influences of σ'_h and σ'_v and supports this criterion.

$$q_c = C0\ p_a \left(\frac{\sigma'_v}{p_o}\right)^{C1} \cdot \left(\frac{\sigma'_h}{p_o}\right)^{C2} EXP\ (C3 \cdot D_r) \qquad (5)$$

where: C0, C1, C2 and C3 = experimental coefficients (Table 1)

p_o = reference stress (= 1 kg/cm²)

The results of a regression analysis based on the above formulation is given in Table 3.6 for Hokksund sand and shows that

C2 >> C1 confirming the accuracy of Eqns. (4) and (5) [as compared to a unique q_c relationship with D_r through σ'_v, Eqn. (3)] for all stress histories.

It may be convenient to correlate cone resistance with confining stress for tests both under B1 and B3 boundary conditions and for NC and OC samples over a given soil density range. This can be achieved by plotting q_c against effective lateral stress on a log-log basis. The results of the SU series seem to fit a straight line:

$$\ln q_c = 6.043 + 0.601 \ln(\sigma'_h) \qquad (R^2 = 0.96) \qquad (6)$$

valid for all OCR's and under both boundary conditions over a density range of 85-100% (q_c values corrected by Lunne and Christophersen method). Using the latter's set of correction factors for q_c seems to fit the data very well, as shown by the R^2 factor.

In order to be able to quantify the effects of different boundary conditions on penetration, the cone resistance values for both NC and OC samples were analysed under BC1 and BC3 for all densities. The regression analysis gave the results as shown in Table 3.7. There appears to be a good correlation between q_c and relative density through the effective mean stress individually for each boundary condition. The correction for OC samples, as pointed out by Lunne and Christophersen (1983), does not appear to depend on the boundary condition used during the test. These results will become important in suggesting possible correction factors to the measured cone resistance values as compared with the factors obtained from the infinite boundary test results. This is treated in Chapter 7. A comparison of the corrected cone resistance values with those from the infinite boundary tests may result in adjustments to the correction values suggested by Lunne and Christophersen.

3.2.3. Cone Resistance – State Parameter – Shear Strength

The state parameter, Ψ, is able to describe sand behaviour including shear strength. Having obtained the steady state line for Hokksund sand [i.e., $\lambda_{ss} = 0.056$], the relationship between q_c and Ψ of Been et al. (1986) can be written in the following form for the SU results:

$$\frac{q_c - \sigma'_m}{\sigma'_m} = 25.77 \text{ EXP } (-11.286\Psi) \qquad (2.16)$$

The ϕ' values from drained triaxial tests of Kildalen et al. (1982) on the same sand were plotted by Been et al. against Ψ and are seen to fit the following exponential relationship:

$$\phi'^{\circ} = 35.894 \text{ EXP } (-0.932\Psi) \qquad (R^2 = 0.90) \qquad (7)$$

During field CPT, the only unknown remaining is the lateral stress, σ'_h, which can be readily obtained by using lateral stress cone penetrometers or cone pressuremeters. Having obtained this, Eqns. (2.16) and (7) can be combined to give the shear strength of the Hokksund sand for any measured q_c value in the field as

$$\phi'^{\circ} = 27.448 \left(\frac{q_c - \sigma'_m}{\sigma'_m}\right) \qquad (8)$$

This equation was used to calculate the shear strength of the SU test series and then correlate to the measured D_r values by a linear relationship obtained as

$$\phi'^{\circ} = 37.31 + 0.079D_r \qquad (D_r \text{ in } \%) \qquad (R^2 = 0.86) \qquad (9)$$

Alternatively, the $q_c = f(\sigma'_m, D_r)$ relationship [Eqn. (3)] was combined with Eqn. (8) to give ϕ' as a function of D_r and σ'_m as

$$\ln \phi'^{\circ} = 3.647 - 0.0388 \ln \sigma'_m + 0.00155 D_r \qquad (10)$$

3.2.4. Sleeve Friction

Another parameter of interest in the calibration of penetrometers has been the sleeve friction, f_s. There has been little success in correlating sleeve friction to soil parameters independently of cone resistance.

A general review of the SU results could indicate that the horizontal stress has a controlling factor on the sleeve friction measurements. On this basis, the f_s values can be related to the horizontal stress for a given sand density. Since the lateral stress under BC1 remains constant during penetration, it is convenient to correlate the measured sleeve friction values of the dense samples to the initial, K_o, lateral stress by the following relationship:

$$f_s = 1.718\ \sigma_h'^{0.985} \quad [BC1,\ NC] \qquad (R^2 = 0.996) \qquad (11)$$

This relationship will be used later to estimate a correction factor for the CPT sleeve friction in conventional chambers as compared to the infinite boundary test results.

The R^2 factor of almost 1.0 indicates how closely the sleeve friction is related to the lateral stress. The same form of relationship also exists for NC results under BC3 as well as for OC results (BC1 + BC3):

$$f_s = 2.354\ \sigma_h'^{0.849} \quad [BC3,\ NC] \qquad (R^2 = 0.983) \qquad (12)$$

and

$$f_s = 2.244\ \sigma_h'^{1.2216} \quad [BC1+BC3,\ OC] \qquad (R^2 = 0.970) \qquad (13)$$

It could be deduced from the data in Tables 3.1 and 3.2 that cone resistance values depend on the lateral stress as well as the vertical stress, thus indicating that sleeve friction and cone resistance might

be related for a given density level. In fact, for given boundary and density conditions sleeve friction has been found to relate linearly to cone resistance on a log-log basis (Fig. 3.3a). The linear relationship on a double logarithmic scale also exists for the small cone (5 cm^2), but with a different slope (also Parkin, 1986). This suggests that the relationship between sleeve friction and cone resistance also depends on the cone size.

Whilst it is tempting to represent the $q_c - f_s$ relationship by a straight line, in Hokksund sand the linear relationship between the two only roughly exists for loose and medium-dense samples at lower stresses, [and hence, lower cone resistances (q_c<250 kg/cm^2), Fig. 3.3b]. Dense samples do not even show this degree of linearity.

As far as f_s is concerned, the boundary condition under which a CC test is carried out, plays an important role in dense and very dense samples, though not in loose ones. When dense samples are tested under BC1 (constant stress), the measured f_s values will be lower than those obtained under BC3 (constant lateral volume, base flexible) for the same cone resistance. The two cases converge at very high cone resistances (q_c > 400 kg/cm^2).

3.2.5. Cone Size

The relative cone size has always been an important criterion in checking the validity of calibration chamber test results. When the small cone is used, a plot of friction ratio (f_s/q_c, in percent) against cone resistance gives a linear variation for dense samples (with BC1 relationship flatter than the BC3) [FIG. 3.4]. For the 10 cm^2 cone, on the other hand, relationships for both boundary conditions are almost flat at low stresses,and hence at low q_c values, but rapidly increase for q_c > 200 kg/cm^2.

Further investigation on the effect of cone size is dealt with in the next chapter on the chamber size effect.

3.2.6. Stress Level

A measure of the cone resistance dependence on stress level alone can be seen from the plot of q_c against σ'_h. The results yield a log-log linear relationship between q_c and σ'_h for both NC and OC dense samples tested by the standard 10cm² cone (Fig. 3.5). The same relationship exists for the small cone (5cm²), but shows a factor of about 1.2 times that of the larger cone.

Stress level also affects the obtained sleeve friction data. Sleeve friction is best related to mean or horizontal stress rather than vertical stress. Figs. 3.6 and 3.7 show plots of f_s against effective horizontal and mean stresses, respectively, for very dense Hokksund sand. It is interesting to note that BC3 values are higher than those under BC1 for both cone sizes. The large cone, on the other hand, yields higher sleeve friction values than the small cone does. Under low stresses ($\sigma'_h < 0.2$ kg/cm² and $\sigma'_m < 0.4$ kg/cm²), all values, in general, tend to converge. The large cone, however, shows a linear relationship under BC1 for both NC and OC samples. One can roughly assume the same trend for the small cone under the same boundary conditions.

Furthermore, when plotted against σ'_h, the curves for both NC and OC samples coincide; but a clear divergence is noticed in the $f_s - \sigma'_m$ relationship even though the linearity is maintained in both cases.

3.2.7. Overconsolidation Ratio (OCR)

Large scale (CC) laboratory tests have shown that penetration resistances are influenced by the current level of σ'_h and remain insensitive to the effect either of the accumulated plastic strain or of the deformation moduli.

From the SU dense tests under different stress histories it was implied that cone resistance is a function of both σ'_v and OCR (Fig.

3.8). This, however, is not the case if σ'_h values are also plotted against each point. The resulting contours indicate that q_c is a function of σ'_h only (to a sufficient accuracy), at least up to OCR=8. This can also be checked from a plot of cone resistance (normalised against mean stress) versus OCR (Fig. 3.9) for a given σ'_v. The first figure shows a slight increase in q_c due to overconsolidation, but for practical purposes, one may assume this dependence of cone resistance on horizontal effective stress applies (Veismanis,1974; Chapman and Donald, 1981).

The same occurs when normalised sleeve friction values (against σ'_h) are plotted either against OCR for a given stress level or against the coefficient of earth pressure at rest, K_o [determined during the initial loading of samples for different stress histories] (Figs. 3.10 and 3.11). The first one shows that normalised sleeve friction is independent of OCR for a given σ'_v. It is apparent from the second figure that for a given stress history, K_o is almost independent of stress level, especially at higher sleeve frictions or lower horizontal stresses.

3.2.8. Deformation Characteristics of Sands

Because of the complexity of the relationship between the cone resistance and the strength and deformation properties, there is no generally applicable analytical solution relating them. Instead, many empirical correlations between cone resistance and deformation modulus have been established.

a. Young's Modulus, E

Because of the non-linearity in the stress-strain relationship, E is usually determined as a secant modulus, computed at an estimated working stress level. Baldi et al. (1982) suggest a factor of safety for foundations on sand to be at least 4; hence, E'_{25} is the common value selected for study (Bellotti et al., 1985), i.e., the secant modulus evaluated at a deviatoric stress level corresponding to one

fourth of the failure stress. Experimental values of E'_{25}, obtained from triaxial tests have been related to the consolidation stresses using an empirical formula (similar to the relationship proposed by Schmertmann, 1976), which also incorporates the influence of relative density on E' (Bellotti et al., 1985), as given below:

$$E'_{25} = C0\ P_a \cdot (\sigma'/P_a)^{C1} \exp(D_r \cdot C2) \qquad (14)$$

where:

σ' = selected consolidation stress component

C0,C1,C2 = experimental coefficients

P_a = reference stress = 1 kg/cm^2.

E'_{25} values have been related to cone resistance values obtained from CC tests at the same densities, as illustrated in Fig. 3.12.

For NC samples, the stiffness ratio (E'_{25} to q_c) falls in a narrow range, showing that it is almost independent of the sample density. Similar results have also been obtained by Schmertmann (1970) and Schmertmann et al. (1978).

For OC samples, on the other hand, the above ratio is several times higher (also by Lambrechts and Leonards, 1978, and Baldi et al., 1985 for this and other similar sands), suggesting that stress and strain history have a major effect on the stiffness of sands but a much smaller effect on the cone resistance. Also, the stiffness ratio, for OC samples, is greatly influenced by the relative density (it decreases as D_r increases).

b. Constrained Modulus, M

In considering the linear relationship between M and q_c, in dense Hokksund sand, at the most favourable diameter ratio and boundary condition for modelling field conditions (small cone and BC_3), Lunne and Kelven, 1981, and Parkin, 1977 suggest $M/q_c = 3$. Though not fully supported by the results of tests at the Norwegian Geotechnical

Institute (NGI) and Italy, a great number of Southampton CC tests show that normalised M values (M/q_c) fit in a narrow range, very little affected by relative density changes, giving $M/q_c \simeq 5 \pm 1$ for loose samples and $M/q_c \simeq 3.5 \pm 0.5$ for very dense samples (Fig. 3.13). For the same values of relative density and consolidation stress, the M/q_c ratio for OC sands is much greater than that for NC ones. This observation confirms that q_c is influenced only to a limited extent by the stress-strain history of the soil, which, on the other hand, has an appreciable influence on sand stiffness.

The Southampton results suggest a linear relationship between M and the square root of q_c for NC samples when a 5 cm² cone is used but with some scattering for 10 cm² cone data (Fig. 3.14). This confirms the effect of cone size on the obtained results. For OC dense samples, on the other hand, a perfect linear M versus $\sqrt{q_c}$ relationship exists for each stress history (OCR), with higher slopes for lower OCR (except OCR=1).

A similar type of relationship also exists between M and square root of sleeve friction ($\sqrt{f_s}$) for both the NC and the OC samples of Hokksund sand tested in the CC (Fig. 3.15). Boundary condition and cone size also effect the obtained results.

Despite Vesic's (1970) belief that no correlation exists between M/q_c and stress (σ'_v or σ'_h), the constrained modulus can be related to the consolidation stress by means of the following empirical formula (Bellotti et al., 1985):

$$M = mo\ p_a \cdot (\sigma'/p_a)^{m1} \cdot \exp(m2 \cdot D_r) \qquad (15)$$

where:

mo , m1 , and m2 = experimental coefficients
σ' = selected consolidation stress component
p_a = reference stress (= 1 kg/cm²)

The SU results show that this formula fits closely to the experimental values for med-dense and very dense samples at low effective horizontal stresses (σ'_h < 0.5 kg/cm²), but underestimates them at higher stresses. For OC samples, on the other hand, the above relationship only fits well with the measured values at stresses higher than about 0.7 kg/cm² and overestimates at lower stresses (Fig. 3.16). This may be due to the fact that average secant constrained modulus values rather than the modulus corresponding to the final increment of the unloading process have been chosen from the experimental results.

This relationship was further modified by Baldi et al. (1986) in order to account for the influence of OCR directly rather than through the increased horizontal stress alone as a result of overconsolidation:

$$M = m_o p_a \left(\frac{\sigma'_m}{p_a}\right)^{m1} (OCR)^{m3} \text{ EXP } (m2 \cdot D_r) \qquad (16)$$

A series of regression analyses performed on both NC and OC specimens of Hokksund sand resulted in the following coefficients for Eqns. (15) and (16) as given in Table 3.8.

Eqn. (16) can also be combined with Eqn. (4) in order to correlate cone resistance with the constrained tangent modulus, resulting in the following form

$$\frac{M}{q_c} = m_o p_a \left(\frac{\sigma'_m}{p_a}\right)^{m1} (OCR)^{m3} \text{ EXP } (m2 \cdot D_r) \qquad (17)$$

Based on this correlation, the following general comments can be made:

- For the same stress history, the ratio of M/q_c decreases as D_r increases. This reflects the different degree to which the D_r influences M and q_c, respectively.

- The $^{M}/q_c$ ratio moderately decreases as the mean effective stress increases.

- For the same values of D_r and σ'_m, the $^{M}/q_c$ ratio increases with increasing OCR.

3.3. Conclusion

It has been shown, indirectly, throughout this chapter that cone response is different for different boundary conditions. Hence, the interpretations of material properties are affected by the BC used. The author feels it necessary to discuss the effects of boundary conditions and the chamber size on the measured stresses separately together with their implications on the material interpretation. The next chapter considers these issues from different perspectives and adjustments to the measured cone stresses are discussed.

TEST	γ_{d_3} t/m3	D_R %	σ'_v kg/cm2	K_o –	OCR –	M kg/cm2	q_c kg/cm2	f_s kg/cm2	d_c cm	BC	
SU1	–	–	–	–	–	–	–	–	–	–	1)
SU2	1.715	91.4	0.63	0.37	1	508	176	0.48	2.52	B1	
SU3	1.717	91.9	0.63	0.35	1	510	133	0.37	3.57	B1	
SU4	1.727	94.4	1.13	0.33	1	638	204	0.70	3.57	B1	
SU5	1.730	95.1	2.13	0.32	1	1020	275	1.16	3.57	B1	
SU6	1.720	92.4	4.13	0.31	1	1250	377	2.13	3.57	B1	
SU7	1.705	88.9	3.13	0.36	1	1378	342	1.97	3.57	B1	
SU8	1.711	90.4	4.13	0.31	1	1190	418	2.71	3.57	B3	
SU9	1.740	97.6	2.13	0.33	1	1075	336	1.94	3.57	B3	
SU10	1.720	92.7	1.13	0.33	1	714	224	1.03	3.57	B3	
SU11	1.706	89.1	0.63	0.41	1	852	163	0.71	3.57	B3	
SU12	1.692	85.6	1.13	0.60	1	–	284	1.29	3.57	B1	2)
SU13	1.717	91.9	1.13	0.95	1	–	323	1.81	3.57	B1	2)
SU14	1.690	85.1	1.13	0.95	1	–	266	1.29	3.57	B1	2)
SU15	–	–	–	–	–	–	–	–	–	–	5)
SU22	1.733	95.9	1.13	0.37	1	887	265	0.73	2.52	B1	
SU23	1.706	89.1	2.13	0.37	1	1187	367	1.05	2.52	B1	
SU24	1.700	87.6	3.13	0.38	1	1275	408	1.35	2.52	B1	
SU25	1.713	90.9	4.13	0.37	1	1595	500	1.58	2.52	B1	
SU26	1.731	95.4	0.63	0.37	1	576	194	0.56	2.52	B3	
SU27	1.720	92.7	1.13	0.37	1	750	265	0.91	2.52	B3	
SU28	1.710	90.2	2.13	0.37	1	1250	408	1.68	2.52	B3	
SU29	1.720	92.7	4.13	0.38	1	1765	540	2.32	2.52	B3	
SU32	1.720	92.7	0.63	0.39	1	576	175	0.57	2.52	B1	3)
SU33	1.630	69.0	0.62	0.38	1	536	98	0.25	2.52	B1	
SU34	1.628	68.5	0.62	0.34	1	329	95	0.39	3.57	B3	
SU35	1.627	68.2	0.62	0.35	1	392	84	0.39	3.57	B1	
SU36	1.610	63.4	2.12	0.38	1	809	238	1.03	3.57	B3	
SU37	1.620	66.2	2.12	0.36	1	850	228	0.90	3.57	B1	
SU38	1.570	51.8	0.62	0.39	1	283	57	0.19	3.57	B3	
SU39	1.550	45.7	2.12	0.40	1	490	112	0.51	3.57	B3	
SU40	1.552	46.3	1.12	0.40	1	329	76	0.28	3.57	B3	
SU41	1.564	50.0	4.12	0.40	1	864	209	1.03	3.57	B3	
SU42	1.472	20.5	0.61	0.47	1	116	20	0.06	3.57	B3	
SU43	1.482	23.9	2.11	0.47	1	302	57	0.19	3.57	B3	
SU44	1.482	23.9	4.11	0.45	1	481	121	0.65	3.57	B3	3)

1) Aborted
2) Not K_o loading
3) Assumed density
5) Test not satisfactory

Table 3.1. CPT results in the calibration chamber on NC Hokksund sand at the University of Southampton (Last et al., 1987)

TEST	γ_{d_3} t/m^3	D_R %	σ'_v kg/cm^2	K_o –	OCR –	M kg/cm^2	q_c kg/cm^2	f_s kg/cm^2	d_c cm	BC
SU16	1.719	92.4	1.13	0.49	2	2307	245	1.03	3.57	B1
SU17	1.680	82.5	1.13	0.60	4	2000	296	1.55	3.57	B1
SU18	1.718	91.9	0.63	0.47	2	1456	163	0.55	3.57	B1
SU19	1.730	95.1	0.63	0.63	4	1530	184	0.71	3.57	B1
SU20	1.733	95.8	0.63	0.81	8	1342	204	0.87	3.57	B1
SU21	1.701	87.9	2.13	0.40	2	3191	347	1.88	3.57	B1
SU30	1.730	91.4	1.13	0.49	2	1974	306	1.15	2.52	B1
SU31	1.730	95.1	1.13	0.61	4	3000	367	1.42	2.52	B1
SU45	1.476	21.9	0.61	0.54	2	927	38	0.16	3.57	B3
SU46	1.481	23.6	0.61	0.63	4	1020	35	0.17	3.57	B3
SU47	1.481	23.6	1.11	0.64	4	1417	66	0.28	3.57	B3
SU48	1.469	19.5	0.61	0.56	2	1457	30	0.14	3.57	B1
SU49	1.473	20.9	1.11	0.56	2	1457	52	0.28	3.57	B1
SU50	–	–	–	–	–	–	–	–	–	–
SU51	1.478	22.6	1.11	0.53	2	1430	60	0.28	3.57	B3
SU52	1.470	19.8	0.61	0.69	8	981	68	0.33	3.57	B1
SU53	1.470	19.8	0.61	0.62	4	1020	56	0.22	3.57	B1
SU54	1.480	23.2	1.11	0.66	4	1457	67	0.36	3.57	B3
SU55	1.472	20.5	2.11	0.57	2	2125	103	0.53	3.57	B3
SU56	1.475	21.5	1.11	0.64	4	1417	63	0.35	3.57	B1
SU57	1.481	23.6	2.11	0.56	2	2550	127	0.64	3.57	B1
SU58	1.489	26.2	0.61	0.71	8	936	56	0.28	3.57	B3
SU59	1.498	29.2	0.61	0.63	4	1085	52	0.18	3.57	B3
SU72	1.623	67.1	0.62	0.78	8	900	78	0.29	3.57	B1
SU73	1.643	72.6	0.62	0.88	8	1020	72	0.27	3.57	B1
SU74	1.616	65.1	0.62	0.47	2	1275	78	0.26	3.57	B1
SU75	1.619	66.0	0.62	0.59	4	1020	95	0.30	3.57	B1
SU76	1.654	75.6	0.62	0.58	4	1133	133	0.36	3.57	B1

1) Aborted

3) Assumed density

4) Special test

Table 3.2. CPT results in the calibration chamber on OC Hokksund sand at the University of Southampton (Last et al., 1987)

TEST	γ_{d3} t/m^3	D_R %	σ'_v kg/cm^2	K_o –	OCR –	M kg/cm^2	q_c kg/cm^2	f_s kg/cm^2	d_c cm	BC
E174	1.692	82.3	1.23	.451	1.00	729	221.5	1.47	3.57	BC1
E175	1.690	81.7	.70	.436	1.00	545	152.9	.81	3.57	BC1
E177	1.692	82.3	2.72	.439	1.00	1075	354.1	2.96	3.57	BC1
E178	1.742	95.6	.70	.438	1.00	553	190.5	1.03	3.57	BC1
E179	1.742	95.6	.70	.442	1.00	532	234.2	.99	2.54	BC1
E180	1.742	95.6	.72	.424	1.00	581	264.7	—	2.00	BC1
E184	1.533	34.0	1.19	.489	1.00	415	28.4	.23	3.57	BC1
E185	1.528	32.3	.64	.479	1.00	300	15.2	.11	3.57	BC1
E186	1.525	31.3	3.18	.506	1.00	613	59.9	.50	3.57	BC1
NO01	1.734	96.0	.62	.460	1.00	733	167.8	--	3.57	BC1
NO02	1.721	93.0	.62	.350	1.00	630	209.0	--	3.57	BC3
NO05	1.510	33.0	.60	.410	1.00	207	22.6	--	3.57	BC1
NO06	1.514	34.0	.60	.370	1.00	205	29.4	--	3.57	BC3
NO09	1.725	94.0	.62	.350	1.00	692	153.0	--	3.57	BC1
NO13	1.710	90.0	.62	.390	1.00	873	185.4	--	2.52	BC1
NO15	1.706	89.0	.62	.320	1.00	637	230.5	--	2.52	BC1
NO18	1.495	28.0	.60	.400	1.00	242	36.3	--	2.52	BC1
NO19	1.499	30.0	.60	.380	1.00	214	11.8	--	2.52	BC3
NO22	1.709	90.0	.62	.360	1.00	692	217.8	--	2.52	BC1
NO23	1.714	91.0	.62	.350	1.00	685	187.4	--	2.52	BC1
NO24	1.533	40.0	.60	.400	1.00	213	60.8	--	2.52	BC3

Table 3.3. CPT results in the calibration chamber on NC Hokksund sand (Italian & Norwegian results) (Last et al., 1987)

TEST	γ_{d} t/m^3	D_R %	σ'_v kg/cm^2	K_o –	OCR –	M kg/cm^2	q_c kg/cm^2	f_s kg/cm^2	d_c cm	BC
E181	1.744	96.1	.64	1.272	14.55	2428	206.6	1.48	3.57	BC1
E182	1.745	96.4	.64	1.265	14.47	2435	354.1	1.44	2.54	BC1
E183	1.744	96.1	.65	1.253	14.40	2466	389.1	--	2.00	BC1
E187	1.528	32.3	1.14	.870	7.28	1985	45.7	.40	3.57	BC1
N003	1.727	94.0	.62	1.000	8.00	2410	229.6	--	3.57	BC1
N004	1.723	93.0	.62	.990	8.00	2560	232.5	--	3.57	BC3
N007	1.498	29.0	.60	.910	8.00	1550	50.0	--	3.57	BC1
N008	1.489	26.0	.60	.750	8.00	1690	52.0	--	3.57	BC3
N010	1.718	92.0	.62	.840	8.00	2580	160.9	--	3.57	BC1
N011	1.510	33.0	.60	.900	8.00	1690	42.2	--	3.57	BC1
N012	1.502	31.0	.60	.930	8.00	1680	40.2	--	3.57	BC3
N014	1.719	92.0	.62	.890	8.00	2140	299.2	--	2.52	BC1
N016	1.710	90.0	.62	.900	8.00	2210	300.2	--	2.52	BC3
N017	1.713	91.0	.62	.980	8.00	2290	313.9	--	2.52	BC1
N020	1.487	26.0	.60	.790	8.00	1570	29.4	--	2.52	BC1
N021	1.480	23.0	.60	.870	8.00	1510	26.5	--	2.52	BC3
N025	1.496	29.0	.60	.740	8.00	1730	49.1	--	2.52	BC1
N026	1.720	93.0	.62	.910	8.00	2460	214.8	--	2.52	BC1

Table 3.4. CPT results in the calibration chamber on OC Hokksund sand (Italian & Norwegian results) (Last et al., 1987)

q_c	C0	C1	C2 x10^{-2}	C3	R^2	TEST SERIES
$f(\sigma'_m, Dr)$	57.63	0.530	1.88	NA	0.94	SU
$f(\sigma'_m, Dr)^*$	19.48	0.549	2.88	NA	0.96	SU+ITAL.+NOR.
$f(\sigma'_m, OCR, D_r)$	53.44	0.590	1.91	0.111	0.95	SU

* after Baldi et al. (1986)

Table 3.5. Results of the regression analyses on Hokksund sand in relating cone resistance to relative density.

Sand Type	C0	C1	C2	C3 x10^{-2}	R^2	No. of Tests
Hokksund	12.393	0.14	0.40	3.38	0.96	64
$30 < D_r < 98$ (%) $0.5 < \sigma'_v < 8.0$ (bars) $1 \leq OCR \leq 8$ with q_c values corrected for CC size effects						

Table 3.6. Results of Regression Analyses relating Cone Resistance to Relative Density and Confining Stresses Separately (after Baldi et al., 1986)

BC	OCR	C0	C1	C2 x10^{-2}	R^2
BC1	1	108.01	0.5764	0.8882	0.983
BC3	1	43.717	0.5592	2.0248	0.966
BC1+BC3	2 - 8	51.612	0.8176	1.9954	0.951

Table 3.7. Results of the regression analysis on the SU results based on the qc = $f(\sigma'_m, D_r)$ of Eqn. 3.3 for different boundary conditions

M	stress history	σ'	m0	m1	m2 x0.01	m3	R^2
f(σ', Dr) Bellotti et al (1985)	NC	σ'_v	208	0.425	1.36	NA	0.95
	OC	σ'_h	2065	0.561	0.38	NA	0.77
	OC	σ'_m	2055	0.569	0.30	NA	0.77
f(σ', D_r, OCR) Baldi et al. (1986)	NC+OC	σ'_m	283.8	0.522	1.32	0.334	0.97

Table 3.8. Results of Regression Analyses on Relating Constrained Tangent Modulus to Stress Level and Relative density

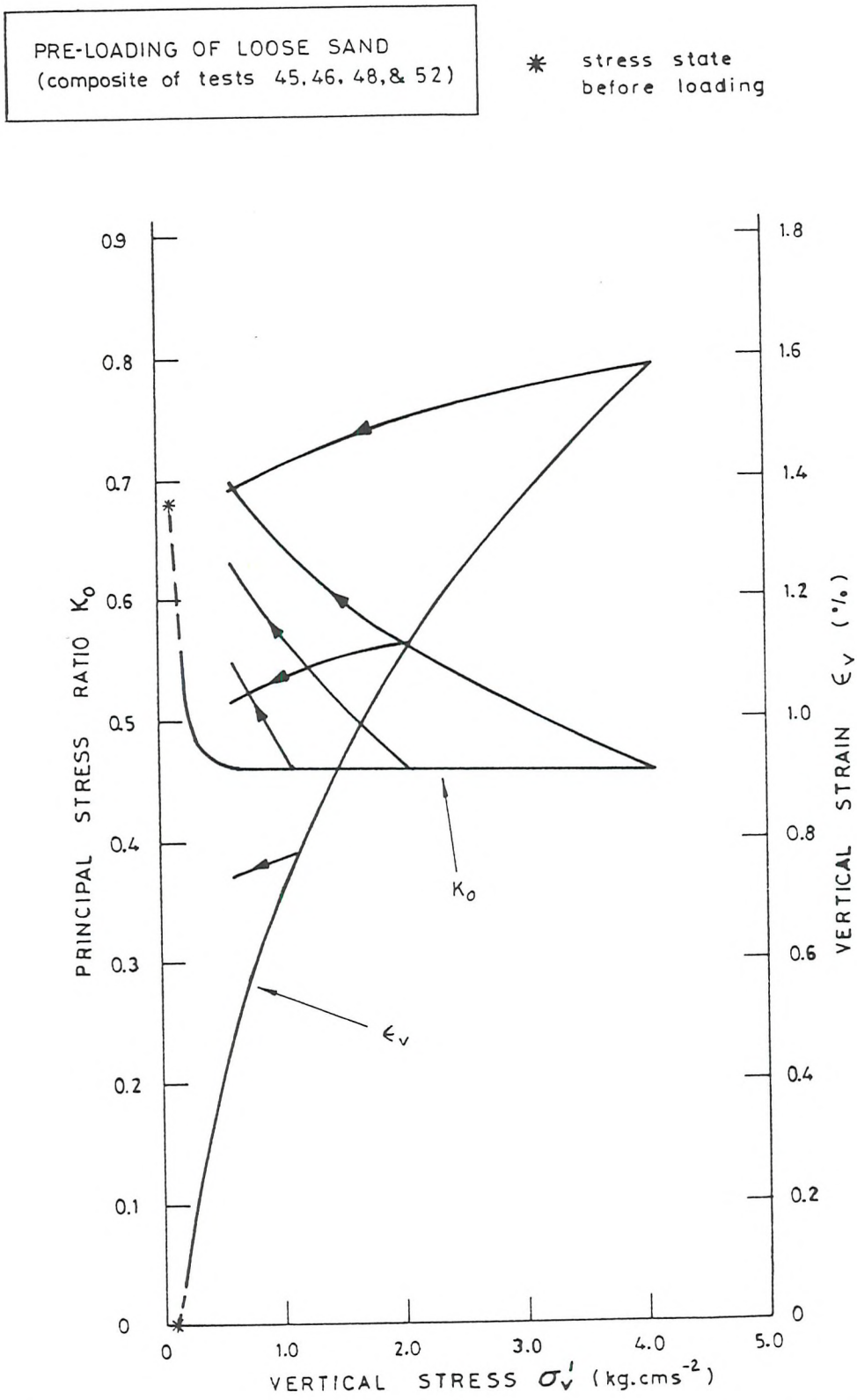

Fig. 3.1a Principal stress ratio, K_o, and vertical strain, ε_v, during loading and unloading – loose samples

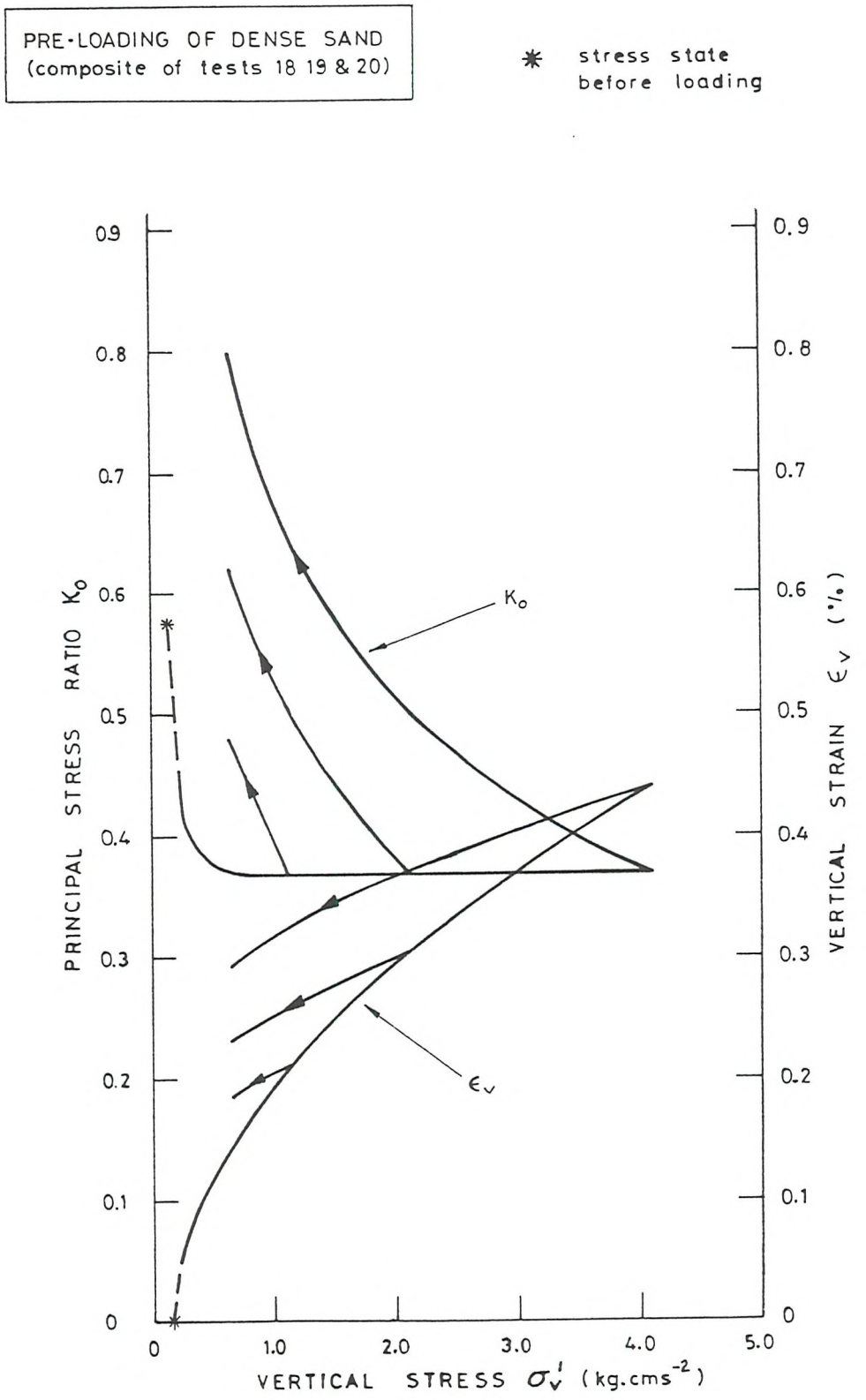

Fig. 3.1b Principal stress ratio, K_o, and vertical strain, ε_v, during loading and unloading – dense samples

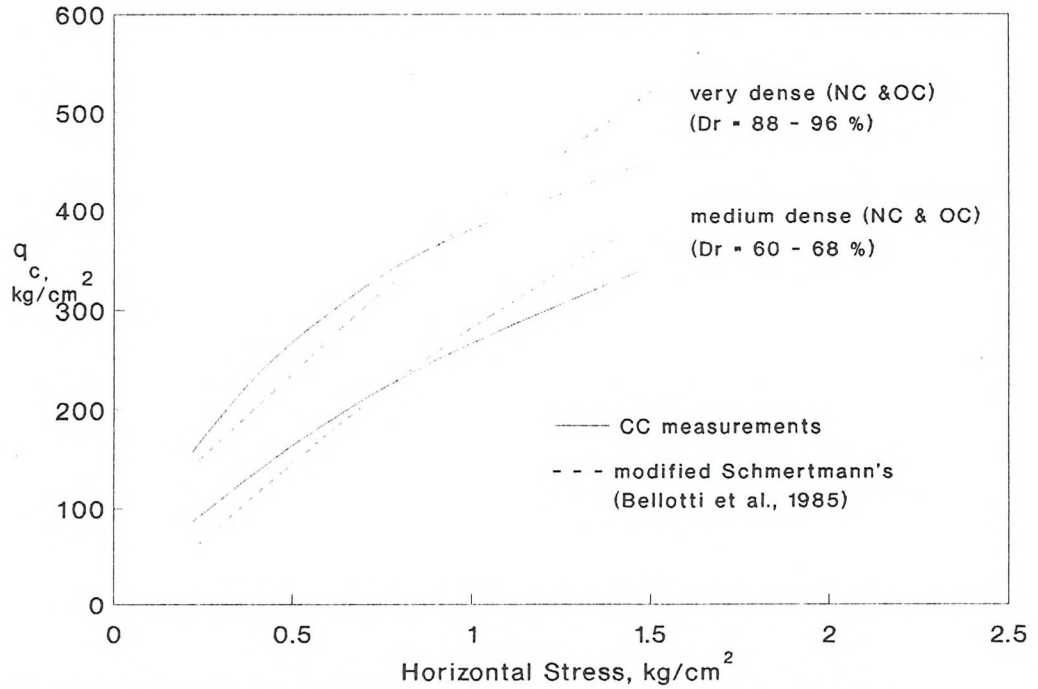

Fig. 3.2 Theoretical and experimental plots of cone resistance vs. horizontal stress for Hokksund sand

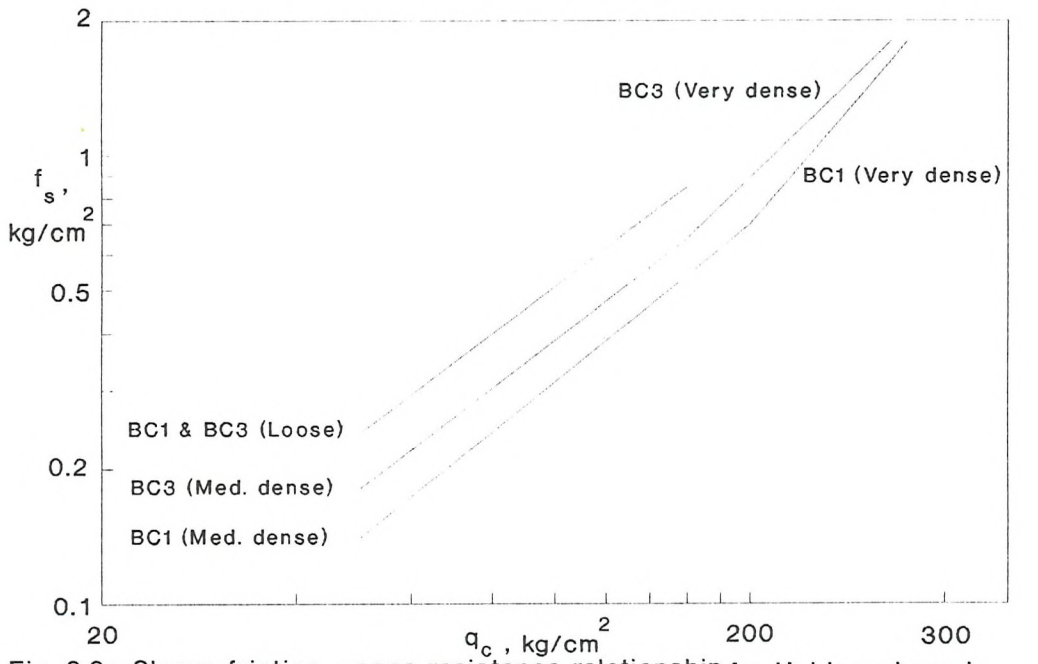

Fig. 3.3a Sleeve friction - cone resistance relationship for Hokksund sand using standard cone

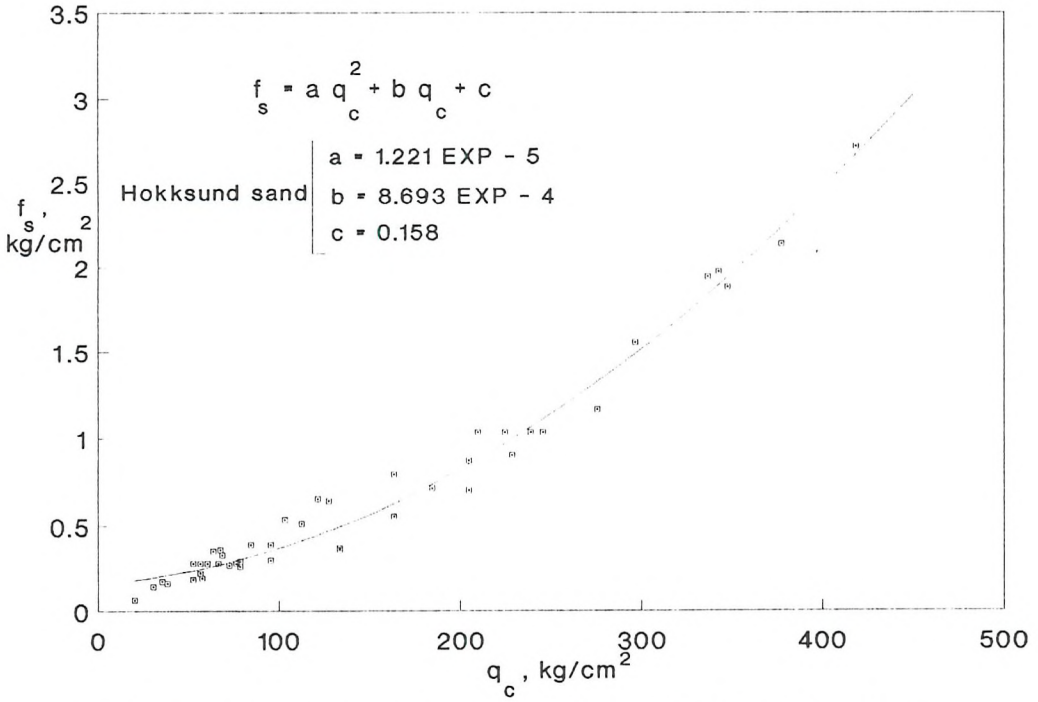

Fig. 3.3b Sleeve friction vs. cone resistance for all BC's and densities

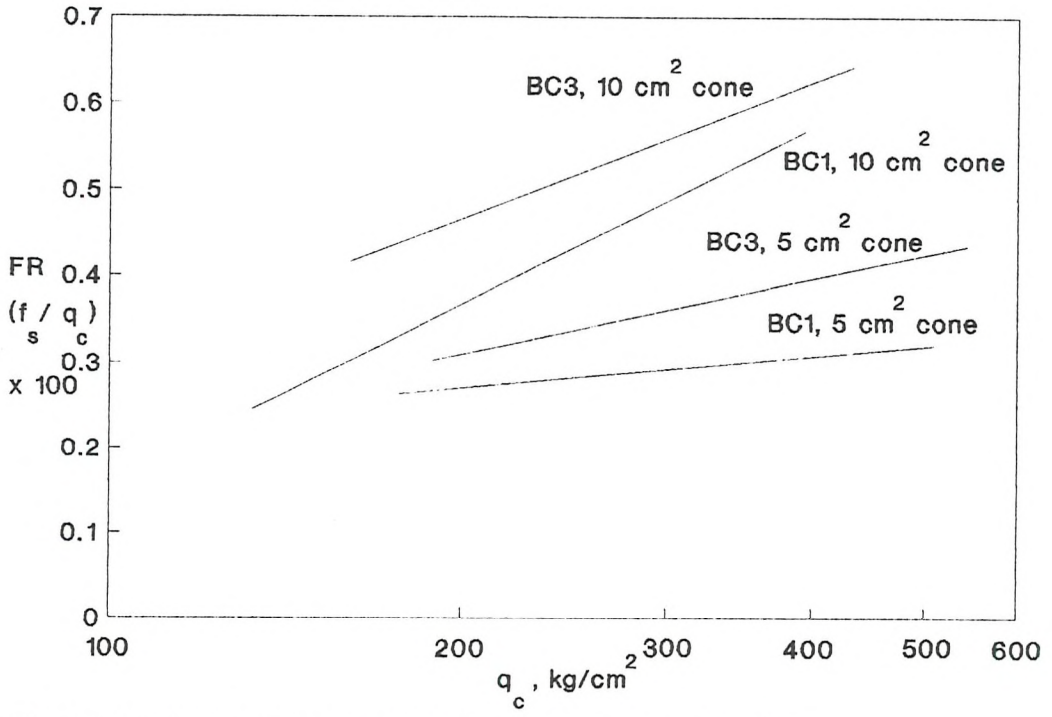

Fig. 3.4 Friction ratio vs. cone resistance for dense samples

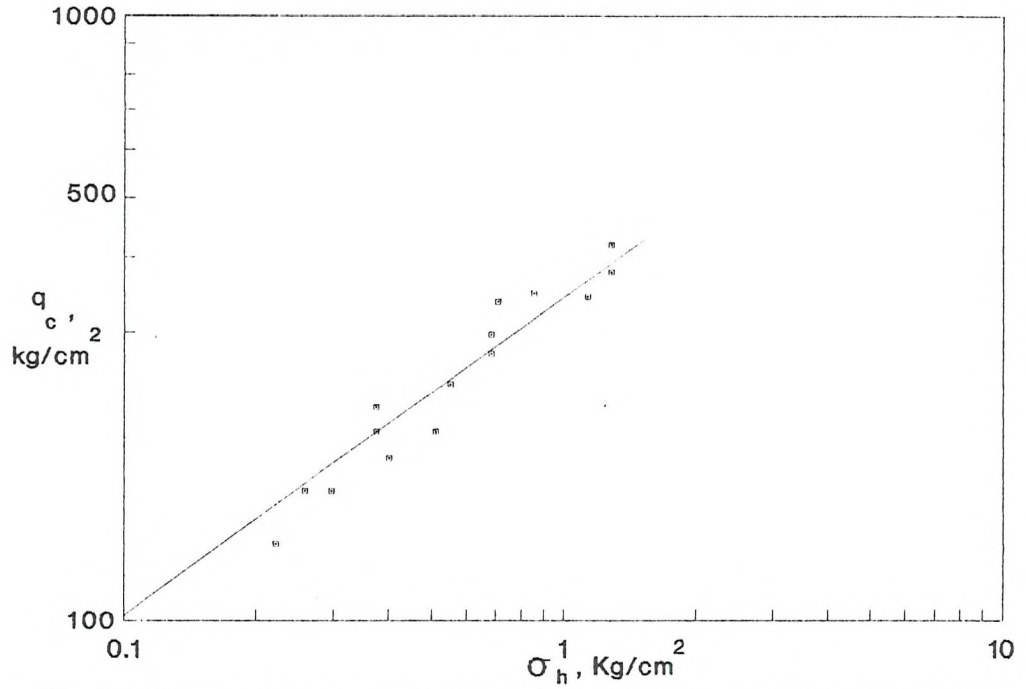

Fig. 3.5 Cone resistance vs. horizontal stress for dense NC and OC sand under BC1 and BC3

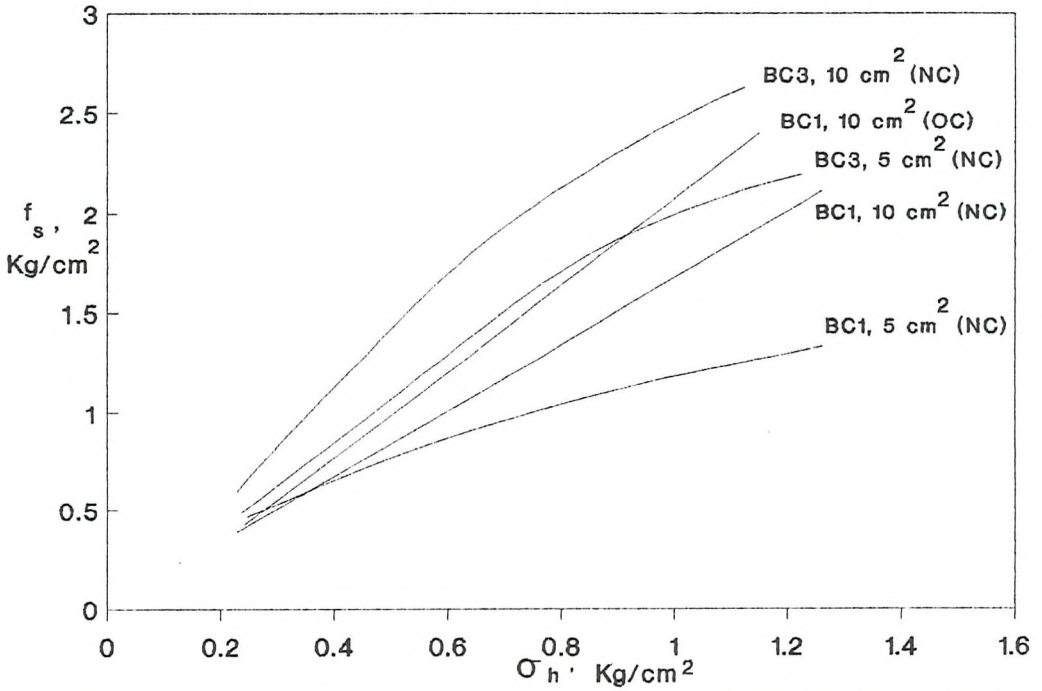

Fig. 3.6 Sleeve friction vs. horizontal stress for very dense Hokksund sand using different cone sizes

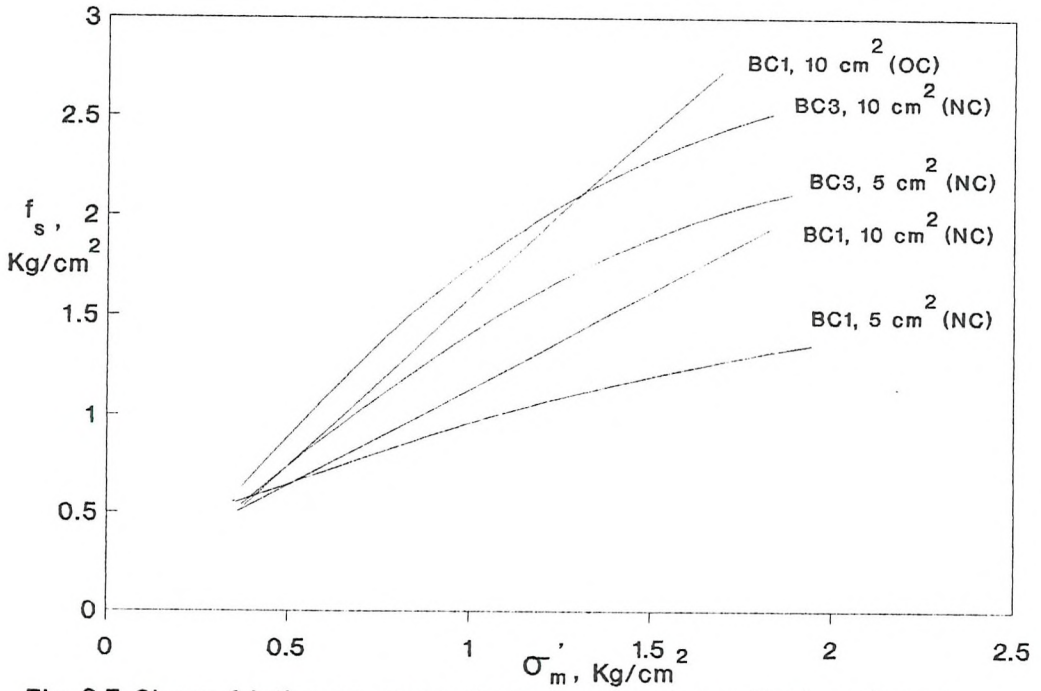

Fig. 3.7 Sleeve friction vs. mean stress for very dense Hokksund sand using different cone sizes

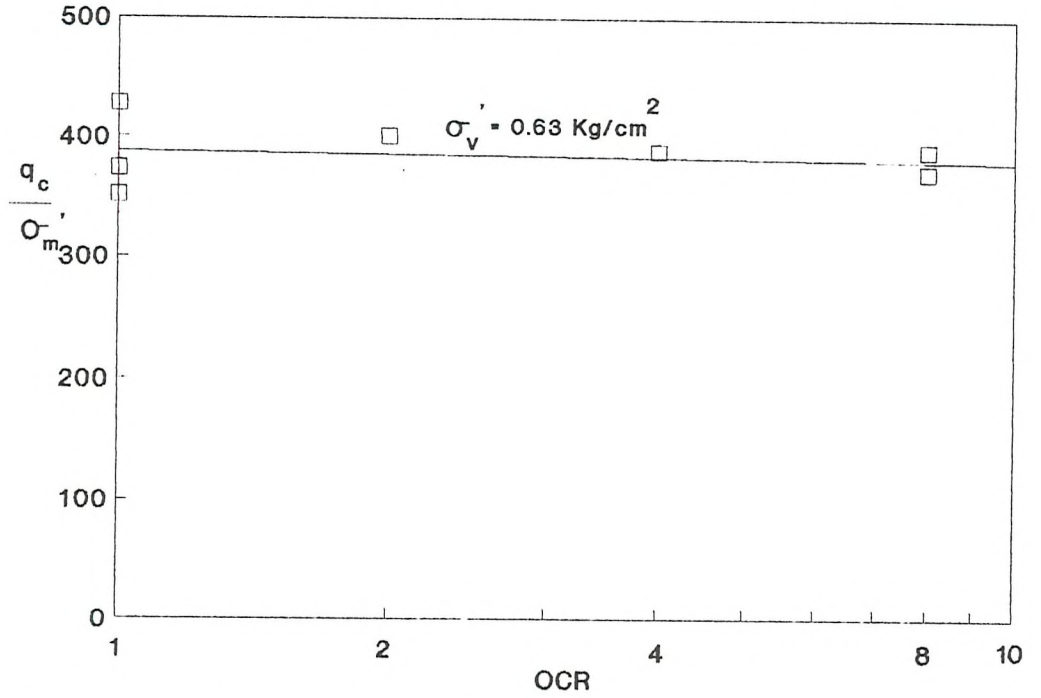

Fig.3.8 Normalised cone resistance vs. OCR for very dense Hokksund sand

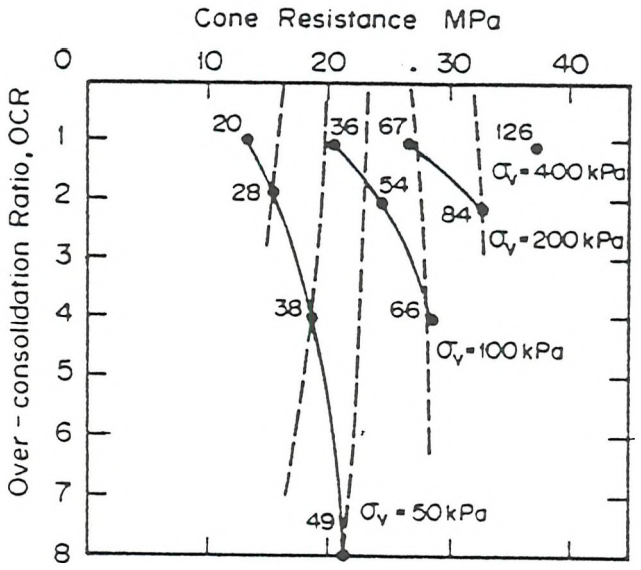

Fig. 3.9 Variation of cone resistance versus OCR (Last, 1985)
[dotted lines are the σ'_h contours at each point]

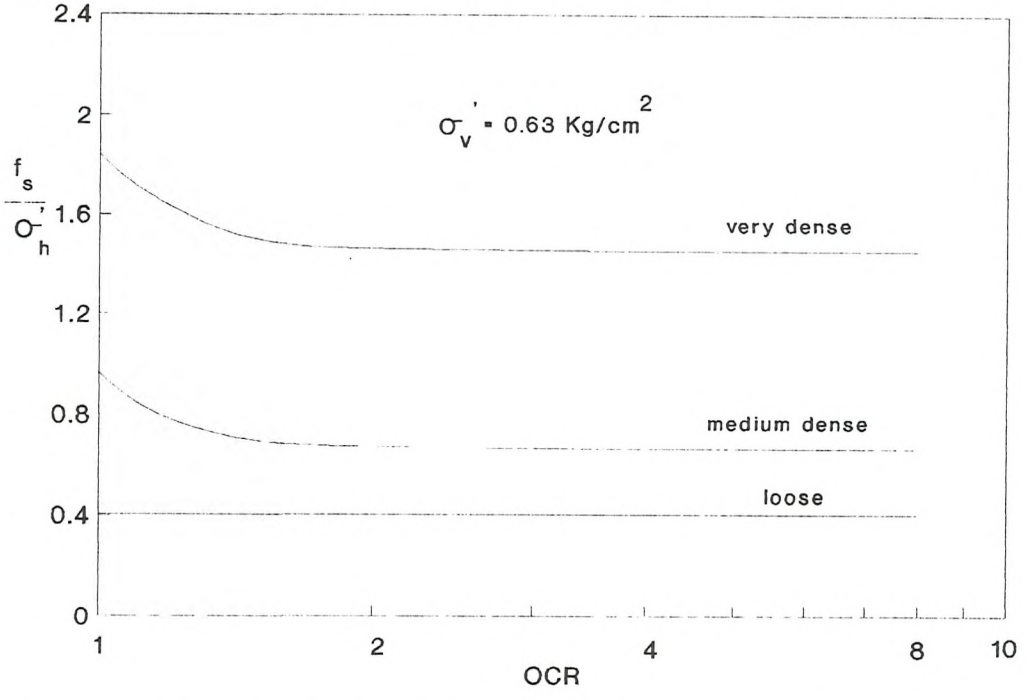

Fig. 3.10 Normalised sleeve friction vs. OCR for very dense Hokksund sand

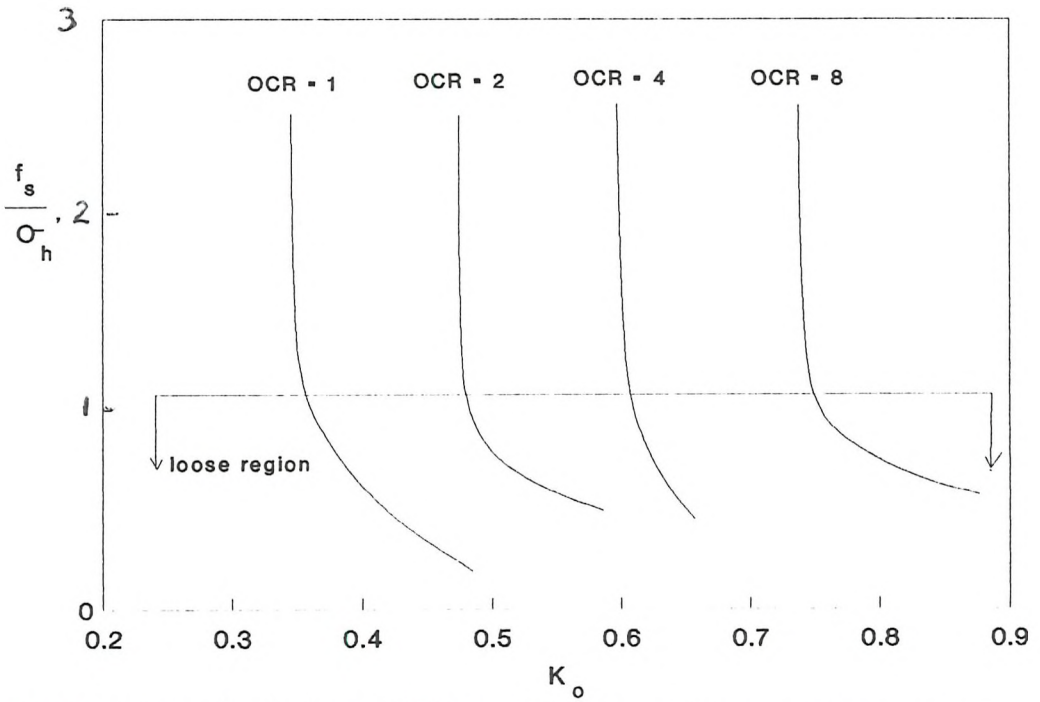

Fig. 3.11 Normalised sleeve friction vs. K_o for very dense Hokksund sand

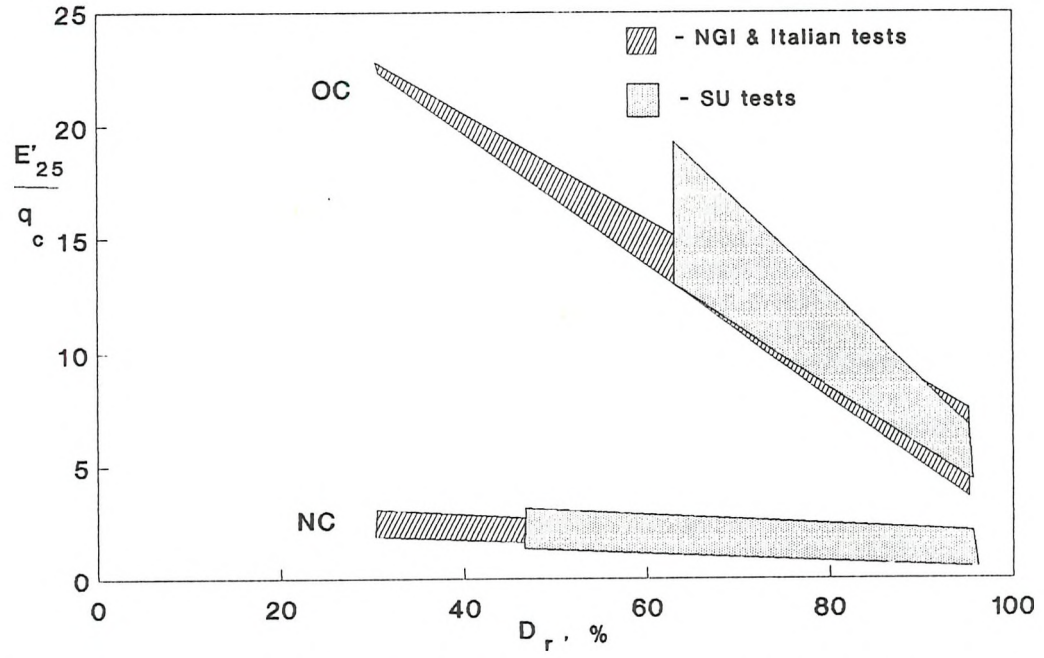

Fig. 3.12 Normalised stiffness vs. relative density for Hokksund sand

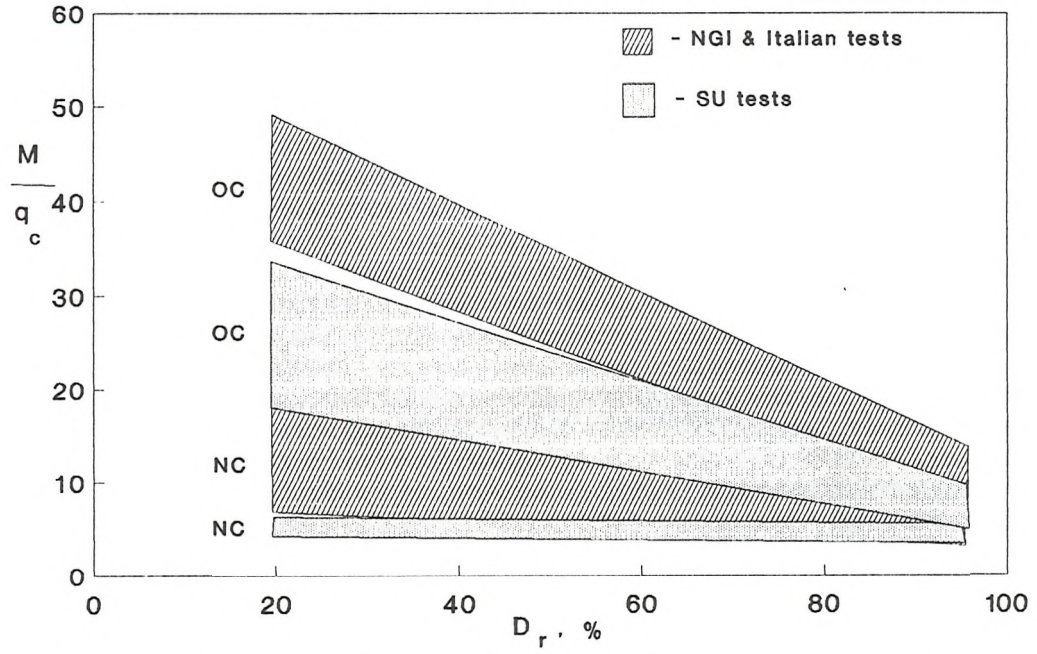

Fig. 3.13 Normalised constrained modulus vs. relative density for Hokksund sand

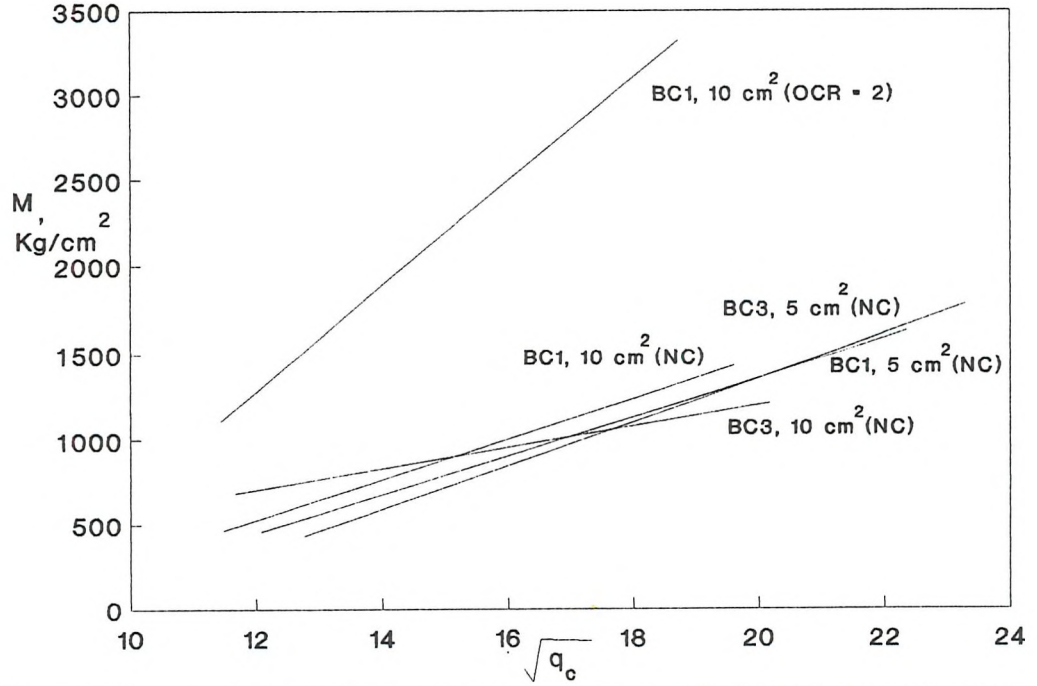

Fig. 3.14 Constrained modulus and cone resistance relationship for very dense NC and OC Hokksund sand using different cone sizes

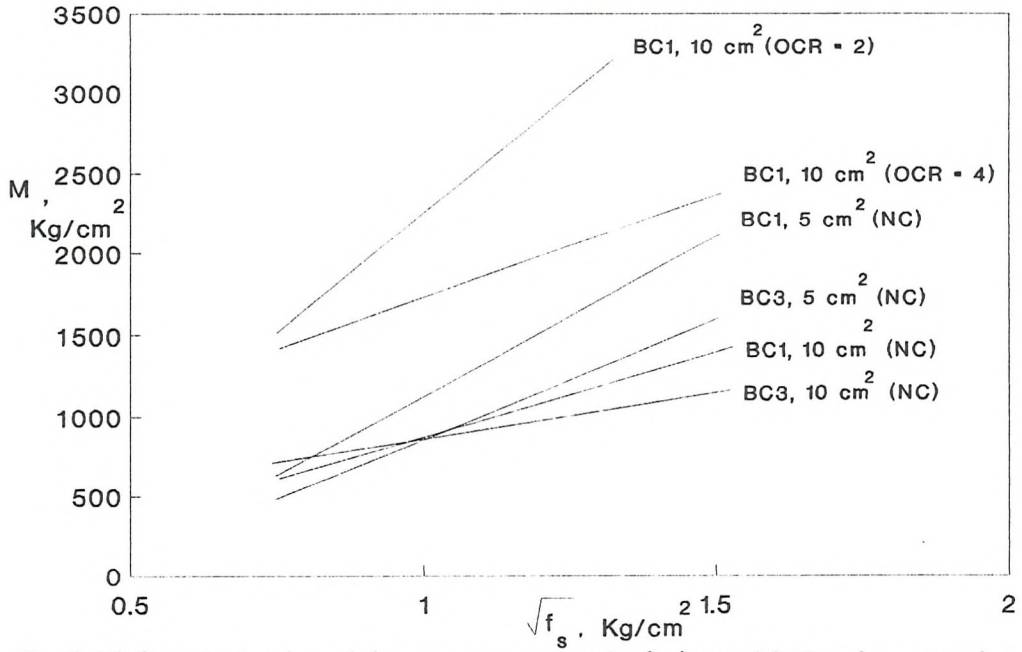

Fig. 3.15 Constrained modulus vs. square root of sleeve friction for very dense Hokksund sand using different cone sizes

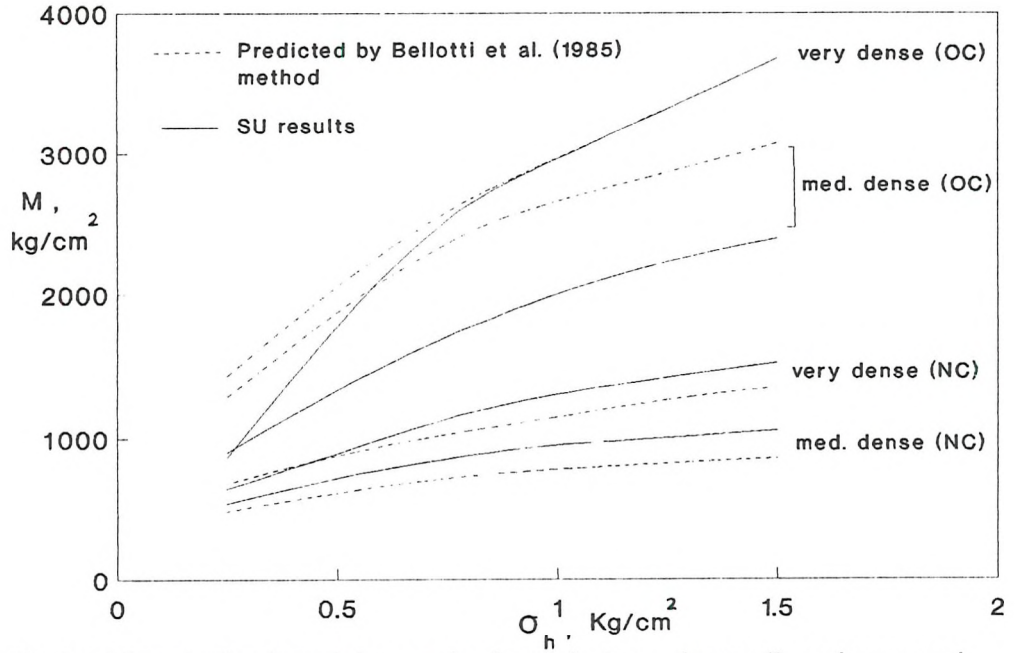

Fig. 3.16 Constrained modulus vs. horizontal stress for medium dense and very dense Hokksund sand

CHAPTER 4

STANDARD BOUNDARY CONDITIONS AND CHAMBER SIZE EFFECTS

4.1. Introduction

Two boundary conditions have become commonly accepted in recent years for the NGI type chamber. Both rely on a hydrostatic water column to support and apply pressure to the cylindrical rubber sleeve that encloses the sample laterally. The BC1 tests control this lateral pressure to remain constant (at a given height) for the duration of the penetration test, the amount of water pushed out of the annulus in this process being measured to enable the diameter change (averaged over the height) of the sample to be determined. The BC3 tests, on the other hand, are run without allowing transfer of water from the lateral annulus so that the average diameter of the soil sample remains essentially constant. Instead, the pressure increase in the water is monitored as a function of penetration.

The two tests were originally considered to represent lower and upper bounds to the true field conditions: soil at the radius of the chamber could reasonably be expected to be subject to an increase in radial stress during penetration, but this would also be accompanied by some increase in radius or circumferential extension. However, based on several series of experiments run and collated at NGI, Lunne and Christophersen (1983) suggest that even BC3 underestimates the cone resistances for dense sands.

The methods used to interpolate and extrapolate from the test results to appropriate field conditions are reviewed in this Chapter as are the general limitations of the approach. Finally, the steps are outlined by which a boundary was designed to approximate the same local

stiffness as sand extending to infinity and to allow, therefore, a more direct evaluation of the test data.

4.2. Chamber Size and Boundary Effects

Probably the most important assumption inherent in CC testing is that the cone resistance value in the field would be in the range BC1 to BC3 as measured in the CC, provided that the material was identical and at the same state of stress and overconsolidation. This assumption is not strictly valid. The effect of chamber size and boundary condition on measured q_c values have been well documented (Parkin and Lunne, 1982; Ghionna, 1984).

The second important assumption is related to the behaviour of different materials. In most cases, chamber tests are not carried out on the same sand actually encountered in the field. Instead, the chamber test correlation for the most similar sand is used and the assumption is made that the different sands will show similar behaviour at the same relative density. There is an additional implicit assumption in this approach that sands which show similar behaviour in triaxial or other laboratory tests will also show a similar in-situ behaviour.

The most obvious problem with calibration chamber testing is that the chamber is not infinitely large, and, therefore, that the cone resistance and sleeve friction may be influenced by the boundary conditions in the chamber.

Calibration chamber tests are generally carried out in 1.2 m diameter chambers and, for the standard cone, the diameter ratio is about 34. Parkin and Lunne (1982) conducted penetration testing using different chamber sizes and different size penetrometers including the standard 10 cm^2 cone and other non-standard ones (e.g., 5 cm^2) to study the chamber size effects. Despite the relatively large diameter ratio of 34 in the standard test, they showed that for very dense Hokksund sand, q_c was still a function of chamber diameter (also deduced from

the Southampton test results of Last et al., 1987) [Fig. 4.1]. Parkin and Lunne state that the penetration resistances in the field will lie between a CC test with zero lateral strain boundary (rigid-wall chamber) and that with a constant lateral stress boundary (BC1). The rigid-wall boundary overestimates q_c, as higher stresses will exist at the radius of the chamber boundary than in the field.

It has been deduced, Figure 4.1, that the results for both boundary conditions converge when the diameter ratio is greater than 50. The true value of q_c, independent of lateral boundary effects, is thus identified and measured q_c values for a given diameter ratio can be adjusted to reflect a diameter ratio of 50.

It is also evident from this figure that the chamber size effect is not very important in loose sands but becomes more important as D_r increases.

The results of CC tests performed in Italy on Ticino sand with different size cones suggest that for dense samples q_c is independent of diameter ratio under BC3. This is different from the results in Hokksund sand (Bellotti et al., 1985; Ghionna, 1984), where a marked chamber size effect is observed under both BC1 and BC3. The actual chamber designs used for both sands are quite similar and the best explanation for the difference seems to be the difference in material type. This explanation is not entirely convincing in that the intrinsic properties of the two sands are in fact quite similar (Been et al. 1987a; Mitchell and Keaveny, 1986). However, the normalised q_c-ψ relationship for the two sands, as reported by Been et al., is different, and in the correct sense to suggest that boundary effects may be smaller for Ticino sand.

The top and base boundary conditions in calibration chambers appear to have been of less concern than the lateral boundary conditions. This is largely because the top and base boundary effects appear to be visible on the cone trace. However, even the central portion of the q_c- depth profile may be affected because the 'bearing

capacity' cone of stress extending below the penetrometer cone tip must be affected both in geometry and in magnitude by the stiffness of the base (and, indeed, the sides) to both shear and normal stress. The boundary control on the base for both BC1 and BC3 tests is uniform stress and is achieved using, essentially, a water-filled bag on top of the chamber piston. The pressure in the bag is the same as the controlling pressure below the piston (after allowance has been made for any friction at the piston rim). A comparison of vertical stresses under the tip of the cone in such a flexible membrane-based chamber and in the field would show the difference. In-situ, it is the vertical stress above the cone that is approximately constant and the stress below the cone is governed by the soil behaviour. In stress controlled chamber tests, the stresses that can develop below the cone are limited and also the vertical stresses above the cone tip are not constant but decreases as q_c increases. In a constant-volume-base chamber test, i.e., one in which penetration takes place with the piston 'locked' in position, there is less effect on q_c, but the flexibility of the membrane over the large chamber base area nevertheless reduces the stress concentrations that can develop under the cone.

This arguement suggests that there may be a difference between q_c in the field and in the calibration chamber due to the base boundaries. Been et al. (1987c) describes a chamber with a true zero strain steel base. The zero strain steel base should result in higher q_c values than in-situ and the constant stress boundary in lower q_c values than in-situ. The results of such chamber tests have shown little difference from that of normal chamber designs, suggesting that the base boundary may have little effect, and that, therefore, it is approximately correct to assume a constant q_c value in the middle of the chamber (Been et al., 1987c).

Based on the work of Parkin and Lunne (1982) and Ghionna (1984), the boundary effects can be quantified and in most cases a modest (less than 20%) adjustment to the measured q_c can satisfactorally reflect the field conditions. On the basis of a limited number of experimental data, Lunne and Christophersen (1983) suggest the following correction

factor, α, to modify the measured cone resistance under BC1:

$$\alpha = \frac{q_c \ (D_c/d_c = \infty)}{q_c \ (D_c/d_c = 33.6)} = 1 + \frac{a \ (D_r - b)}{100 - b} \qquad (1)$$

where:

a , b = empirical coefficients; they are assumed to be the following for the two sands (Bellotti et al., 1985):

Hokksund sand: $0.25 \leq a \leq 0.35$, $b \simeq 30\%$

Ticino sand: $0.10 \leq a \leq 0.20$, $b \simeq 40\%$

Based on the analysis of the CC tests on Hokksund sand, Baldi et al. (1982) have suggested some multipication factors, r, to be applied to q_c measured in a chamber with $D_c/d_c = 34.2$ [presumably under BC1], shown in the following table:

Class of sand	stress History	r
Med-dense	NC	1
	OC	1
Dense	NC	1.08
	OC	1.39
Very dense	NC	1.18
	OC	1.67

Table 4.1. Tentative values of correction factor, r, for chamber size effect

As can be seen from this table, for dense OC and very dense OC samples, it is necessary to increase the measured cone resistance by about 40% and two-thirds, respectively. This shows how much the chamber size can effect the results, and the empirical correlations between penetration resistances and other soil parameters, most of which are based on limited experiments or empirical coefficients, further add to the uncertainty.

Baldi et al. (1982) also used some experimental data from triaxial tests to compute the cone resistance by Vesic's (1972) theories of spherical and cylindrical cavity expansion [see Eqns. 2.11 and 2.12] and to compare the results with the values measured in the calibration chamber (corrected for size effects using the data from Table 4.1). The results indicated that expansion theory is able to predict the q_c values with a sufficient degree of accuracy for dense and very dense sands, particularly when one refers to cylindrical cavity expansion.

Smits (1982) believes that BC1 tends to underestimate, and that tests in the rigid-wall chambers tend to overestimate the field cone resistance: BC3 should be avoided as its compatibility with actual in-situ penetration is not well defined. Further, the accuracy of simulation of the in-situ cone resistance by the BC1 and the rigid wall tests may be estimated from cylindrical cavity expansion calculations. For the plane strain deformation case it is obtained as

$$\frac{q_c}{q_c(BC1)} \simeq 1 + \left(\frac{d}{D}\right)^2 \cdot I_r \tan \phi \qquad (2)$$

The 'rigid-wall' is actually the steel shell of the chamber. It is regarded as stiffer than the soil would be and its stiffness is allowed for in the calculations as shown below:

$$\frac{q_c}{q_c(\text{rigid-wall})} \simeq 1 - \frac{\omega-1}{1-2\nu+\omega} \left(\frac{d}{D}\right)^2 \cdot I_r \tan \phi \qquad (3)$$

where $\omega = \frac{D \cdot G}{s\ E_s}$

in which,

q_c = actual cone resistance

q_c (BC1), q_c (rigid-wall) = cone resistance measured with BC1 and in a rigid-wall chamber, respectively

d = cone diameter

D = diameter of calibration chamber

I_r = rigidity index of soil

G = shear modulus of soil

s = wall thickness of the rigid chamber

E_s = Young's modulus of steel chamber wall

ν = poison's ratio of soil

4.3. The Effects of the Boundary Conditions on the General Shape of Cone Resistance Profile

The series of CPT's performed in an all-rigid chamber at King's College (Chen, 1986) suggests that, in testing dense samples of sand, failure occurred mainly by punching shear, indicated by the monotonic increase in resistance with penetration depth (Fig. 4.2). The results of tests with all-flexible boundary conditions, on the other hand, show that cone resistance profiles reach distinct asymptotic values at early stages of penetration (Fig. 4.3). The difference in response must effectively be due to the change in the boundary conditions. When testing very dense samples, it is obvious that in all-flexible conditions, the boundary tends to yield in order to accommodate the large zone of displacements. But in the all-rigid case, the rigid boundary cannot provide any yield and instead restricts the soil from deforming beyond the boundary line. Further penetration is only possible with increasing levels of resistance resulted from the stress field becoming ever more enhanced. This process is accompanied by progressive densification and even mass crushing of the sand.

The condition of constant volume in the lateral boundary [BC3 of the tests in Southampton in the NGI chamber allows zero average lateral boundary deformations. Veismanis (1974) and Last (1982) argued that the true field condition would be between BC1 and BC3 cases. One can argue that BC3, although controlling zero average boundary deformation, is not truly a zero deformation test. Numerous dense tests in a rigid sidewall chamber have shown that there are major increases in the normal stress as penetration proceeds with peak values attained at the level of the tip. Radial displacement data of Chapter 2 have shown

regions of major displacements extending as far as the boundaries and volume change measurements that recorded overall dilation. Therefore, in constant lateral volume (BC3) tests, deformations will still occur and local expansion must be accompanied by contraction elsewhere. An exaggerated illustration of the possible deformation behaviour (Fig. 4.4) involves bulging of the sample at the cone tip level compensated by a decrease in sample diameter below this bulb. In this way the sample can still expand laterally whilst maintaining zero average boundary deformation. This is probably why there is such close similarity between the trends of the BC3 and BC1 series in Fig. 4.1 both of which have flexible sidewalls. The same trend can be observed in the cone resistance profiles under both boundary conditions (from the series of tests performed at Southampton SU series (Last et al., 1987)) where constant lateral volume tests tend to peak at the very beginning of penetration and may even decrease to lower values than those of the constant lateral stress tests. The constant lateral volume configuration of the BC3 series is neither a rigid zero displacement boundary nor a flexible constant stress condition. The q_c values from tests with this configuration therefore cannot be interpreted as upper or lower bounds to the field values.

It is also evident from Fig. 4.1 that in dense tests the q_c values measured in a rigid chamber are closer to the estimated field value than a flexible test value at the same diameter ratio.

The effect of boundary condition on cone resistance profiles can be represented in another form. Chen (1986) compared the results of X-ray measurements of deformation during cone penetration testing with the idealised behaviour in the near vicinity of the cone tip based on an expanding perfectly spherical cavity under different boundary conditions. His key interest in this parametric approach was the effect of angle of dilation, ψ. The data from the analytical model show a family of curves of cavity pressure against penetration under different dilation angles as compared to the q_c profile (Figs. 4.5 to 4.8). In Fig. 4.5, comparison between the $\psi = -8°$ curves for the loose infinite and flexible models show close similarity; the effect of the two BC's

appears to yield a higher q_c in the infinite boundary case. This agrees with the experimental observations that penetration in loose sands is not significantly influenced by the boundary condition. The q_c-profile comparison, however, shows a substantial difference between theory and experiment. Extrapolating the trends of the theoretical curves, it would appear that a theoretical value of ψ of at least +40° would have to be applied to achieve comparable data.

In Fig. 4.6, the q_c-profile for a dense flexible boundary shows an acceptable similarity with the infinite boundary case during the early stages of penetration. At further penetration the experimental data appears to rise toward the theoretical infinite curve.

In rigid-boundary tests, loose samples show the same trend as in the flexible boundary case (Fig. 4.7). However, the magnitudes of the cavity pressure are always higher in the rigid model than in the corresponding flexible case. The dense rigid tests (Fig. 4.8) repeat the progressive increase in cavity pressure with angle of dilation as in the flexible cases.

The theoretical curves of the flexible boundary model in Fig. 4.6 appear to peak at early stages of penetration. In rigid boundary models, on the other hand, the curves are continuous throughout the whole penetration, with no tendency for a plateau section to be reached.

4.4. Proposed Chamber Modifications

To overcome the boundary condition effects discussed in the preceeding sections, one is left with the option of either increasing the size of the chamber up to a point where such effects become minimal or of modifying the chamber to simulate an ideal infinite boundary. The second choice would not only make more efficient use of the existing chamber but would hold out the prospect that - if the design were successful - future calibration chambers could be made smaller, cheaper, and thus more common! (The present chamber, on loan from the

Norwegian Geotechnical Institute was very expensive to make and requires considerable laboratory spaces and crane facilities to operate.

The modification of the calibration chamber would mean that the boundaries would have to be designed in such a way that the imposed stresses from the soil would produce strains at this radius which would correspond to those that the same soil to infinity would undergo with the same stress at this radius. Since the strains required were greater than could be accommodated by a simple metal jacket it was necessary to use a compressible layer rather than a stretched hoop. Also, since the prime function of the chamber is to calibrate penetrometers as they travel down through the soil, the stiffness provision needed to be local so that it would be possible to have an approximate modelling of the variation of stress and displacement with depth at any stage in the penetration process.

This last requirement presents a theoretical difficulty since a local deformation will affect the stress/strain field in the vicinity and thus the apparent stiffness of neighbouring zones. To model this 3-D coupling would not be practicable and the best that could be achieved would be complete de-coupling of local stiffness from its neighbours - essentially Winkler foundation theory applies to the chamber walls. To ascertain the required stiffness, therefore, it would be sufficient to devise a plane-strain experiment with no depth variation (except that imposed by gravity) and a hydrostatic pressure state at the boundary. For this, a full length central cylindrical cavity of 150 mm diameter could be made to expand into the soil and thus model the expansion of the whole chamber to a one eighth scale. Moreover, the chamber boundary stress/volume change could be controlled during the expansion test to model the soil behaviour already exhibited at the early stage of expansion in the walls of the expansion cavity thus giving a very close approximation to infinite boundary conditions. This, essentially, would correspond to a full length pressuremeter test and such tests have received considerable attention in the past both experimentally and theoretically.

There is a second difficulty, however. The required boundary stiffness achieved during a particular expansion test would be for that test soil and for its particular density and stress levels. Again, it would not be practicable to design a variable stiffness (or, at least, not with the time and the money constraints imposed) so that one stiffness would need to be chosen. By running a series of expansion tests with very dense Hokksund sand (to have the most pronounced boundary effect) under a range of stress histories it would be possible to pick out one each of normally consolidated and a given ratio of overconsolidated initial stress conditions which would require the same boundary stiffness and allow both soil conditions to be investigated. The results of the expansion tests would then give the ideal operating stress levels for both NC and OC samples of Hokksund sand under which standard cone penetration testing (CPT) could be performed to simulate field testing. The cone tip resistance and its sleeve friction profiles could then be compared with those of the previous Southampton University tests (SU series) performed under both constant lateral stress and constant lateral volume boundary conditions.

It has always been of interest to obtain, both experimentally and theoretically, deformation patterns of some kind around the penetrometer and throughout the soil mass surrounding it. This is all the more important if one wishes to compare theoretical expansion predictions with those achieved during the corresponding experiments. As has already been discussed, embedded measuring devices tend to interfere both with the initial stress distribution and with the subsequent stress and deformation behaviour being measured. However, the nature of the stiffness boundary envisaged makes it relatively easy to measure local stress and deformation behaviour at the chamber boundary. The radial stiffness material would bear on the inner steel shell of the chamber which could thus be strain-gauged to measure local hoop strain in the steel (and thus - after allowing for the Poisson's ratio effect - the radial stress applied to the shell) and also the local axial strain (whose rate of change would be an indication of any

vertical shear load transmitted to the wall). The calibrated stiffness of the boundary would then also give the corresponding strains in the soil. Several columns of such gauges would allow detection of variation from the true axial symmetry otherwise assumed in the theory and in the experimental design set-up.

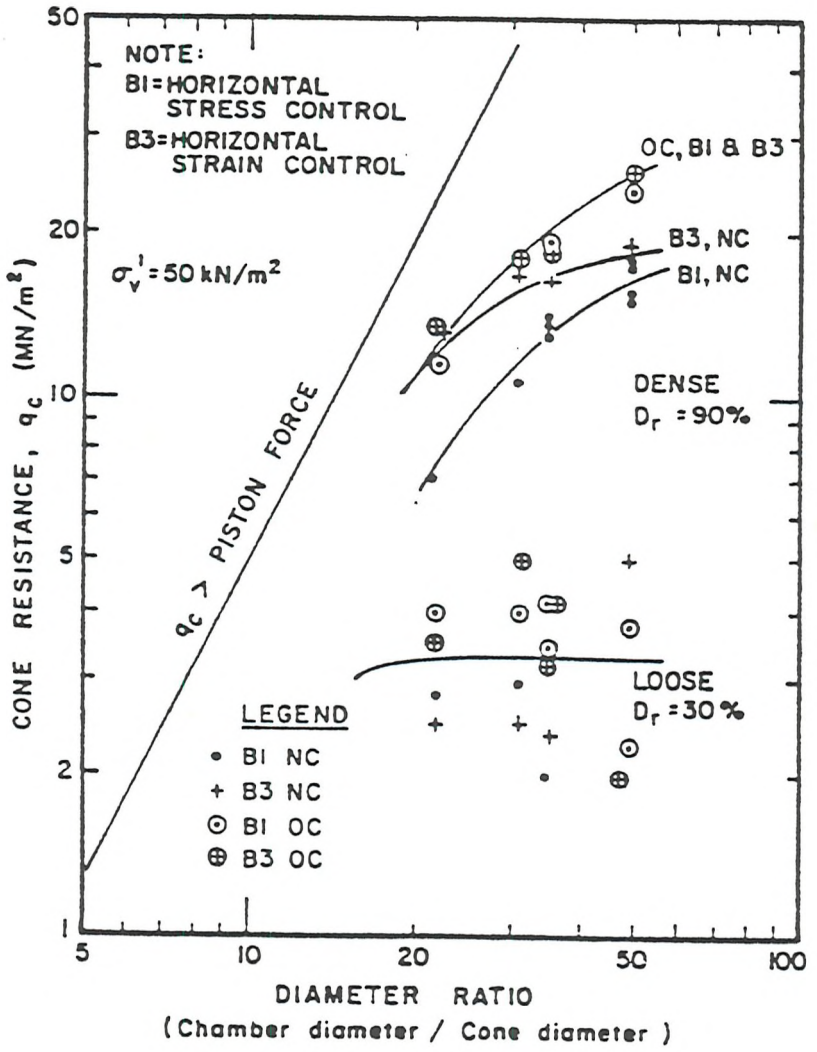

Fig. 4.1 Effect of chamber size and boundary conditions on the CPT for Hokksund sand (Parkin and Lunne, 1982 and SU results of Last et al., 1987)

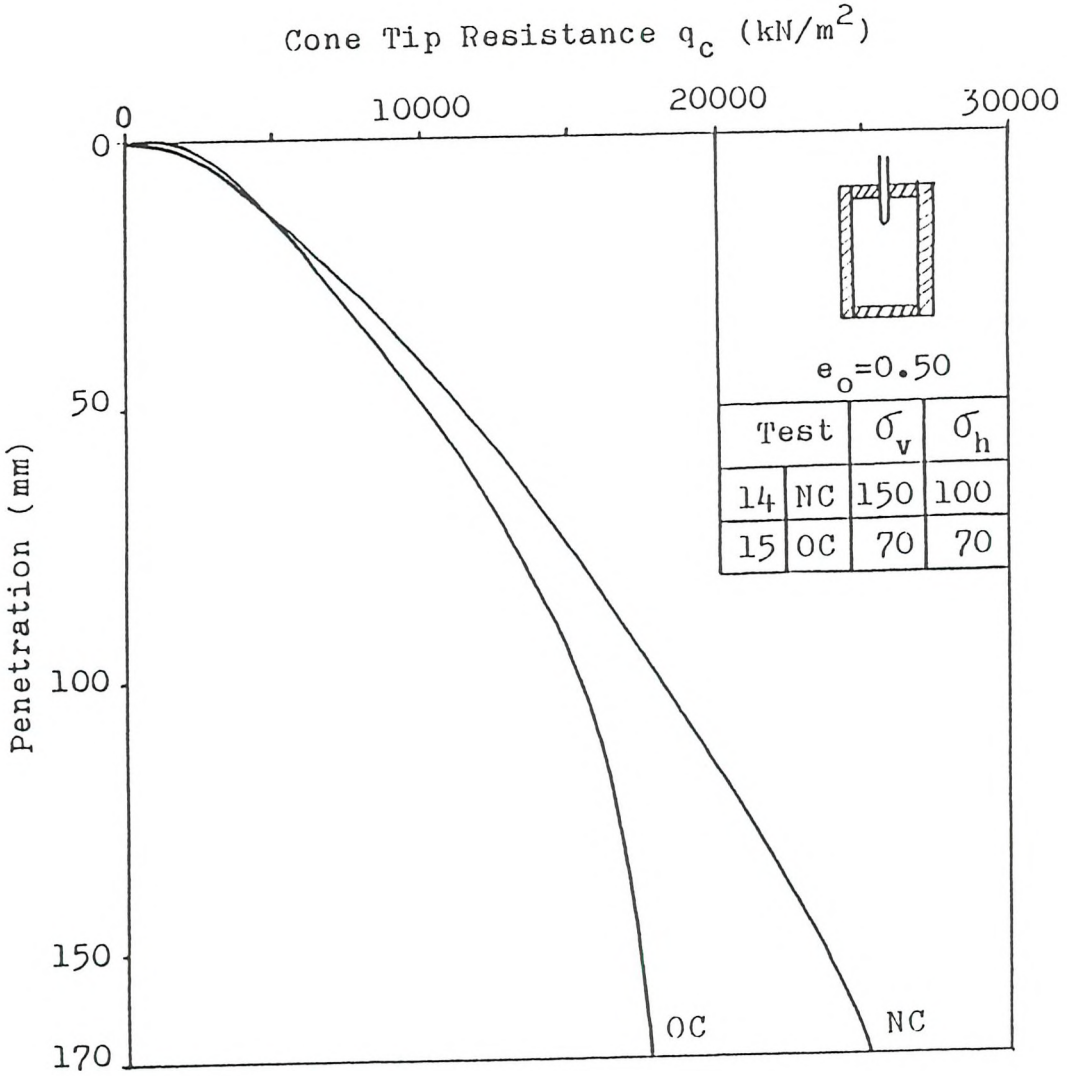

Fig. 4.2 Cone resistance profiles for 'all-rigid' dense tests (Chen, 1986)

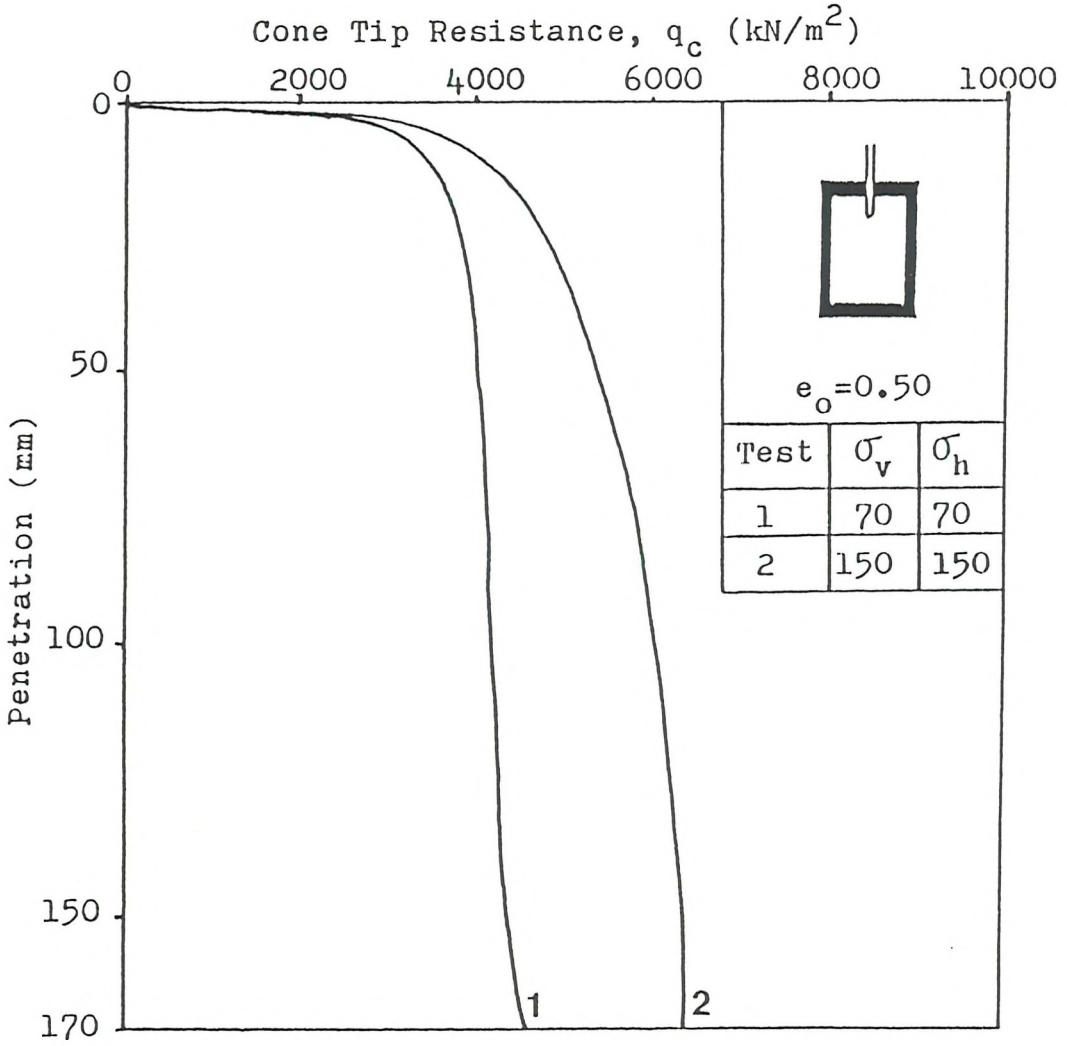

Fig. 4.3 Cone resistance profiles for 'all-flexible' dense tests (Chen, 1986)

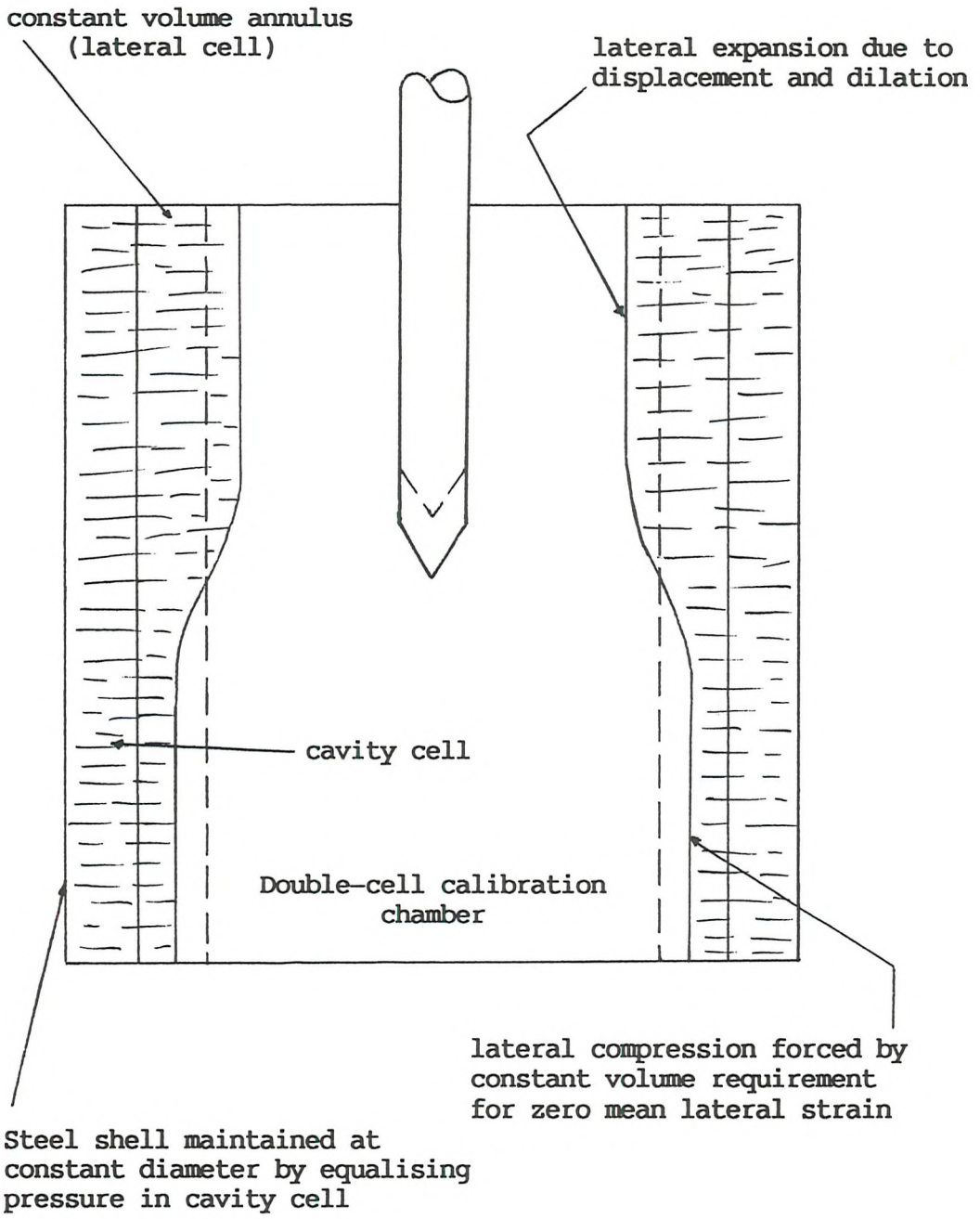

Fig. 4.4 Deformation behaviour of dense sand during penetration with constant lateral volume (BC3)

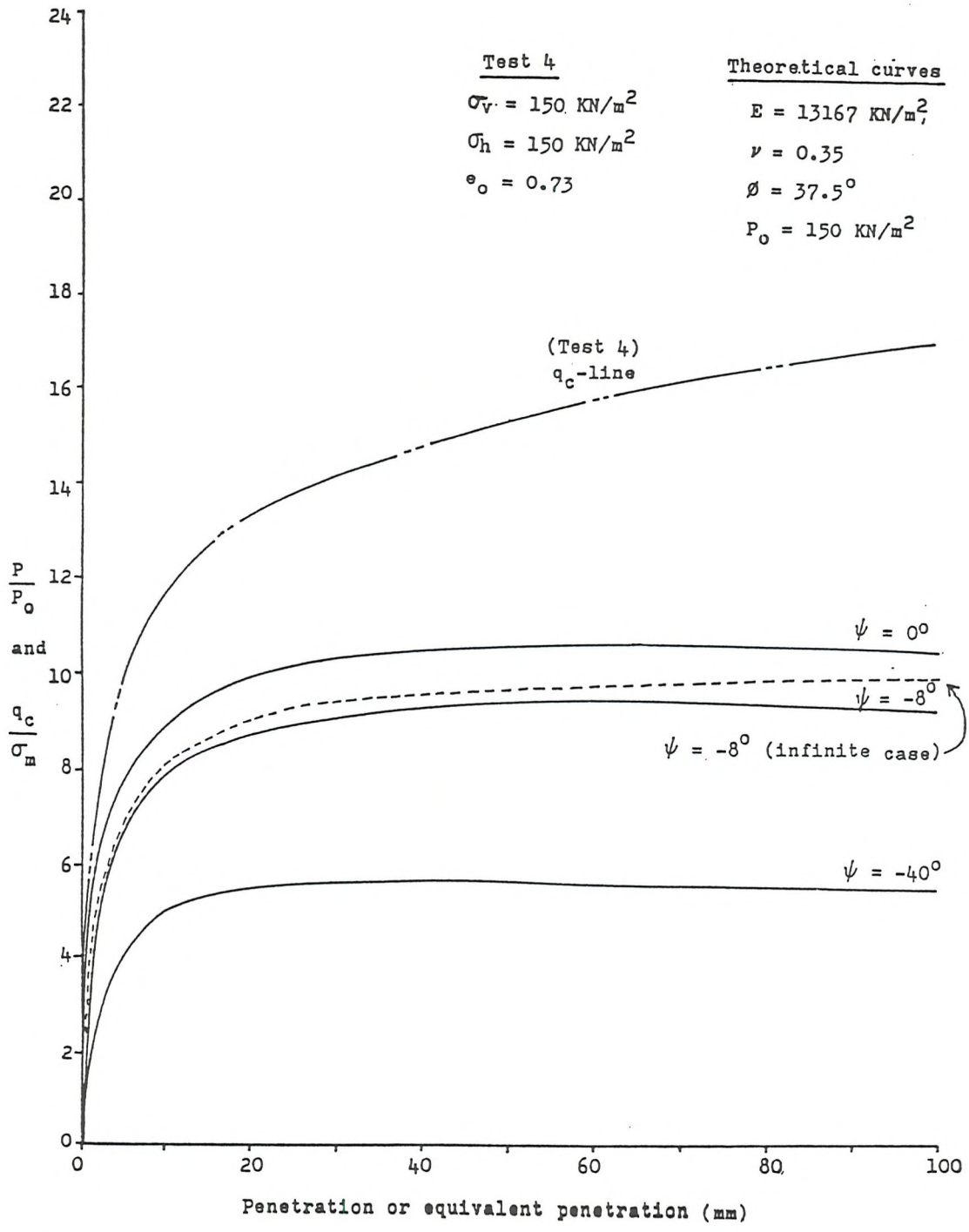

Fig. 4.5 Cavity expansion Pressure vs. equivalent penetration depth for loose samples in 'all-flexible' tests (chen, 1986)

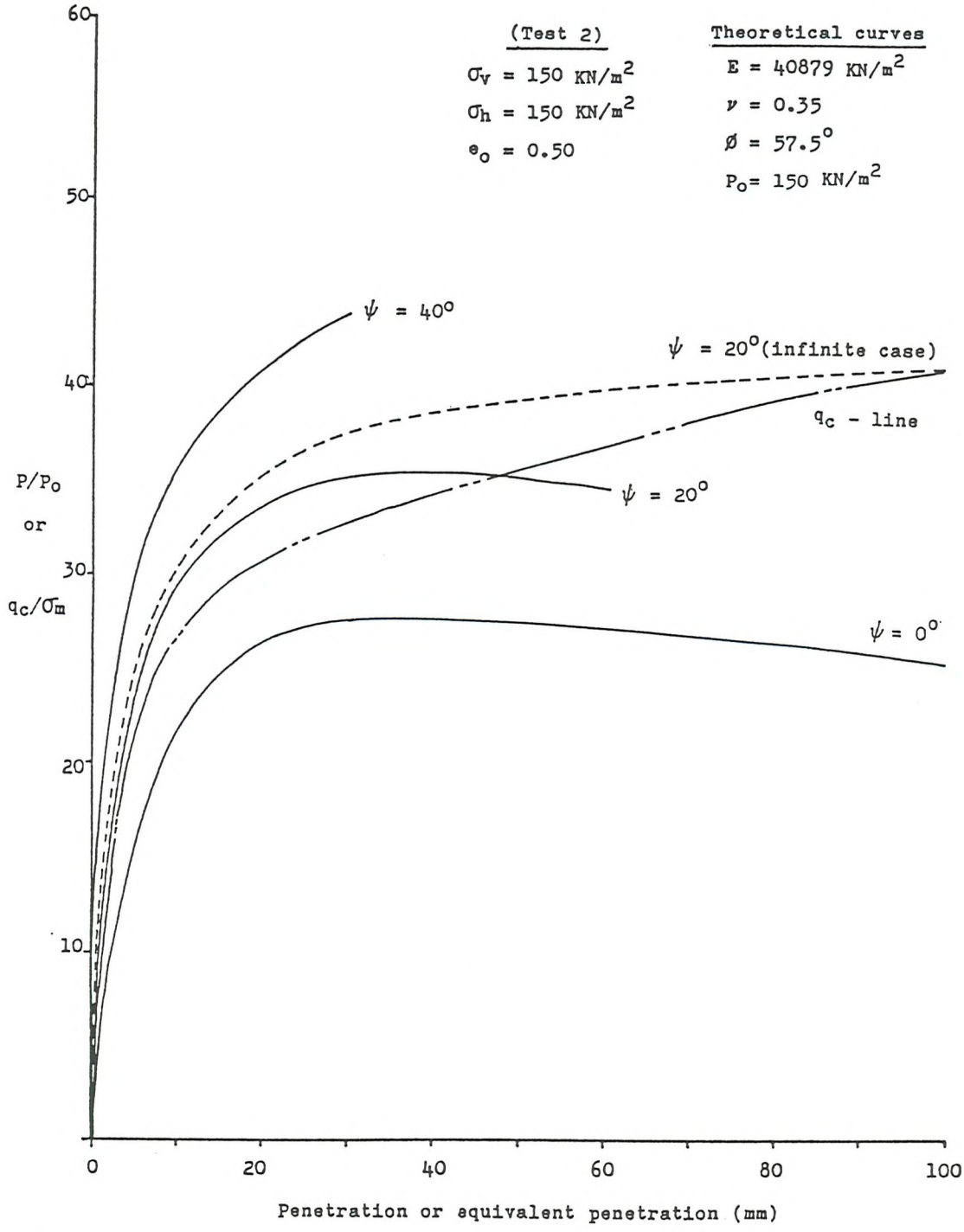

Fig. 4.6 Cavity expansion Pressure vs. equivalent penetration depth for dense samples in 'all-flexible' tests (chen, 1986)

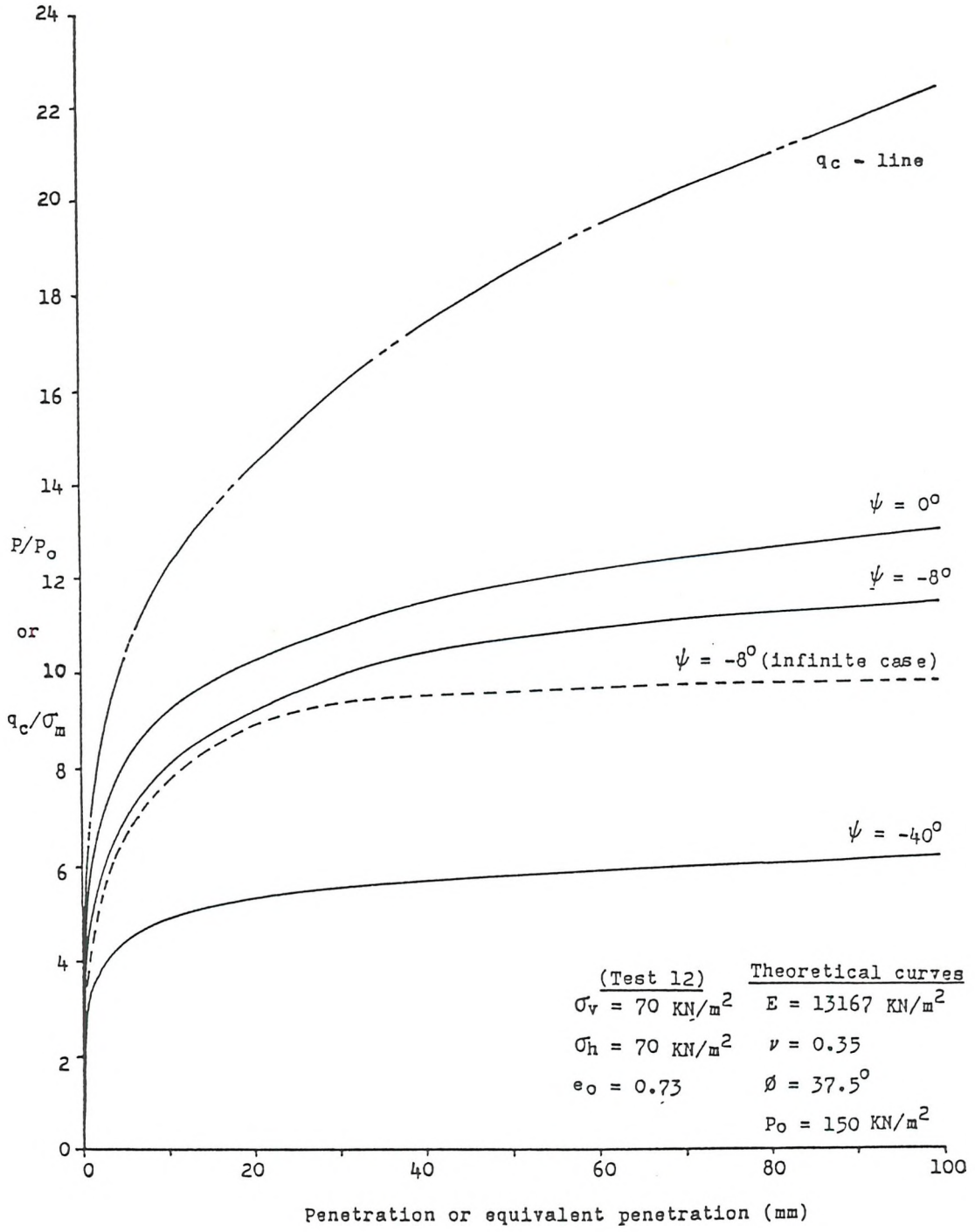

Fig. 4.7 Cavity expansion Pressure vs. equivalent penetration depth for loose samples in 'all-rigid' tests (chen, 1986)

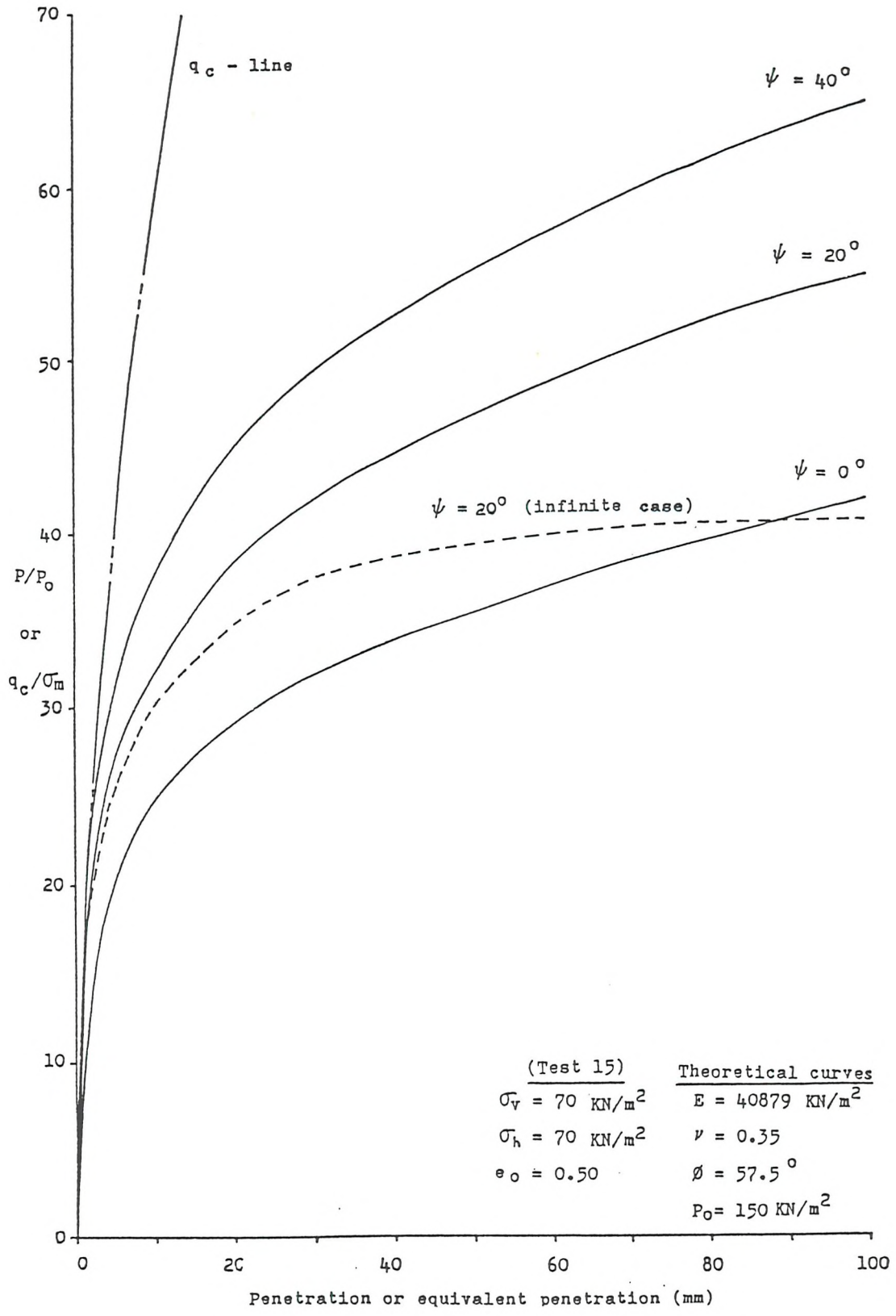

Fig. 4.8 Cavity expansion Pressure vs. equivalent penetration depth for dense samples in 'all-rigid' tests (chen, 1986)

CHAPTER 5

Expanding Cylinder Test Series

5.1. Introduction

It has been shown in the last two chapters that CPT results in the calibration chamber are affected by both the constant lateral stress or constant lateral volume boundary conditions and the chamber size. To counter this, it was proposed to modify the chamber boundaries to model a more natural soil behaviour by provision of a compressive layer around the boundary which would model more closely the stiffness of the soil extending to infinity.

The soil shear stiffness in the horizontal plane, however, could not be obtained from conventional soil tests which are not capable of isolating the in-plane shear stiffness of a transversely isotropic medium. The solution was to carry out an expansion test (with the axis of the expanding cylinder along the vertical/normal of the plane of isotropy) which would not only give the required stiffness on analytical grounds but would, in fact, model the expansion of the outer boundary of the soil sample at the reduced scale of the expanding cylinder boundary. Since, except for the small effect of gravity on both the vertical stress in the soil and the pressure in the confining water, the expansion would be purely cylindrical and plane strain, the resulting average boundary stiffness would be the true Winkler stiffness required. Thus, a full length central cylindrical cavity of 150 mm diameter could be made to expand and thus model the expansion of the whole chamber to a one eighth scale. The principal of an expanding cylinder test, which is equivalent to the central portion of a pressuremeter, is that, in theory, the boundary conditions are

controlled and well defined, as are the stress and the strain conditions in the surrounding soil mass. The characteristics of the sand can be deduced from measurements of the pressure and the change in volume [radial strain] of both inner and outer soil boundaries.

It can be shown that the pressure/expansion relationships obtained from expanding cylinder tests in an infinite body of homogeneous material (linear or not) are independent of the size of the expanding cylinder used for monotonically increasing pressure expansion tests. By using this property, a series of tests were carried out in the calibration chamber under equivalent infinite boundary conditions. The internal pressure/expansion relationships, obtained from these tests were, in turn, imposed on the outer boundary so that the same stress/strain behaviour was followed at both radii.

Ideally, a chosen rubber strip stiffness would only apply to a very limited range of soil conditions with different stress levels for different stress histories as for NC and OC tests at a given density. However, the testing programme was extended to include the nearby stress level and history of some of the previous Southampton University tests, performed under constant lateral stress or constant average lateral strain boundary conditions, for which all the necessary data were available. These tests can be summarised as follows:

1. NC-Dense tests with vertical pressure, σ'_v = 4.0 and 2.0 bar

3. OC-Dense tests with σ'_v = 1.0 bar (OCR=4) and 0.5 bar (OCR=8)

5.2. APPARATUS AND TESTING PROCEDURE

5.2.1. Design of the Expanding Cylinder Model

To achieve plane-strain cylindrical expansion it was, of course, necessary to install a central expanding cylinder running the full length (height) of the sample. Such a model would still be affected by the top and bottom boundaries of the chamber, but by monitoring only

the middle third for volume change these end effects could be substantially eliminated and a plane strain deformation in the middle region achieved. Fig. 5.1 shows a diagram of the designed model.

The expanding cylinder consists of three components: end pistons, former, and the divided rubber sleeve.

The 1mm thick rubber sleeve is made up of three sections: one middle section (420mm long)and two end sections (each 540mm long). The sleeve is fixed to the end pistons by O-rings and fixing plates.

The end pistons are designed to be able to compress during the vertical consolidation of the soil sample. There are four connections through the top piston to supply water to and bleed air from the middle and end sections.

The former is a soil drain pipe 150mm in diameter with 5mm thick wall. Water under pressure is used to expand the rubber sleeve surrounding the former into the soil.

One of the features of this design is its ability to compensate for any top and bottom boundary effects by maintaining equal pressures to both outer and central sections but from different sources, so that the volume change supplying the central section could be measured independently of that of the outer sections. Moreover, the pressure of the water inside the former was controlled from the same source as the outer sections so that the former would remain essentially unstressed during the expansion process.

5.2.2. Preparation of the Model for Testing

The filling and deairing of the expanding cylinder needed to be done by either placing it completely in a tank full of water in a vertical position or burying it in sand [not the main testing sand!] to prevent the ballooning of the rubber sleeve under the hydrostatic pressure of the column of water. The flow connections would be sealed

off on completion of filling and deairing, leaving the water under a slight suction so that the outside support from the cylinder could be removed. It would be centred at its base and held vertical by three thin rods at the top which would remain in position until pluviation was complete.

5.2.3. Sample Preparation and Testing Procedure

The pluviation process is the same as that for CPT, except that the diffuser meshes at the bottom of the raining device [see next Chapter on features of CC design] are sealed off by a 150 mm disc at the centre to mask out the expanding cylinder. After the sand surface is leveled off, the platen and the lid are lowered on top of the chamber. The narrow section at the top of the expanding cylinder (Fig. 5.1) has been designed to pass through the central hole of both the platen and the chamber lid to stand clear of the top for easier access to the connection valves. The clearance around this section is normally covered by a piece of cloth to absorb any water that may spill during connection or removal of the water-filled connection hoses.

The sample is first consolidated under K_o conditions (no radial strain) up to the desired vertical stress level. [The pressure sensed at the lateral boundary due to K_o consolidation is continuously applied to the cavity in the double shell of the chamber wall to maintain zero strain for the inner shell and thus true K_o conditions for no volume change in the lateral space between the sample and the inner shell].

The first test intended prior to boundary modification was of a constant lateral pressure type during which the inner shell of the calibration chamber between the lateral and cavity cells would naturally remain undeformed by maintaining the same constant pressure in the two cells. However, in the modified chamber which had strips of rubber placed between the inner shell and the sample the expansion of the sample would cause the inner shell to deform unless the sum of rubber strip and lateral water pressures could be maintained constant.

If the cavity between the two shells is sealed and its pressure monitored, then a constant pressure would indicate no deformation of the inner shell (and, therefore, a constant total stress against the inner surface of this shell). The constancy of this pressure is achieved indirectly by appropriate adjustment (decrease) of the water pressure in the lateral cell to counteract the increasing pressure in the rubber strips as the soil expands.

As part of the CC modification, a total of five annular pockets were designed in the base to measure either the volume change during a CPT or the pressure build up during an expansion test [see next chapter]. During K_o consolidation, these pockets were sealed except for connection to their respective pressure gauges, after a vertical pressure of 1.0 kg/cm^2 had been reached. This maintained enough pressure on the strips to seal off the individual pockets throughout the test. The pressure readings during the consolidation stage would show if the pressurising base piston were sticking. During the expansion process, on the other hand, they could be used to check the pressure distribution on the base due to expansion without violating the plane strain criterion.

The data recorded during K_o consolidation included piston and lateral pressures and volume changes as well as the base pocket pressures. The additional data recorded during the expansion stage included the cavity and expansion pressures and the volume change of the expanding cylinder's middle section. Fig. 5.2 shows the experimental set up during an expanding cylinder test.

A preliminary analysis of the results of the first expansion test, performed under constant lateral stress prior to the boundary modification, gave an average linear stiffness (Pressure versus deflection) of 1.0 bar/mm at the early stages of expansion. The subsequent expansion tests were carried out after the modification, and included tests with just the lateral boundary stiffness.

The potential versatility and attraction of expanding cylinder testing is the ability to deduce soil parameters such as deformation moduli and strength (i.e., angles of shearing resistance, ϕ', and dilation, ψ,) for the sand. Such tests have received considerable attention in the past both experimentally and theoretically in analysing the performance of pressuremeters. A brief review of previous analyses on pressuremeter test results and their relevance to the current project is now given.

5.3. Background to the Plane Strain Analysis of Pressuremeter Tests

There have been numerous attempts to analyse the results of expansion tests performed on samples of sand in the laboratory. Earlier analyses have been presented by Gibson and Anderson (1961), Ladanyi (1963), and Vesic (1972). The first one ignores volume changes, the other two incorporate volume change in different ways.

Since the early work of Roscoe (1953), successive research workers at Cambridge have contributed to the development of the Simple Shear Apparatus (SSA) [see Bassett (1964), Cole (1967), Stroud (1971) and Budhu (1979)]. Hughes et al. (1977) performed an analysis on the results of plane-strain shear tests in the SSA. Later, Jewell et al. (1980) and Fahey (1980, 1986) performed analyses on the results of pressuremeter tests in a triaxial chamber (both "cast in-situ' and 'drilled in' tests). Their analyses were on the expansion of an infinitely long thick hollow cylinder of sand, based on the model used by Hughes et al, to determine whether the values of the parameters obtained from the tests were influenced by the finite length of the pressuremeter (i.e., the end effects). They also studied the influence of the finite radius of the sand samples compared with the infinite dimensions relevant to the in-situ tests.

Stroud (1971) carried out four different tests on Leighton Buzzard sand in an initially dense condition and three tests on initially loose sand. Each test of the two sets was conducted with a different (but

constant) value of the vertical effective stress. For all tests, after the peak stress ratio is reached, the value of stress parameter ratio t/s' [where $t = 1/2\ (\sigma'_1 - \sigma'_3)$ and $s' = 1/2\ (\sigma'_1 + \sigma'_3)$] and the ratio of volumetric strain to shear strain remained sensibly constant over a substantial range of strain. Similar behaviour was observed in all Stroud's other tests in which the stress levels were varied (as happens in a pressuremeter test). The results of seven tests have been plotted as shown in Fig. 5.3. Stroud's results agreed well with Rowe's (1971) stress dilatancy theory which relates the stress ratio and dilation rate [see Eqn. (15)]. These experimental observations were later used by Hughes et al. (1977) in the interpretation of pressuremeter tests. A study done by Jewell et al. (1980) in which the pressuremeter test was simulated in a large triaxial chamber has provided some justification for the use of the method of analysis of Hughes et al. (1977), but, on the other hand, leaves open the question of the validity of the assumption that the expansion of the pressuremeter is identical with that of an infinitely long cavity (neglecting the end effects in the analysis).

There exist, however, differences between the deformation of a sample in a SSA and that around the expanding cavity in a pressuremeter. The most significant difference is the assumption of no rotation of principal axes during a pressuremeter test while the principal directions of stress and strain both rotate in a test in the SSA (Fahey, 1986). In addition, the stress paths imposed on the soil elements in t-s' space are different for the two tests. During the elastic phase of the pressuremeter test, there is no change in the mean normal stress, so that the stress path remains vertical in a Mohr-Coulomb plot until failure occurs (Fig. 5.4). In a SSA test, unlike the assumed stress path in the pressuremeter test, the mean normal stress increases even in the elastic region (Fahey, 1980). In theory, if an elastic soil is subjected to simple shear (achieved by maintaining a constant vertical stress on the sample and applying the shearing force to it), there should be no change in mean normal stress in the elastic region, which is not the case in the SSA. Fahey (1980) believes this to be due to either the test being, in reality, not a

single element plane strain test, or due to the inadequacy of elasticity for describing the prefailure behaviour of sand. If the latter reason is the main one, then the actual stress path in the pressuremeter test may also be very different from the assumed stress path shown in Fig. 5.4.

In the analysis of the expansion of a cavity in sand as a simulation for a pressuremeter, an infinitely long cavity is generally assumed which is contained in a material extending to infinity in all directions. Also, the material property and the initial stress condition are assumed to be constant with depth. In idealisation it is assumed that a finite length cavity is expanded in an infinitely thick-walled cylinder, confined between rigid frictionless boundaries at the top and the bottom.

In an idealised form, a dense sand is assumed to have, initially, an elastic behaviour until a limiting value of stress ratio, [stress obliquity], σ'_1/σ'_3, is reached, and that the material continues to fail at that value of stress ratio over the range of shear strain applicable to the pressuremeter test (Fahey, 1980), which in the case of a self-boring pressuremeter is never greater than about 30%. The initial idealisation used by Hughes et al.(1977) was that the behaviour could be taken to be rigid up to failure. The necessary condition to reach the failure stress ratio is that the corresponding strain is unique and that the material properties are independent of the radius in the soil surrounding the cavity. The assumption of linear (elastic) prefailure behaviour is made to enable their analysis to be extended to a cylinder of finite thickness. In addition it is assumed that the dilation rate is also constant over this same range of shear strain (Fahey, 1980, 1986). The soil is, therefore, characterised by elastic parameters G (shear modulus), ν (poisson's ratio), and by angles of friction and dilation (ϕ and ψ).

Jewell et al. (1980) obtained good agreement between the observed behaviour and that predicted from the analysis, indicating that, if end effects could be neglected, the Hughes et al. analysis would be

appropriate, at least for dense sand.

Basically, during a pressuremeter test, the soil surrounding the expanding cavity is assumed to undergo plane strain deformation. If an initial isotropic stress state is assumed, then throughout the test, the major, minor, and intermediate stresses are fixed in the radial, hoop, and vertical directions, respectively (i.e. no rotation of principal stress axes occurs). In a normally consolidated soil, the vertical stress, σ'_z, is initially the major principal stress, but it is assumed that during a pressuremeter test in such a soil sample the radial stress, σ'_r, rapidly becomes the major principal stress. Thus, even in this case no rotation of principal axes occurs, although the major and intermediate principal stress directions interchange when the radial stress becomes greater than the vertical stress.

As far as the axially symmetric (transversely isotropic) distribution of stress and strain is concerned, the vertical stress plays no role in the stress equilibrium equation. The vertical stress is normal to the plane of shearing, and it is a dependent stress. It adopts whatever value is necessary to prevent any strain occuring in the vertical direction to correspond to a plane strain situation. All the analyses, so far, have assumed that the vertical stress has no influence on the behaviour of the soil so that when the soil fails according to a Mohr-Coulomb failure criterion, it fails with the radial effective stress as the major and the circumferential effective stress as the minor principal stress. The failure is reached on the horizontal plane throughout the soil. Fig. 5.5a shows the profile of radial and circumferential stresses with radius for the two assumed phases.

It will be shown in the following analysis that in all the chosen tests (both NC and lightly OC ones) the vertical stress is still the major principal stress when failure is reached at the cavity wall and continues to be so until a point where the radial stress grows to dominate it. In this case it is invalid to assume that the behaviour of the soil only depends on the radial and circumferential stresses immediately after the expansion starts. Fig. 5.5b shows a profile of

the change of the three principal stresses with radius expressed symbolically. Note that three distinguished phases are recognized in this set-up. The elastic phase is the same as that in Fig. 5.5a. In the first plastic phase, the plastic flow is mainly in the zθ plane. Hence, the decrease in σ'_z and σ'_θ is controlled by the stress obliquity in this plane. Since the vertical height should remain constant under plane-strain conditions, the decrease due to vertical plastic strain is counter-balanced by an equal increase from elastic strain. In the second plastic phase, however, the plasticity is controlled in the rθ plane, where the increase in both radial and circumferential stresses is related by the stress obliquity in this plane, whereas the vertical stress changes elastically.

Wood and Wroth (1977) and Mair and Wood (1987) discuss a case where K_o is about 0.6 (similar to the tests under OCR= 4 with σ'_z = 1.0 bar and OCR = 3 with σ'_z = 1.5 bar performed in this series). The radial and circumferential stresses at the end of K_o consolidation are equal and there is only one Mohr's Circle of stresses. When a cylindrical cavity is expanded elastically in this material, there is no tendency for volume change to occur. The radial stress increases and the circumferential stress decreases until a point where the Mohr-Circle drawn with σ'_z as the major and the σ'_θ as the minor principal stress touches the Mohr-Coulomb failure envelope. Failure then occurs on an inclined θz plane and the radial stress is, at failure, the intermediate principal stress. Jewell et al. (1980) suggest that the zone in which this happens is always a thin annulus of sand moving outwards during the test, so that local relief of σ'_z may prevent large vertical displacements occurring.

It is believed that NC and lightly OC soils, with low K_o values are likely, in practice, to show significant departure from elasticity before failure is reached. This behaviour has been supported by laboratory test results (Wood and Wroth, 1977; Wood, 1981) which show that in such soils the vertical stress starts off as the major principal stress.

5.4. Expanding Cylinder Test Results

The expanding cylinder test program comprised a total of six tests, in addition to the test before the boundary modifications. They were carried out on dense samples of Hokksund sand under different consolidation pressures and lateral boundary conditions. The boundary condition for every test was chosen to utilise the information obtained from the previous test(s). The first three tests were performed at a vertical pressure of 4.0 Kg/cm^2 (NC); the lateral boundary conditions, respectively, included constant pressure, true infinite with the stiffness properties deduced from the constant pressure one and the expansion earlier in the test, and the last one being under constant rubber-strip stiffness properties alone as an approximation to the field conditions and conforming to the constant stiffness under which the penetration tests themselves would be carried out. The fourth test had a consolidation pressure of 2.0 Kg/cm^2 (NC) with the same boundary conditions as the second test. The last two samples were overconsolidated ones: one consolidated to the same vertical pressure as the first three then relaxed to a vertical pressure of 1.0 Kg/cm^2, thus giving an OCR = 4, again under true infinite boundary conditions, and the other one consolidated to a maximum past pressure of 4.5 Kg/cm^2 then relaxed to a 1.5 Kg/cm^2 pressure with OCR = 3 but performed under constant lateral stress conditions. A complete description of the expansion tests series is given in Appendix I. A summary of the derived elastic moduli is given in Table 5.1. The results of the pressure/expansion curves for the early stages and the overall view are given in Figs. 5.6 and 5.7.

The series of tests performed indicate that normally consolidated samples need to be tested at a vertical stress of about 2.0 bars and the OC ones at stress level of about 1.0 bar with OCR = 4 in order for the rubber-strip stiffness to simulate the boundary stiffness conforming to an infinite chamber.

Next, the results of the expanding cylinder tests that were performed under true infinite field conditions, i.e. tests 2, 4, and 5,

are analysed. The behaviour of the principal stresses as a function of the soil strain will be discussed with reference to different testing conditions [i.e. consolidation stresses and stress histories] at the end of the next section. Some of the parameters (i.e., ϕ' and ψ) will be compared with those obtained by an alternative approach based on the expansion of a cylindrical cavity in a thick elastic-perfectly plastic (Mohr-Coulomb) material (as given in Appendix II).

5.5. A New Method of Analysis for Expanding Cylinder Tests in a Simulated Infinite Sample

The aim in this section is to give a step-by-step procedure for the analysis of the expanding cylinder test results and to distinguish patterns in the stress-strain behaviour of different tests during expansion. The analysis is first reviewed generally followed by a formatted iterative-type procedure, as outlined in sub-section 5.5.1. Some additional notes regarding the mathematical formulations and derivations are discussed in sub-section 5.5.2.

This analysis relies on the data recorded during an expansion test, namely the pressures and the volume changes in both inner and outer boundaries. The results of the three tests have been plotted in 2 sets of graphs. Set [1] graphs (Figs. 5.8 to 5.10) show the plots of expansion pressure versus lateral pressure during the expansion stage. Set [2] graphs (Figs. 5.11 to 5.13) have been plotted to show the relationship between the expansion pressure and the internal and external volume changes for the entire expansion process. These have been summarised in Table 5.2. The steps involving this analysis are discussed with reference to Tables 5.3 to 5.5, for the three tests respectively, with columns of data for different parameters. The elastic properties used for these tests were obtained using the procedures and additional laboratory tests as described in Appendix III.

To enable a numerical analysis, the soil in the chamber is to be divided into a known number of annuli, the radii of which successively

increase by a common factor to cover the entire soil radius. By so doing it becomes possible to choose increments such that the strain in one annulus is the same as that of the next inner annulus on the previous step and that this relation applies simultaneously to all the annuli. This is because of the equilibrium requirement that, for a given $\sigma_r - \sigma_\theta$, the rate of change of radial stress with radius be inversely proportional to the radius (i.e., independently of the stress/strain relationship). Thus, two annuli with the same stress history are directly comparable (and have the same radial stress jump between their inner and outer radii) if the ratio of their radii are the same. Table 5.6 illustrates the successive steps in calculation of the radial stresses on the annulus boundaries of Table 5.3. The number of annuli chosen, therefore, determines the number of steps required for the state of strain in the inner annulus [denoted as the first annulus] to propagate to the outer boundary. For example, the radial stress at the interface of the fifth and sixth annuli in any step would become that at the sixth and seventh annuli interface in the next subsequent step. The amount of volume change [in the form of dilation/compression] of each annulus will, of course, depend on the actual volume of the individual annuli: the ratio of increase is the square of the common factor for successive annuli.

The analysis consists of two parts: part (1) is a stress-strain regime which depends entirely on the experimental results (i.e., the pressure and strain in the inner and outer boundaries); part (2), on the other hand, requires an iteration process in order to obtain the necessary parameters. These two procedures are discussed more in the following sub-sections:

5.5.1. Stress-strain regime at the inner and outer boundaries

To simplify explanation of the analysis, an initial procedure is presented in this sub-section in order to obtain a systematic sequence of stress/strain data at both the inner and outer boundaries. The steps involved at this stage are,initially:

1. Divide the sample into 11 annuli, the radii of which successively increase by a factor of 1.202 to give the inner soil radius of 8 cm and the outer soil radius of 60.54 cm.

2. Assume an initial cavity stress increment results in an elastic stress distribution for the whole soil and thus find the starting radial stress at the boundary of each annulus. Note that the outer boundary stresses for the next eleven steps will be those of the consecutive inner annuli of this initial distribution (cf. Col#1 in Tables 5.3 to 5.5 and the left-hand column in Table 5.6).

3. Use the internal and external volume change - pressure diagrams (Figs. 5.8 to 5.13) to find the corresponding radial stress and the circumferential strains at the inner and outer boundary for the entire expansion process.

4. Having obtained the radial stresses at the boundaries of the first annulus, find the mean radial stress for this annulus. Then use the equilibrium equation in the $r\theta$ plane to obtain the mean circumferential stress [Col#5] for this annulus.

In this way, the entire data for Columns [1] to [5] and, hence, Col#[9] can be obtained directly from the experimental data before any iteration is carried out. The deduction of further information concerning soil behaviour is discussed in the next sub-section.

5.5.2. Iteration Procedure for the Analysis

Once the radial stresses and the cavity strains for both the inner and outer boundaries for each step are calculated, the next task is to perform a simple loop-type iteration in order to analyse the data. This is described in the following steps, some of which include some mathematical derivations that are necessary for the task.

1. From the mean circumferential strain, $\bar{\varepsilon}_\theta$ [Col#9], for the inner annulus, calculate the mean radial strain, $\bar{\varepsilon}_r$ [Col#10], for this

annulus using the strain-compatibility relationship, developed as below:

Let the circumferential strains at radii r and (r+δr) be denoted by $^{\varepsilon}\theta_r$ and $^{\varepsilon}\theta_{r+\delta_r}$, where

$$\varepsilon_{\theta_r} = \frac{u_r}{r} \quad \text{and} \quad \varepsilon_{\theta_{r+\delta r}} = \frac{u_r + \delta u}{r + \delta r} \tag{1}$$

with u being the displacement at r and the δu as the change in the displacement across δr. Also,

$$\varepsilon_{r_r} = \frac{\delta u}{\delta r} \tag{2}$$

Then

$$\varepsilon_{\theta_{r+\delta r}} = \frac{\varepsilon_{\theta_r} \cdot r + \varepsilon_{r_r} \cdot \delta r}{r + \delta r} = \varepsilon_{\theta_r} + \delta\varepsilon_\theta \tag{3}$$

After simplification this equation can be written in a format similar to the stress equilibrium equation as

$$\frac{\delta\varepsilon_\theta}{\delta r} = \frac{\bar{\varepsilon}_r - \varepsilon_{\theta_r}}{r} \tag{4}$$

Or both strains in terms of the mean values as

$$\bar{\varepsilon}_r = \delta\varepsilon_\theta\left(\frac{r}{\delta r} + \frac{1}{2}\right) + \bar{\varepsilon}_\theta \tag{5}$$

2. For a measured (or assumed) value of ϕ'_{cv}, use Rowe's (1971) stress-dilatancy relationship to find the strain obliquity in the rθ plane, $^{N}\psi_{r\theta}$ [Col#7] as follows:

$$N_{\phi'_{r\theta}} = N_{\phi'_{cv}} \cdot N_{\psi_{r\theta}} \tag{A.II.34}$$

where

$$N_{\phi'_{r\theta}} = \frac{\bar{\sigma}'_r}{\bar{\sigma}'_\theta} = \frac{1 + \sin\phi'}{1 - \sin\phi'} = \frac{1 + \sin\phi'_{cv}}{1 - \sin\phi'_{cv}} \cdot \frac{1 + \sin\psi}{1 - \sin\psi}$$

3. Find the change in the total mean circumferential strain between the two consequtive steps.

4. For an assumed value of strain obliquity in the zθ plane, $N_{\psi_{z\theta}}$ [Col#8], find the same as that from step (3) from the following equation which includes the effects of elastic strain changes as well as of the plastic flow from both the radial and the vertical directions.

$$\delta\bar{\varepsilon}_\theta = \delta\bar{\varepsilon}_\theta^{\,e} + \delta\bar{\varepsilon}_\theta^{\,p}\Big|_{r\theta} + \delta\bar{\varepsilon}_\theta^{\,p}\Big|_{z\theta} \qquad (6)$$

in which $$\delta\bar{\varepsilon}_\theta^{\,p}\Big|_{r\theta} = \left(\delta\bar{\varepsilon}_r^{\,e+p} - \delta\bar{\varepsilon}_r^{\,e}\right) \cdot N_{\psi_{r\theta}} \qquad (7)$$

and $$\delta\bar{\varepsilon}_\theta^{\,p}\Big|_{z\theta} = \delta\bar{\varepsilon}_z^{\,p} \cdot N_{\psi_{z\theta}} = -\,\delta\bar{\varepsilon}_z^{\,e} \cdot N_{\psi_{z\theta}} \qquad (8)$$

where the $\delta\bar{\varepsilon}_r^{\,e+p}$ in Eqn. (8) is the change in the mean total strain in Col#10.

The elastic strain changes can be obtained from the stress-strain relationships for a transversely-isotropic mass (see Eqns. A.VI.1a to 1c) in which $\delta\sigma'_z = (N_{\phi_{z\theta}} \cdot \delta\sigma'_\theta)$ in the first plastic phase.

5. Match the value obtained from Step (4) by the same from step (3) [Col#9]. The trial and error process is continued for different strain-obliquity in the zθ plane until the match is made.

Due to the difficulty in deducing extremely small stress and strain values from the experimental curves, a justifiable simplification may be to use a constant strain obliquity during the

first plastic phase, possibly equal to the the maximum strain obliquity developed at the end of K_o consolidation. This would not mean that in NC tests the vertical stress would stay constant. On the contrary, due to the constant drop of the circumferential stress during the first plastic phase, the vertical stress decreases. In OC samples, due to the very small obliquity in the $z\theta$ plane that results from the unloading of the vertical stress in order to achieve the desired stress history, it may not be justified to keep this obliquity constant. The analysis of the chosen OC test showed that the vertical stress would have to be kept constant while the obliquity increased.

This routine of iterative solution is repeated for every step of expansion. Since the steps started with the plastic behaviour at the cavity wall, then after eleven steps, the volume change in the outer cell would correspond to very first one. This continues until such point where radial and vertical stresses become equal. This is the end of the first plastic phase where the vertical stress ceases to control the plastic flow. Beyond this point, the plasticity will be governed by the Mohr-Coulomb failure criterion in the $r\theta$ plane. The analysis in the second plastic phase is similar to that in the first one except that in the latter case $^{N}\psi_{z\theta}$ is no longer applicable and the stress-equilibrium is governed by the radial and circumferential stresses: the vertical stress becomes elastic. All three stresses are at a state of increase in this phase while the vertical height still remains constant (i.e. the vertical strain is still zero). Hence, the change in the vertical stress can be obtained elastically as

$$\delta\bar{\sigma}'_z = \nu'(\delta\bar{\sigma}'_r + \delta\bar{\sigma}'_\theta) \qquad (9)$$

which will then be added to the $\bar{\sigma}'_z$ value from the previous step to give the current value of the mean vertical stress for the step.

5.6. Discussion of the Results of the Analysis

The profiles of the three principal stresses for the annulus next to the cavity against the mean cavity strain for that annulus have been plotted in Figs. 5.14 to 5.16 for the three tests. They show how the initial vertical stress in both of the NC tests decreases, whereas that in the OC test stays constant: the corresponding radial and circumferential stresses increase and decrease, respectively, in all three cases. It is interesting to note that despite the difference in consolidation conditions, all three tests begin the phase change at the same cavity strain (at about 0.1 %). The vertical stress in each of the NC samples reaches its end of consolidation stress at a cavity strain of about 6%. The circumferential stress, on the other hand, reaches its initial, K_o, level at a cavity strain of about 2% for all three tests.

Fig. 5.17 is a summary of the vertical stress profile for the three previous figures. The results of K_o consolidation show nearly equal lateral stresses for the 2.0 bar NC and the 1.0 bar (OCR = 4). Despite the difference in their behaviour in the first plastic phase, the vertical stress profiles in the second plastic phase coincide. This even applies to the 4.0 bar NC test along the second plastic phase if the stresses are normalised to the same value of the second phase.

Based on the numerical analysis requirement that the cavity strain move out by the same amount from one annulus to its adjacent one after one step of expansion, it was possible to obtain an average soil strain (weighted on the volume of each annulus) for every step of expansion during both plastic phases. Hence, the amount of total dilation/ compression of the soil versus its average strain for the entire expansion stage has been plotted for all the tests in Fig. 5.18. All three start off by compressing during the first, and part of the second, phase. The 4.0 bar NC test keeps on compressing throughout the whole process until the vertical stress at the cavity happens to reach its initial level (with the radial stress at the cavity reaching as high as 11.0 bar!). The 2.0 bar NC test, on the other hand, starts to dilate as a whole a few steps before the vertical stress at the cavity

reaches its initial, K_o, level. The cavity radial stress at the start of dilation is about 4.0 bar. The OC test lies in between the two Normally Consolidated tests with the average dilation starting at a cavity radial stress of 5.0 bar.

The response of soil element dilation to radial expansion is shown in Fig. 5.19 where strain obliquity is plotted versus the cavity pressure for the inner annulus of the three tests. This figure shows the similarity in response of 2.0 bar NC and 1.0 bar OC tests (which have approximately the same starting radial stress) against expansion and occurs earlier than that for the 4.0 bar test (even in terms of cavity strain - cf. Tables 5.3 to 5.5). It will be shown later in Chapter 7 that a similar response to penetration exists between the first two tests.

Having found the mean radial and circumferential strains of the inner annulus for every step of expansion, it is possible to obtain the volumetric and shear strains for this annulus throughout the tests. These have been plotted in Fig. 5.20 for the three tests. The same pattern of volumetric compression as shown in Fig. 5.18 is confirmed in this figure as well. The 4.0 bar test shows considerable volumetric compression (negative volumetric strain) which stretches to a shear strain of about 3.5% whereas the other two tests show very slight volumetric compression extending to less than 1% shear strain.

Fig. 5.20 also shows the remarkable similarity in the net dilation rate of the soil for the three tests. The 4.0 bar test has a net dilation angle in the later stage of the test of $\psi = 5°$ with the other two giving a value of about 6°. These are confirmed by the obliquity calculations in the second plastic phase for each test, and result directly from the obliquity chosen for individual step (Tables 5.3 to 5.5).

The analysis of a cylindrical cavity in a thick cylinder of sand (Appendix II) shows that dilation angles can be obtained from plots of cavity pressure versus cavity strain [on a double logarithmic basis]

which contain a linear portion having a slope, S, such that

$$\sin\psi = \frac{2\,N_{\phi'_{CV}} \cdot S - (N_{\phi'_{CV}} - 1)}{N_{\phi'_{CV}}} \qquad \text{(A.II.36)}$$

Such plots have been made for the analysed samples in Fig. 5.21 for the triaxially measured value of $\phi'_{CV} = 36°$. The ψ angles correspond very well by the two methods, at least up to a cavity strain of 1% beyond which the figure shows an increased slope and thus implies an increased ψ value (as already hinted at for the 2.0 bar NC test in the previous figure).

In the second plastic phase, data in Tables 5.3 to 5.5 show that the strain obliquity in the rθ plane, $N_{\psi_{r\theta}}$, reaches its limiting value at a circumferential strain of about 1% for all three tests. The starting stress values for which this applies are summarised in Table 5.7 for all three tests. Beyond this point, the theoretical Mohr-Coulomb plasticity equations with constant soil parameters may be applied. In the 2.0 bar test, this stretches as far as a cavity strain of 9%, giving a shear strain of 17% at the end of expansion, where σ'_z just reaches its initial, K_o, value.

Test No.	σ'_z bars	OCR	K_o	G_i	G_{ur}	G_{uf}	Remarks on Boundary Conditions
				bar			
1	4.28	1	0.298	833	–	833	Constant Lateral Stress
2	4.20	1	0.317	833	–	1660	True infinite
3	4.15	1	0.301	833	833	2500	Infinite using Rubber only
4	1.00	4	0.517	417	417	–	Same as Test 2
5	2.00	1	0.255	417	–	500	Same as Test 2
6	1.52	3	0.617	693	–	633	Constant Lateral Stress

Table 5.1. A summary of the expanding cylinder tests

σ'_z bar	OCR	G bars	E′ bars	ν'	ν	M bars	E bars
4.20	1	833	3228	0.21	0.261	3500	2100
1.00	4	417	2354	0.21	0.282	2500	1070
2.00	1	500	1860	0.21	0.202	2000	1200

Table 5.2. The elastic constants derived from the selected tests

ΔV lateral (cc) Col#1	ΔV cavity (cc) Col#2	σ'_r Col#3	$\bar{\sigma}'_r$ Col#4	$\bar{\sigma}'_\theta$ Col#5	$\bar{\sigma}'_z$ Col#6	$\bar{N}_{\psi_{r\theta}}$ Col#7	$\bar{N}_{\psi_{z\theta}}$ Col#8	$\bar{\varepsilon}_\theta$ Col#9	$-\bar{\varepsilon}_r$ Col#10
		kg/cm^2						$\times 10^{-5}$	
0.0000	0.0000	1.3294	1.3294	1.3294	4.200	0.2597	0.8206	–	–
0.19172	0.19172	1.3486	1.3390	1.3102	4.200	0.2655	0.8326	1.1352	1.1352
0.2770	0.2767	1.3570	1.3528	1.3076	4.1210	0.2700	0.8250	1.3521	1.3295
0.4002	0.3978	1.3679	1.3625	1.3030	4.0780	0.2740	0.8050	1.9969	1.9113
0.5782	0.5600	1.3823	1.3751	1.2966	3.9510	0.2790	0.7950	2.8125	2.6738
0.8354	0.8100	1.4025	1.3922	1.2848	3.8490	0.2850	0.7905	4.0558	4.0122
1.2067	1.2559	1.4295	1.4160	1.2688	3.7750	0.2950	0.7855	5.8618	5.7563
1.7439	1.8000	1.4660	1.4478	1.2488	3.6670	0.3095	0.7800	8.4966	8.6077
2.5195	2.5500	1.5160	1.4910	1.2185	3.5202	0.3308	0.7700	12.271	11.772
3.6402	3.6100	1.5855	1.5508	1.1719	3.3244	0.3648	0.7600	17.926	19.672
5.2595	5.2595	1.6835	1.6345	1.1004	3.1450	0.4187	0.7750	26.258	26.975
7.5990	7.5990	1.8200	1.7518	1.0078	2.8486	0.4973	0.7700	38.068	37.436
10.979	11.200	2.0100	1.9115	0.9141	2.6000	0.6105	0.7850	55.655	60.558
15.846	16.840	2.2531	2.1316	0.8065	2.3125	0.7752	0.7850	83.012	99.004
22.913	25.480	2.5620	2.4076	0.7239	2.3000	0.8794	0.7850	125.29	153.55
		INTERFACE OF THE TWO PLASTIC ZONES							
32.069	38.950	2.938	2.750	0.7261	2.385	0.9837	–	190.75	243.96
46.386	59.290	3.380	3.159	0.7779	2.482	1.0549	–	290.84	365.58
71.918	89.450	3.895	3.637	0.8619	2.600	1.0962	–	440.35	532.99
103.08	133.45	4.500	4.197	0.9346	2.733	1.1666	–	659.90	760.09
146.03	196.71	5.210	4.855	1.0237	2.890	1.2319	–	977.44	1064.1
210.17	286.55	6.045	5.627	1.1191	3.072	1.3062	–	1430.7	1468.7
303.97	413.20	7.014	6.530	1.2975	3.299	1.3071	–	2071.6	2015.7
435.79	591.70	8.138	7.576	1.5046	3.562	1.3079	–	2973.5	2765.6
641.40	820.20	9.443	8.791	1.7473	3.868	1.3067	–	4240.0	3829.0

N.B. Cols. [1] and [2] are for 42 cm height of expansion and lateral cells

Col. [3] is the stress at the soil inner boundary

Cols. [4] to [10] relate to conditions in the middle (mean) of inner-annulus

Table 5.3. The expanding cylinder analysis results for Test No. 2, σ'_z = 4.20 bars (NC)

ΔV lateral (cc) Col#1	ΔV cavity (cc) Col#2	σ'_r Col#3	$\bar{\sigma}'_r$ Col#4	$\bar{\sigma}'_\theta$ Col#5	$\bar{\sigma}'_z$ Col#6	$\bar{N}_{\psi_{r\theta}}$ Col#7	$\bar{N}_{\psi_{z\theta}}$ Col#8	$\bar{\varepsilon}_\theta$ Col#9	$-\bar{\varepsilon}_r$ Col#10
		kg/cm^2						$\times 10^{-5}$	
0.00000	0.00000	0.5202	0.5202	0.5202	2.0400	0.2597	1.0186	–	–
0.16000	0.16000	0.5299	0.5283	0.5118	2.0120	0.2696	1.0200	0.8015	0.7882
0.23120	0.23200	0.5339	0.5319	0.5098	2.0020	0.2739	1.0180	1.1605	1.1631
0.33404	0.40198	0.5397	0.5368	0.5052	1.9890	0.2840	1.0180	1.8769	3.6088
0.48262	0.62000	0.5482	0.5441	0.4976	1.9650	0.2900	1.0180	3.0256	4.0105
0.69729	0.91275	0.5605	0.5544	0.4873	1.9301	0.3013	1.0180	4.5377	4.9100
1.00745	1.3500	0.5774	0.5690	0.4768	1.8910	0.3213	1.0180	6.6989	7.4122
1.45557	2.0050	0.6011	0.5893	0.4601	1.8378	0.3500	1.0190	9.9325	11.206
2.10301	3.0000	0.6342	0.6177	0.4372	1.7601	0.3970	1.0190	14.817	17.294
3.03844	4.6000	0.6803	0.6573	0.4060	1.6540	0.4662	1.1090	22.500	29.136
4.38900	6.9500	0.7447	0.7125	0.3615	1.5055	0.5950	1.0190	34.194	41.646
6.34200	11.200	0.8340	0.7894	0.3026	1.3027	0.7850	1.0190	54.266	77.083
9.16300	15.300	0.9480	0.8910	0.2696	1.1225	0.8582	1.0190	79.085	82.500
13.2400	22.400	1.0871	1.0176	0.2594	1.1076	1.0190	1.0190	111.61	117.52
		INTERFACE OF THE TWO PLASTIC ZONES							
23.000	32.855	1.255	1.171	0.2657	1.051	1.1448	–	163.58	173.83
35.505	47.950	1.452	1.354	0.2906	1.095	1.2096	–	239.22	247.93
52.270	69.900	1.682	1.567	0.3257	1.147	1.2497	–	348.01	350.69
77.308	100.35	1.950	1.817	0.3693	1.208	1.2773	–	503.10	489.24
114.82	143.80	2.262	2.106	0.4215	1.280	1.2978	–	722.81	679.43
171.80	204.85	2.625	2.444	0.4834	1.364	1.3128	–	1032.2	938.10
263.43	290.45	3.046	2.836	0.5623	1.463	1.3098	–	1466.3	1296.2
398.00	410.05	3.535	3.291	0.6501	1.577	1.3148	–	2073.8	1786.0
595.57	577.00	4.102	3.819	0.7570	1.710	1.3103	–	2922.2	2465.7
876.20	809.80	4.760	4.431	0.8781	1.864	1.3106	–	4105.6	3407.4
1282.76	1134.0	5.524	5.142	1.0167	2.042	1.3136	–	5755.0	4708.0
1881.5	1587.0	6.410	5.967	1.1831	2.250	1.3101	–	8055.5	6564.0

N.B. Cols. [1] and [2] are for 42 cm height of expansion and lateral cells

Col. [3] is the stress at the soil inner boundary

Cols. [4] to [10] relate to conditions in the middle (mean) of inner-annulus

Table 5.4. The expanding cylinder analysis results for Test No. 5, σ'_z = 2.0 bars (NC)

ΔV lateral (cc) Col#1	ΔV cavity (cc) Col#2	σ'_r Col#3	$\bar{\sigma}'_r$ Col#4	$\bar{\sigma}'_\theta$ Col#5	$\bar{\sigma}'_z$ Col#6	$\bar{N}_{\psi_{r\theta}}$ Col#7	$\bar{N}_{\psi_{z\theta}}$ Col#8	$\bar{\varepsilon}_\theta$ Col#9	$-\bar{\varepsilon}_r$ Col#10
		kg/cm^2						$\times 10^{-5}$	
0.00000	0.00000	0.5170	0.5170	0.5170	1.0300	0.2597	0.5175	-	-
0.16000	0.16000	0.5380	0.5367	0.5233	1.0300	0.2664	0.5112	0.8015	0.7882
0.23120	0.23125	0.5414	0.5397	0.5210	1.0300	0.2691	0.5135	1.1584	1.1397
0.33404	0.33424	0.5462	0.5438	0.5179	1.0300	0.2728	0.5166	1.6734	1.6455
0.48262	0.48292	0.5530	0.5496	0.5128	1.0300	0.2873	0.5217	2.4177	2.3779
0.69729	0.69799	0.5628	0.5579	0.5043	1.0300	0.2873	0.5305	3.4931	3.4348
1.00745	1.0200	0.5766	0.5697	0.4943	1.0300	0.2994	0.5412	5.0841	5.3304
1.45557	1.4960	0.5962	0.5864	0.4796	1.0300	0.3176	0.5579	7.4486	7.9130
2.10301	2.2030	0.6240	0.6101	0.4586	1.0300	0.3456	0.5834	10.951	11.866
3.03844	3.3400	0.6620	0.6430	0.4359	1.0300	0.3832	0.6138	16.410	20.284
4.38900	5.1100	0.7150	0.6885	0.3996	1.0300	0.4475	0.6695	25.016	32.106
6.34200	7.9200	0.7865	0.7508	0.3610	1.0300	0.5401	0.7410	38.575	52.110
9.16300	12.300	0.8810	0.8338	0.3187	1.0300	0.6800	0.8395	59.861	81.492
13.2400	18.540	1.0050	0.9430	0.2671	1.0300	0.9169	1.0015	91.302	110.07
		INTERFACE OF THE TWO PLASTIC ZONES							
19.129	27.905	1.155	1.080	0.2721	1.060	1.0308	-	137.49	164.58
27.638	41.590	1.334	1.245	0.2792	1.096	1.1578	-	205.73	236.08
39.931	61.250	1.545	1.440	0.3008	1.142	1.2431	-	304.46	330.02
58.412	89.245	1.790	1.668	0.3452	1.199	1.2548	-	445.53	457.78
85.670	128.79	2.075	1.933	0.3941	1.265	1.2738	-	645.48	630.89
126.16	184.50	2.406	2.241	0.4536	1.342	1.2829	-	927.50	870.49
191.27	262.50	2.791	2.599	0.5199	1.431	1.2983	-	1323.4	1193.9
292.63	371.70	3.238	3.015	0.6011	1.535	1.3027	-	1877.5	1646.6
453.54	524.40	3.757	3.498	0.6952	1.657	1.3067	-	2209.0	1987.9
704.37	737.10	4.359	4.058	0.8076	1.798	1.3051	-	3734.0	3136.0
1061.7	1035.0	5.057	4.708	0.9394	1.962	1.3018	-	5246.0	4368.0

N.B. Cols. [1] and [2] are for 42 cm height of expansion and lateral cells

Col. [3] is the stress at the soil inner boundary

Cols. [4] to [10] relate to conditions in the middle (mean) of inner-annulus

Table 5.5. The expanding cylinder analysis results for Test No. 4, σ'_z = 1.0 bars (OCR = 4)

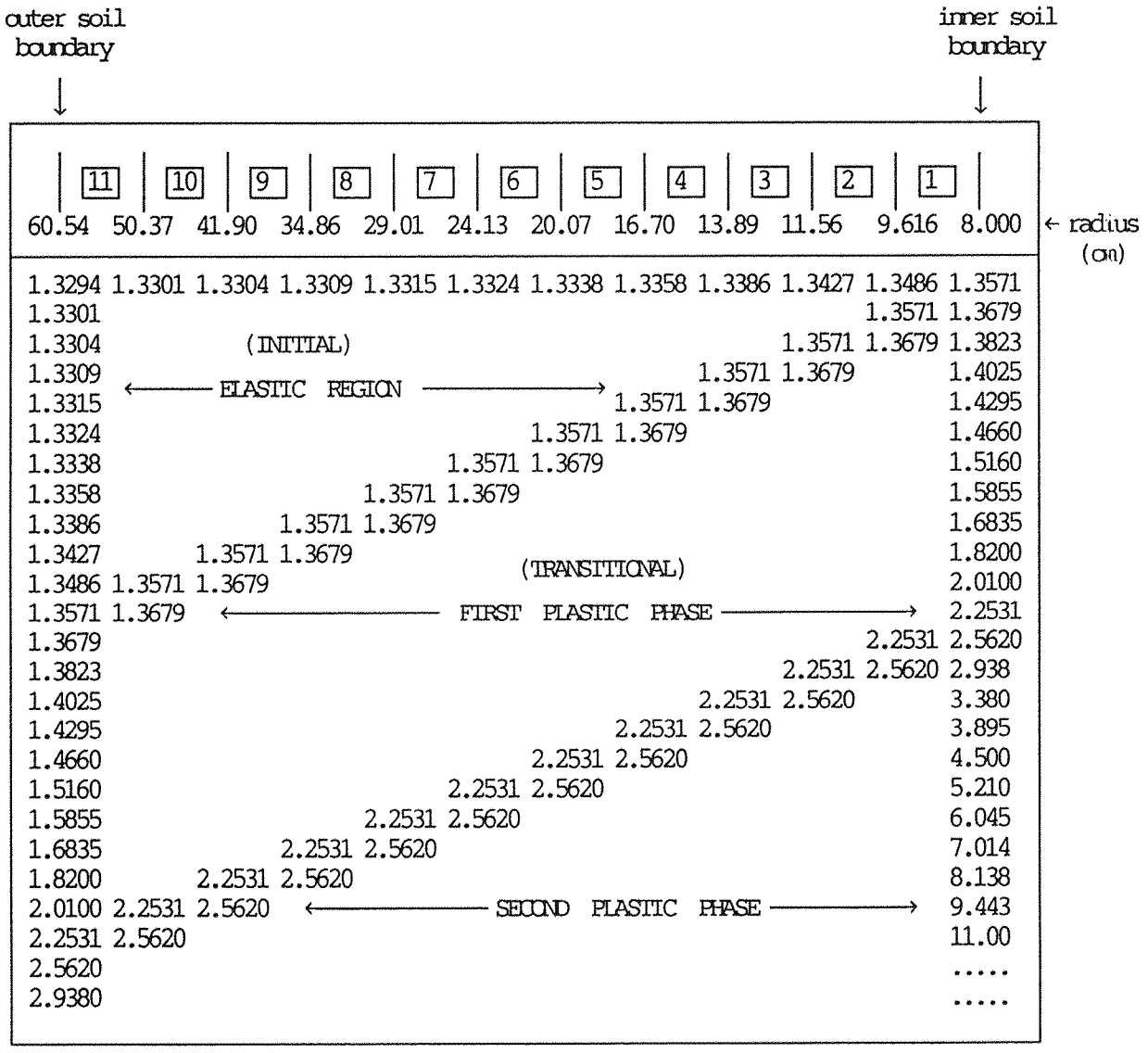

1.3294	1.3301	1.3304	1.3309	1.3315	1.3324	1.3338	1.3358	1.3386	1.3427	1.3486	1.3571
1.3301										1.3571	1.3679
1.3304									1.3571	1.3679	1.3823
1.3309								1.3571	1.3679		1.4025
1.3315							1.3571	1.3679			1.4295
1.3324						1.3571	1.3679				1.4660
1.3338					1.3571	1.3679					1.5160
1.3358				1.3571	1.3679						1.5855
1.3386			1.3571	1.3679							1.6835
1.3427		1.3571	1.3679								1.8200
1.3486	1.3571	1.3679									2.0100
1.3571	1.3679										2.2531
1.3679										2.2531	2.5620
1.3823									2.2531	2.5620	2.938
1.4025								2.2531	2.5620		3.380
1.4295							2.2531	2.5620			3.895
1.4660						2.2531	2.5620				4.500
1.5160					2.2531	2.5620					5.210
1.5855				2.2531	2.5620						6.045
1.6835			2.2531	2.5620							7.014
1.8200		2.2531	2.5620								8.138
2.0100	2.2531	2.5620									9.443
2.2531	2.5620										11.00
2.5620											.....
2.9380											.....

TABLE 5.6 Illustrative table showing successive steps in calculation of normal stresses (kg/cm^2) on annulus boundaries of Table 5.3

initial σ'_z kg/cm^2	OCR	σ'_r	$\bar{\sigma}'_r$	$\bar{\sigma}'_\theta$	$\bar{\sigma}'_z$	$\bar{N}_{\psi r\theta}$	$\bar{\varepsilon}_\theta$	$-\bar{\varepsilon}_r$
		kg/cm^2					x 10^{-5}	
4.2	1	6.045	5.627	1.1191	3.072	1.3062	1430.7	1468.7
2.0	1	2.625	2.444	0.4834	1.364	1.3100	1032.2	938.1
1.0	4	2.406	2.241	0.4536	1.342	1.2829	927.5	870.5

Table 5.7. The stress and strain values at limiting obliquities for the analysed tests

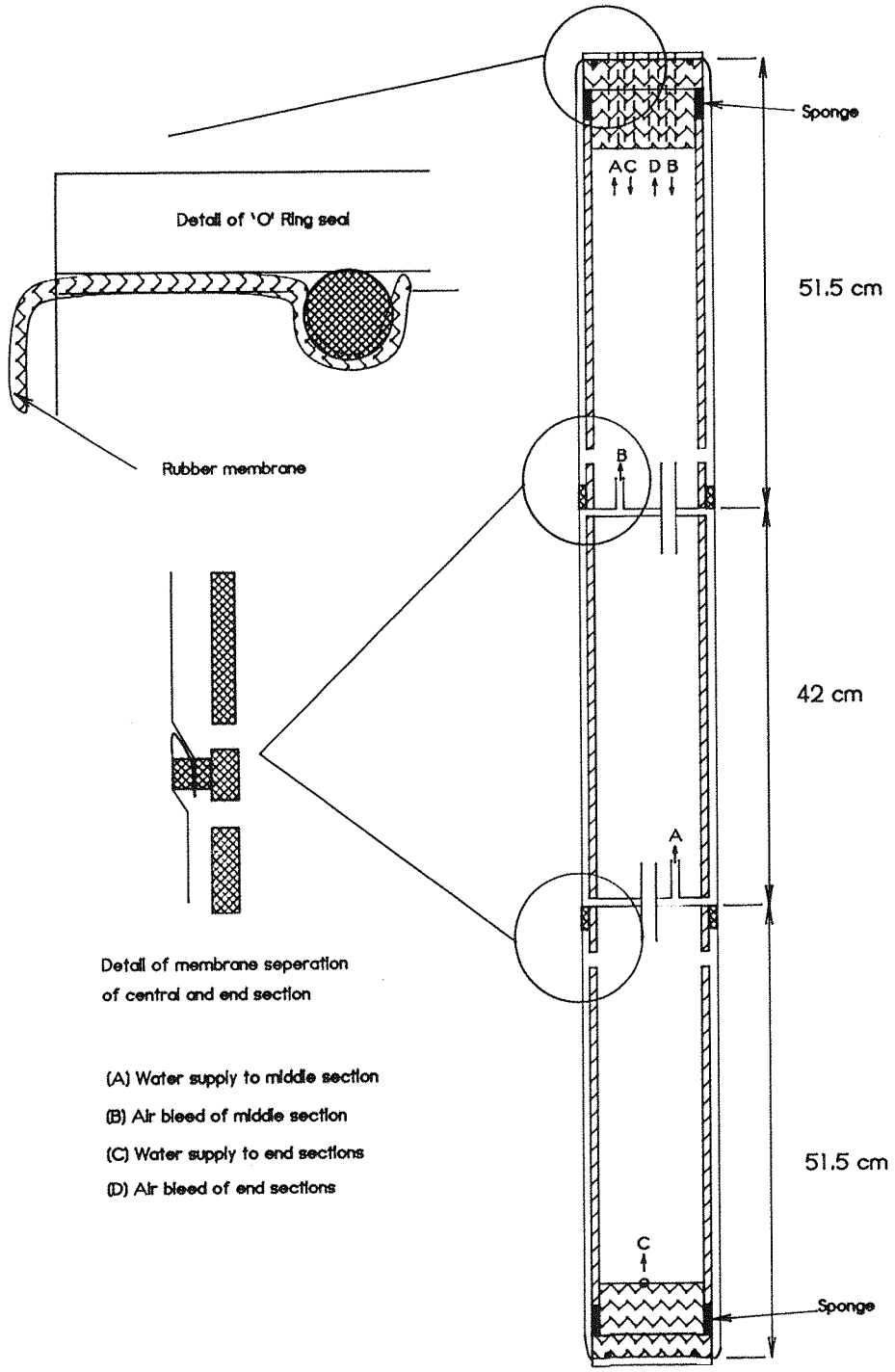

Fig. 5.1 Schematic diagram of the full length expanding cylinder

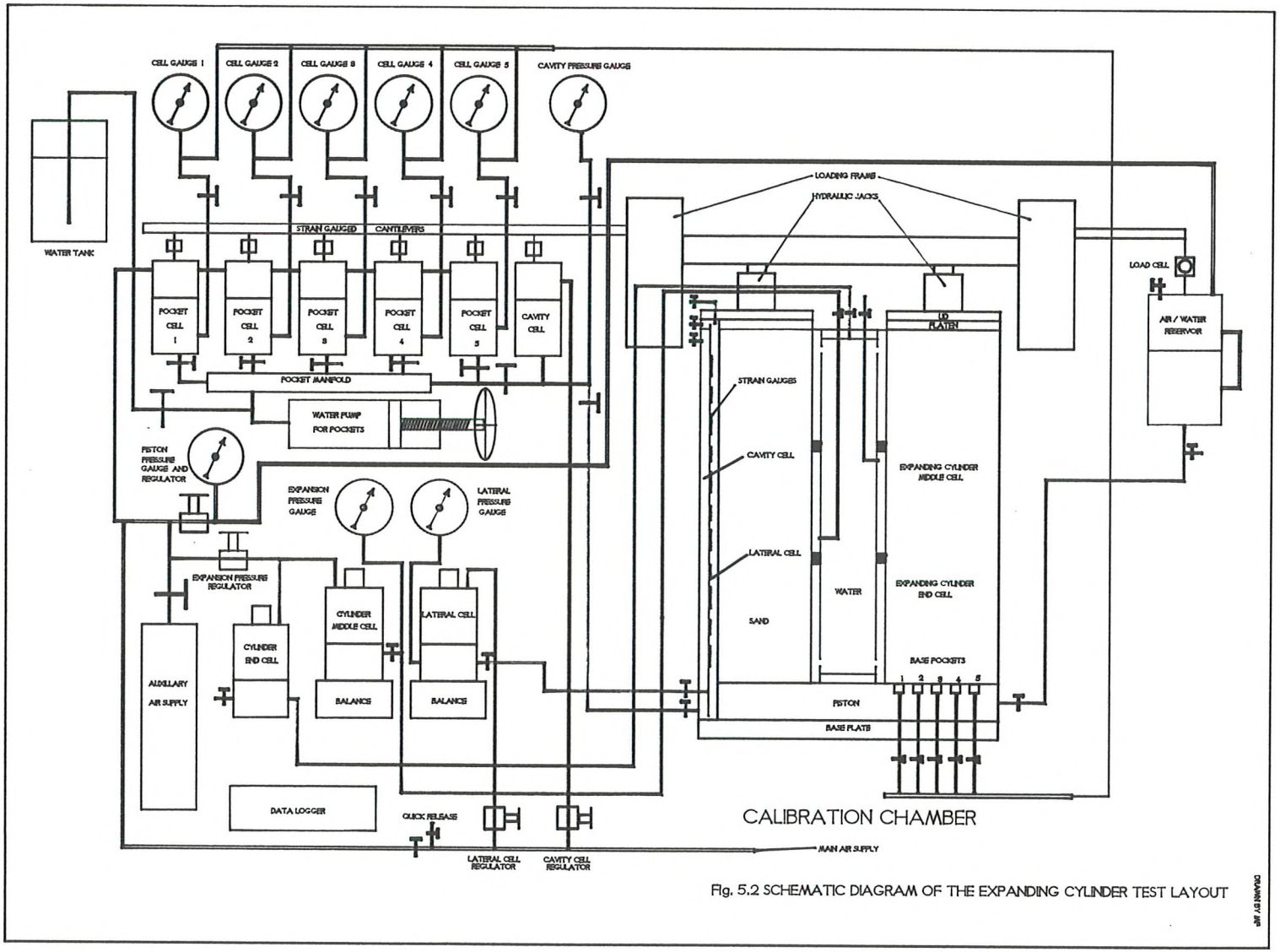

Fig. 5.2 SCHEMATIC DIAGRAM OF THE EXPANDING CYLINDER TEST LAYOUT

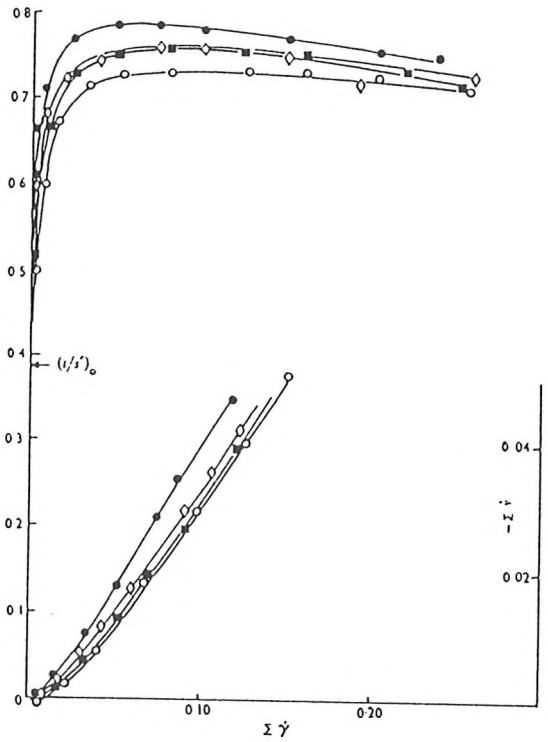

(a) dense

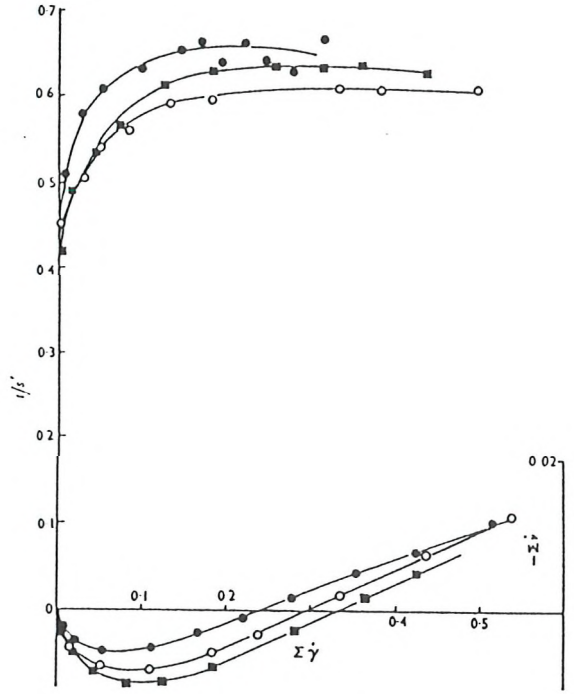

(b) loose

Fig. 5.3 Results of simple shear tests on Leighton Buzzard sand (Stroud, 1971)

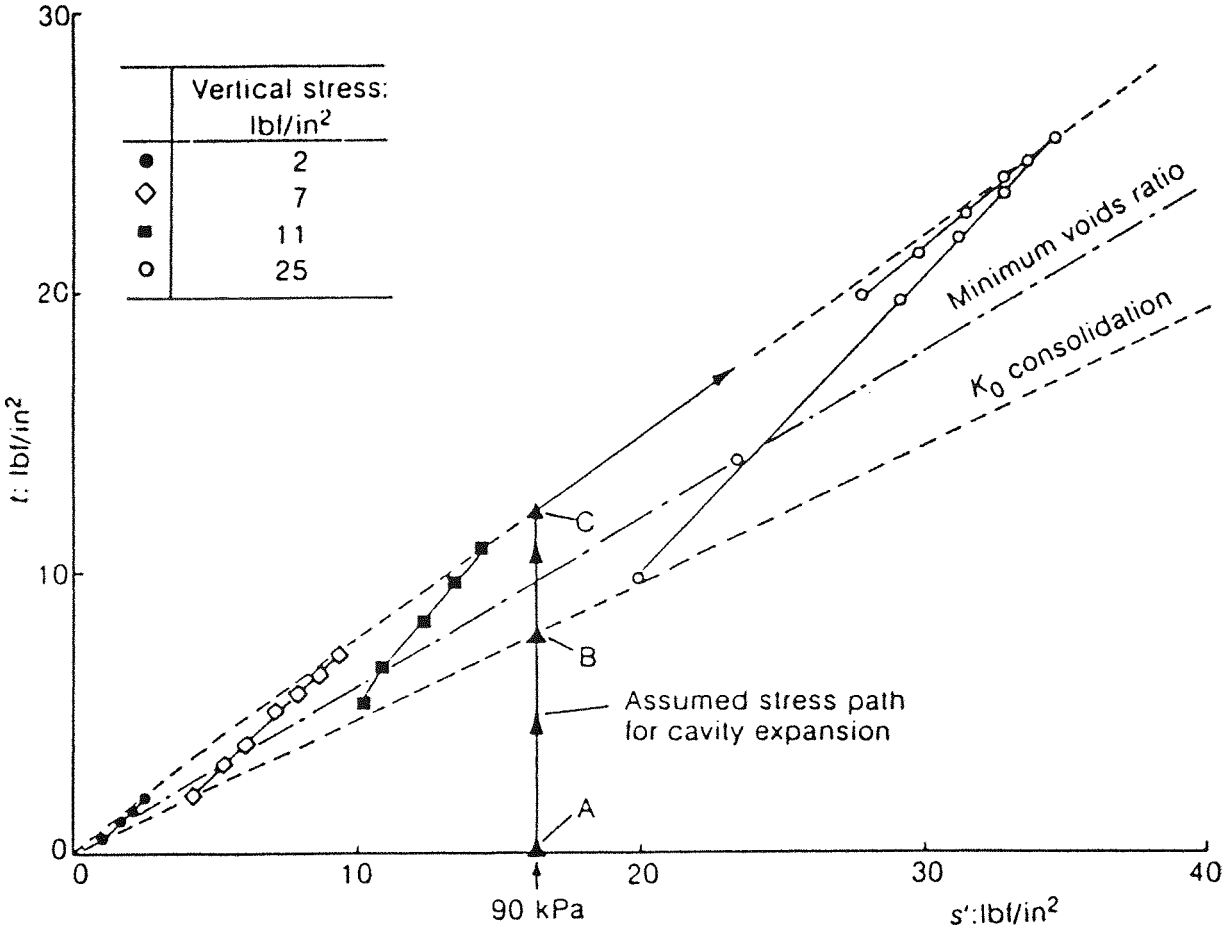

Fig. 5.4 Stress paths measured by Stroud (1971) in the SSA compared with the assumed stress path for cavity expansion

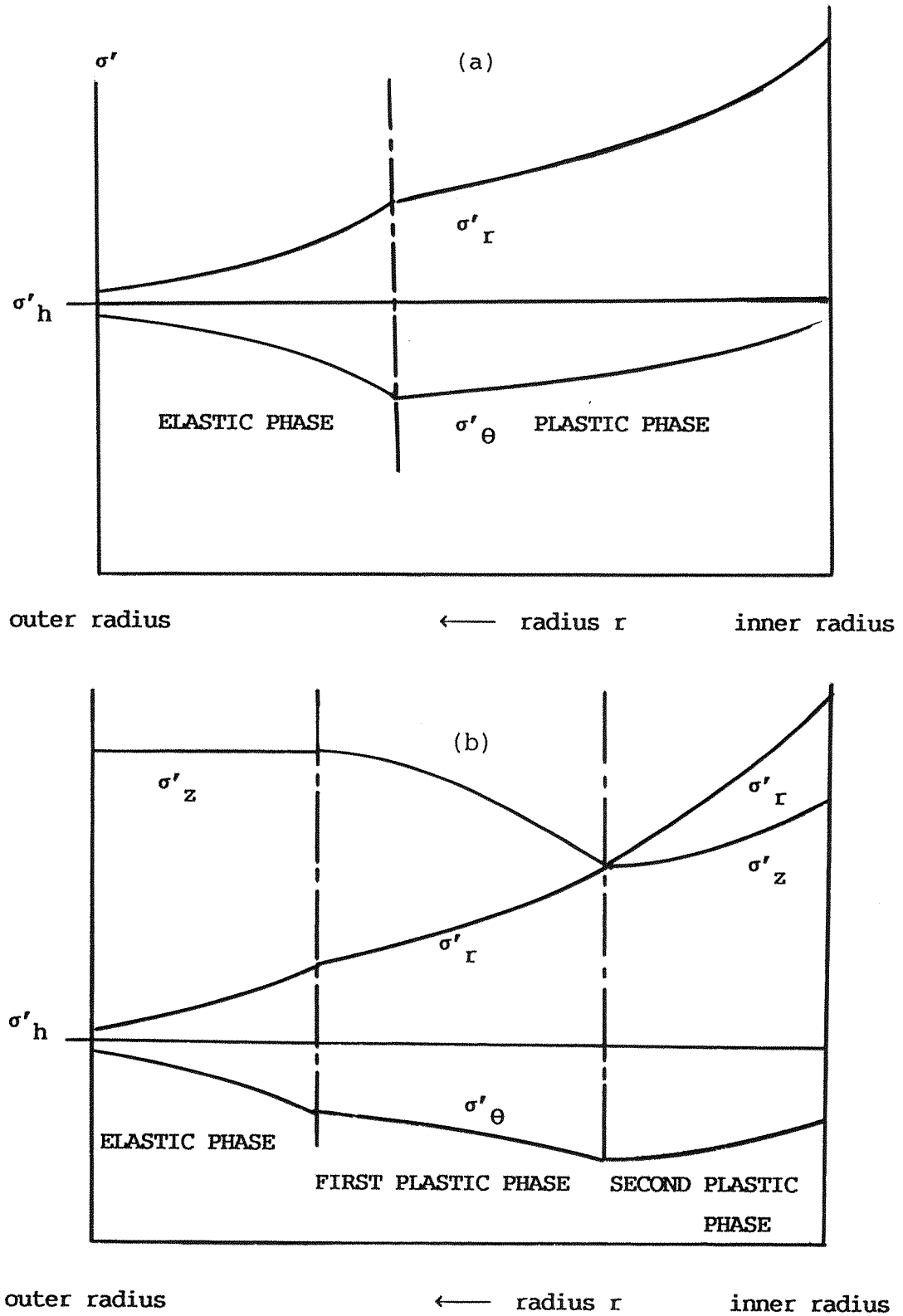

Fig. 5.5. A symbolic representation of the changes in the principal stresses along the radius for: a- two phase and b- three phase analysis

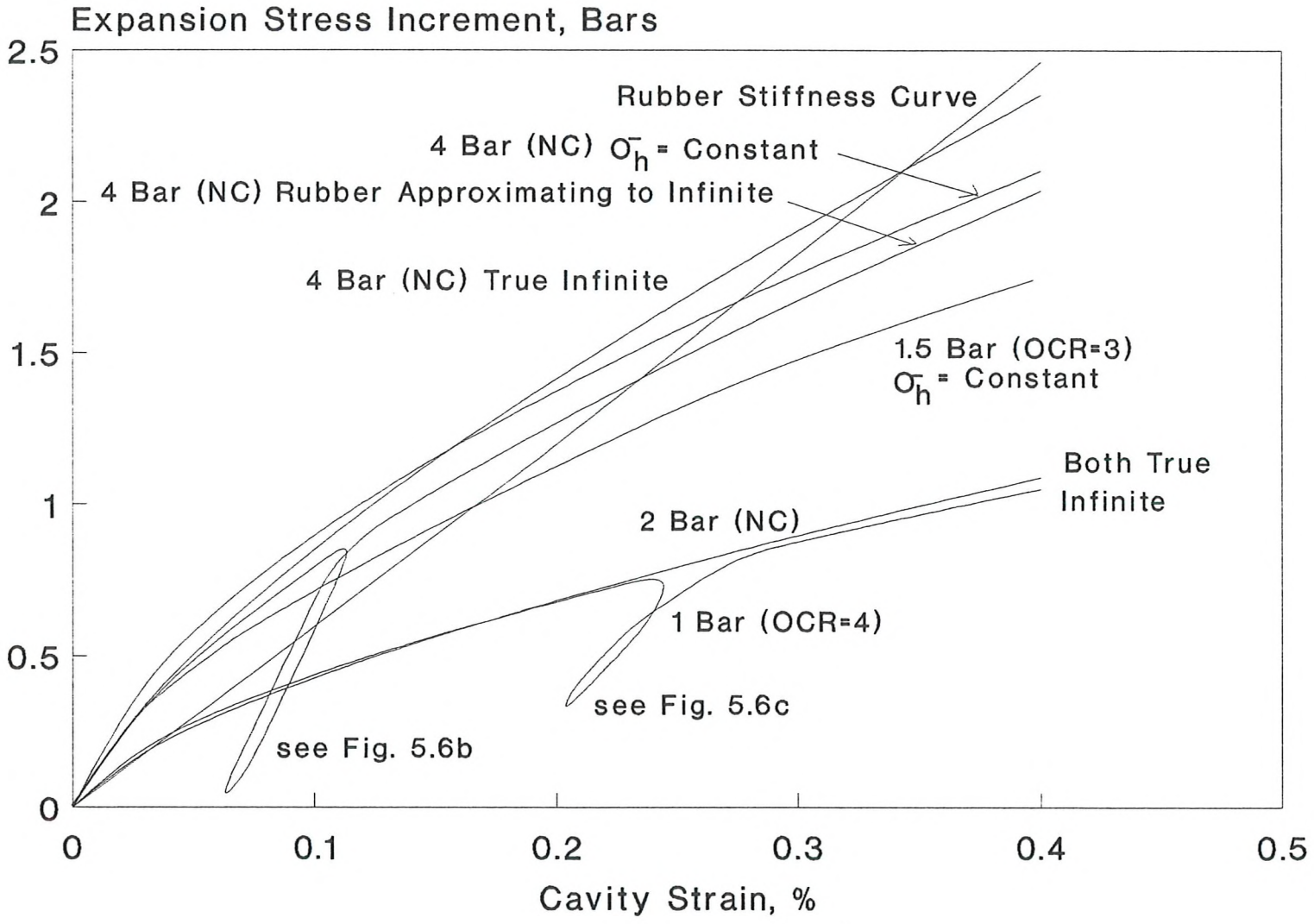

Fig. 5.6a Stress strain diagrams at the early stages of expansion

Fig. 5.6b Enlargement of the unload-reload loop for the 4 Bar NC test

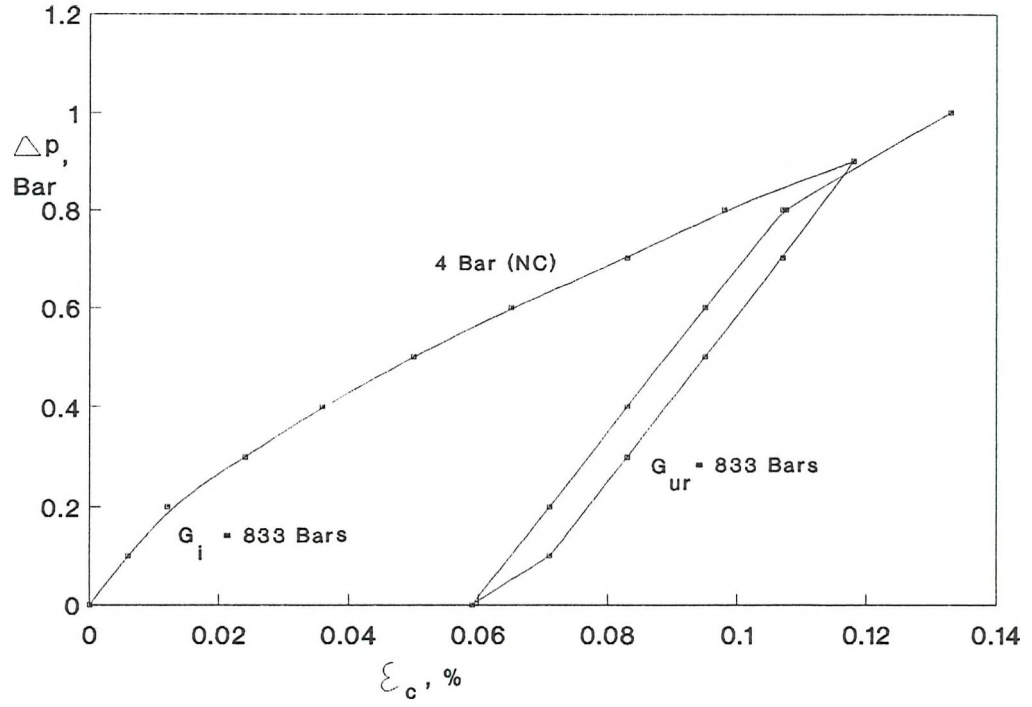

Fig. 5.6c Enlargement of the unload-reload loop for the 1 bar (OCR = 4) test

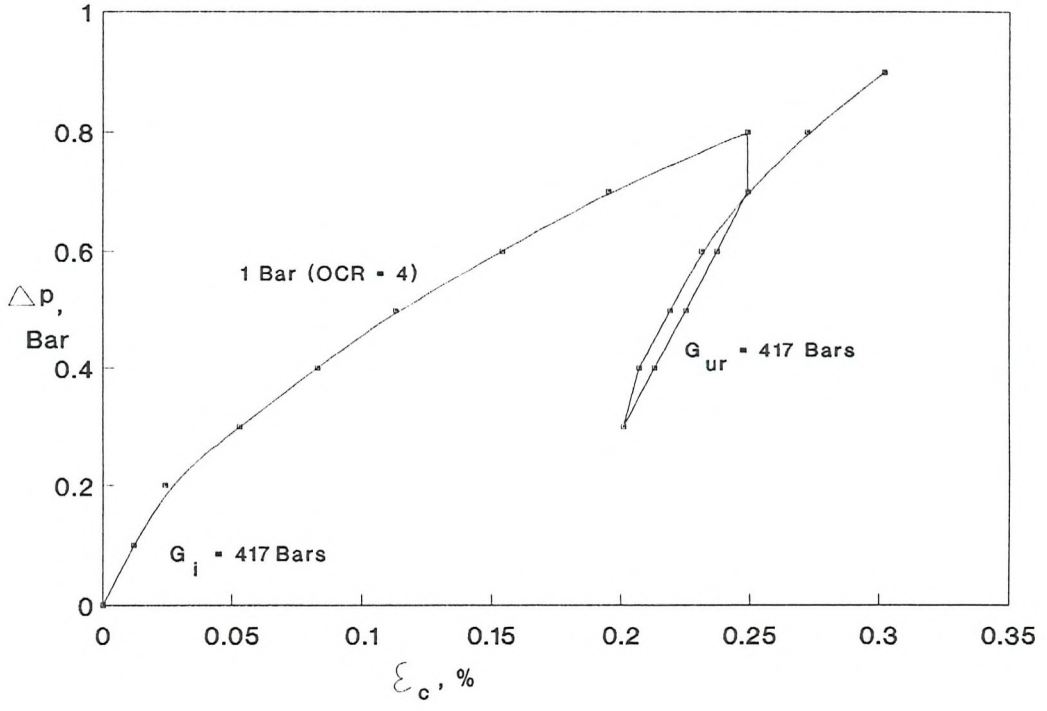

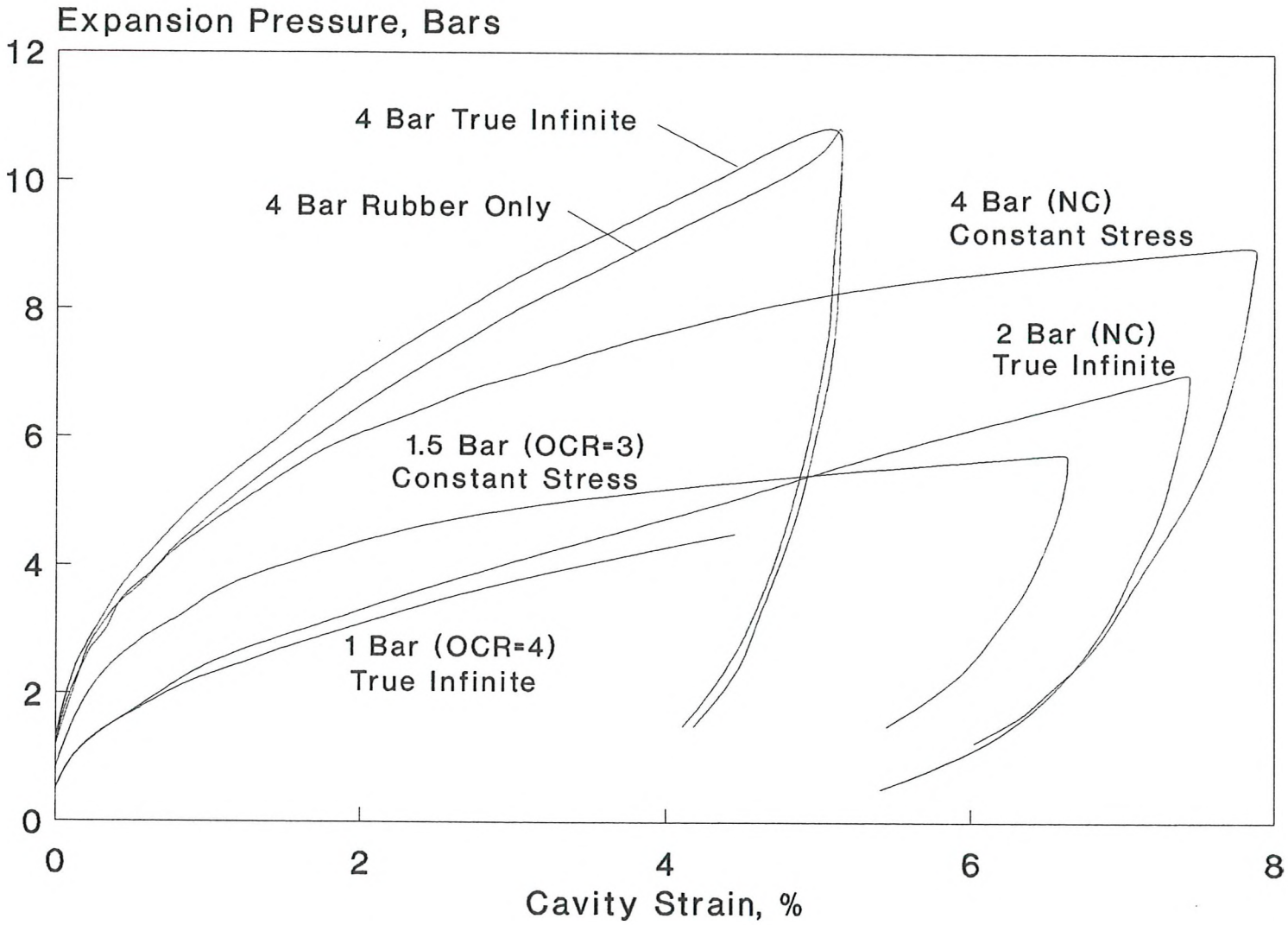

Fig. 5.7 Stress strain relationship at the cavity during expansion and unloading

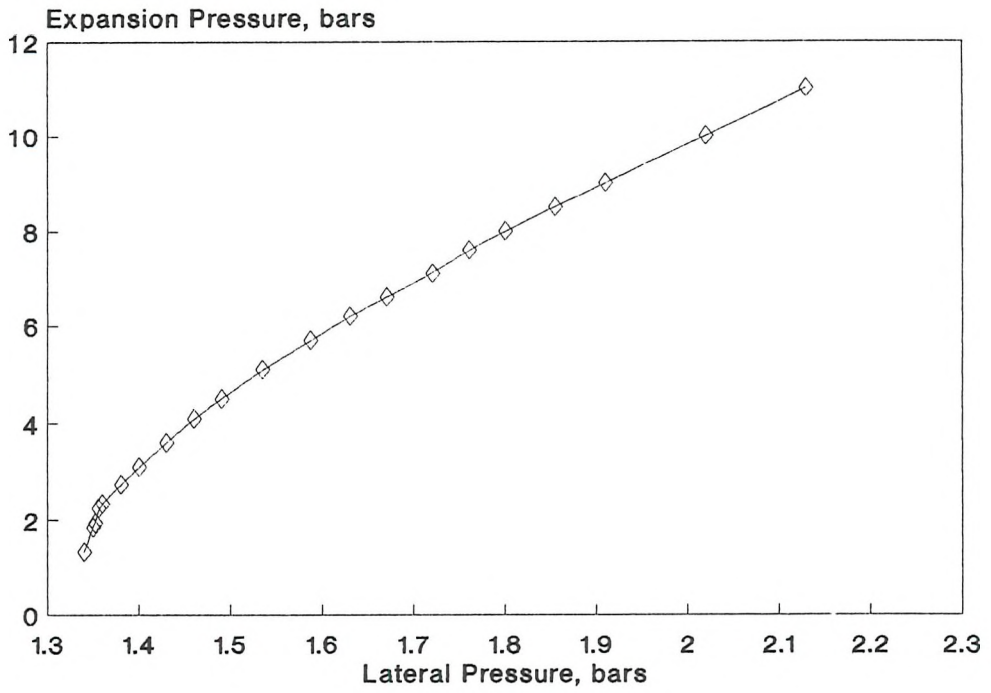

Fig. 5.8 Expansion pressure vs. lateral pressure (4.0 bars NC)

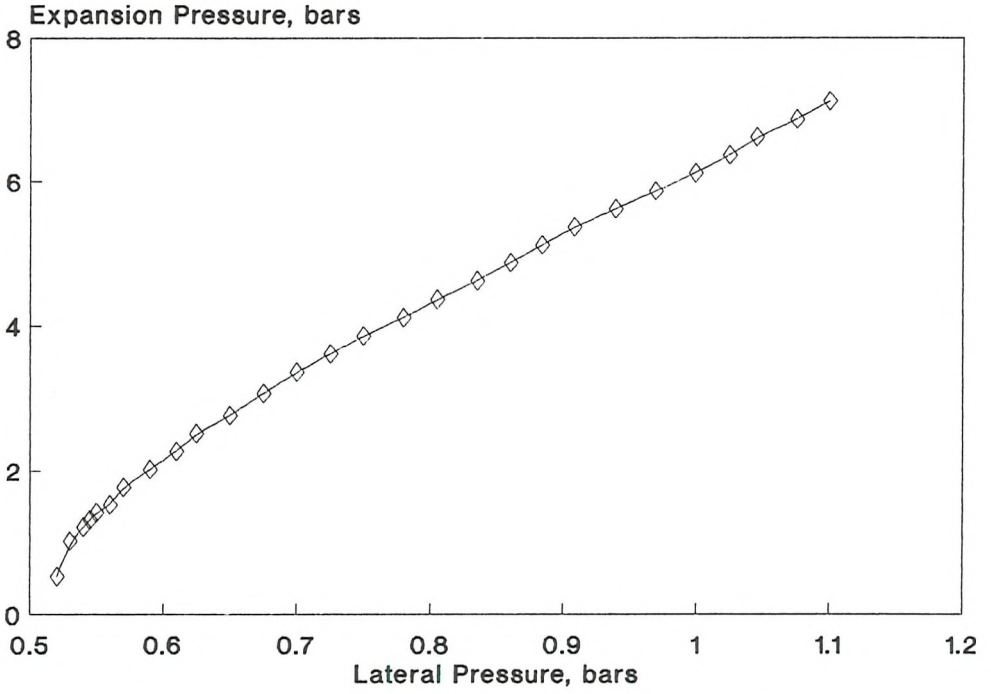

Fig. 5.9 Expansion pressure vs. lateral pressure (2.0 bars, NC)

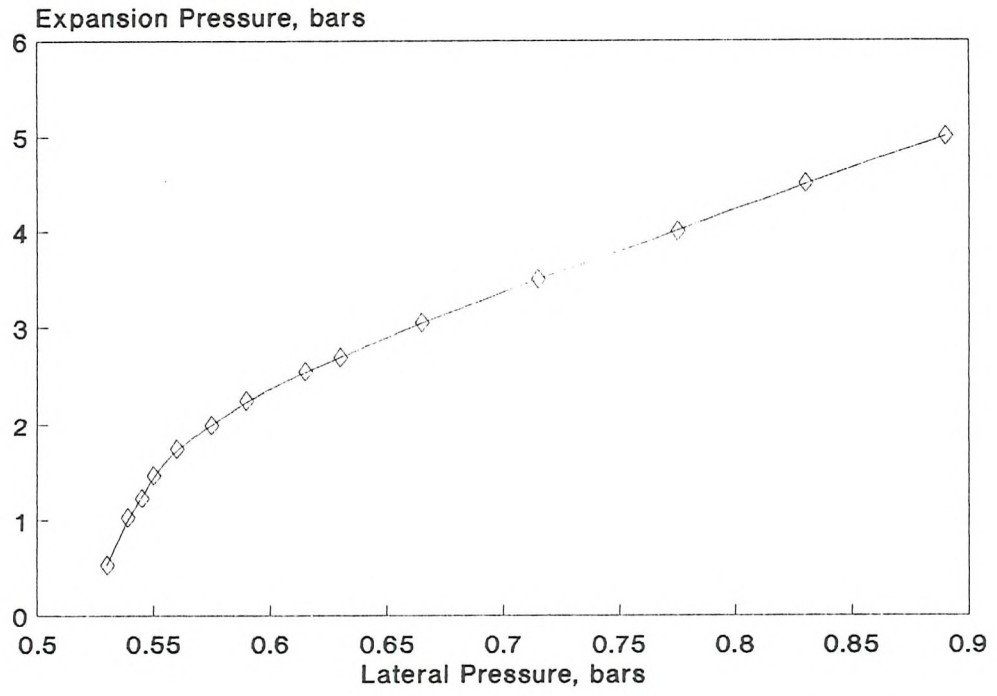

Fig. 5.10 Expansion pressure vs. lateral pressure (1.0 bars, OCR = 4)

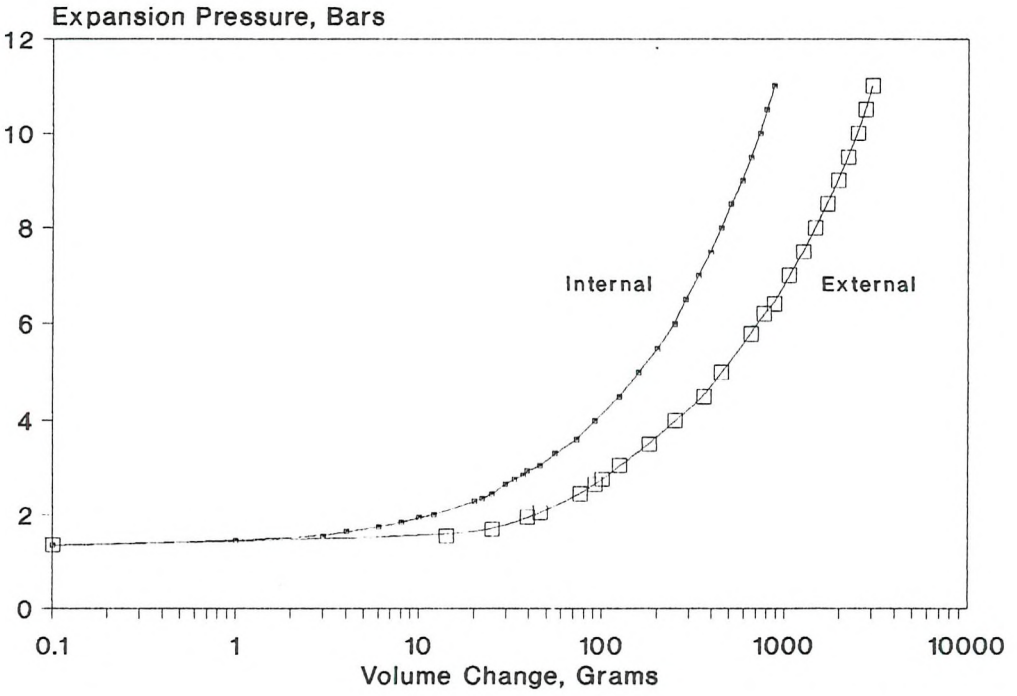

Fig. 5.11 Internal pressure vs. internal and external volume changes (4.0 bars, NC)

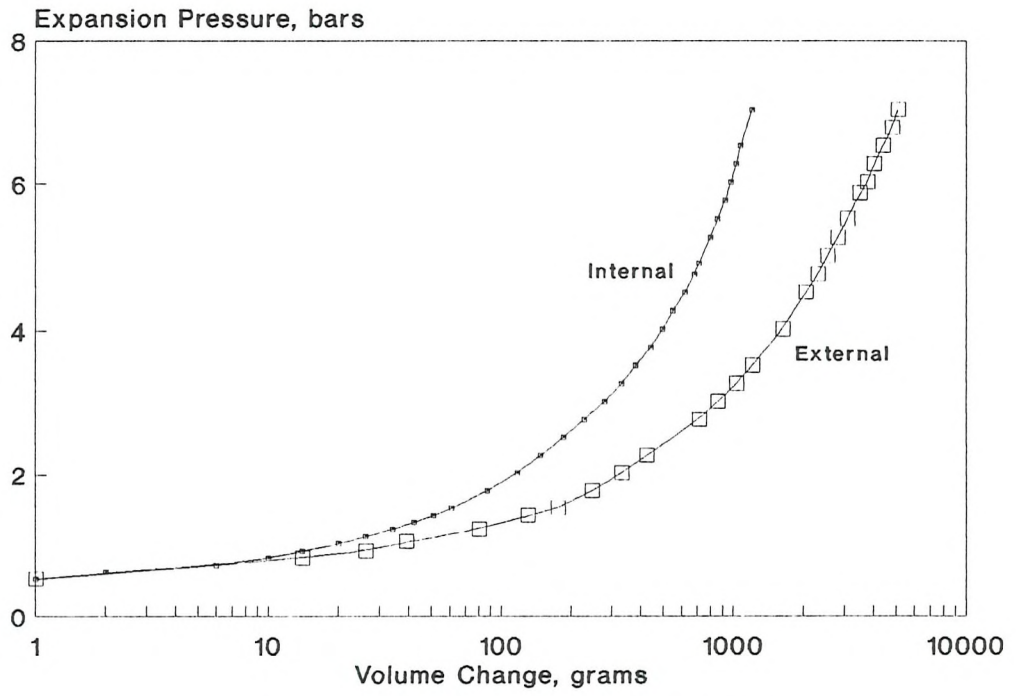

Fig. 5.12 Internal pressure vs. internal and external volume changes (2.0 bars, NC)

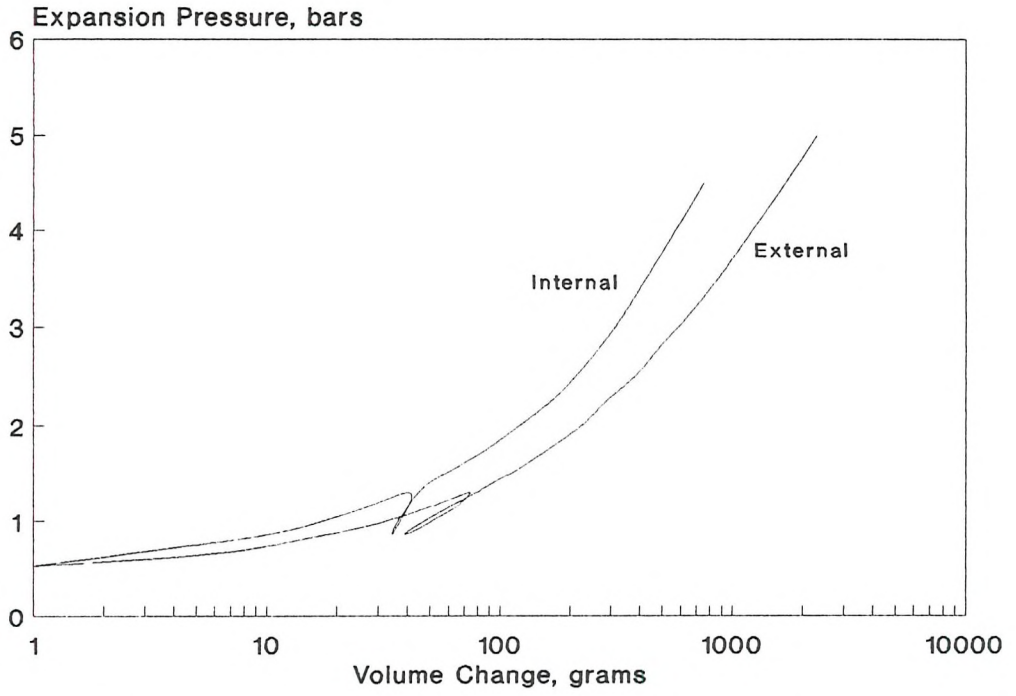

Fig. 5.13 Cavity pressure vs. cavity and lateral volume changes (1.0 bar OCR=4)

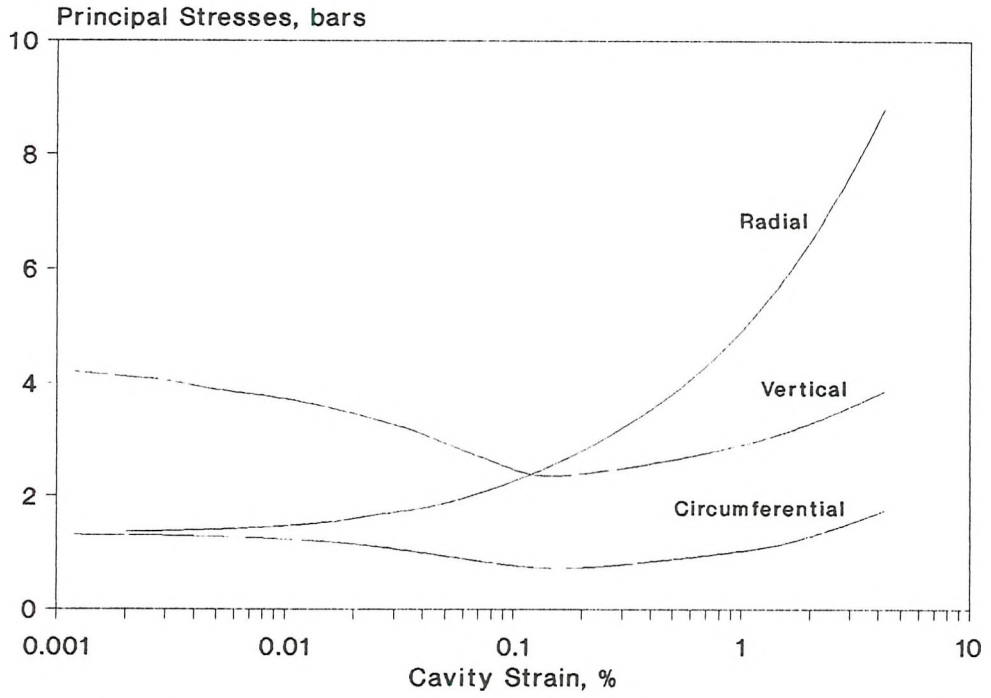

Fig. 5.14 Principal stresses vs. cavity strain during expansion (4.0 bars, NC)

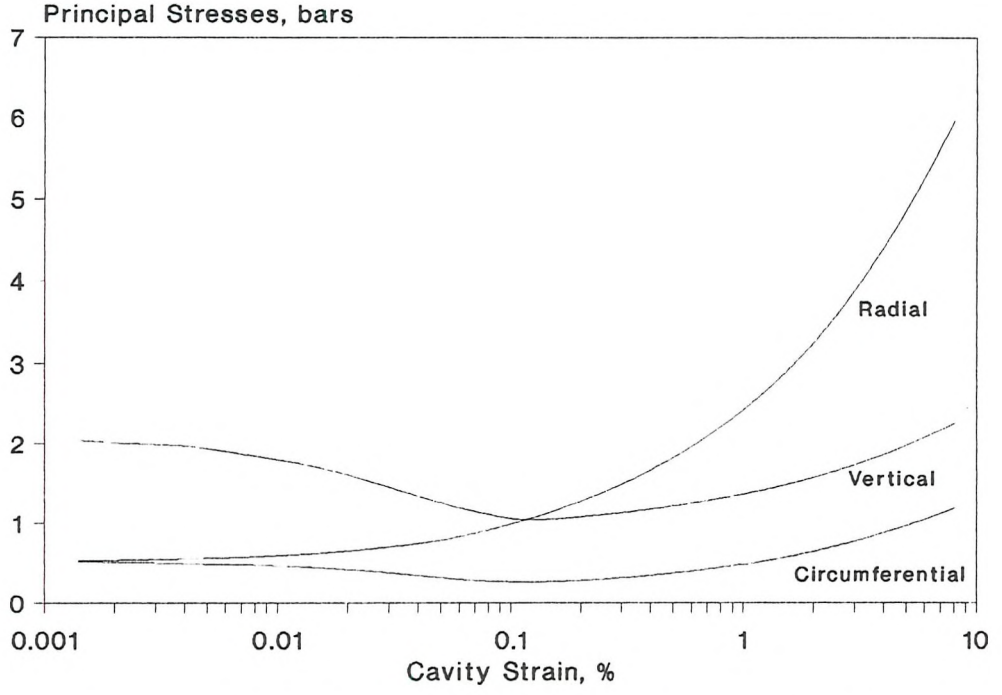

Fig. 5.15 Principal stresses vs. cavity strain during expansion (2.0 bars, NC)

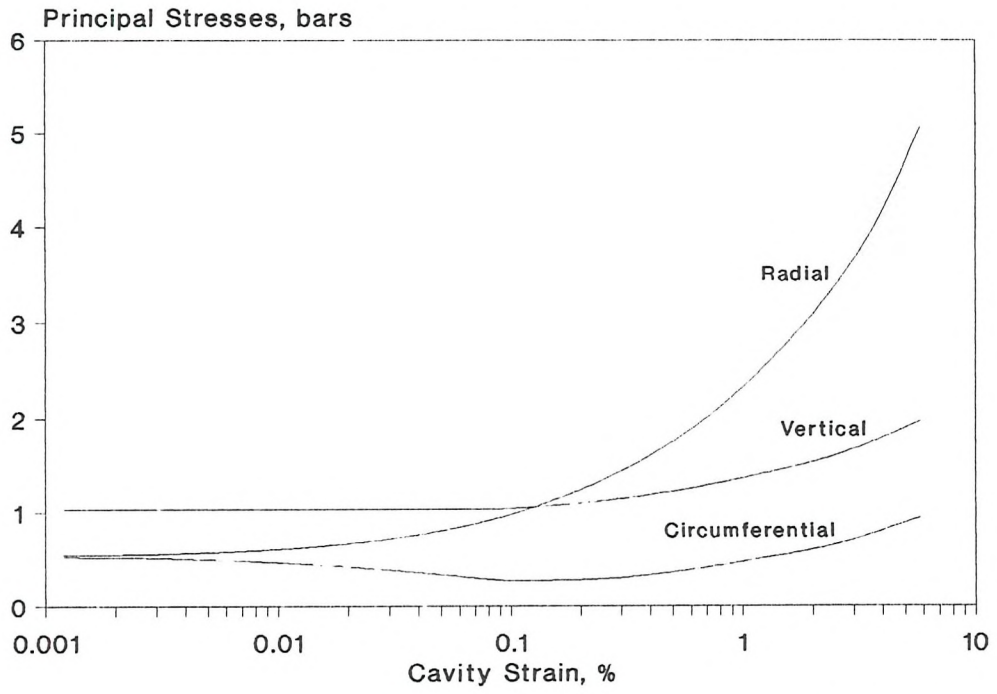

Fig. 5.16 Principal stresses vs. cavity strain during expansion (1.0 bar, OCR=4)

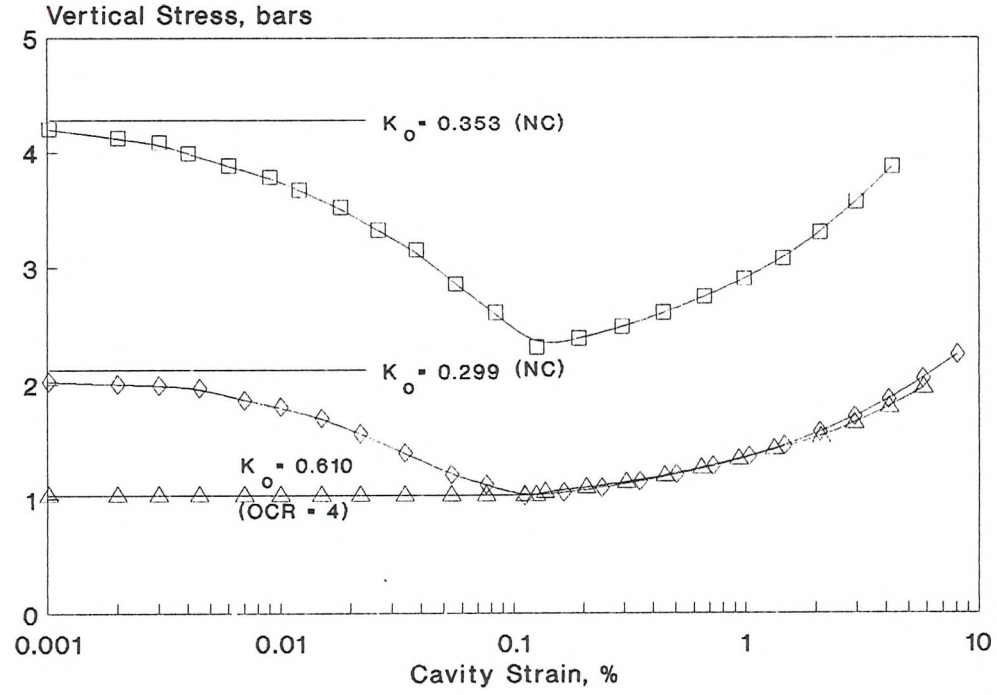

Fig. 5.17 Vertical stress profiles during expansion for the three tests

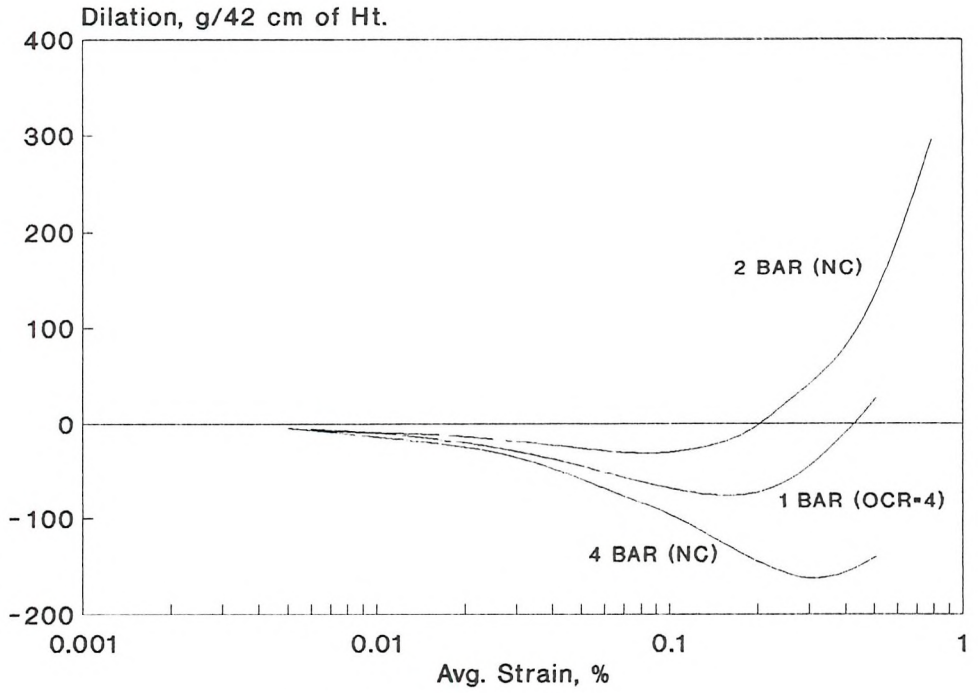

Fig. 5.18 Overall dilation vs. average strain during expansion

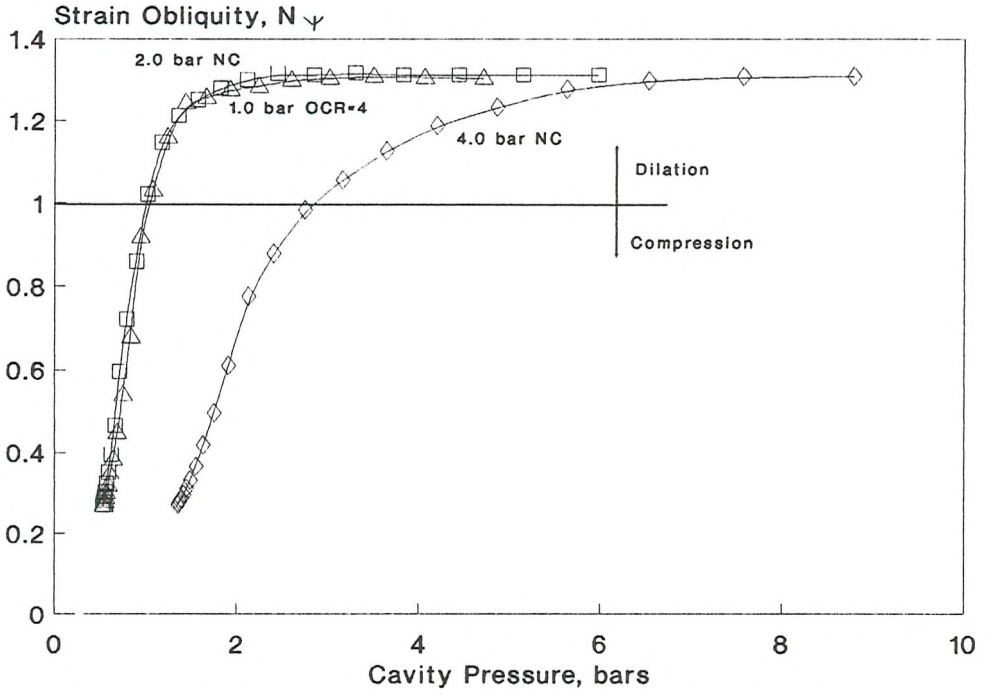

Fig. 5.19 Strain obliquity vs. cavity pressure during expansion

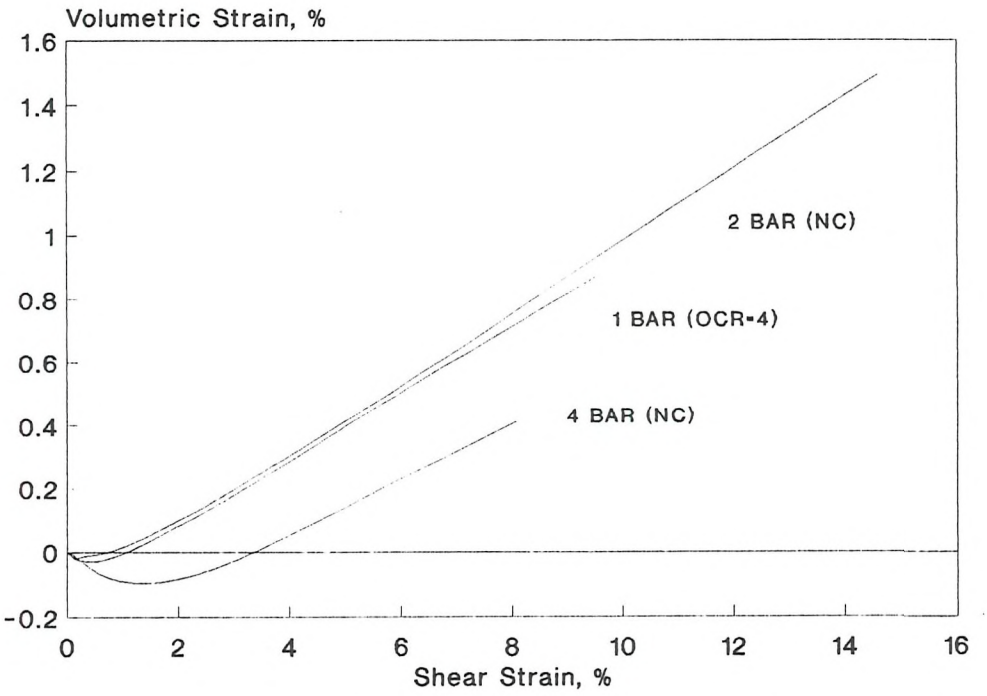

Fig. 5.20 Volumetric strain vs. shear strain during expansion for different tests

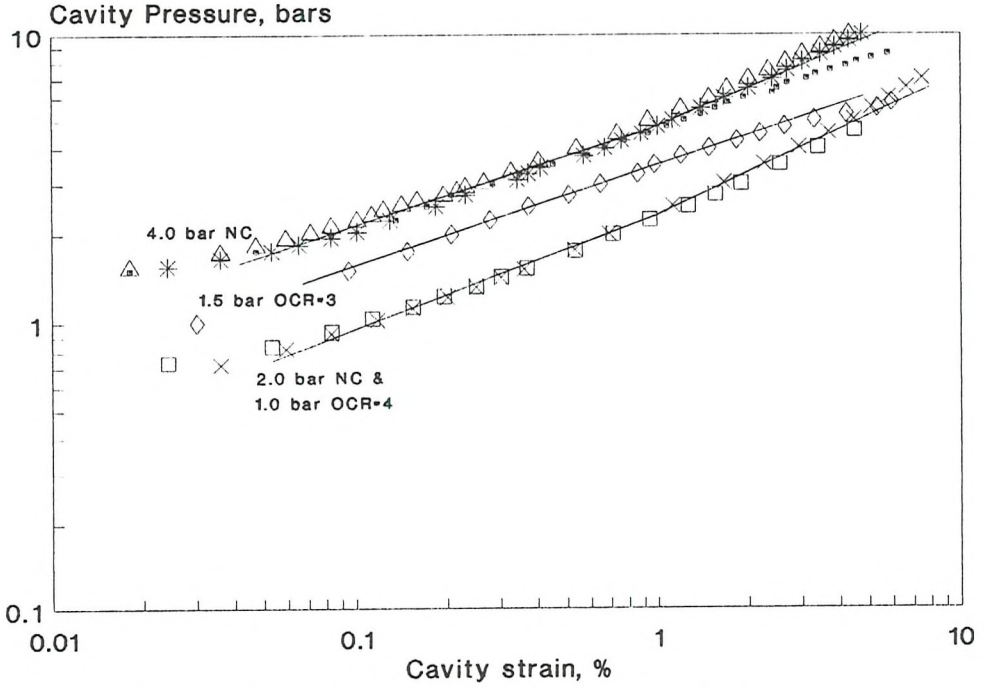

Fig. 5.21 Cavity pressure vs. cavity strain during expansion

CHAPTER 6

CALIBRATION CHAMBER DESIGN

6.1. INTRODUCTION

Calibration chamber testing originated because of a need to examine the behaviour of field penetrometers under laboratory conditions where the soil properties, stresses and strains could be accurately controlled and measured. The chamber also provided a suitable environment in which to conduct model studies and to calibrate a variety of soil instruments, e.g. cone penetrometers.

In this chapter, the main characteristics of the existing N.G.I. calibration chamber are briefly reviewed and the modifications required to model a more realistic soil behaviour are discussed.

6.2. Brief History

The NGI chamber described in this section was the fourth of its type to be built and is similar in design to the other three chambers constructed. These are the County Roads Board of Victoria (CRB) chamber and those at the University of Florida and Monash University. Since its original construction in 1976, two more similar chambers have been built in Italy. A comparison of the chambers geometry can be seen in Table 6.1. The NGI chamber has the same sample diameter as the Monash and Florida ones with an average depth of the two (1.215m in diameter by 1.5m in height. In the recent modifications, the size has changed slightly to 1.209m diameter by 1.470m height).

This chamber facilitates the application of controlled triaxial stress and strain fields to a large carefully prepared sample of sand. A full description of the chamber is given by Chapman (1975) and Last (1979). The chamber comprises six major components, each of which is briefly described below:

6.2.1. The Base

This provides a flat solid surface on which the rest of the chamber is mounted. The base is made from 40mm steel plate which also seals off the bottom of the chamber. It must be mounted on a strong floor to which the reaction frame is also connected. A displacement transducer penetrates both the floor and the chamber base to sense the movement of the piston.

6.2.2. Piston and Cylinder

The cylindrical soil sample is centred vertically by a fixed platen at the top and a piston at the base. The latter travels in a short cylinder fixed to the chamber base: an O-ring located in a groove on the inside of the cylinder provides a seal. A leak-proof seal here is vital to ensure correct operation of the chamber. Vertical load is applied as a fluid pressure below the piston (air in the original design, but now water to allow greater control of vertical displacement). The vertical displacement of the piston is not only monitored with the long travel displacement transducer, which is located below the base plate, but also by the amount of the fluid pushed into, or out of, the piston/cylinder compartment. In the original design, the moving transducer rod kept its contact with the underside of the piston under the effect of a dead hanging weight. As part of the modifications, this rod was permanently fixed to the underside of the piston in a manner that allows the piston to swivel on the dome headed rod and, hence, avoids the uncertainty of whether or not the transducer and piston remained in contact.

6.2.3. Chamber barrel

This encloses the sample and forms the outer wall of the chamber. It is constructed as a double cylinder providing 2 walls of 6.5mm steel plate around the sample. The double wall construction provides a means of controlling lateral deformation during sample compression. At the top of the barrel, the two concentric walls are welded to a metal ring on which the lid seals with an O-ring. At the base, the walls are welded onto another metal ring which seals against the base.

6.2.4. Membranes

These enclose the sand sample on the sides and base. The base membrane was made from 3mm thick neoprene rubber and the side membrane was of 1.5mm thick rubber sheets, vulcanised together to form an open ended cylinder. Both membranes are sealed at the bottom, around the top edge of the piston, by a steel ring and fixing bolts. The space between the base membrane and the top of the piston is filled with water, which is intended to ensure a uniform pressure distribution across the base of the sample and the top of the piston. It also allows the actual vertical pressure at the base of the sample to be measured without influence of piston friction . An even distribution of pressure across the top of the piston, when it is raised, helps to ensure that there is no tendency for the piston to tilt, and so jam its sides against the cylinder.

The lateral stress is changed by varying the pressure of the water contained in the lateral cell (an annular space enclosed by the chamber barrel inner-shell and the lateral flexible membrane) as in a conventional triaxial test. The change in cell pressure is produced by regulating the air pressure at the air/water interface of the lateral reservoir. Average lateral displacement is monitored by measuring the change in the volume of the lateral reservoir. This requires an equal fluid pressure in the cavity between the two shells of the chamber wall to that in the lateral cell so that the inner shell has no tendency to deform and change volume.

6.2.5. Top Platen

The top platen transfers the upward thrust of the piston via the sand to the lid. The top boundary of the sample is sealed around this platen. The seal is important as it prevents the sand becoming wet when the lateral cell of the chamber is filled with water. This seal is vital in the vertical loading phase. There are, in effect, 2 seals at the boundary around the platen in both original and new designs. A secondary seal is made by the strap clamping the membrane to the sides of platen (in the old design) or at the top rim of the external wall (in the new version). The membrane is mainly sealed against the underside of the lid under a vacuum drawn between the platen and the lid. Thus, the top platen forms a rigid boundary by being held flat against the lid through this suction.

6.2.6. Lid and Reaction Frame

The lid closes off the top of the chamber, sealing around the top edge of the chamber barrel on an O-ring. A steel boss with a central hole, through which the penetrometer is pushed, is attached at the centre of both the platen and the lid. Because the total vertical force provided by the piston may considerably exceed the weight of the soil, the chamber lid must also be restrained. The chamber structure does not have sufficient rigidity in itself for this purpose and the lid is, therefore, supported against a structural reaction frame anchored to the laboratory strong floor. The connection between the reaction frame and the lid is through a pair of hydraulic jacks fed from a hydraulic multiplier that automatically balances the force of the loading piston. This ensures that minimal displacement occurs at the top platen of the sample, and, under these conditions, the base transducer records the total axial compression of the sample.

The reaction frame also carries the hydraulic cylinder that is used to push the penetrometer into the chamber (its pump is flow-limited to give the standard penetration rate of 2 cm/sec). The driving ram is secured to the crosshead, and the penetrometer enters

the sample through a central hole in the lid. The frame itself is pivoted near its base to allow it to be swung down away from the top of the chamber. This is accomplished by another hydraulic cylinder (see Fig. 6.1) connected to the side of the frame. Lowering the frame allows the lid to be removed and the chamber filled or emptied of sand.

6.3. New Boundaries

The original chamber design only allowed control of the lateral and base stresses and average measurement of the normal components of surface strain through volume change of the water in both compartments. The operation of the chamber could only be done under constant volume or constant stress conditions. It is obvious that calibration chamber test results are affected by both the constant stress and the constant volume boundary conditions and by the chamber size. To minimise these effects, one is left with the options of either increasing the size of the chamber up to a point where such effects become minimal, or of modifying the chamber to simulate an ideal infinite boundary. The second choice would not only make more efficient use of the existing chamber but would hold out the prospect that - if the design were successful - future calibration chambers could be made smaller, cheaper, and thus more common!

However, the attempt to model more natural boundary behaviour is limited by two factors:

a) Unless a variable stiffness design can be implemented the boundary can only be designed for one soil stiffness.

b) A uniform stiffness boundary, even for sand deformation in its elastic range, does not model the response to arbitrary surface loadings of a cylindrical cavity in an infinite elastic medium: only a variable stiffness, locally controlled by a computer-based boundary element type of algorithm, could achieve such a response in a physical model. A uniform stiffness boundary is analogous to the Winkler stiffness often assumed in foundation

problems.

An original design that would have allowed for variable stiffness (though not under computer control) proved to be beyond the available financial resources and a basically constant stiffness design was adopted. Since the boundary stiffness would be most noticeable with a very dense sand, the required stiffness needed to be determined for Hokksund sand in this state under different consolidation stresses and histories (see Chapter 5). The modification of the calibration chamber for this purpose would mean that the boundaries would have to be designed in such a way that the imposed stresses from the soil would produce strains at this radius which would correspond to those that the same soil to infinity would undergo with the same stress at this radius. Since the strains required were greater than could be accommodated by a simple metal jacket it was necessary to use a compressible layer rather than a stretched hoop. Also, since the prime function of the chamber is to calibrate penetrometers as they travel down through the soil, the stiffness provision needed to be local so that it would be possible to have an approximate modelling of the variation of stress and displacement with depth at any stage in the process.

In the case of an expanding cylinder test (which is essentially 2-dimensional) an infinite boundary beyond the outer soil diameter may be simulated without the need to modify the present lateral boundary by increasing the boundary pressure to correspond to the required increase in radial stress.

The results of the expansion tests showed both from the initial tangent and, more clearly, from a small partial unload/reload loop in one of the tests that a stiffness of **1.0 bar/mm** could be specified for the NC 2 bar vertical stress sample and for an OC (4 bar rebounded to 1 bar vertical stress) sample of the same high density.

This stiffness was achieved by using strips of rubber, 6mm square and placed at 14 mm centres, which would distort in compression by an

applied normal stress. The boundary, so designed, allows for a working deflection of 3 mm, i.e. a strain of 0.5% on the 600 mm radius of the sample. These strips transfer to the inner wall of the chamber that part of the lateral stress on the soil which is not carried by the pressure of the lateral fluid. In so doing, the strips distort by extending sideways and compressing radially so that the rubber itself essentially deforms in shear without change of volume. During a normal penetration test the fluid pressure is held constant (or very nearly so) so that the stiffness experienced by the boundary is that of the rubber strips alone. Though based on theoretical curves for such distortion, the resulting stiffness was checked by the experimental compression of a 150 mm square plate prepared with the strips of the chosen rubber. Plates 6.1 to 6.3 and Figs. 6.2 to 6.3 show the new boundary set up.

The top and bottom boundaries of the soil should also exhibit stiffness properties. For this stiffness to be approximately modelled, the uniform pressure bag at the base had to be replaced. The required stiffness could be estimated based on the confined vertical and the lateral shear moduli. However, the value so obtained is somewhat higher than that found for lateral expansion and, for convenience, the same rubber strip spacing (and therefore the same stiffness) has been used as on the lateral wall.

The base strips were placed circumferentially on a 6mm circular hard rubber mat grouped to form four semi-circular annuli which were enclosed by continuous strips around the edges to form pockets (Plate 6.1a). Later in the process, the base annuli were changed to form five full circular pockets. The connection to each annulus is made through the piston cylinder and out of the base plate (Plate 6.1b). The annuli are then connected to external volume/pressure measuring vessels via separate pressure gauges. This makes it possible not only to control the pressure in the fluid but, by weighing, to determine the volume change of each pocket and the average of the base separately during the test. To do this, each pressure vessel was suspended from a small strain gauged cantilever (Plate 6.2). Each vessel was designed with its

own air supply valve at the top in order to be able to control the pressure in individual pockets separately and, hence, seal each one with a known quantity of air, if required, so that the fluid exhibits 'stiffness' - an increase in pressure with fluid expelled. This was not implemented for the current experiments (and some thought would be required to ensure sufficient linearity over the pressure range required). However, the concept is one method by which the stiffness of the ends might be increased if that were thought necessary.

The top boundary pockets were arranged as for the base with four semi-circular annuli with the outlets designed to exit through the central boss of the platen. These pockets were not utilised for volume and pressure control during the penetration testing though the stiffness of the rubber strips was utilised. The top rubber strip mat was not used in the expansion tests which required plane strain. (The rubber strips in the base were active during the expansion test but under constant volume control so that the radial distribution of pressure could be monitored. The constant volume constraint allowed plane strain to be properly modelled.)

The lateral boundary rubber strips are arranged vertically on the inner shell wall for two reasons. The first is to facilitate the deairing process in the lateral space; the second to provide a measure of vertical shear stiffness at the boundary (not possible with a simple pressure membrane). The order of this shear stiffness is that of the radial stiffness, but no attempt has been made to predict the required stiffness from elastic moduli, nor to devise a means for its experimental determination, though the shear stress itself was monitored. Plate 6.3 shows the arrangements on the lateral wall.

Since the rubber bag that contains the soil is only 1.5mm thick, it was necessary to use a thicker rubber in order to distribute the load evenly onto the strips. The space between the inner shell and the bag containing the soil allowed a 19mm thick Neoprene rubber curtain to be used. It was bolted in three parts to the top rim of the chamber and

was allowed to hang under its own weight. This curtain would transmit axial and radial stresses from the soil to the inner shell through the rubber strips, though the high vertical stiffness of the curtain reduced its effectiveness for monitoring the rate of change of axial stress which would otherwise have given a good indication of the rz shear transmitted.

The same curtain material was used in the form of a circular mat at the bottom and the top. The rubber strips at the top were fixed onto this thick mat. The bottom mat, however, was placed loosely on top of the mat of rubber strips. To protect the main 1.5 mm rubber bag, a second bag of similar thickness was placed inside the chamber and designed to cover the base mat as well. Fig. 6.2 shows the arrangements at the base and at the lower end of the lateral wall.

During early penetration tests, the soil level at the top was 25 mm lower than before to allow for the extra thickness of the rubber-strips. In this way, the lateral membrane could be placed over the top of the platen, as originally set up, with the lateral fluid being flushed through ports in the lid. To facilitate the assembly at the top and the lateral filling process, it was decided to fix the mat directly to the top platen with a permanent metal ring around the edge, as shown in Fig. 6.3. Also a circular metal plate was bolted to the central boss. This latter would ensure that channels provided from the individual top annuli were sealed, and hence guided to the outlet holes provided through the central boss. The platen was suspended from the top lid with bolts through the top and a central clamping bush that was screwed externally to the boss at the centre. The gap between the platen edge and the inside of the lid was filled with a lean-mix concrete and an extra 6 mm rubber mat fixed around the top rubber mat to fill the space between the central plate and the outer ring. This also required an extra annulus of 6 mm rubber to be glued to the already overhanging rubber shoulder to eliminate any gap between the soil and lid after assembly.

This allowed the lateral double membrane containing the soil to be folded over the barrel rim and clamped permanently (as used to be done temporarily during pluviation). The lateral fluid would then be flushed through the top valve provided on the rim. This is discussed in detail in Section 6.7.1.

6.4. Instrumentation

All the function of the original instrumentation has been retained and can be recorded on a data logger. This includes control and monitoring of lateral and vertical fluid pressures on the sample and any accompanying volume change, control of the fluid pressure between the two chamber walls (referred to as the cavity cell),measurement of the piston movement and also, of course, the cone and sleeve stresses together with the vertical displacement of the penetrometer.

New instrumentation includes the strain gauging of the inner wall of the chamber. A knowledge of the stress distribution in the inner shell of the calibration chamber provides not only the boundary stress variation in the soil mass but also (via a separate calibration test for the rubber strip stiffness) the actual local deformation of the soil as a function of height. To achieve this, the strain gauges were placed both horizontally and vertically in four different columns (90 degrees from one another). Each column consists of 11 strain gauges: 6 vertical gauges and 5 horizontal. The chamber wall was subdivided (for instrumentation purposes) into 5 horizontal bands each of 25 cm height to leave about 12 cm at the top and bottom of the wall uninstrumented. Hence, each band has a centrally placed circumferential gauge at each of the four columns to determine the cavity strain of each band, and a vertical strain gauge is placed at similar intervals between the bands (and at the top and bottom of the extreme bands) to determine the vertical strain (the mean of two edge values for each band) both so that the Poisson's ratio effect could be allowed for in the stress calculation and, it was hoped, to provide information on the change of vertical stress across any band and thus the shear load transmitted to the band. (It is now thought that the latter function has little value

as much of the shear load from the sample is transmitted through the thick rubber curtain directly to the top of the chamber from which it is supported). For cone penetration testing purposes, where there exists a radial symmetry, one column of gauges would, theoretically, have been sufficient. Having four columns not only gives additional confidence in the experimental measurements but also enables any circumferential variation of data to be monitored for asymmetric devices such as the Marchetti Dilatometer and to illuminate any horizontal variation in stress or strain (due to soil non-uniformity) that might be present. The gauges are individually four-wire connected to the data logger using a 1/4 (quarter) bridge variation which eliminates lead errors and allows any one gauge to be ignored if its performance proves to be faulty. Plate 6.4 also shows the set of strain gauges set up at each column. Strain gauge bonding to the chamber inner surface required special surface preparation and treatment prior to bonding and the sealing needed to be both waterproof and to provide protection from any possible damage. The complete process is discussed in Appendix IV.

In the analysis of the CPT results, the radial transfer of load (by shear) between one band and its neighbour has been ignored as compared with the load carried by circumferential tension within the band.

The base pockets were connected to their individual pressure gauges and volume change measuring vessels, which were suspended from strain-gauged cantilevers. During an expansion test, the pockets would be connected only to the pressure gauges to monitor the pressure distribution across the base of the sample. During a cone penetration test, on the other hand, the base pockets and their vessels were connected to a common air pressure, measured by an air pressure gauge and a pressure transducer.

Since the volume change in the cavity cell involved for either of the expansion or the penetration tests was small, a smaller vessel, similar to those used for the pockets, was utilized and was also

suspended from a strain-gauged cantilever. To enable more direct comparison with the lateral cell the water pressure gauges chosen were identical of 0.005 bar sensitivity for the two cells. In addition both cells had electrical pressure transducers for data logging.

The lateral cell was connected to a larger vessel (a triaxial cell used for the 100 mm in diameter samples) to allow larger volume change control. During an expansion test, which did not require continuous measurements as compared to a penetration test, the vessel was weighed on a balance with an accuracy of 1 gram. In the original design, a larger air-water reservoir was used for this purpose which was suspended from a load transducer. This reservoir, in the new design, was used to supply water to the piston compartment. During the current penetration tests, however, the lateral cell vessel was suspended for weight change measurements. The expansion cylinder middle and end sections (with their common air pressure regulator and pressure gauge) were connected to similar cells, of which only the one for the middle section was weighed.

All the strain, deflection and pressure sensors were monitored both during the K_o preparation of the soil to the required stress state and (at 5 cm, 2.5 second intervals) during penetration insertion. They were also monitored for a short time afterwards as the stresses were relaxing.

6.5. Data Acquisition System

The outputs of the various strain gauges, displacement and pressure transducers were passed to a standard 'Orion' data-logger belonging to the Civil Engineering Department at the university and were either printed out directly (during the stress application stage when increments of stress were normally at about 1 minute intervals), or temporarily recorded on internal magnetic tape (during the fast acquisition stage of penetrometer insertion) before subsequent print-out at the end of the test.

6.6. The Cone Penetrometer

The standard 10 cm^2 electrical friction cone penetrometer was used in the CP series. This cone is normally attached to a rod of the same diameter and, thus, does not provide any relief of diameter behind the tip. A full description of this penetrometer and the smaller version (5 cm^2) can be seen in Last's report (1979). The main advantage that this cone offers is the ability to give a continuous measurement of the stresses at the tip of the cone and the sleeve behind it during use. The reference procedure for use of the cone can be found in ISOPT-1 (1988) and ISOCCT-1 (1991).

6.7. Operation of the Chamber

The procedure for conducting a test in the chamber involves three major steps. These are:

1. Forming the sand sample.

2. Applying stresses to the sample.

3. Expansion or penetration of the sample.

Prior to the first stage, it was necessary to saturate the base pockets by siphoning the water through the central valve on the base membrane. Some water will be pushed out during sand filling as the connection between the pockets and the individual weighing vessels are left open both at this stage and during subsequent loading up to 1 bar vertical pressure to ensure a good seal at the edges of the pockets. After the first test, however, the process of adding or removing water from these pockets would be different, since they needed saturating only once. At the end of a test, the pockets would remain open during the sand removal stage until the chamber was half emptied. This balanced out the pressure from the half full chamber with the head difference between the base pockets and their corresponding cells. They would then be closed and remain so until the sand filling for the next

test reached about mid-height. This restriction was to prevent the pocket cells becoming empty as a result of the hyro-static head difference.

6.7.1. Forming the sand sample

Prior to the modification, the lateral membrane was supported, by using a sample former - an open ended perforated metal cylinder - during sample formation to form a cylindrical sample. This former was lowered into the chamber before sample formation and was pulled out after the top platen was placed on the sand and the lateral space filled with water. After modification, however, the thick rubber curtain provided a permanent former for the lateral membrane and eliminated the danger of damage to this membrane during removal of the former. During the sample formation, a small vacuum was applied to the lateral cell to hold the lateral membrane and thick curtain firmly against the rubber strips.

Sample formation is achieved by a technique known as pluvial compaction. The sand is rained from an overhead storage device to form a simulated in-situ deposit. The device, which fits directly into the top of the calibration chamber, allows the sand to rain continuously over the whole area of the chamber (see Fig. 6.4). The sand is stored in an overhead cylindrical hopper. At the base of the hopper there are two shutter plates through which the sand will pour if the holes in the plates are correctly aligned. The second shutter plate can be exchanged with other plates which have holes of a different size. This changes the intensity of flow from the hopper and in this way the density of the resulting sample can be varied. The lower plate is moved horizontally under the action of an air cylinder. This movement will either stop or start the sand rain, depending upon the relative positions of the holes in the two plates.

The sand falls a minimum distance of 75 cm from the shutter plates in a series of well defined jets. The sand then passes through a diffuser which disperses the jets into a fine rain. The diffuser

consists of two circular screens of fine rectangular mesh which are separated by a distance of 20 cm and which are cross orientated through 45° in order to maximize the dispersive effect. The diffuser itself is maintained above the rising surface of the sand deposit by a system of lifting wires which are commonly linked to an air cylinder. This air cylinder is then used to raise the diffuser in a series of steps so that the distance between the diffuser and the deposited sand is always between 20 and 40 cm. Under these conditions Jacobsen (1976) found that the density of a 1.0 m high sand deposit varied by less than 1 % from top to bottom.

The sand jets can be viewed through the perspex wall of the spreader and occasionally the holes in the shutter plates have to be cleared because of the blockages. For this reason one section of the perspex is in fact hinged to form a door. A small extractor vaccum is applied to the space below the shutter plates to minimize the dust hazard.

Once the chamber has been slightly overfilled the sand rain is halted and the sand spreader removed using an overhead crane. The exposed sand surface is screeded across the top of the chamber down to a depth of about 25 mm below the rim.

In the old preparation procedure, once the sand surface was prepared, the top platen was lowered onto the sand surface. The side membranes would seal around the top platen after which water would be allowed to enter the chamber before removal of the former. In the new set up, the lateral cell filling can commence before the composite lid (including the top platen) is lowered onto the sand surface.

Lateral Cell Filling Procedure

In this arrangement, the main water supply feeds water into an auxilliary supply tank located 60 cm above the chamber, which has separate connections to the chamber lateral cell and to a lateral air/water reservoir located at mid-chamber height (referred to as the

lateral cell and the lateral tank, respectively). The water in this supply tank can be partially de-aired under a vacuum before being used to fill and de-air any cell or connection line. The only outlet from the lateral cell, apart from the supply and cell-to-gauge lines at the base, is from the the top of the chamber barrel directly below the welded rim to the lateral tank. A horizontal channel has been provided on the rubber strips directly below the rim to ensure that water runs from each channel between the vertically oriented rubber strips via this channel to the lateral outlet. The lateral cell is de-aired by circulated de-aired water from the supply tank upwards through the cell to the lateral tank under a partial vacuum.

The cavity cell is filled in the same manner as the lateral cell.

6.7.2. Stressing the Sample

In preparation for loading, the loading frame is raised and the reaction jacks are connected and pumped up slightly. Once it is certain that all the lines are saturated, a complete scan of the required data is made.

For all tests the initial stressing of the sample was made under K_o conditions - that is, the lateral dimension of the sample was not allowed to change during the compaction or overconsolidation stage of the stress application. Hence, the pressures in the lateral and cavity cells are balanced up to keep the inner-shell undeformed. Since there could be no change in the volume of the lateral cell, there would be no change in stress in the rubber strips. Under these conditions, the diameter of the sample should theoretically remain constant and the fluid pressure in the lateral cell would represent that required to sustain this state.

To begin the K_o consolidation, the vertical pressure is increased in small increments (0.25 bar below 2 bar and 0.33 bar above 2 bar) by regulating the air supply to the top of the piston air/water reservoir. A pressure transducer and a pressure gauge are used to monitor the

hydraulic piston pressure. As the vertical pressure increases, the sand tries to expand in the lateral direction. This increase in volume is resisted, by the inner shell and results in a rise in lateral pressure which then requires an increase in the pressure of the cavity cell (by forcing water into it until the two pressure are once again balanced. The force applied to the lid by the reaction jacks is automatically increased by the pneumatic multiplier operating from the piston pressure. When equilibrium has been obtained after each increment of vertical stress, a complete scan of the data is made.

For normally consolidated (NC) samples the loading is monotonic up to the desired vertical stress level. For overconsolidated (OC) samples the vertical stress is increased up to a predetermined value and then relaxed down to the desired test level, the condition of zero lateral volume change being maintained throughout.

The base rubber strips have been designed at a 1.0 bar/mm stiffness up to 2.0 bar of pressure during calibration. The pockets are all opened to atmospheric pressure up to a vertical pressure of 1.0 bar so that the rubber strips carry this stress. Above this pressure, the pocket connections are closed and any increase in vertical piston pressure is matched by the same increase of pressure in the pockets. The piston and base pocket pressures together with the lateral and cavity pressures are constantly monitored on the data-logger screen so that very sensitive adjustments are possible during the consolidation phase.

The top pockets (now part of the lid system) are, on the other hand, open to atmosphere during the entire consolidation phase and the whole vertical pressure is carried by the rubber strips. (The top pockets are removed for the expansion tests).

Once the desired stress level has been reached, the main water supply to the piston from the piston air/water reservoir is closed off. The second connection from the piston to the pressure transducer and gauge remains open at all times. The lateral pressure tank is, then,

brought up to the same pressure as in the lateral cell before connection between the two is made (through the bottom outlet). This can be checked by monitoring any weight change in the lateral tank, under suspension, and allowing it to stabilise.

As mentioned earlier, all strain gauges, etc., were datalogged at the completion of each step. At completion of loading an interval of about 15 minutes would normally occur before the start of the penetration test itself.

6.7.3. Cone Penetration

The sand is now prepared for penetration. The calibration of the penetrometer is checked. The data-logger is set to scan a complete set of data at 5 cm (actually 2.5 seconds) intervals - with a standard penetration rate of 2 cm/sec, controlled by a hydraulic flow valve on the pump. The penetrometer is then positioned in the loading frame with the push rod attached to the hydraulic cylinder and the cone tip placed on the sand surface in the central hole of the lid. The penetration is stopped at about 125 cm when the limit of the hydraulic piston is reached. The data-logger was normally left running for a further 40 seconds to obtain data on any subsequent stress relaxation that might occur in the cone and sleeve readings and in the boundary stresses.

Unlike the traditional tests with this aparatus, there are no options for the boundary conditions during penetration. Whereas the earlier tests would normally include both BC1 and BC3 lateral boundary conditions in the testing programme so that the perceived limits of boundary effects would be covered, the new tests have been designed so that each test should - as closely as possible - experience the actual local stiffness expected in the field. This new design relies on the lateral fluid remaining at constant pressure (the change in volume being monitored) whilst any local expansion of the soil sample would result in compression of the rubber strips and inferred from the circumferential stress in the inner-shell since the latter gives the change in local boundary stress and, by calibration, the local boundary

strain.

The base piston of the chamber was held at constant height during penetration (made possible by using water rather than air beneath the piston) and, as with the lateral boundaries, both base and top of the soil sample relied on the stiffness properties built in to the rubber strip construction at these surfaces.

Once penetration had been completed, the penetrometer would be withdrawn from the chamber and the chamber would then be ready for dismantling and sand removal.

6.7.4. Removal of Sand

After completion of the penetration process, the sample is unloaded slowly and the water in the lateral cell emptied out. The loading frame is lowered back and the chamber lid removed.

During penetration some particle crushing occurs in the high stressed area around the penetrometer tip. In order to re-use the sand and to maintain constant soil properties every effort is made to remove all the crushed sand. This is achieved by pushing a hollow metal cylinder (normally 4 to 6 inches in diameter) down the axis of the chamber in the path of the penetrometer and the sand entering at the base essentially vacuumed out of the free end. The remaining sand in the chamber is then removed manually by shovelling it into a self emptying bucket and before storing in a large cylindrical hopper that is fixed permanently on top of the pluviation chamber. After each bucket filling, it is weighed using a load cell that is suspended from the over-head crane. The total weight of the removed sand then determines its relative density.

6.8. Basic Properties of Hokksund Sand

Hokksund sand is an angular fluvio-glacial deposit found in the Drummen river valley near Oslo, Norway. The mineralogical composition

of the sand was determined by X-ray diffraction (Quartz 35%, Felspar 45%, Mica 10%, Amphibole 5%, and another 5% of unidentified ingredients). A standard sieve analysis of the sand shows that it is a uniform, medium sized sand which contains negligible fines. Its high percentage of feldspar, known to be generally softer than quartz, may lead to reduced hardness and perhaps an increase in the mineral friction angle (Lee, 1966).

The calculation of the relative density relies on a knowledge of the maximum and minimum void ratios (e_{max} and e_{min}) of the sand. These are obtained by measuring the maximum and minimum densities experimentally, but there is no accepted standard for this determination. Several procedures have been used to determine these values. These include the Proctor standard, dry tilting, and wet and dry pouring and tamping.The maximum and minimum void ratios for this test series were obtained by dry pouring through a funnel and wet tamping in layers, respectively.

The specific gravity of the sand grains was determined by means of a pycnometer giving an average value of 2.70.

WHEN	WHERE	SIZE
1969	ORIGINAL CRB MELBOURNE	H = 0.91 m D = 0.76 m
1971	UNIV. OF FLORIDA GAINESVILLE	H = 1.22 m D = 1.22 m
1973	MONASH UNIVERSITY MELBOURNE	H = 1.82 m D = 1.22 m
1976	N.G.I. OSLO U. SOUTHAMPTON 1980	H = 1.50 m D = 1.22 m
1978	ENEL - CRIS MILAN	H = 1.50 m D = 1.22 m
1981	ISMES BERGAMO	H = 1.50 m D = 1.22 m

Table 6.1. Summary of CRB (Vic. Road) type chambers (Holden, 1991)

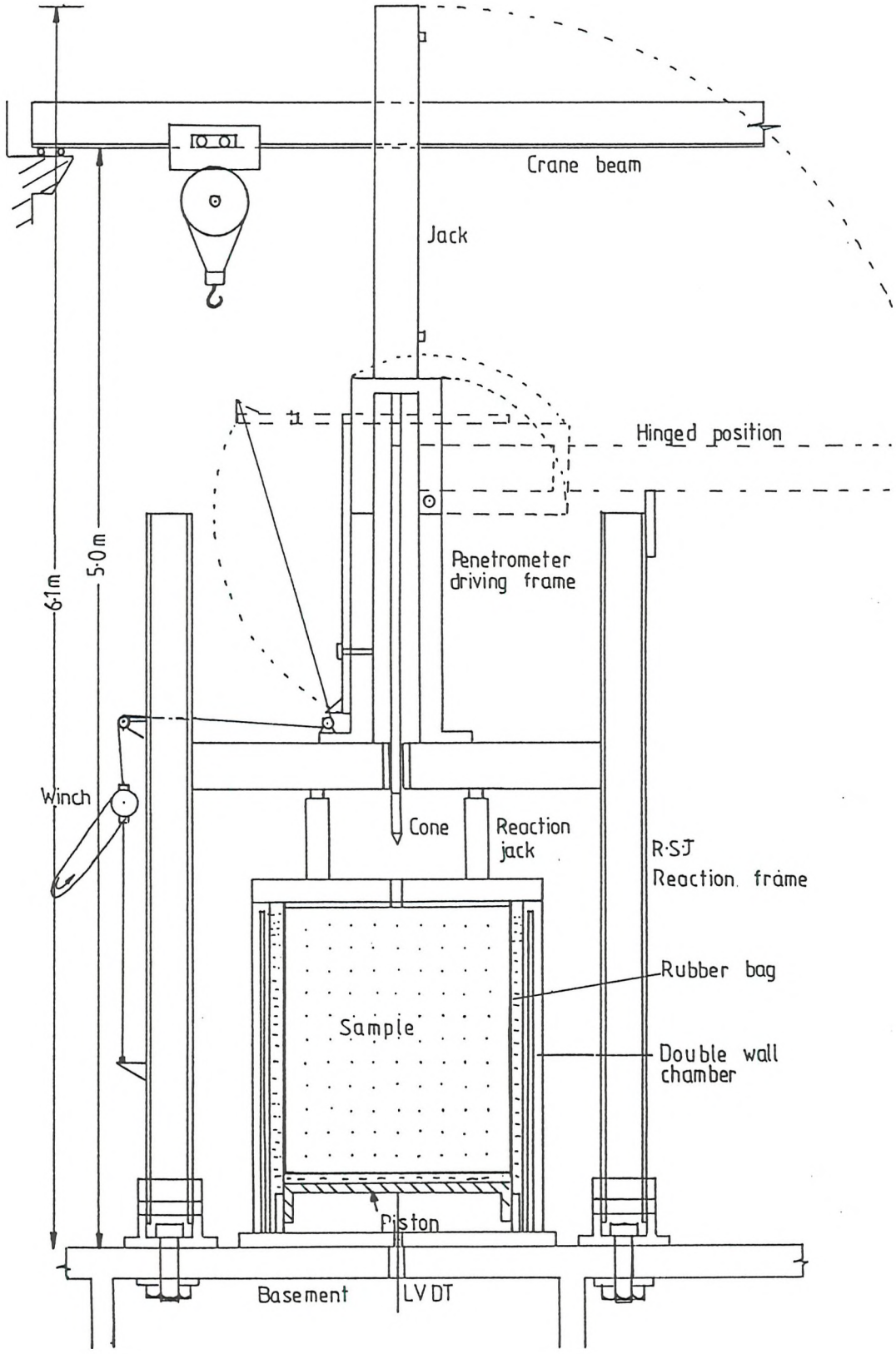

Fig. 6.1 Overall view of the calibration chamber

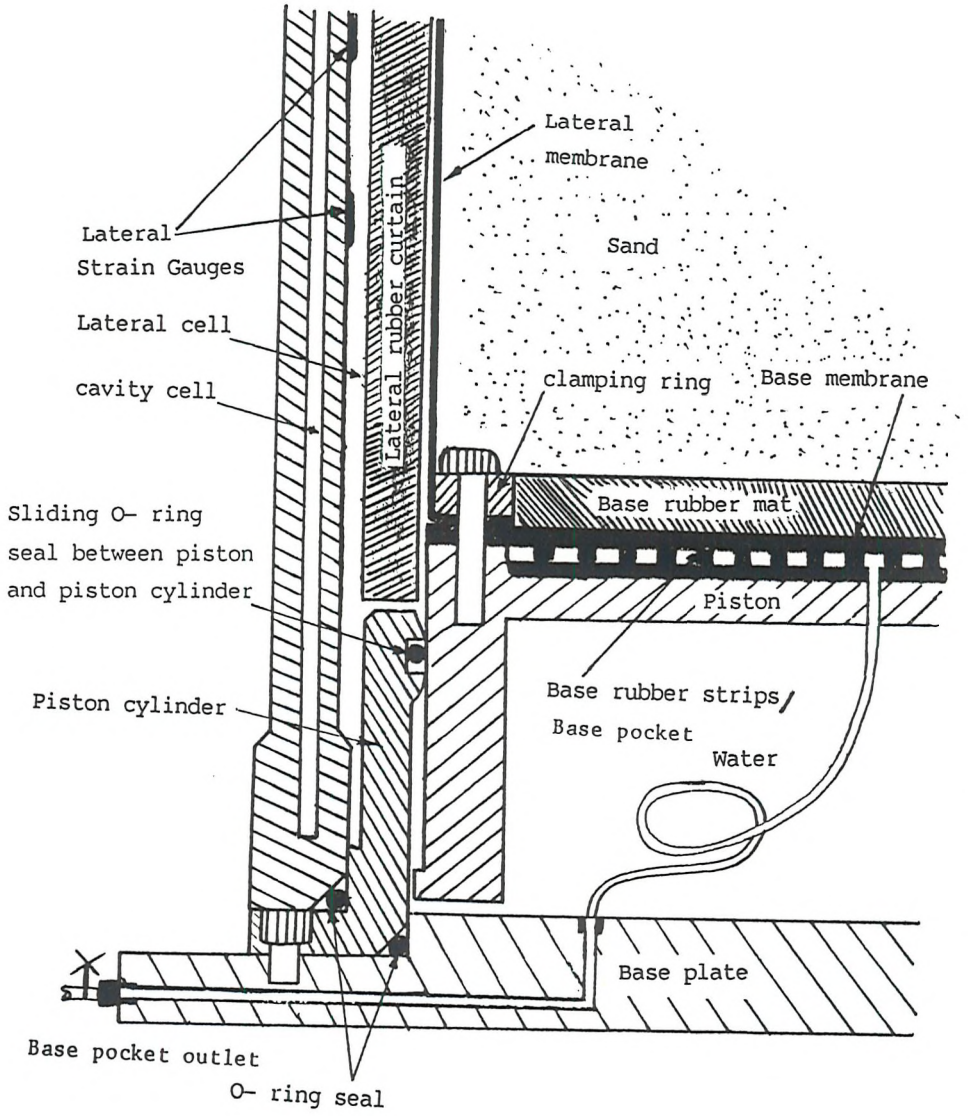

Fig. 6.2 Details of the chamber at the base and at the lower end of the lateral wall

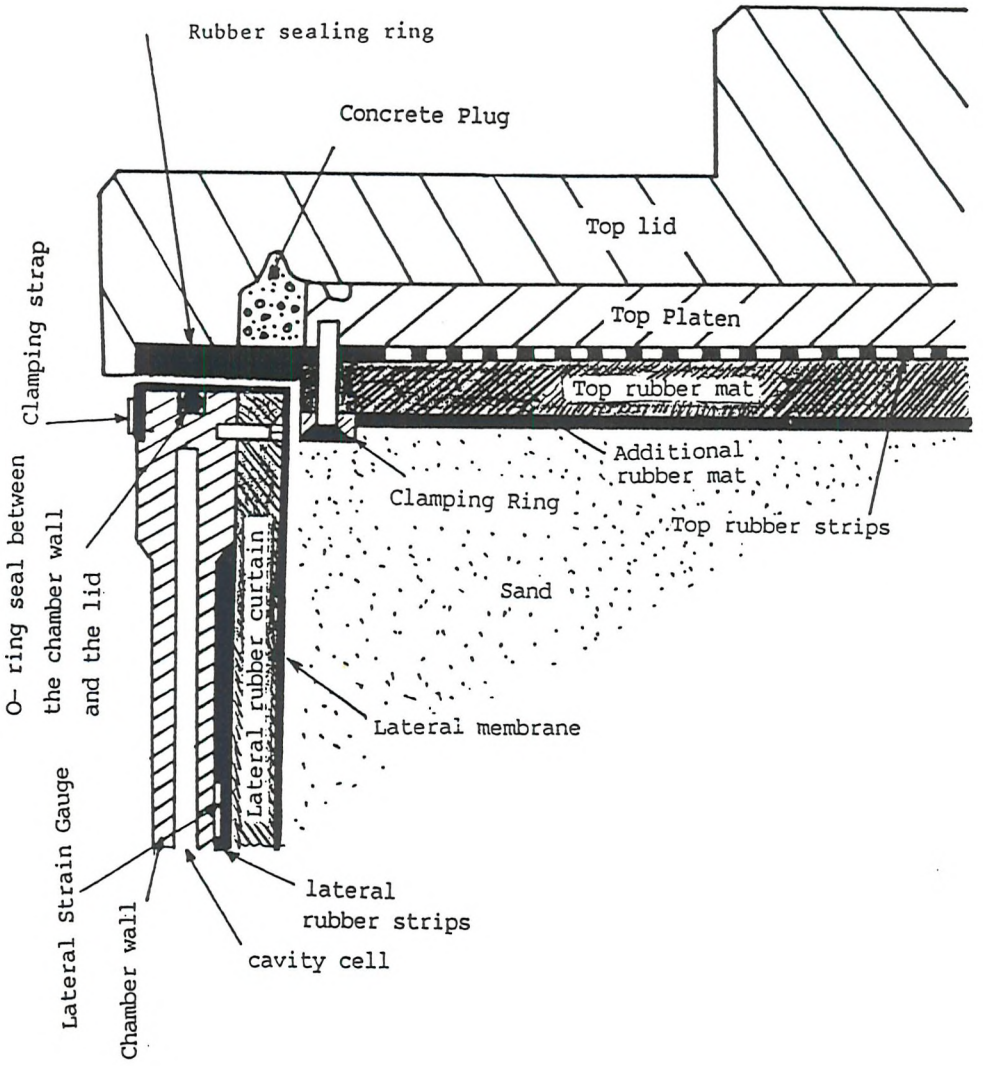

Fig. 6.3 Details of the chamber at the top

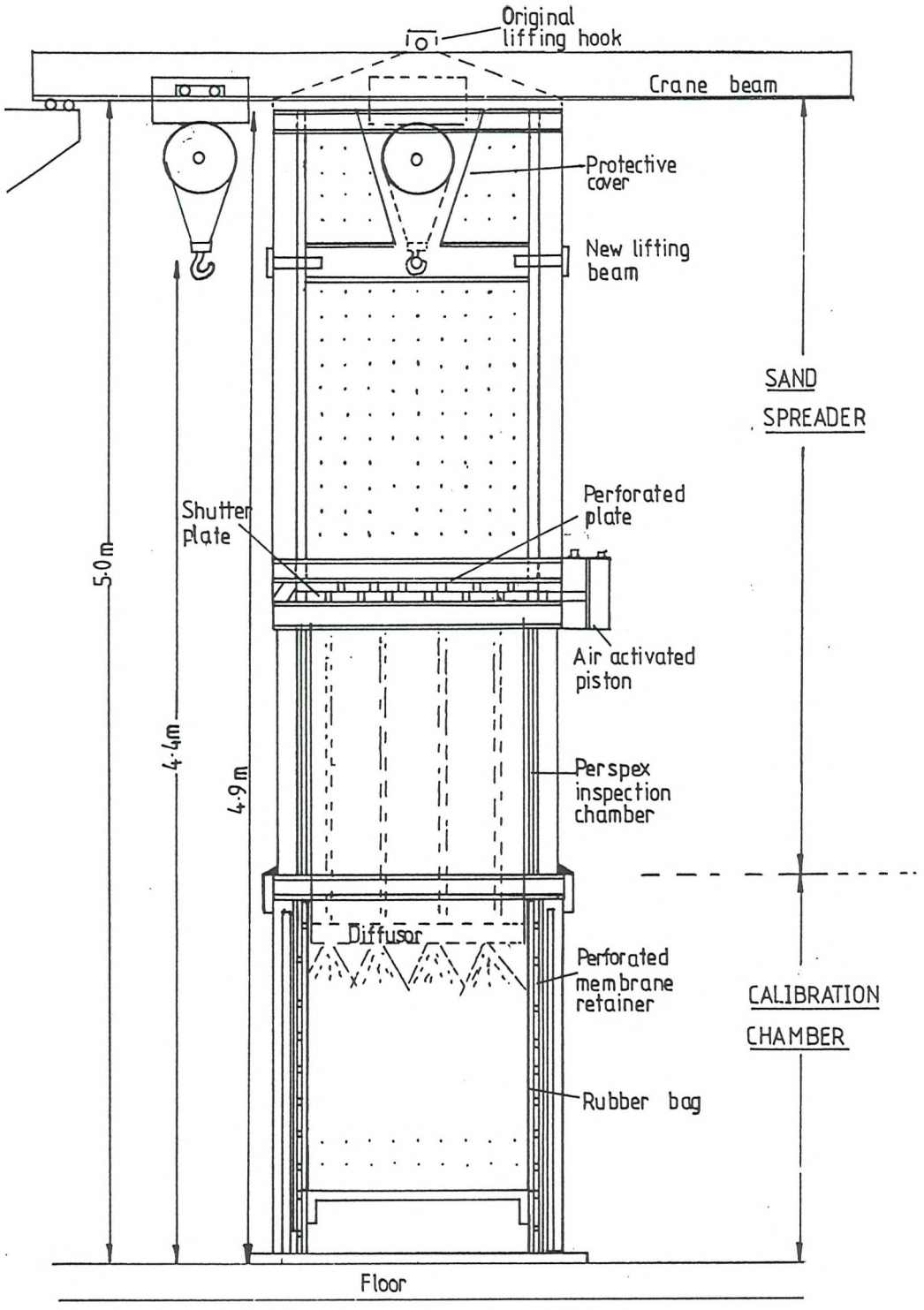

Fig. 6.4 Sand spreader in position

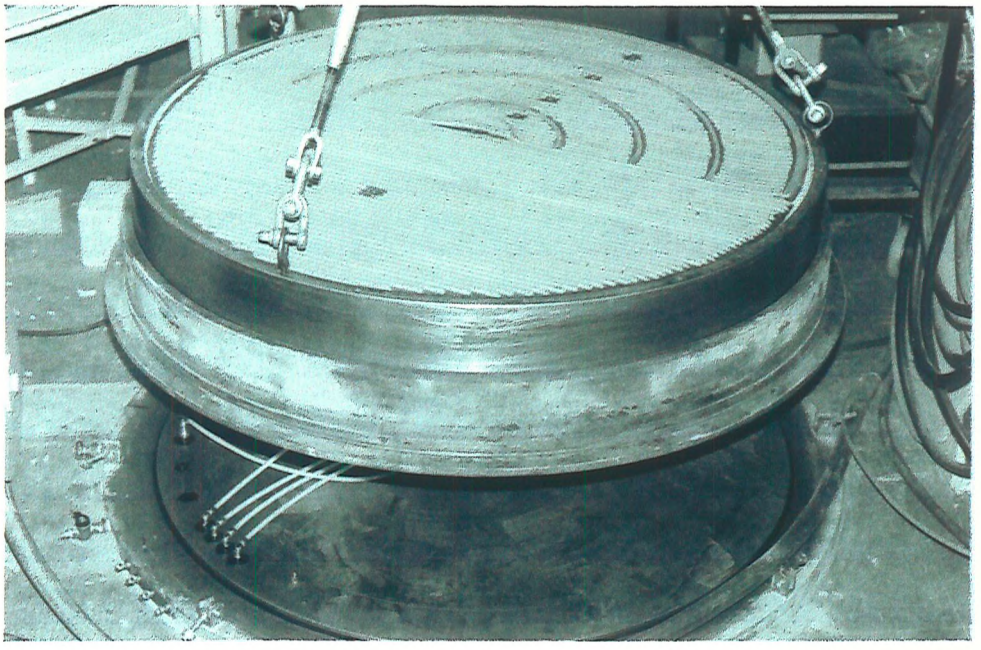

(a)

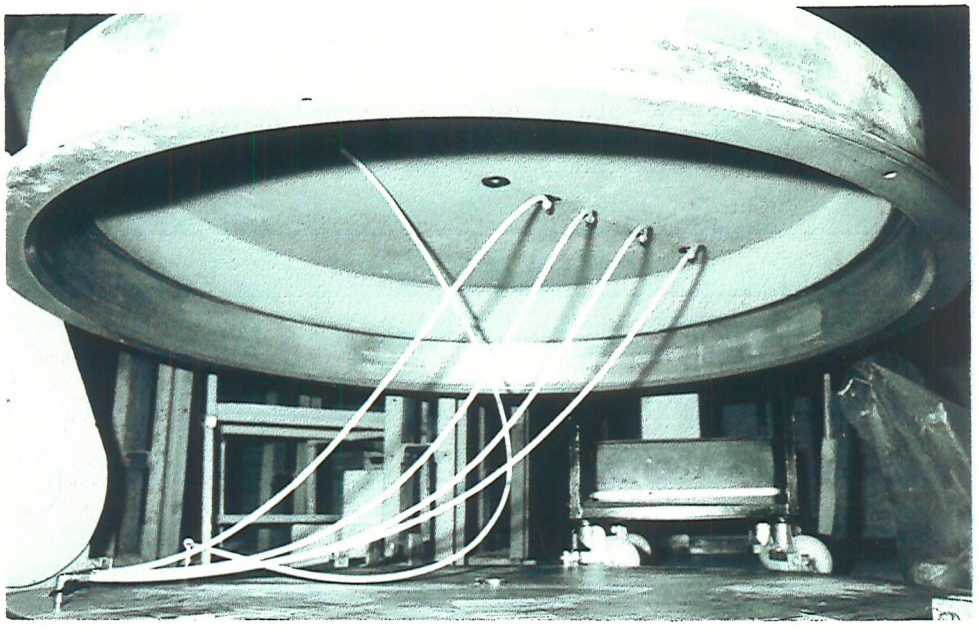

(b)

Plate 6.1 (a) Base semi-annular pockets; and (b) details of their connections under the piston

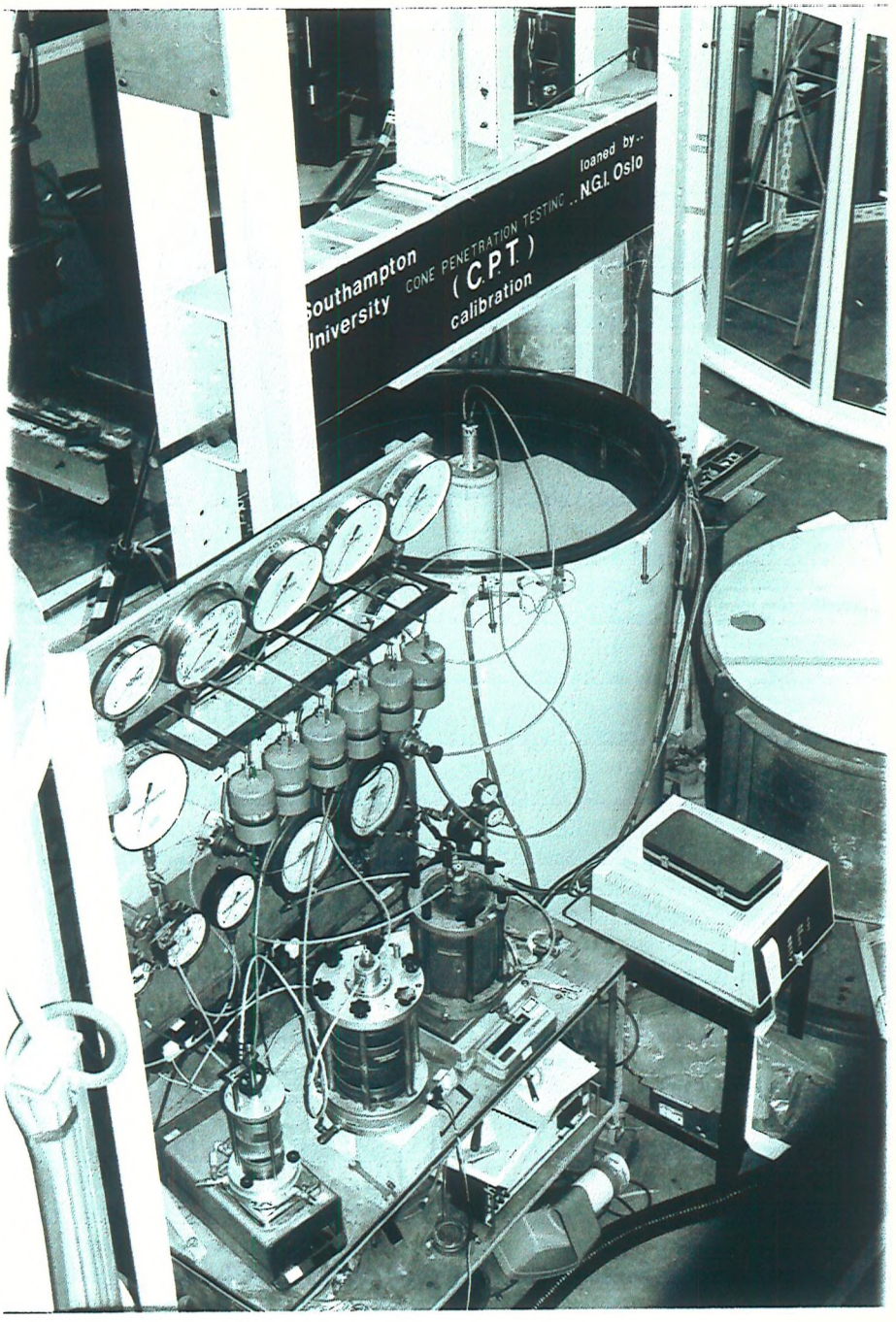

Plate 6.2 Expanding cylinder test layout showing the suspended pressure vessels and partially filled chamber

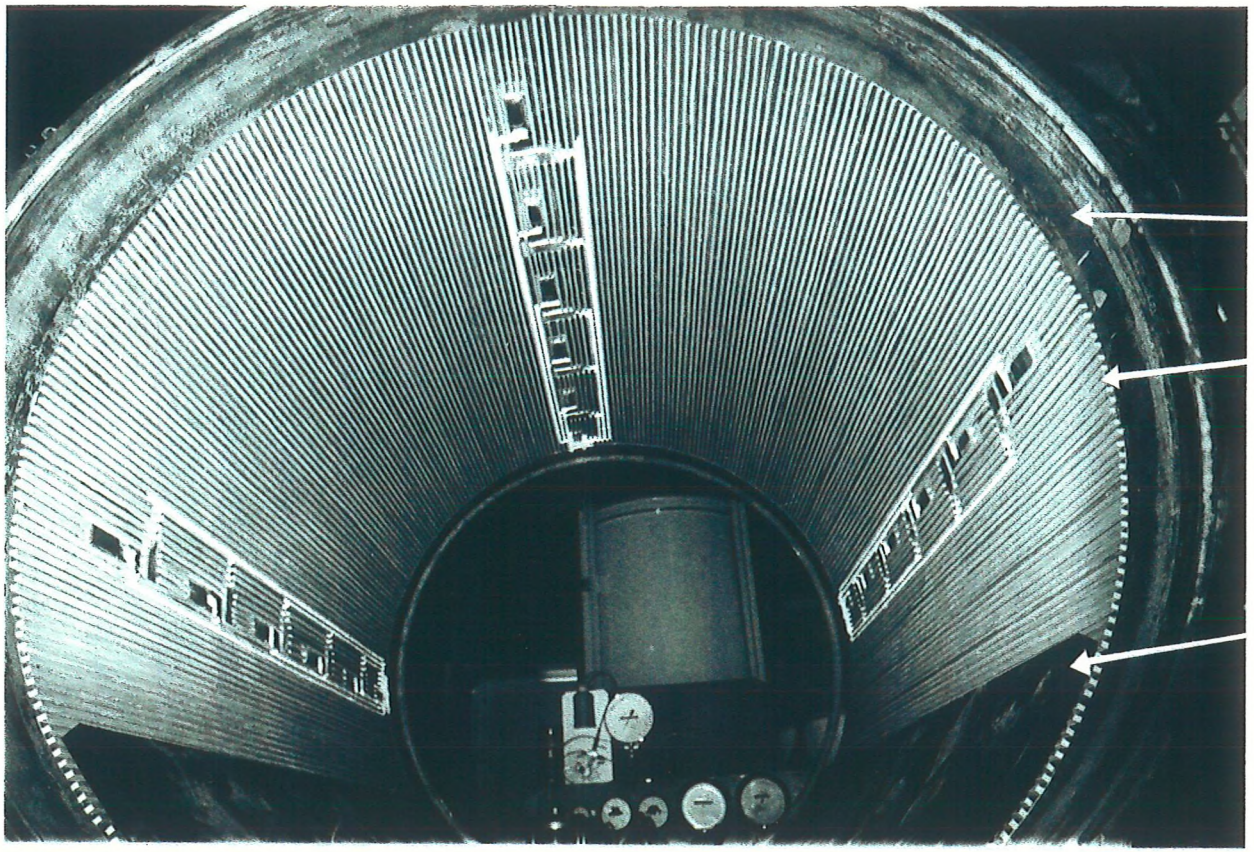

Plate 6.3 The arrangement of rubber strips and thick mat with columns of strain gauges

CHAPTER 7

CONE PENETRATION TEST SERIES

7.1. Introduction

The series of full length expanding cylinder tests performed in the calibration chamber revealed useful information regarding different boundary conditions and the response of the boundary stiffness under different situations. Since the penetration testing can only be performed under a constant lateral stiffness, as obtained by the rubber strips running longitudinally along the depth of the inner-shell, one is left with the option of using the rubber strips stiffness as a close approximation to the true field conditions. This means that, at the end of the consolidation stage, before penetration begins, the lateral cell is opened to the lateral reservoir which has a pressure controlled regulator. Since the cavity cell is maintained at the same pressure as the lateral cell during the entire K_o stage, the inner shell remains undeformed. Any further increase in the lateral stress of the soil during penetration is taken locally by the rubber strips and shown in the changes registered by the circumferential and the vertical strain gauges. This load in the rubber strips will cause the inner shell to deform slightly (too quickly to allow pressure balancing with the cavity which remains under constant - air regulated - pressure). Any slight increase in the lateral fluid pressure (as was noticed once a pressure transducer was introduced and the pressure was able to be more accurately measured) will have been due to restrictions in the flow of fluid from the lateral cell to the lateral reservoir.

The expansion tests indicated that the ideal stress level for dense normally consolidated samples needed to be about 2.0 bars vertically in order to allow the stiffness properties of the rubber to simulate an infinite boundary chamber. The dense over-consolidated samples, on the other hand, would have to be consolidated under K_o

conditions up to a vertical stress of about 4.0 bars and then unloaded (relaxed) to a vertical pressure of 1.0 bar, thus producing an OCR = 4. It happens that both the respective NC and the OC conditions resulted in the same horizontal stress of about 0.5 bar.

The tests discussed in this chapter were performed on both medium-dense (D_r = 60 to 70%) and dense to very dense (D_r = 85 to 100%) samples of dry Hokksund sand under the aforementioned stress conditions. For comparison purposes, some additional tests were performed under different stress levels and stress histories. A schematic diagram of the cone penetration layout is shown in Fig. 7.1.

One of the primary interests in running these CPT's was to obtain some information on the stress distribution both in the lateral and bottom boundaries. Hence, some of the tests needed to be performed at a modified speed. Due to the limitations on the data logging system, which was later resolved, it was decided to maintain the standard 2 cm/sec penetration speed but with a one minute halt after every 2.5 seconds (about 5 cm of penetration). This allowed a complete scan to be made of all the data after stabilisation. Later tests allowed the data to be stored on a magnetic tape without halts. These were then printed out after the completion of the test.

7.2. Test Results

The test results are summarized in Table 7.1 for a total of 17 cone penetration results under different stresses and histories. References will also be made to some relevant tests from the earlier, SU, tests at Southampton University which had B1 and B3 boundary conditions [see Tables 3.1 and 3.2]. Columns (2) to (8) of Table 7.1 relate to the state of the sand after pluviation and during the subsequent stressing; whilst the remaining columns summarize the penetration results. Detailed plots for individual tests are given in Figs. 7.2 to 7.18 for K_o and ε_v versus vertical stress, and in Figs. 7.19 to 7.28 for q_c and f_s as a function of depth of penetration. Figs. 7.29 to 7.44 give the boundary stresses down the side of the chamber

and across its base at 25 cm intervals of penetration for each test.

As was mentioned in the last section, the lateral pressures in the penetration stage of the tests were found to be somewhat higher than intended because the lateral fluid was not escaping freely. This was detected after a pressure transducer had been installed in the line from the chamber to the pressure gauge. One method for correcting these tests is to assume that this excess pressure is equivalent to a slight overconsolidation of the already NC sample. Hence, the q_c and f_s values in Cols. 9 and 12 have been corrected by using the Bellotti et al. (1985) relationship for over-consolidated Hokksund sand in which the q_c value (for a constant D_r) is found to vary with the 0.573 power of the mean stress. The analysis of earlier SU tests under BC1 and BC3 indicates that cone resistance and sleeve friction have approximately constant proportionality (q_c = 250 times f_s). This reasoning is used to apply the same correction factor for sleeve friction, as well. The correction factor used for q_c and f_s in each test is given in column (13) and the reverse process would give the actual measured values. The drainage condition for the lateral fluid was improved (following test CP13) by fixing a second drainage outlet from the chamber to the lateral reservoir.

The testing programme comprised two sets: one for very dense sand with OCR values of 1, 4, 8, and 16 relative to a maximum past vertical pressure of 4 kg/cm^2, and the other for medium-dense sand with OCR values of 1, 4, and 16 relative to the same maximum past pressure. Since the boundary stiffness was designed for a dense NC sample to be tested at a vertical pressure of 2.0 kg/cm^2 and for a dense OC sample to be tested at a σ'_v = 1.0 kg/cm^2, the designed stiffness for the NC samples of very dense sand at a σ'_v = 4.0 kg/cm^2 was slightly low, whilst that for the medium dense samples was rather high.

As was mentioned earlier, during the K_o consolidation phase the fluid pressures in the cavity and lateral cells were kept equal to prevent the inner shell of the chamber from deforming. The strain gauges readings during this phase registered an increase in the

circumferential strains, and conversely a decrease in the vertical strains. This could have been due either to leakages from the lateral cell in the chamber or to the existence of trapped air in the cavity cell either of which would have resulted in a reduction of volume in the lateral cell and thus stress in the rubber strips. Alternatively, a slight over-compensation in the reaction jacks at the top of the cylinder would result in a shortening of the chamber and an accompanying Poisson's ratio increase in diameter. The former seemed the most probable and the changes of strain were converted into equivalent lateral pressures using a local calibration and have been included in the calculations of Table 7.1 (columns 4 to 7). The strain gauge readings, however, were not uniform in all four columns: two opposite columns seemed to show signs of very slight tensile strains, and also, in some tests, either stayed undeformed or experienced compression during both loading and penetration stages. The adjacent opposite pair seemed to show positive circumferential strains. This led to the conclusion that the chamber may have deformed from a cylindrical cross-section into an elliptical shape possibly as a result of non-uniform pluviation. This phenomenon and its effects on the soil stresses is discussed in Appendix V.

The first six tests were performed under less ideal conditions since samples showed densities that varied with depth due to poor pluviation (because some holes in the shutter plates became blocked during pluviation) or were conducted at a non-standard speed of penetration (one minute interval after every 5 cm at standard penetration rate). The first group resulted in less dense samples. The results are plotted against the matching sets of the later standard tests (CPT7 to CPT17) to show both the effect of density variation and the penetration speed on the obtained q_c and f_s profiles with depth. The results of these tests are analysed in the next section and are compared with the previous tests under BC1 and BC3 on Hokksund sand.

7.3. Analysis of the Test Results

The changed boundary conditions of the new CP test series can only be fairly judged against the previous results (SU series) if the basic soil properties remain unaltered. That this is so is confirmed by the particle size distribution curve from the current series as compared with the same from an SU test sample and from another one obtained at the NGI as in Fig. 7.45. This is also checked with reference to other soil properties (obtained directly or deduced 'indirectly' from empirical corelations with the cone resistance or sleeve friction, as shown in Chapters 2 and 3) in the following sub-sections.

7.3.1. Shear Strength

Internal friction angle is another soil property that can be used to check that soil conditions of the CP test series are similar to that of the previous SU set. The results of shear-box tests on the sand during the current series as well as those from the SU and NGI tests are shown in Fig. 7.46 which are superimposed on the curves proposed by Schmertmann (1978) between ϕ' and D_r. This figure shows that the loose samples fall in Schmertmann's fine sand region whereas the dense ones fall in his medium sand region, as shown to be the case by the particle size distribution curve.

7.3.2. State Parameter

Since Ψ combines the influence of both void ratio and stress level with reference to an ultimate steady state, it can show the state of the sand used in different tests series.

Using the state parameter and cone resistance relationship [Eqn. (2.16)] to correlate shear strength of sand to the measured cone resistance [Eqn. (3.8)] and to the relative density through q_c-D_r-σ'_m relationship [Eqn. (3.10)], the ϕ' values for the CP series were obtained, as shown in Table 7.2. The ϕ' values together with Eqn. (3.9) have also been superimposed on Fig 7.46 curves. This equation appears

to overestimate the friction angle for very loose samples, thus placing the Hokksund sand in the coarse sand region. For very high densities, however, this gives a good estimate of ϕ'. The ϕ' values obtained by Eqn. (3.10) are, on the average, 1.0° higher than those obtained directly by Eqn. (3.9), which may reflect the appropriateness of the q_c-D_r-σ'_m relationship.

The effectiveness of the new boundary conditions can also be investigated in regards to the determination of in-situ shear strength values from the measured cone resistance values. Based on limited test results at the time, Robertson and Campanella (1983) and Lunne and Christophersen (1983) correlated the bearing capacity factor N_q ($=q_c/\sigma'_v$) with the shear strength of sands (Fig. 7.47): q_c values were taken from CPT in the CC and corrected for chamber size and boundary effects as described by Lunne and Christophersen (1983); ϕ' values were taken from standard size triaxial tests on samples built in to the same densities as the CC samples. Fig. 7.47 also includes the results of the new boundary tests with ϕ' values taken from earlier triaxial tests at NGI (Kildalen et al. 1982) and Southampton. It shows that using the N_q vs $\tan\phi'$ relationship recommended by Lunne and Christophersen is quite conservative for NC samples while it fits on the average for OC samples.

7.3.3. Coefficients of Earth Pressure at Rest

From the continuous measurements of both the vertical and horizontal stresses during the consolidation phase of the CP tests, reliable values of the coefficient of earth pressure at rest, K_o, were determined for both NC and OC samples, as shown in Figs. 7.1 to 7.17. As far as NC samples are concerned, the results show that this can be roughly estimated by a linear relationship as

$$K_o^{NC} = 0.51 - 0.002(D_r) \qquad (1)$$

This yields a K_o of 0.31 for a very dense normally consolidated sand (D_r = 100 %).

The CP series on medium dense to dense sand, for a limited range of overconsolidation ratio, suggests the following empirical relationship

$$K_o^{OC} = K_o^{NC} + C \cdot \log_2(OCR) \qquad (2)$$

in which $C = 0.177 - 0.0005 D_r$ $\quad [D_r$ in %]

The K_o value at 4.0 kg/cm^2 of 0.35 and the rate of change of K_o value per $\log_2$ cycle on rebound of 0.14 for dense samples [as given by Last (1979) with D_r = 90%] compare reasonably well with the equivalent values for the current series of 0.335 and 0.132, respectively, as obtained from Eqns. (1) and (2). [see Figs. 7.48 and 7.49]. The form of these two equations between K_o^{NC} and D_r and between K_o^{OC} and OCR are both different from those normally quoted in the literature and fit the data rather better. Note that the constant C given in Eqn. (2) relates only to the testing range of medium-dense to very dense sand; the value for loose sand is much lower. Thus C, itself, must be regarded as a variable (and the functional relationship non-linear) if a wider density range is to be considered.

7.3.4. Cone resistance - Relative Density

The important results for determining the significance of the controlled stiffness boundaries are those for the penetrometer itself. A careful analysis of the data suggests the following, dimensionally homogeneous, relationship between cone resistance and density which fits remarkably well to the CP test results of all stress histories

$$q_c = (210.94\ \sigma_h - 24.517\ \sigma_v)\ e^{0.028\ (D_r - 60)} \quad (R^2 = 98) \qquad (3)$$

A similar correlation also exists between sleeve friction and relative density [see section 7.3.6].

(The minus sign of the σ_v term suggests the effect of overconsolidation rather than the negative effect of σ_v).

This was demonstrated in another way in Chapter 3 where the degree of dependency of cone resistance to both the vertical and horizontal confining stress of the SU test results was not constant [Eqn. (3.5)], since NC samples showed a better relationship to vertical stress with the OC samples related better to the horizontal stress. The relationship appears to underestimate some of the OC test results of the CP series with the opposite effect on the NC ones. This led the author to believe that in NC sands it may only be necessary to consider the vertical stress effect in the following form suggested by Schmertmann (1976 and 1978) [although with only pseudo-dimensional homogenity and not quite as accurate as Eqn. (3)]

$$q_c = C0\ p_o \left(\frac{\sigma'}{p_o}\right)^{C1} EXP\ (C2 \cdot D_r) \qquad (4)$$

where: C0, C1, C2 and C3 = experimental coefficients
p_o = reference stress (= 1 kg/cm²)
σ' = the confining stress in kg/cm^2

The OC samples, on the other hand, could be related to either the horizontal or the mean stress (or in the form given in the above equation with more weighting on the horizontal stress than the vertical one).

To check this correlation for the CP series, the mid-height chamber cone resistance values of different tests were superimposed on the curves obtained from the above relationship in Figs. 7.50 to 7.52 through vertical, horizontal or mean stress. Some of the earlier Southampton tests (SU series) with B1 and B3 boundary conditions have also been shown in these figures. As far as the NC samples are concerned, the $q_c - \sigma'_v$ plot of the Schmertmann curves tend to over-estimate the infinite boundary (IB) results. Lunne and Christophersen (1983) and Lunne (1991) suggested a 25 % increase to the Schmertmann curves to simulate the field conditions. This overestimates the IB results to an even greater degree. It should, however, be noted

that the above authors recommended these curves only for NC, unaged, clean, fine to medium quartz sands with rather high lateral stress (K_o = 0.45 as compared with the Maximum K_o of about 0.32 for most of the NC CP series tests).

Cone resistance - effective mean stress plots, on the other hand, seem to fit the data rather well, especially for medium dense samples.

Cone resistance was related to relative density through the square root of σ'_v by Lancellotta (1983) for different normally consolidated sands, including Hokksund sand [Fig. 7.53]. The results of the CP series, also shown on this figure, fit the following empirical equation:

$$D_r = 107.5 \log \frac{q_c}{\sigma'^{0.5}_v} - 203.4 \qquad (R^2 = 0.95) \qquad (5)$$

(stresses in kg/cm^2)

This fiqure also shows the cone resistance values corrected by Baldi et al. (1986) and Lunne and Christophersen (1983) procedures.

Assuming the tests with the new infinite boundary conditions represent real field conditions, the measured q_c values can be used to predict the relative densities and, hence, compare with those predicted using interpretation procedures such as recommended by Lunne and Christophersen (1983) and Baldi et al. (1986). This is illustrated in Table 7.2 from which it can be seen that using, such interpretation procedures, the relative density is underpredicted by 12-17% (absolute values) for the very dense sand and by 5% or less for medium dense sands. Using the charts given by Baldi et al. the D_r is underpredicted by 2 to 11% for very dense sand; for medium dense sand the predicted values are very similar to the measured.

Since the effect of boundary condition is most pronounced in the dense samples, it is possible that in such samples cone resistance, and for the same reason the sleeve friction, can be related to the confining stress alone for a range of densities. On this basis, a series of regression analyses were performed on the CP results between q_c and the confining stresses on both NC and OC samples. The results, however, showed that vertical stress alone is not capable of defining the behaviour of the cone resistance in the NC samples. In fact, the accuracy of the cone resistance and the lateral stress relationship of the CP series in the following form, although based on limited tests results, is much higher than the same with vertical stress

$$q_c = 387.3\ \sigma_h^{0.657} \qquad (R^2 = 0.97) \qquad (6)$$

where both q_c and σ_h are in kg/cm^2.

In comparison with the SU results this indicates a rise over the BC1 results ranging from 10 to 20 percent for a lateral stress ranging from 0.5 to 1.25 bar, respectively, with virtually no correction necessary for the BC3 results. The OC results, however, indicate a rise to the equivalent SU results ranging from 9 % for a lateral stress of 0.5 bar decaying down to zero for a lateral stress of 1.25 bar. For the ideal testing conditions of 2.0 bar NC and 1.0 bar (OCR = 4) where the lateral stress at the end of K_o, on the average, is about 0.63 bar, the necessary correction factor to the NC (BC1) and OC results of the SU set are, respectively, 12 % and 7%. This suggests that the CP results give q_c values that are about 13 % and 17 % , respectively, smaller than the field values suggested by Lunne and Christophersen. The extremely dense samples (e.g. CPT Nos. 7 and 8 with $D_r \geq 99$ %), however, seem to match the field values.

7.3.5. Constrained Modulus - Cone Resistance

The determination of soil deformation parameters from in-situ tests is of great practical interest because of the sensitivity of deformation modulus to even small disturbance, especially at low

strains (Jardine et al., 1984). Therefore, it is important that the constrained tangent modulus, M, is obtained from the penetration results of tests with boundaries that closely resemble field conditions (i.e., the CP series).

The constrained tangent modulus, determined from the consolidation phase [i.e. from one dimensional loading and unloading in the calibration chamber], as discussed in Chapter 3 appears to be a function of both the applied stress and the over-consolidation ratio as well as the relative density of the sample. A careful analysis of the results of both the SU and the CP series showed that the relationship between the constrained modulus and the relative density of the normally consolidated samples is best described through the vertical confining stress by using the following equation:

$$\ln\left(\frac{M}{p_o}\right) = \left\{4.06 + 0.88\left(\frac{\sigma'_v}{p_o}\right)^{0.5} + \left[2.1 - 0.1\left(\frac{\sigma'_v}{p_o}\right)\right] \cdot \frac{D_r}{100}\right\} \qquad (7)$$

where D_r is in percent and p_o is the reference pressure (=1.0 kg/cm^2). Since σ'_v can be estimated in the field as γh, the only unknown remaining in this equation is relative density. From the relationship proposed between cone resistance and relative density through vertical confining stress for the NC sample, a value for D_r can be estimated for the measured in-situ q_c value. It is also convenient to eliminate relative density in the $q_c = f(\sigma'_v, D_r)$ and $M = f(\sigma'_v, D_r)$ to get the in-situ M value for Hokksund sand as a function of only the cone resistance and the vertical stress as follows:

$$M = 90.685\ P_o(q_c/P_o)^{(0.413)}(\sigma'_v/P_o)^{(0.205)} \qquad (8)$$

in which M, q_c, σ'_v and P_o are all in kg/cm^2. The use of this equation in the field requires a knowledge of the stress history of the sand. If the sand is overconsolidated, an equivalent NC cone resistance should be used instead.

This equation has been plotted for a range of σ'_v values between M and q_c in Fig. 7.54 over which the results of CP series have been superimposed. Apart from one test, the 2.0 bar NC results fall on the $M = 3.5q_c$ line. The 4.0 bar NC tests, on the other hand, fall above the $M = 5q_c$ line.

The graph in Fig. 7.55 of computed constrained modulus, M, values against experimental values shows the same sort of scatter as found in the previous SU tests. Both series indicate a range of values for computed M depending on whether the mean stress or the horizontal stress was used in the individual calculations using Eqn. 3.15.

7.3.6. Sleeve Friction

It will be shown in the next chapter that the measured sleeve friction agrees remarkably well with the sleeve stress obtained through the analysis of full length expanding cylinder tests under the same confining stresses.

The sleeve friction data in the form of sleeve stress profiles are shown in Figs. 7.18b to 7.27b. They show a general increase of f_s values with depth - not consistent with the expectation that they should increase to asymptotic values as penetration becomes sufficient to reach steady-state field stresses. (Naturally, the poor modelling of sand to infinity at the base of the chamber affects the end of the penetration curves). Estimated asymptotic values might be expected to represent field conditions most closely.

The analysed results of expanding cylinder tests in Chapter 9 will show that sleeve friction can be closely related to the far field lateral stress (i.e., initial K_o stress). On this basis, a regression made on the results of only 3 tests (CP15 to CP17) indicate a good fit for NC and OC samples in the form

$$f_s = 0.821\ \sigma_h^{1.006} \qquad (R^2 = 0.99) \qquad (9)$$

The power of the lateral stress of almost 1.0 suggests a nearly linear relationship between the sleeve friction and the lateral stress for the medium dense samples. This relationship has been generalised for both NC and OC samples for all densities in a form similar to that given for the cone resistance as follows

$$f_s = (0.866 \cdot \sigma_h - 0.053 \cdot \sigma_v)\, e^{0.032\,(D_r - 60)} \quad (R^2 = 0.99) \qquad (10)$$

This relationship is dimensionally homogeneous and shows a remarkable degree of correlation, This suggests an increase of about 26 % to the measured f_s values as given by a typical 2.0 bar NC test under BC1. The OC samples also show increased f_s values by at least 14 %.

The experimental f_s values have been plotted against those calculated by this relationship in Fig. 7.56 for the CP series. The results for the non-standard tests as well as those with non-uniform densities have also been included in this figure which shows that the one minute halt has relaxed the local stresses slightly, resulting in reduced sleeve friction values. The non-uniform density tests, as expected, resulted in low f_s values, as well.

The similarity of the form of relationships developed for q_c and f_s with D_r, as shown in Eqns. (6) and (10), led the author to believe that from a single cone penetration test one should be able to obtain the necessary information regarding the stress state of the soil. This could be achieved by combining these equations so as to obtain a single relationship between q_c and f_s through K_o. On this basis, the results of the CP test series fit remarkably well to the following relationship:

$$q_c = f_s^{0.695}\,(193.1 - 5.46 / K_o) \qquad (R^2 = 0.98) \qquad (11)$$

(q_c and f_s in kg/cm^2)

In principle one could thus obtain K_o from the two measured stresses and thus the field ratio of σ_h to σ_v. However, the K_o effect is very small and could be masked by uncertainties in local soil properties affecting the more dominant constants of the equation.

7.4. Conclusion

In comparing the experimental results with those obtained through different empirical correlations, the following factors should be borne in mind:

- there are still some uncertainties involved in how representative the new boundary conditions are for true field conditions, but the author is fairly confident that they are closer to field conditions than the BC1 and BC3 conditions that have been used before.

- the new tests are strictly valid only for Hokksund sand whereas the Lunne and Christophersen curves were evaluated based on test results from a range of sands.

INFINITE BOUNDARY TESTS (Stresses in kg/cm^2 referred to mid-height												
Test No. (1)	D_r % (2)	σ'_v (3)	σ'_h (4)	σ'_m (5)	Nom. OCR (6)	K_o (7)	M^* (8)	q_c (9)	q_c^{max} (10)	f_s (11)	f_s^{max} (12)	corr fact % (13)
CP1$	90.7	4.15	1.394	2.313	1	0.336	1602	285	331	2.05	2.68	-
CP2$@	83.2	2.15	0.711	1.191	1	0.331	1060	127	220	0.60	0.84	-
CP3$	85.1	2.15	0.737	1.208	1	0.343	1612	107	220	1.14	1.48	-
CP4	88.0	2.15	0.728	1.202	1	0.339	1670	155	238	0.59	0.91	-
CP5$	85.1	2.15	0.721	1.197	1	0.335	1710	257	265	1.55	1.80	-
CP6$	98.6	1.15	0.621	0.797	4	0.54	2290	242	255	1.41	1.69	-
CP7	99.8	1.145	0.603	0.784	4	0.527	2820	322	328	1.74	1.96	-
CP8	99.0	2.15	0.660	1.157	1	0.307	1925	307	317	1.83	2.10	-
CP9	91.0	2.052	0.672	1.132	1	0.327	720	229	245	0.97	1.07	-2.6
CP10	94.8	2.10	0.561	1.074	1	0.267	950	255	264	1.26	1.46	-2.6
CP11	88.0	1.024	0.475	0.658	4	0.464	2620	202	203	0.94	0.97	-4.2
CP12	87.2	0.518	0.365	0.416	8	0.705	1970	185	194	0.80	1.00	-5.5
CP13	97.6	0.276	0.277	0.277	16	1.003	950	162	173	0.67	0.89	-8.4
CP14	97.6	3.993	1.339	2.224	1	0.335	2170	432	433	2.85	3.09	-1.2
CP15	64.0	4.022	1.604	2.410	1	0.399	1230	205	275	1.26	1.63	-0.5
CP16	69.0	1.030	0.636	0.767	4	0.617	2180	138	152	0.58	0.76	-0.9
CP17	64.9	0.268	0.313	0.298	16	1.168	750	52	87	0.24	0.37	-1.5

Notes : $ - one minute halt for every 5 cm of standard penetration

$@ - a 5 minute halt for every 40 cm of standard penetration

* - M values are tangent moduli (or last step of loading or unloading) for both NC & OC tests

Also note that q_c and f_s values (columns 9 to 12) are the measured values adjusted by the corrections factors (column 13)

Table 7.1. Summary of the CP test results

Test No.	OCR	σ'_v bars	σ'_m bars	$K_{o_{OC}}$	$K_{o_{NC}}$	$q_{c_{OC}}$	$q_{c_{NC}}^{*}$	D_r % meas.	D_r % Baldi et al	D_r % Lunne &Chr.	ϕ'° Eqn. 3.9	ϕ'° Eqn 3.1
CP1$^{\$}$	1	4.15	1.394	0.336	0.336	331	331	90.7	83.6	83	43.1	43.6
CP2$^{\$@}$	1	2.15	1.191	0.331	0.331	220	220	83.2	81.7	69	42.2	43.3
CP3$^{\$}$	1	2.15	1.208	0.343	0.343	220	220	85.1	81.7	69	42.2	43.5
CP4	1	2.15	1.202	0.339	0.339	238	238	88.0	84.1	74	42.5	43.4
CP5$^{\$}$	1	2.15	1.197	0.335	0.335	265	265	96.9	87.4	78	42.9	43.6
CP6$^{\$}$	4	1.15	0.797	0.540	0.336	255	166	98.6	91.9	78	44.2	45.1
CP7	4	1.145	0.784	0.527	0.31[a]	322	215	99.8	102	85	45.2	45.2
CP8	1	2.15	1.157	0.307	0.307	307	307	99.0	93.1	84	43.5	44.5
CP9	1	2.052	1.132	0.327	0.327	229	229	96.9	87.4	78	42.5	43.4
CP10	1	2.10	1.074	0.267	0.267	255	255	94.8	88.0	77	43.1	44.3
CP11	4	1.024	0.658	0.464	0.31[a]	202	148	88.3	89.3	75	44.0	44.7
CP12	8	0.518	0.416	0.705	0.31[a]	185	99	87.2	95.0	78	45.4	45.4
CP13	16	0.276	0.277	1.003	0.31[a]	162	65	97.6	98.2	80	46.5	46.9
CP14	1	3.993	2.224	0.335	0.335	432	432	97.6	92.4	82	42.4	43.3
CP15	1	4.022	2.410	0.399	0.399	205	205	64.0	65.0	55	39.6	40.9
CP16	4	1.030	0.767	0.617	0.399	138	108	69.0	73.0	62	42.1	43.1
CP17	16	0.268	0.298	1.168	0.399	52	29	64.9	57.3	57	42.0	44.5

Notes : $ - one minute halt for every 5 cm of standard penetration

$@ - a 5 minute halt for every 40 cm of standard penetration

* - As proposed by Schmertmann (1978)

$$\left(q_{c_{OC}} / q_{c_{NC}}\right) = 1 + 0.75 \left(K_o^{OC} / K_o^{NC} - 1\right)$$

Table 7.2. Comparison of measured and computed D_r values together with the computed friction angles

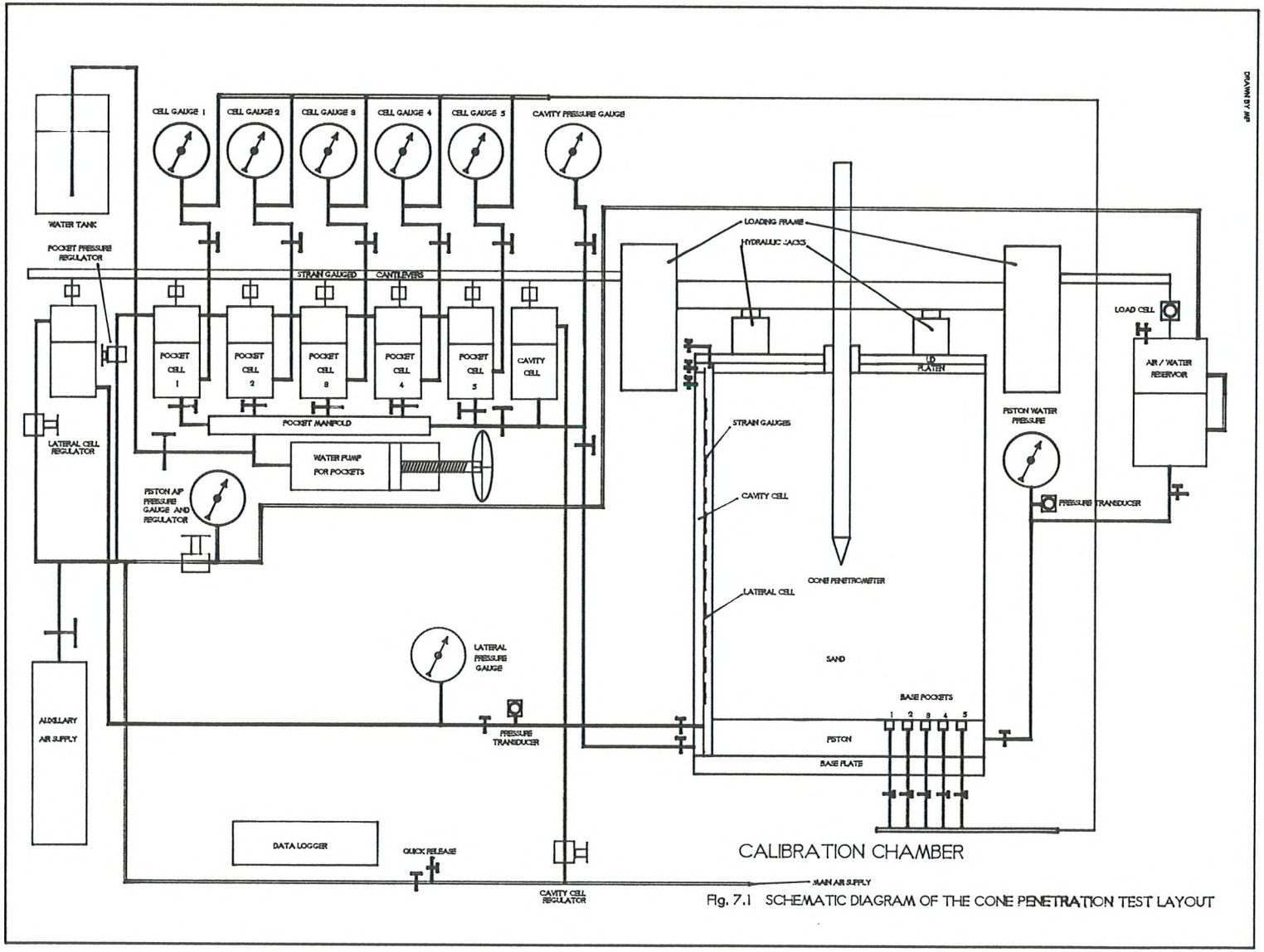

Fig. 7.1 SCHEMATIC DIAGRAM OF THE CONE PENETRATION TEST LAYOUT

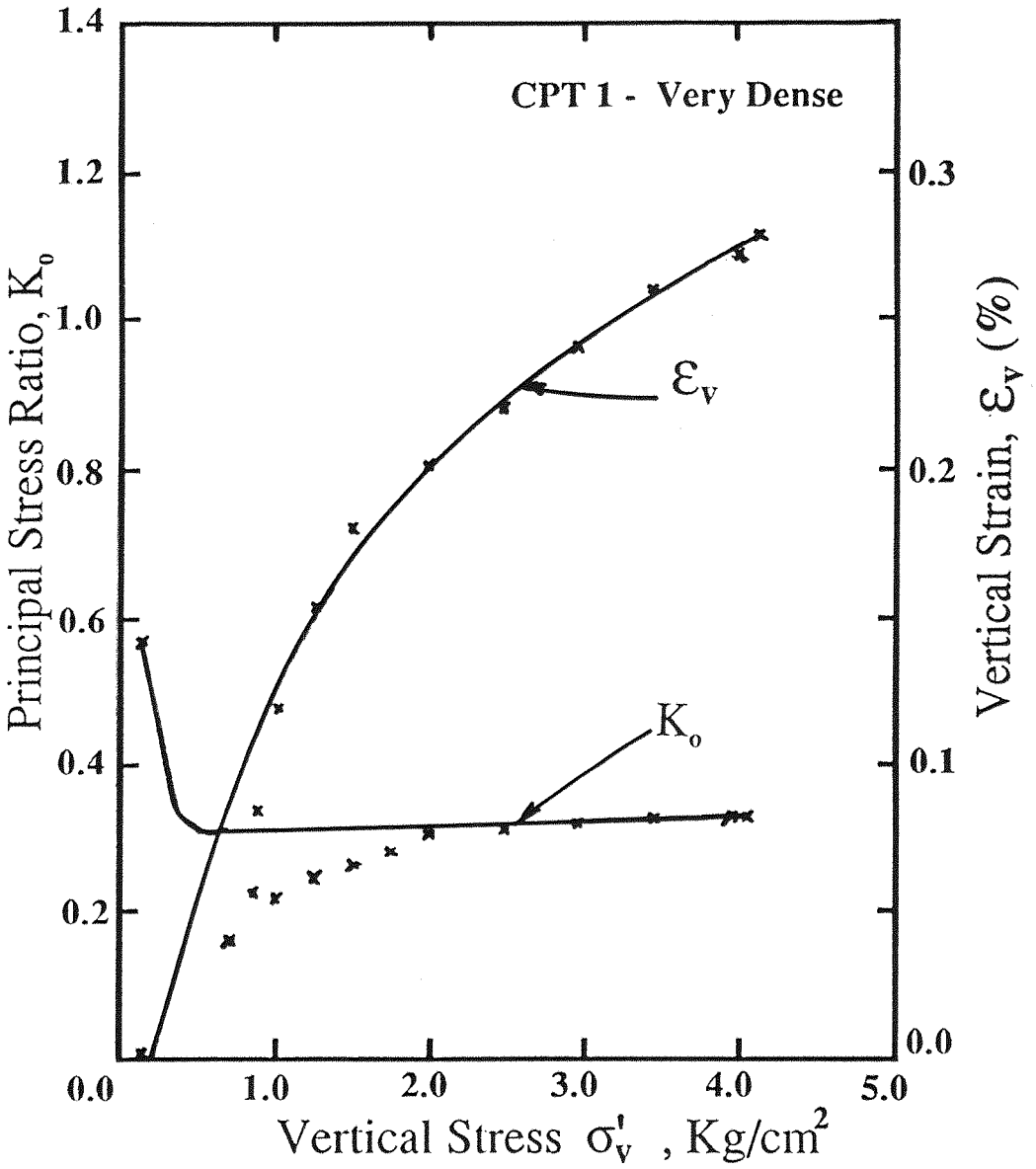

Fig 7.2 Principal Stress Ratio and Vertical Strain during Loading

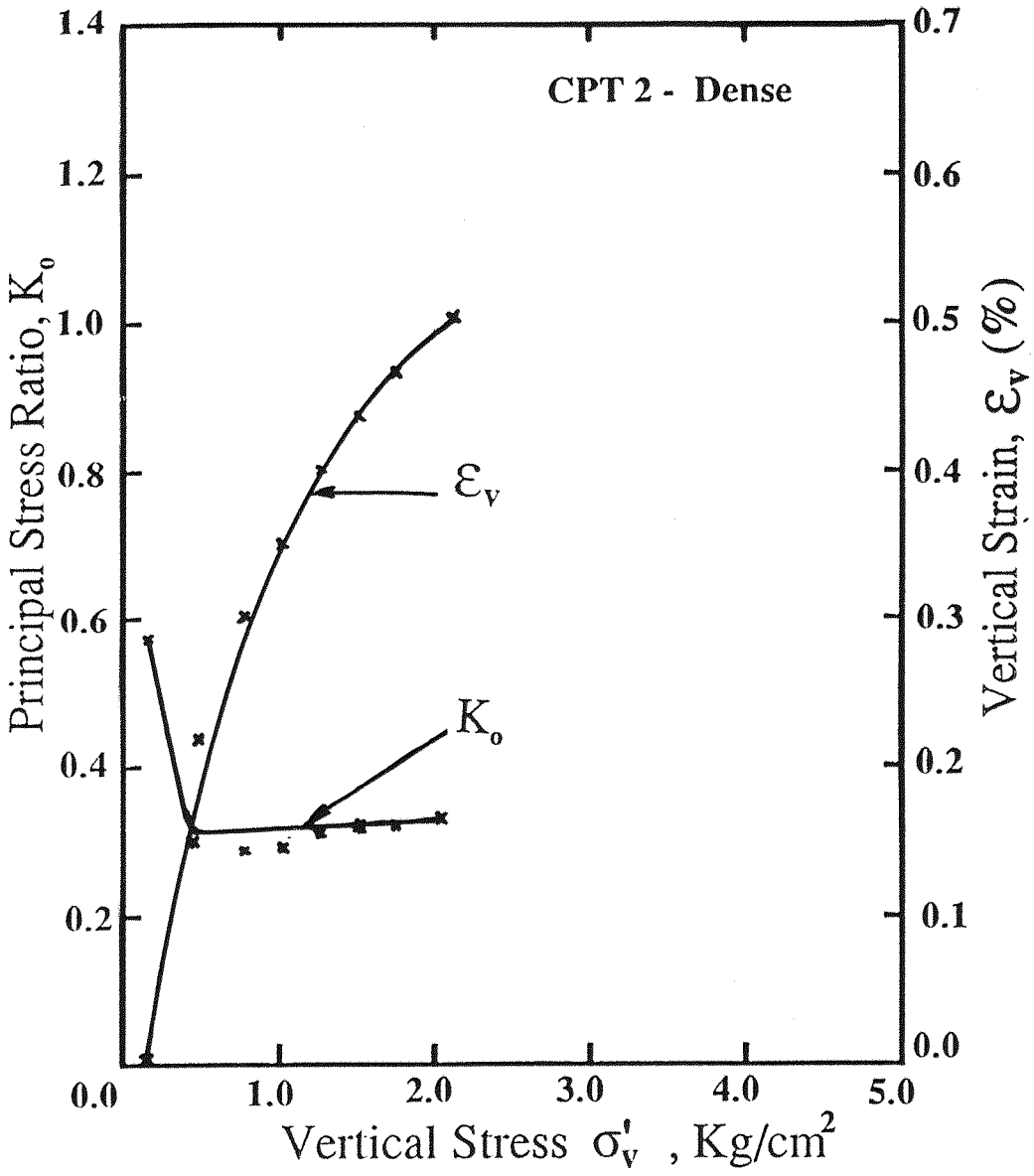

Fig 7.3 Principal Stress Ratio and Vertical Strain during Loading

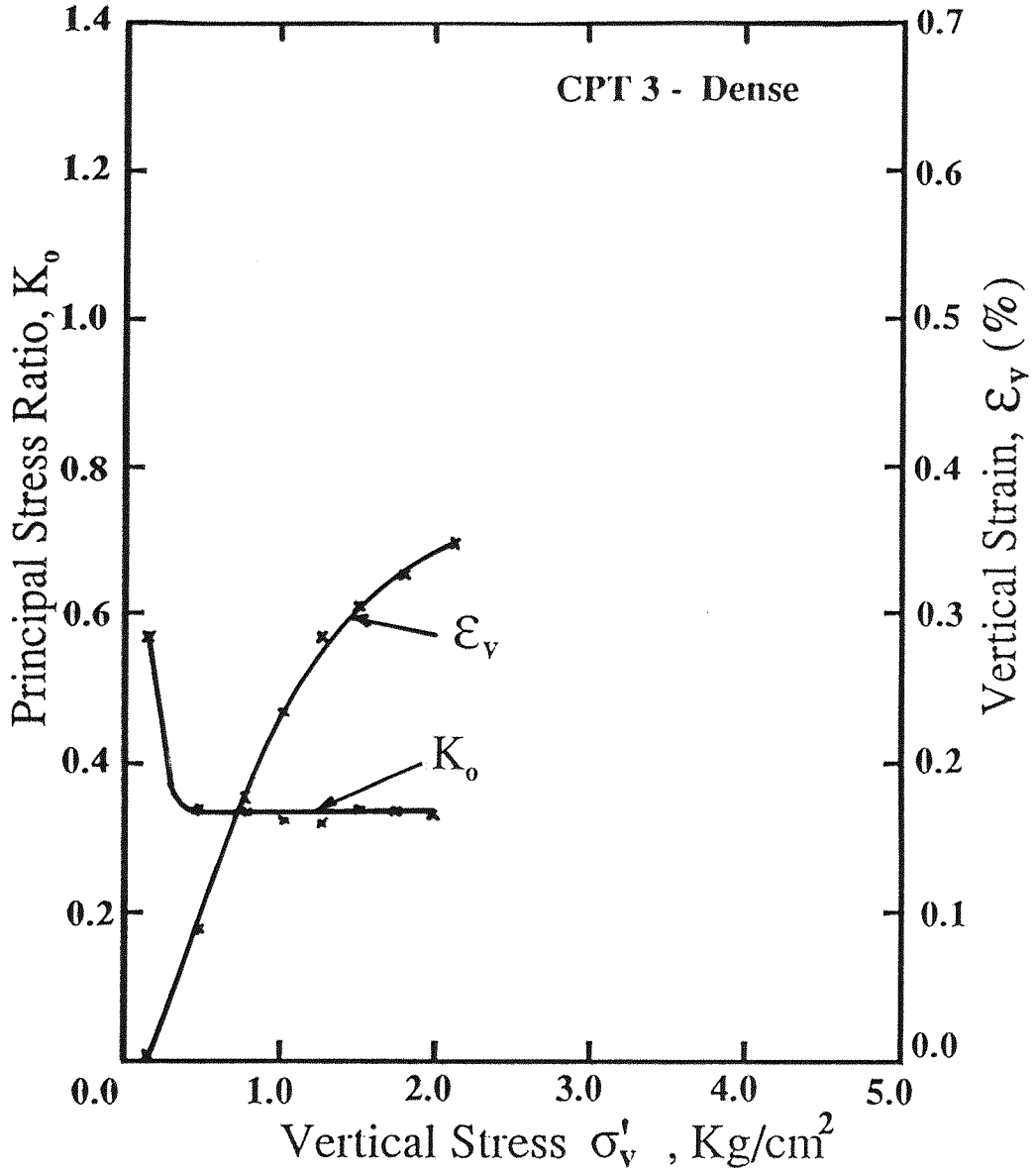

Fig 7.4 Principal Stress Ratio and Vertical Strain during Loading

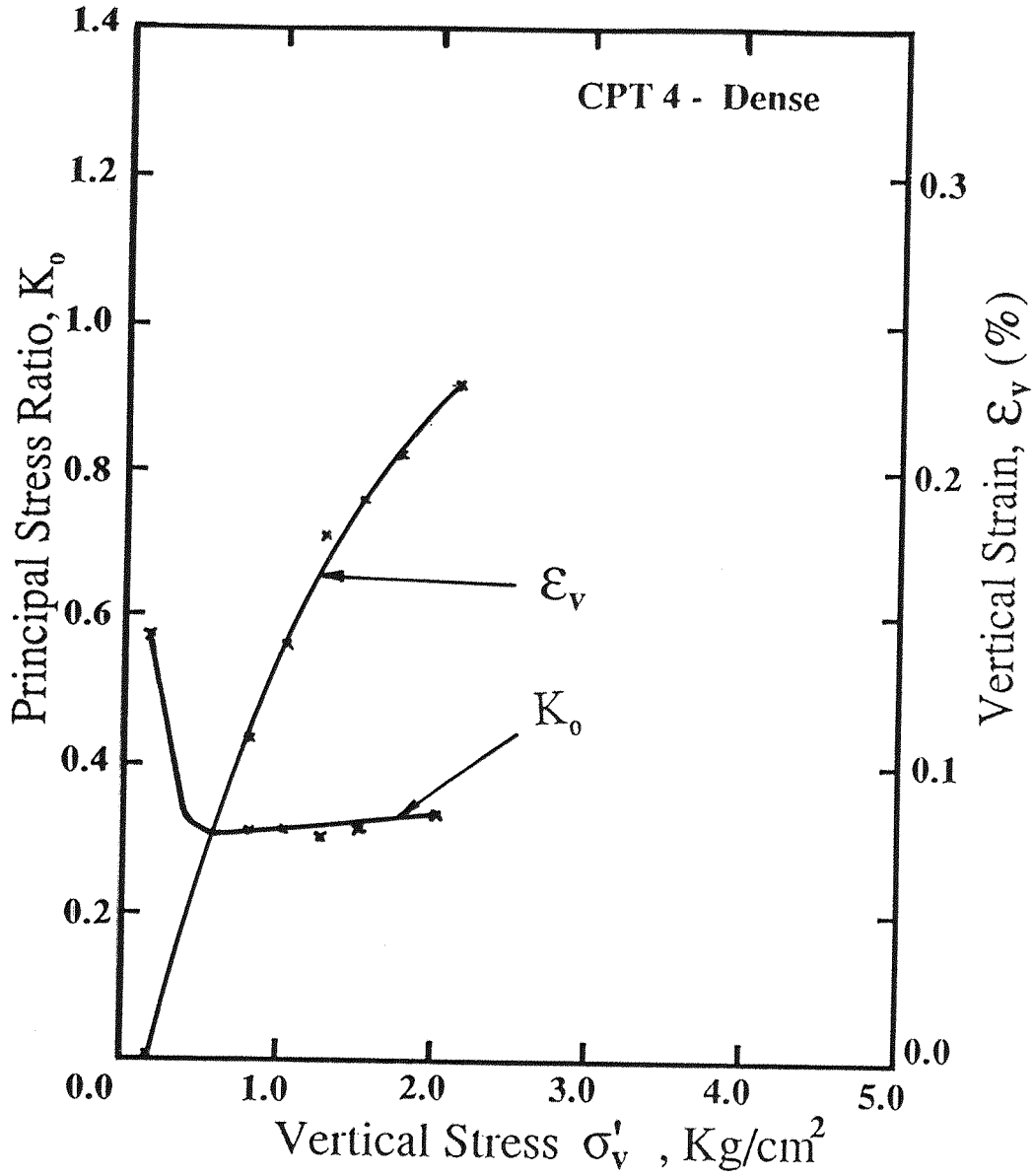

Fig 7.5 Principal Stress Ratio and Vertical Strain during Loading

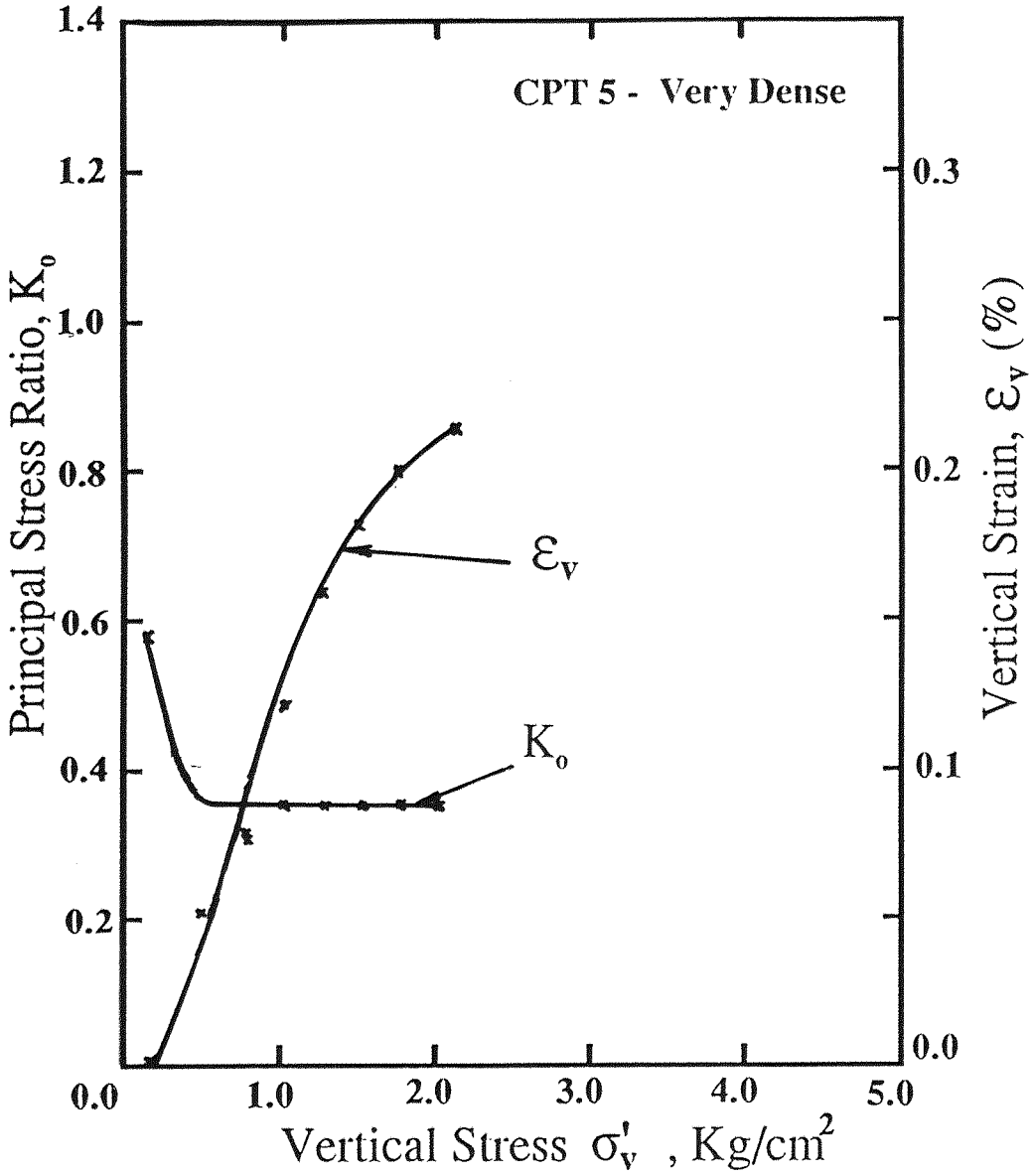

Fig 7.6 Principal Stress Ratio and Vertical Strain during Loading

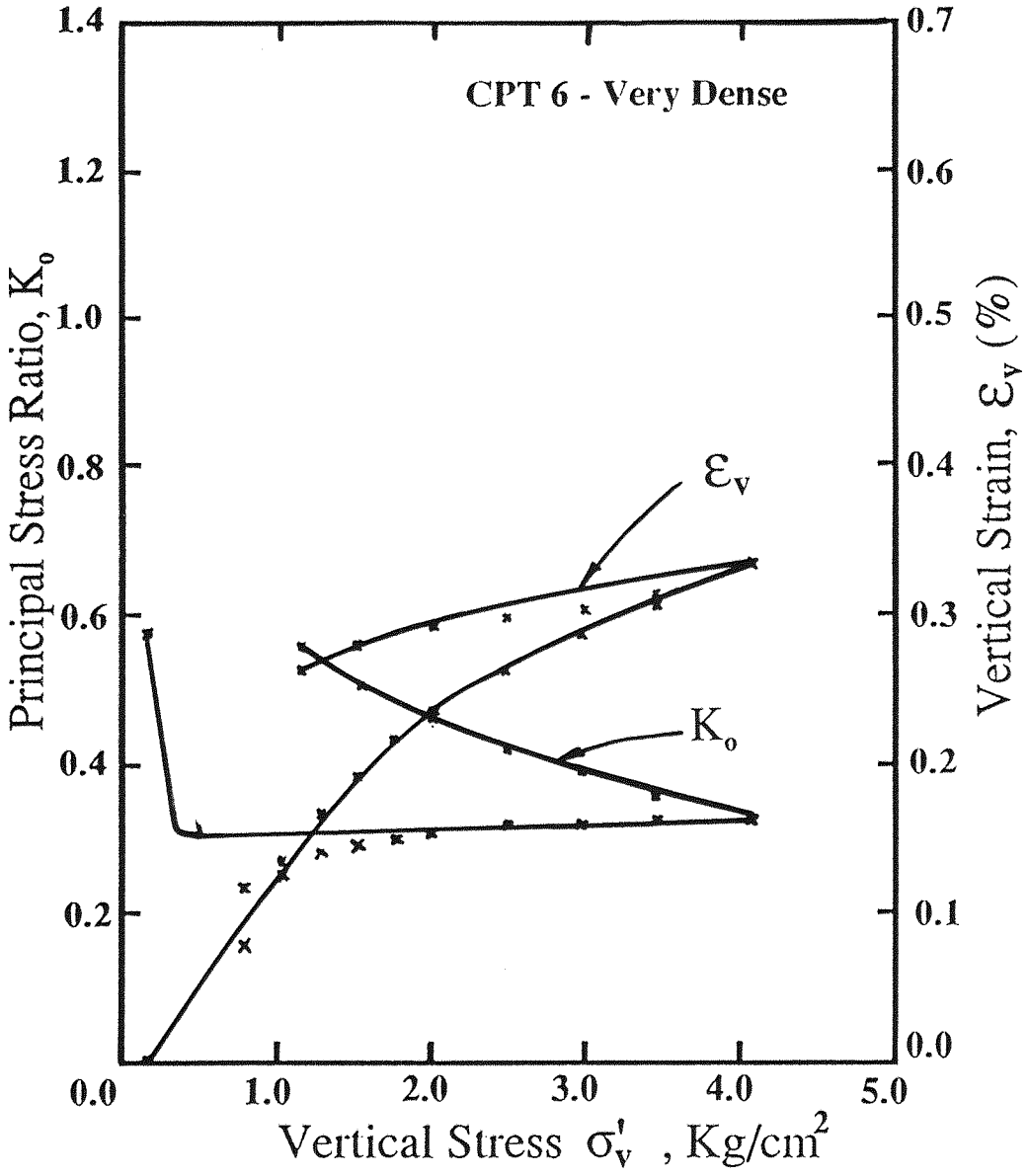

Fig 7.7 Principal Stress Ratio and Vertical Strain during Loading

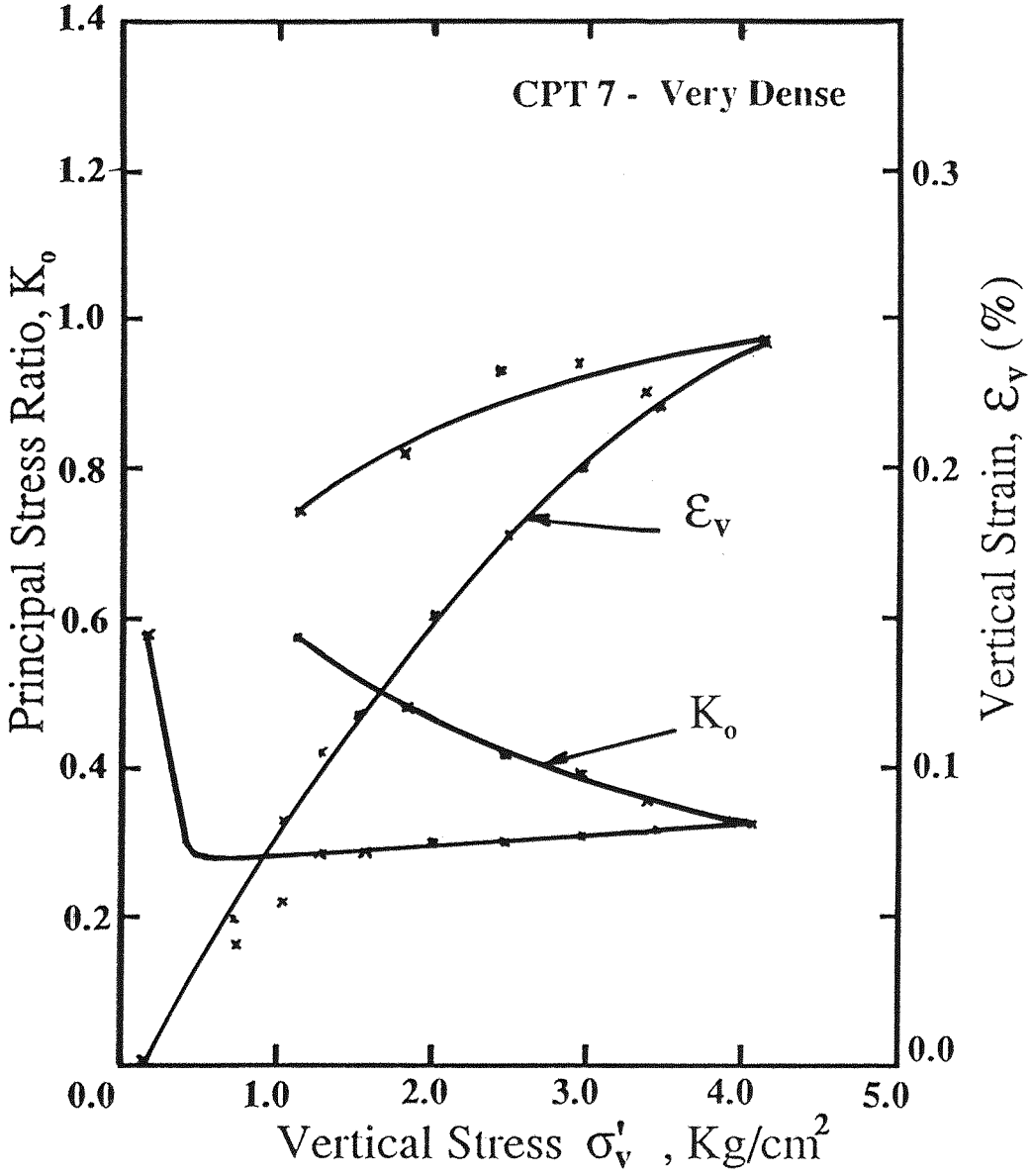

Fig 7.8 Principal Stress Ratio and Vertical Strain during Loading

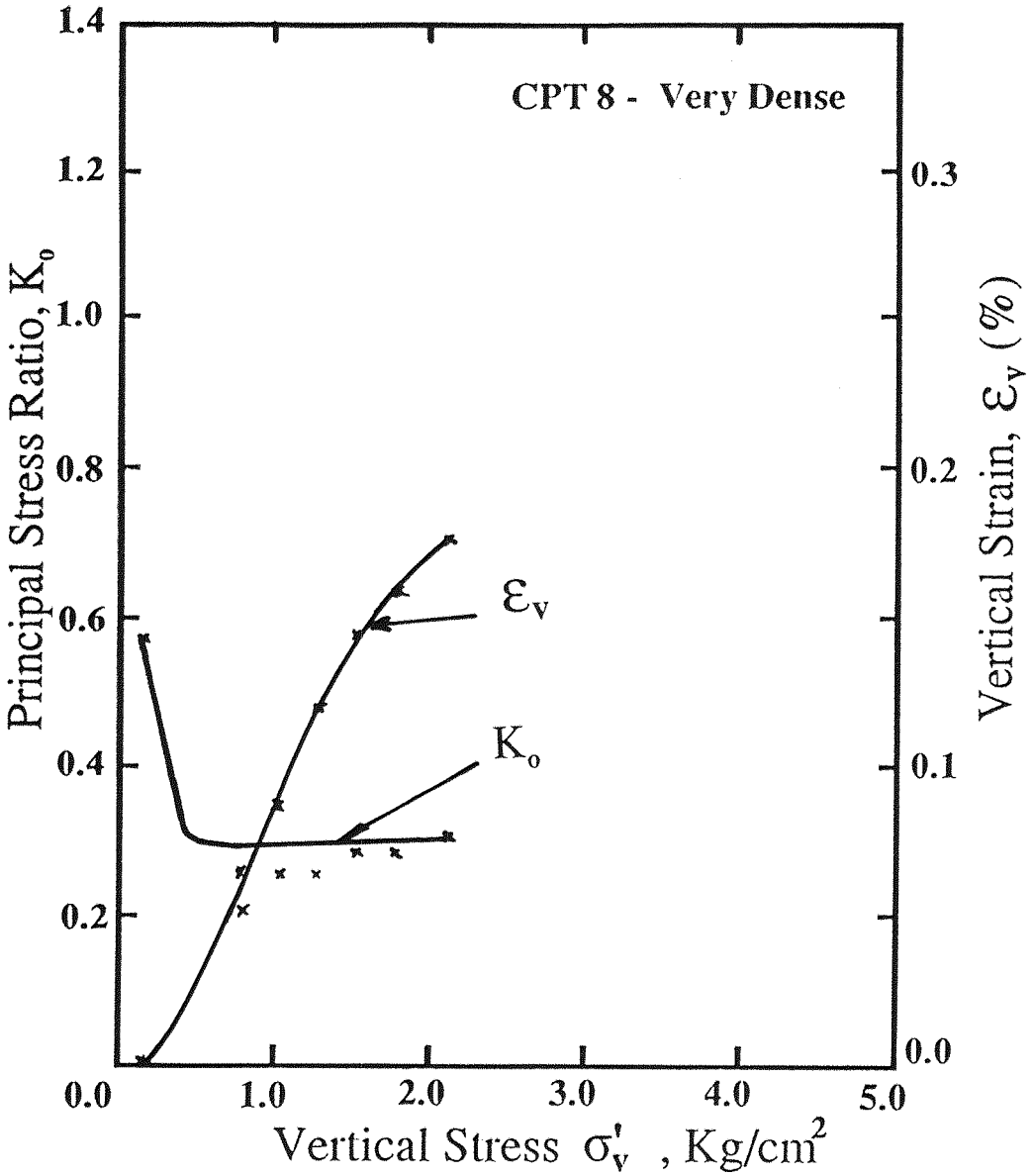

Fig 7.9 Principal Stress Ratio and Vertical Strain during Loading

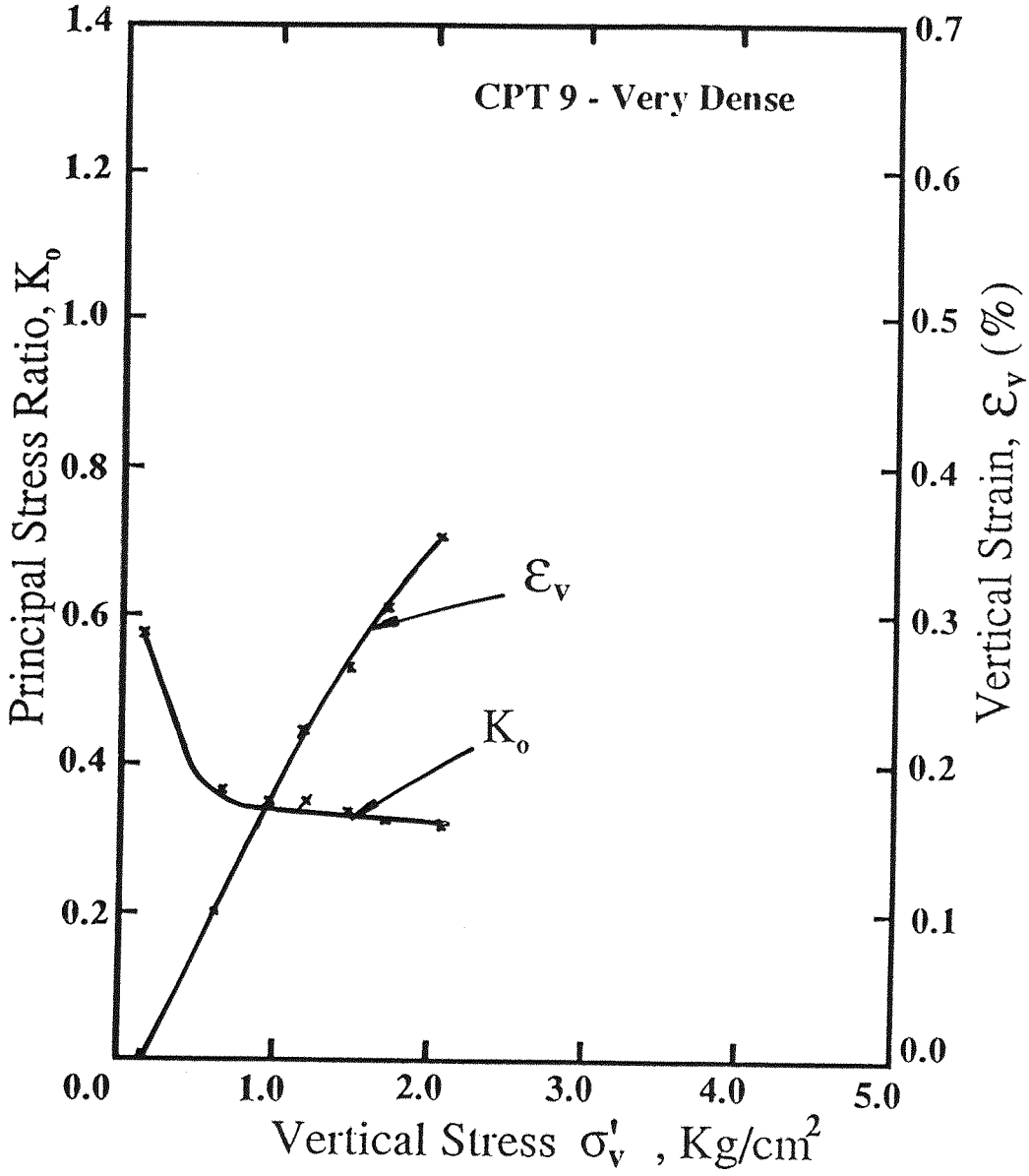

Fig 7.10 Principal Stress Ratio and Vertical Strain during Loading

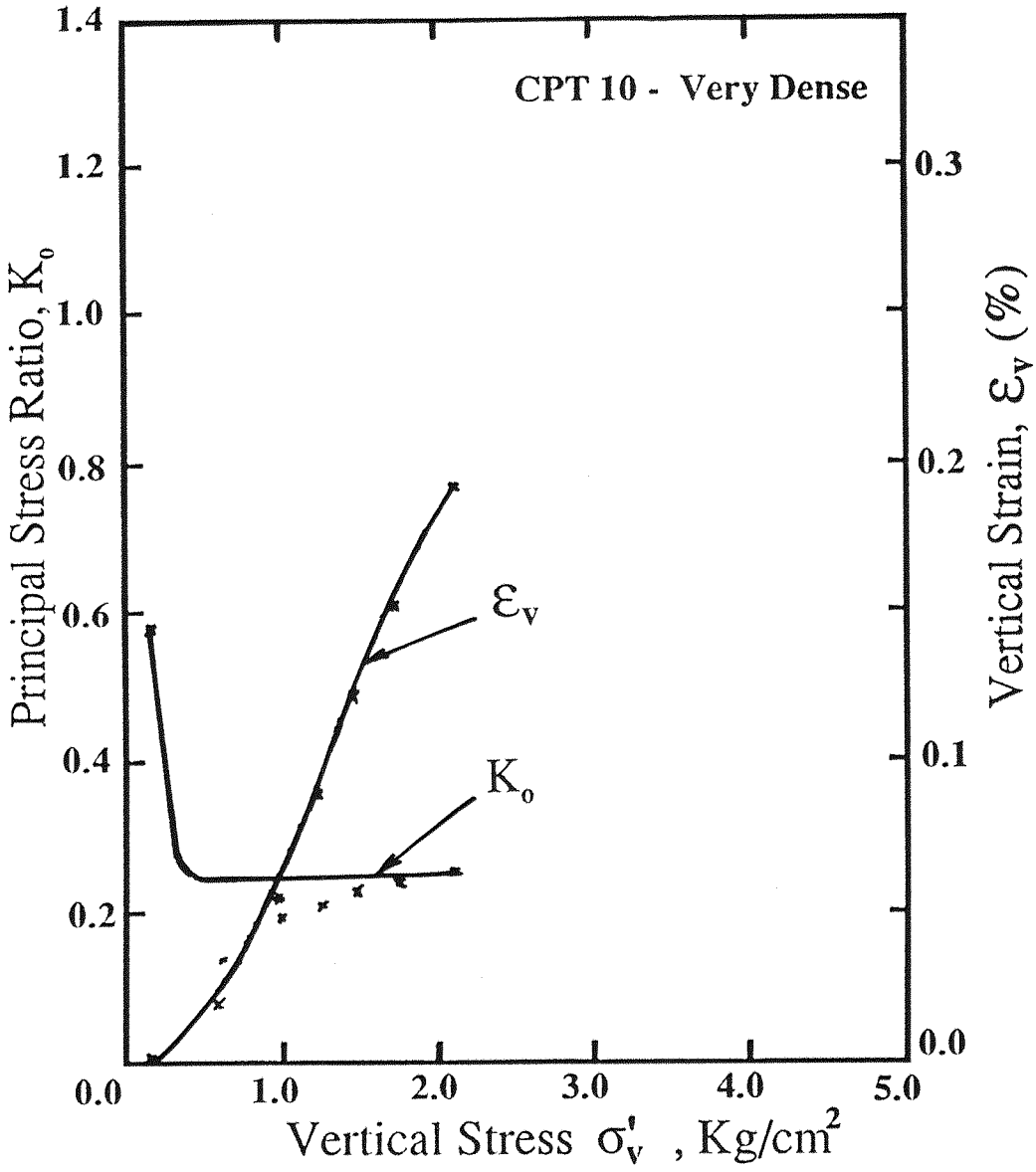

Fig 7.11 Principal Stress Ratio and Vertical Strain during Loading

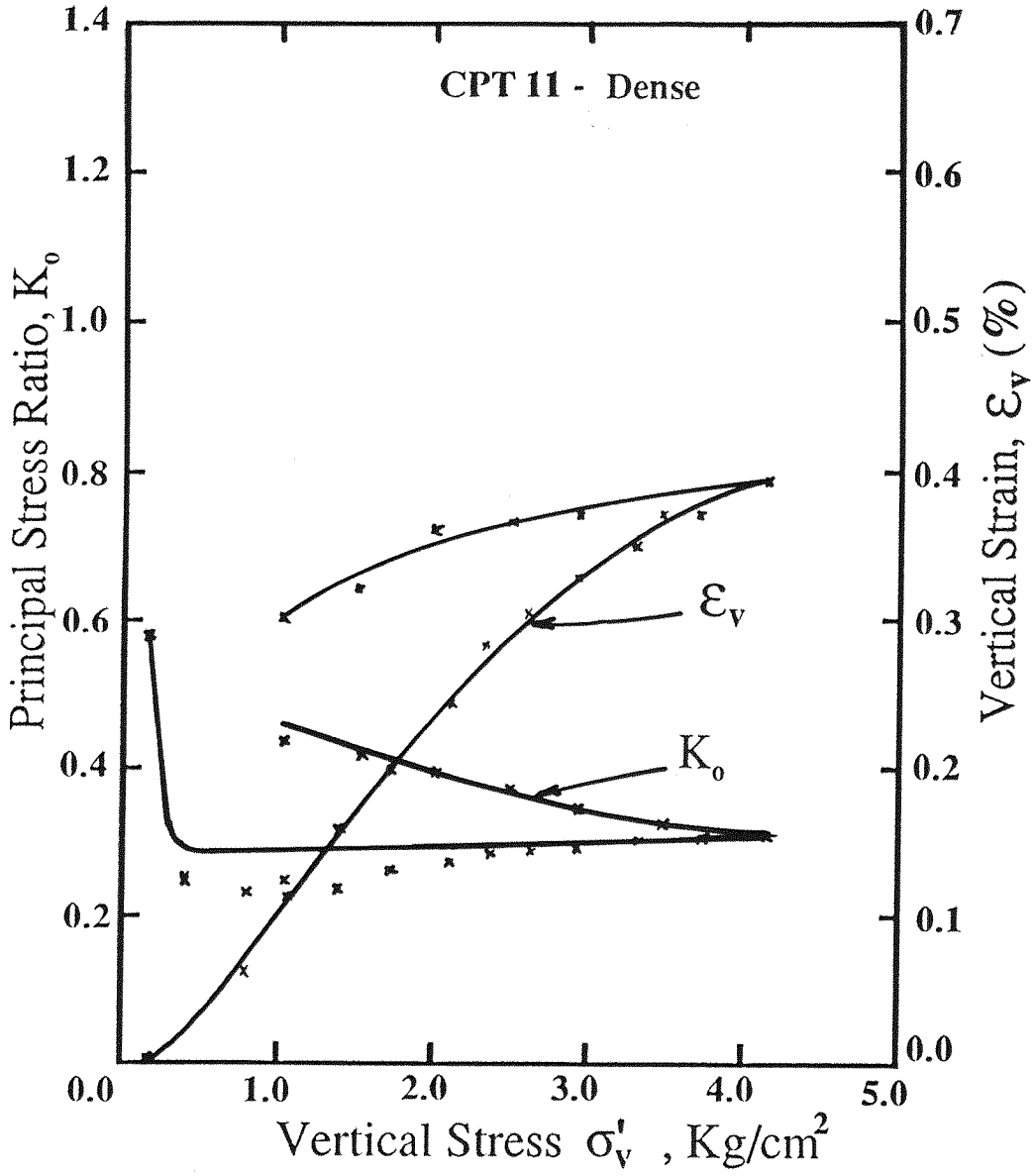

Fig 7.12 Principal Stress Ratio and Vertical Strain during Loading

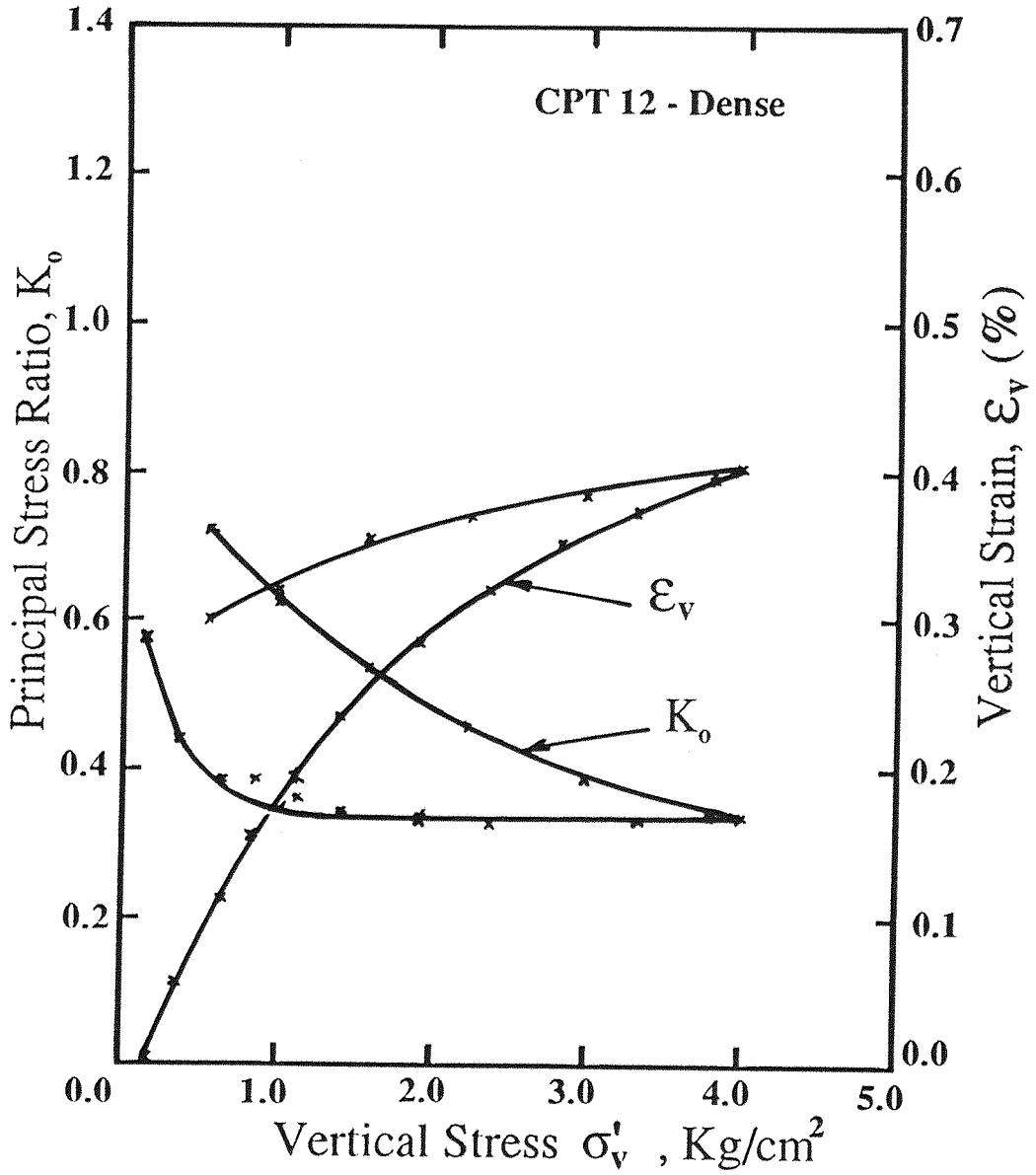

Fig 7.13 Principal Stress Ratio and Vertical Strain during Loading

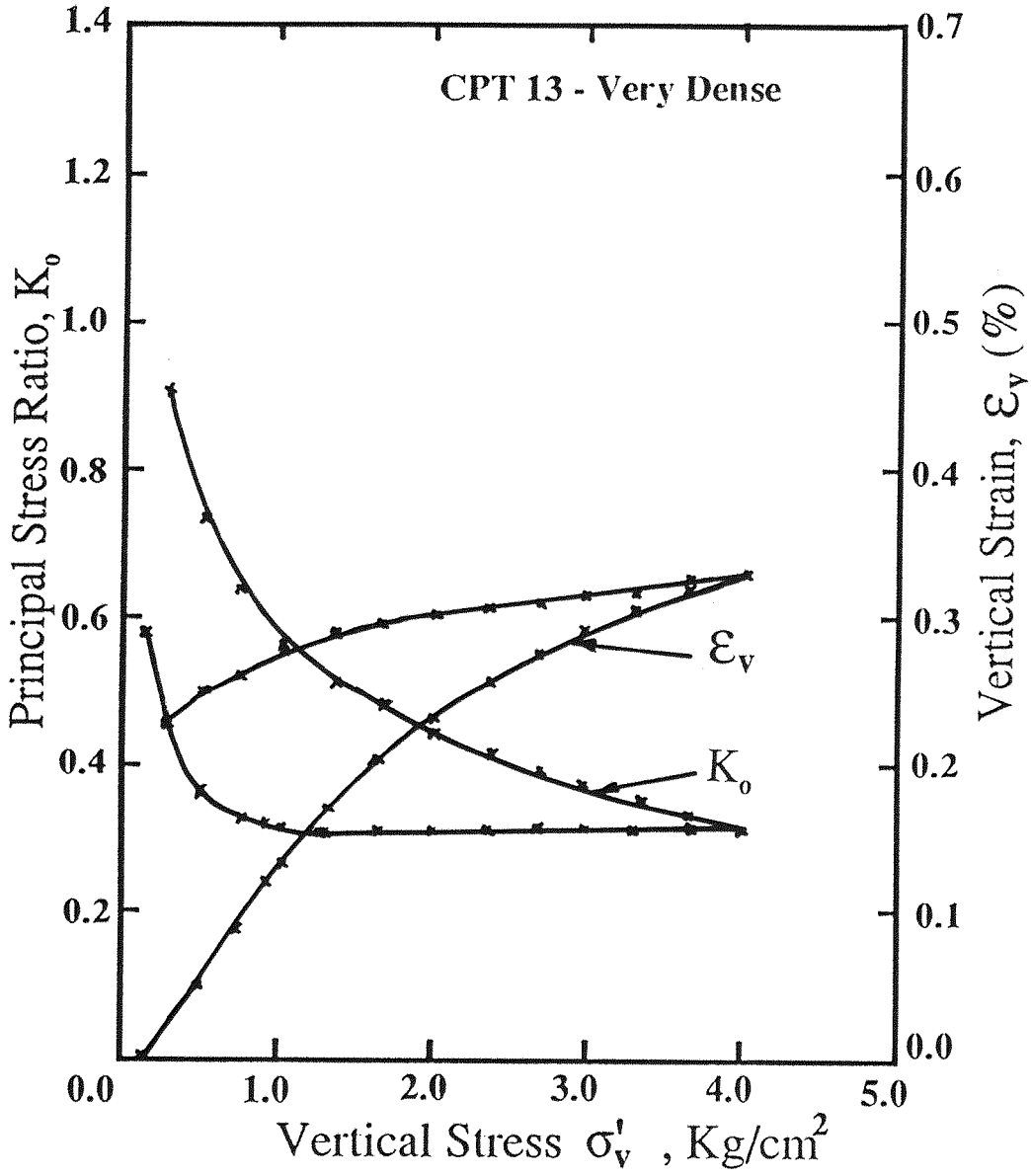

Fig 7.14 Principal Stress Ratio and Vertical Strain during Loading

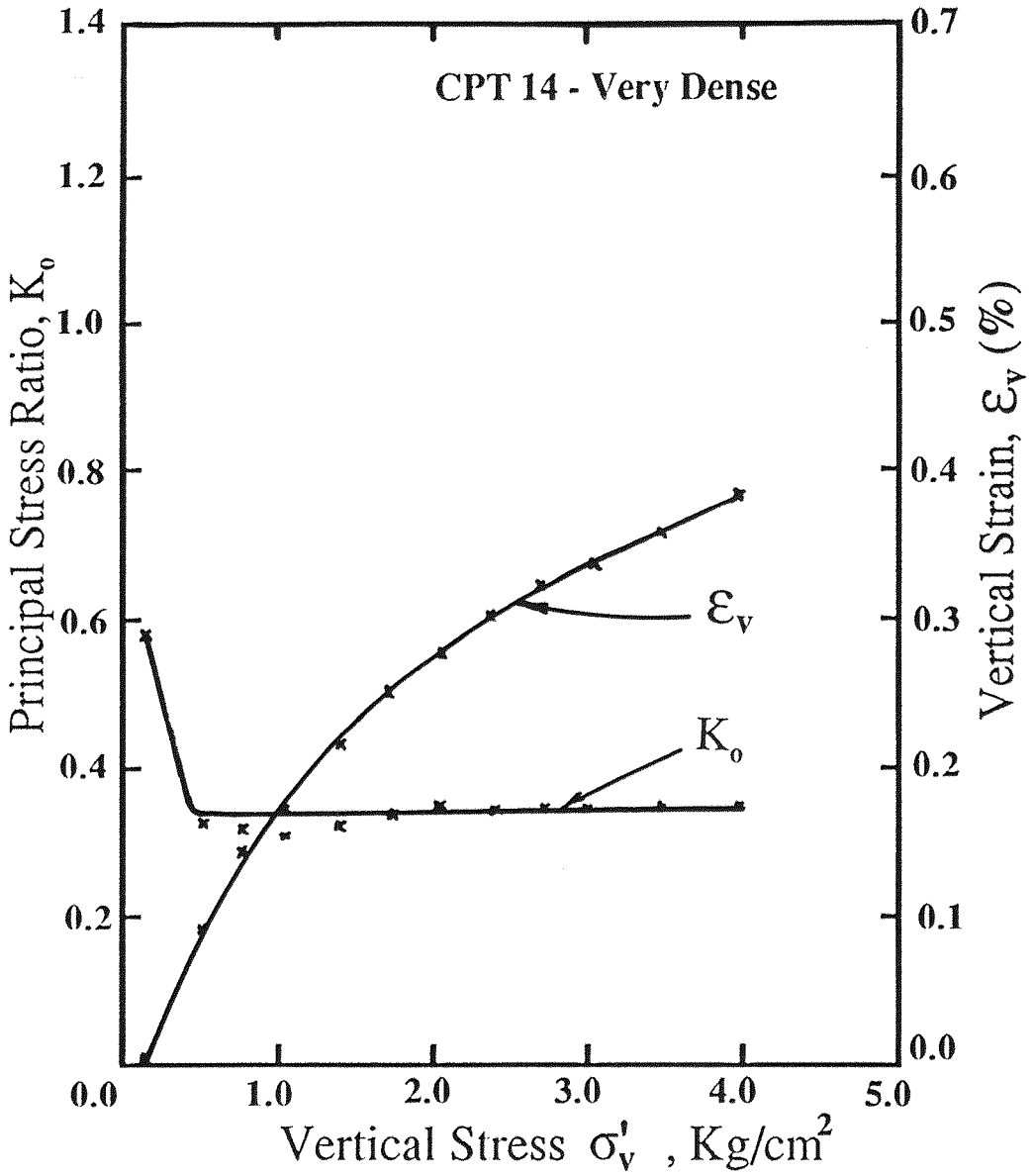

Fig 7.15 Principal Stress Ratio and Vertical Strain during Loading

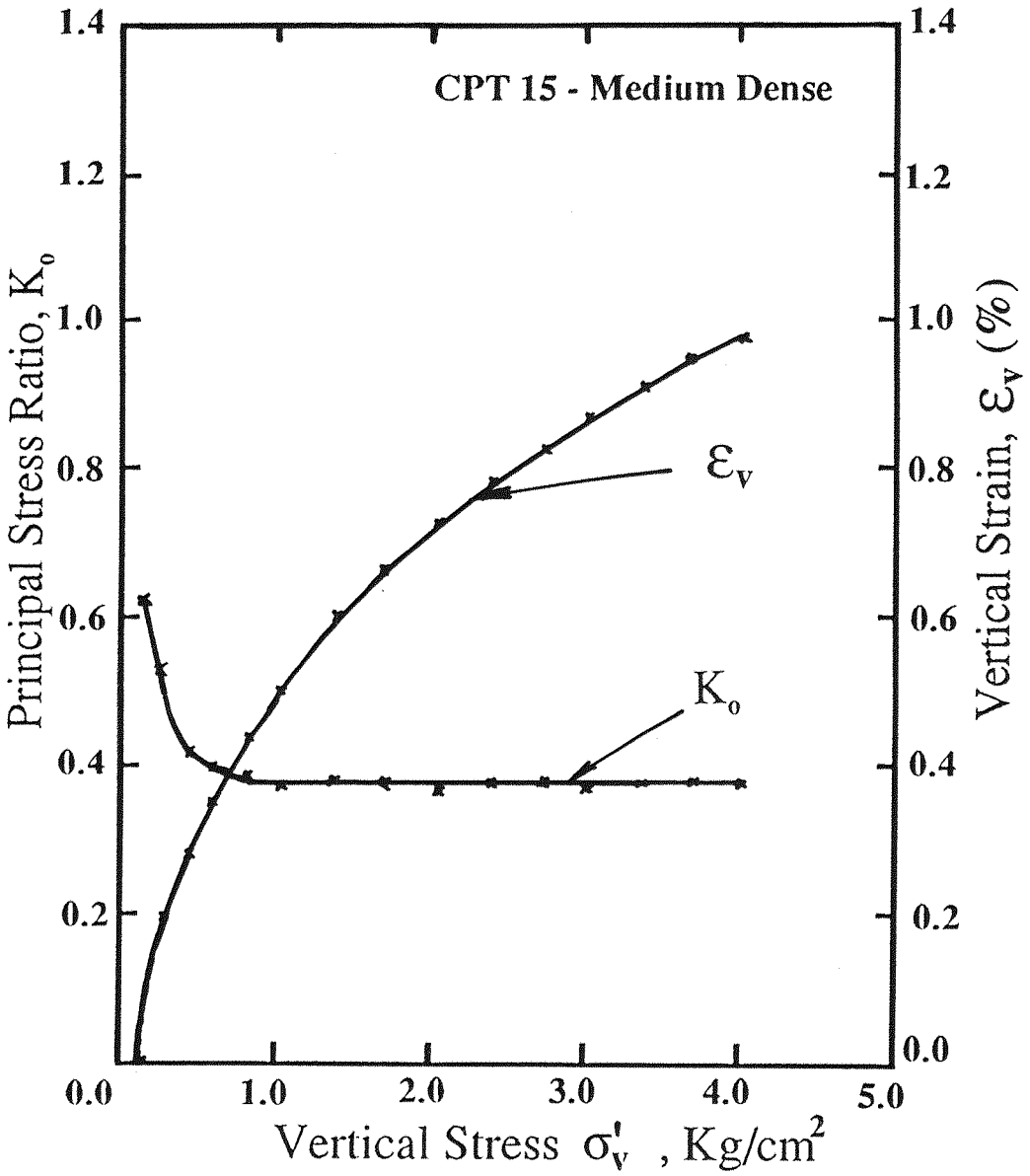

Fig 7.16 Principal Stress Ratio and Vertical Strain during Loading

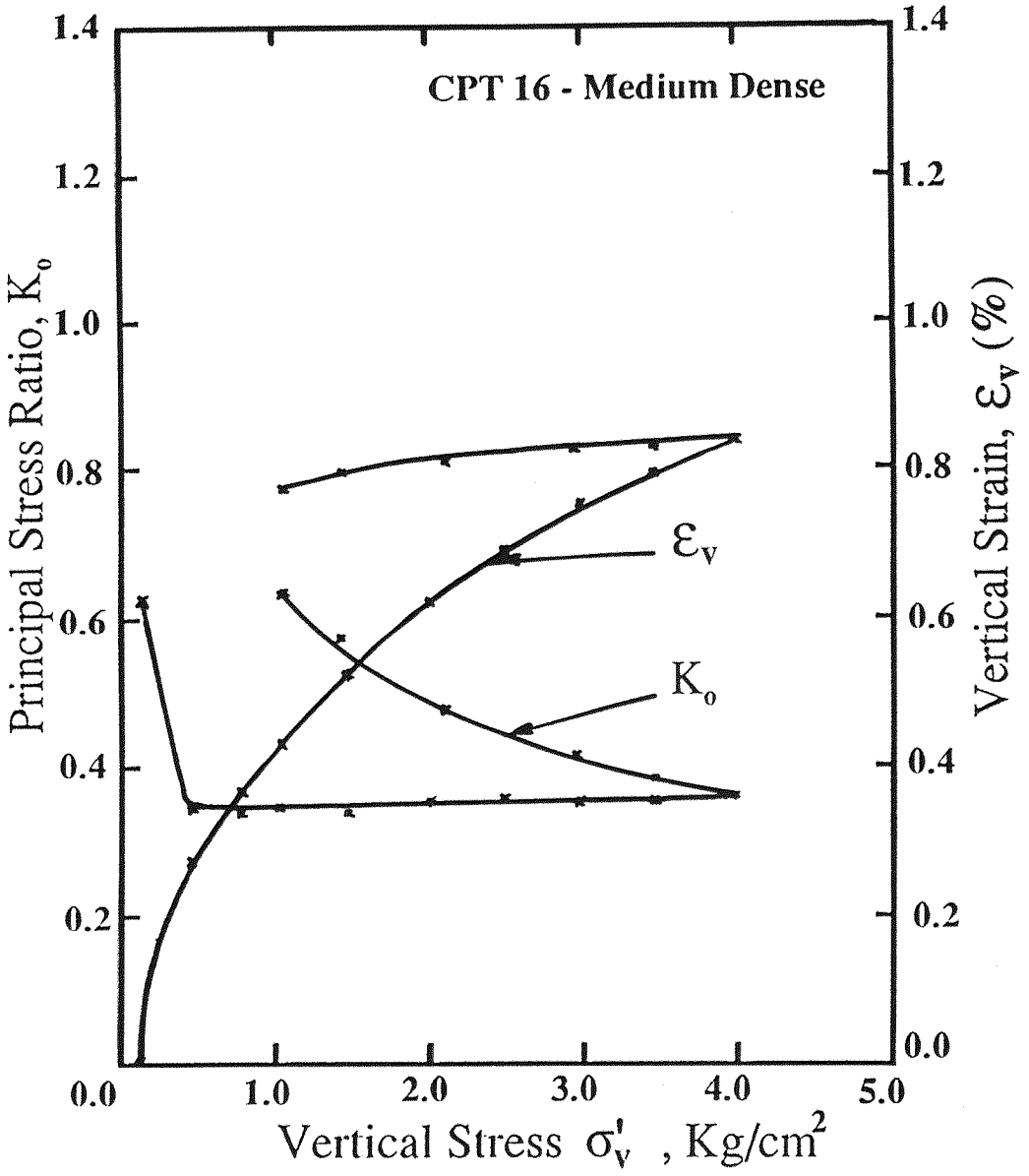

Fig 7.17 Principal Stress Ratio and Vertical Strain during Loading

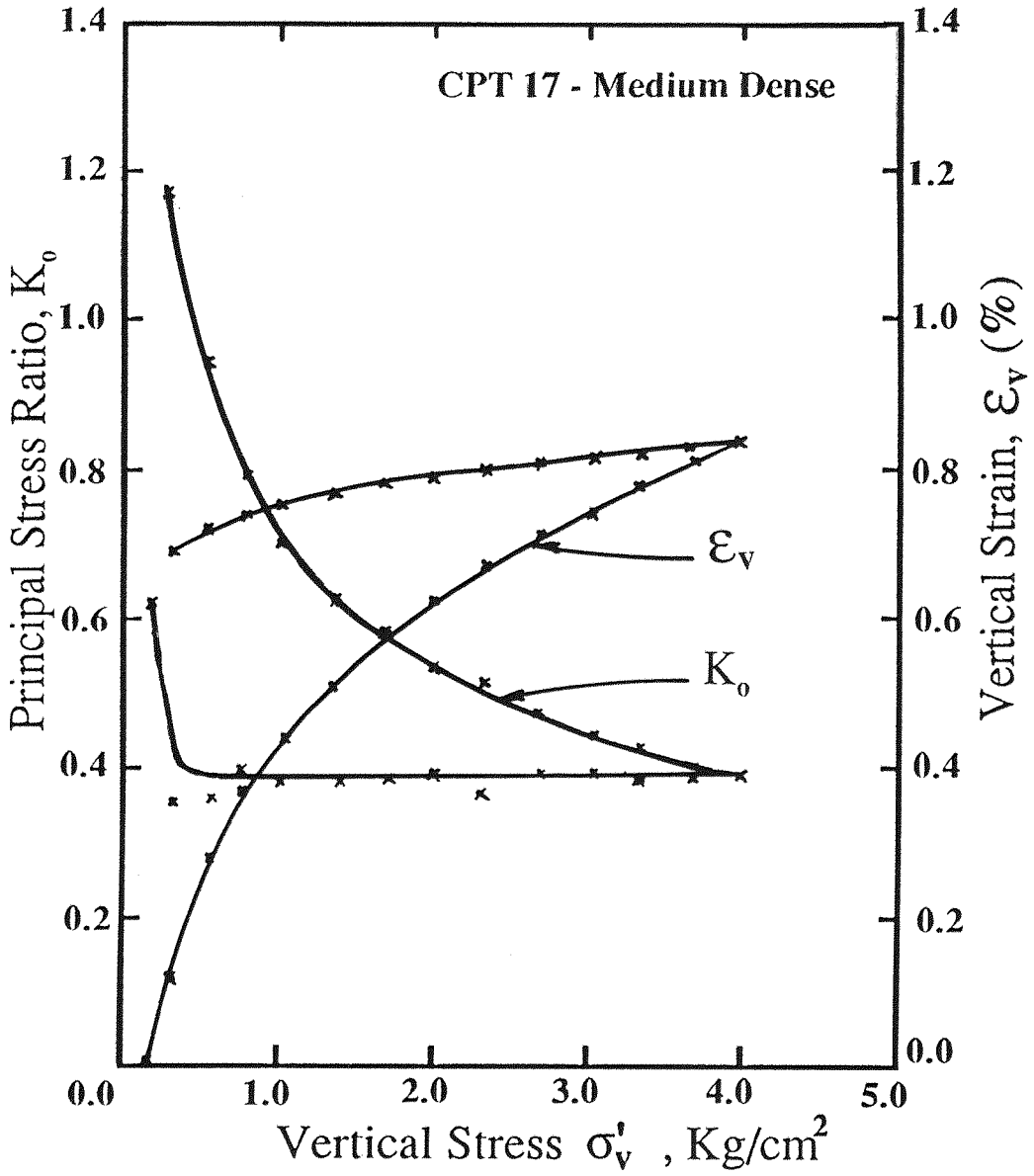

Fig 7.18 Principal Stress Ratio and Vertical Strain during Loading

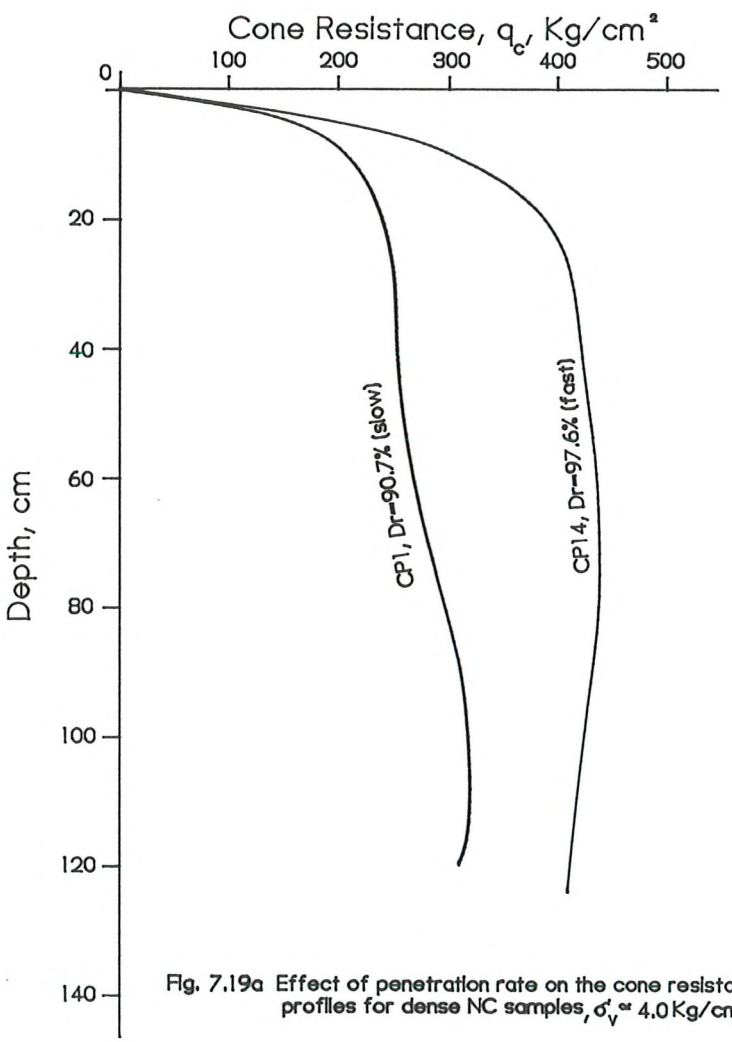

Fig. 7.19a Effect of penetration rate on the cone resistance profiles for dense NC samples, $\sigma'_v \simeq 4.0$ Kg/cm²

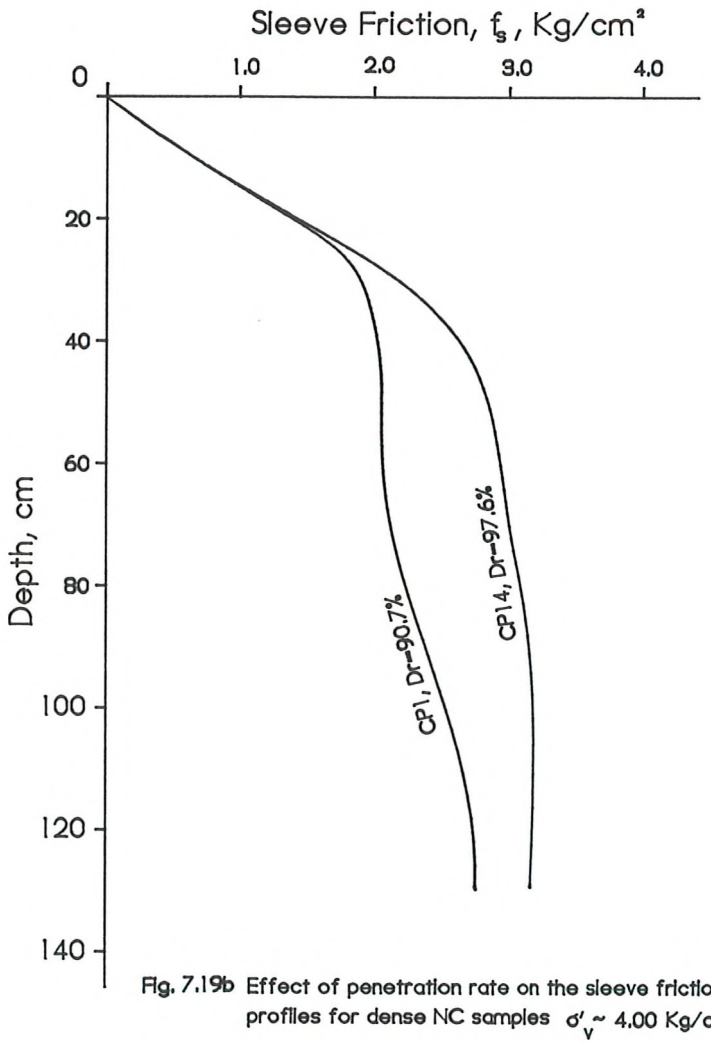

Fig. 7.19b Effect of penetration rate on the sleeve friction profiles for dense NC samples $\sigma'_v \sim 4.00$ Kg/cm²

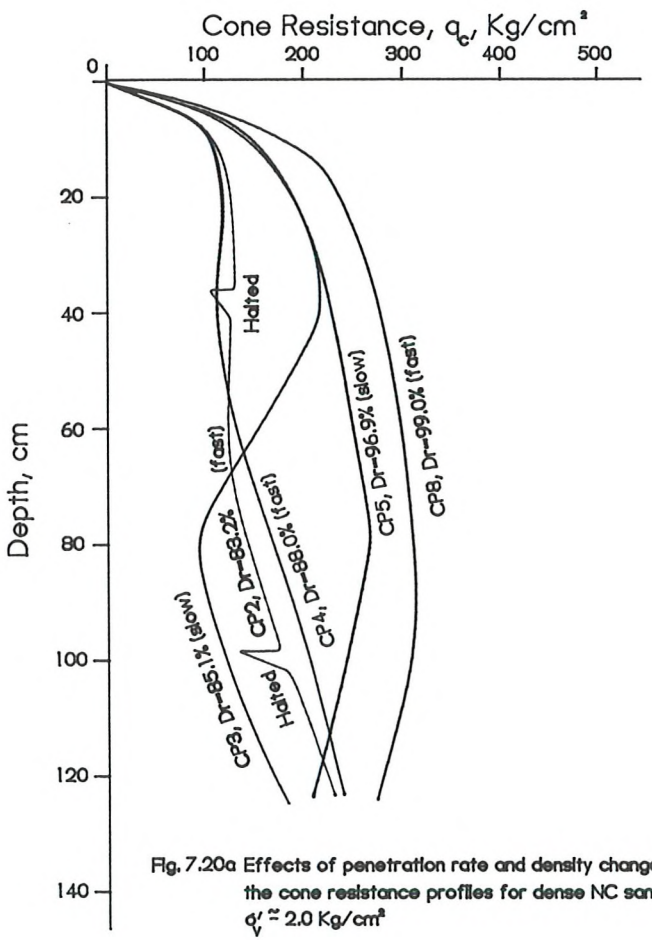

Fig. 7.20a Effects of penetration rate and density changes on the cone resistance profiles for dense NC samples, $\sigma'_v \simeq 2.0$ Kg/cm²

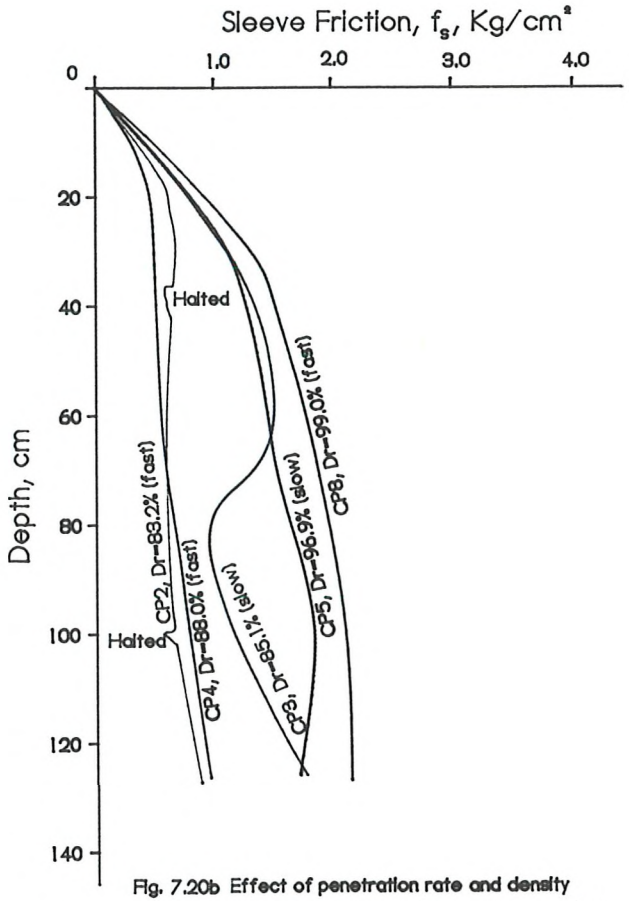

Fig. 7.20b Effect of penetration rate and density on sleeve friction profiles for NC samples $\sigma'_v \simeq 2.00$ Kg/cm²

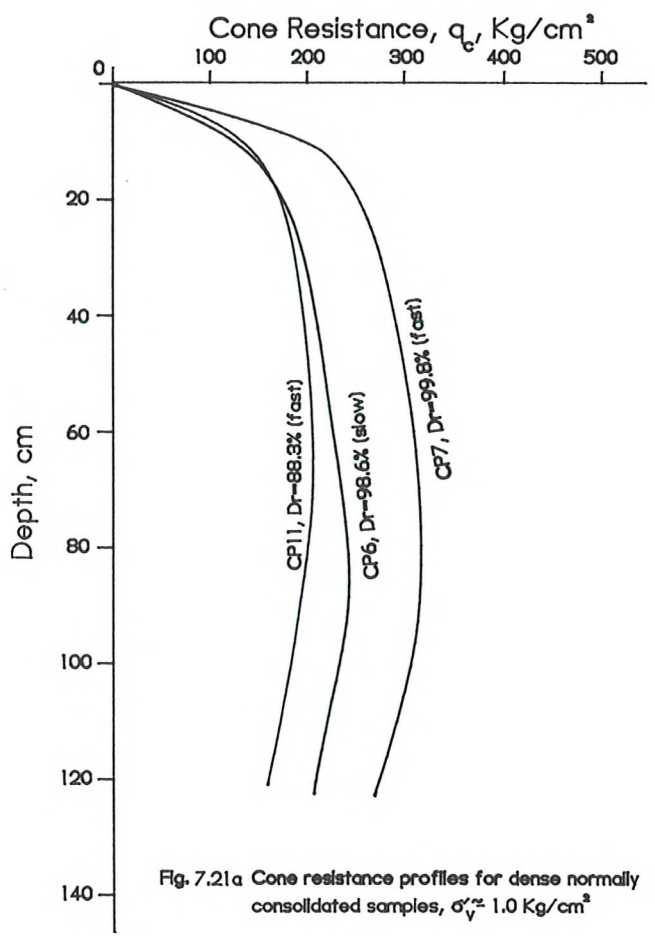

Fig. 7.21a Cone resistance profiles for dense normally consolidated samples, $\sigma'_v \simeq$ 1.0 Kg/cm²

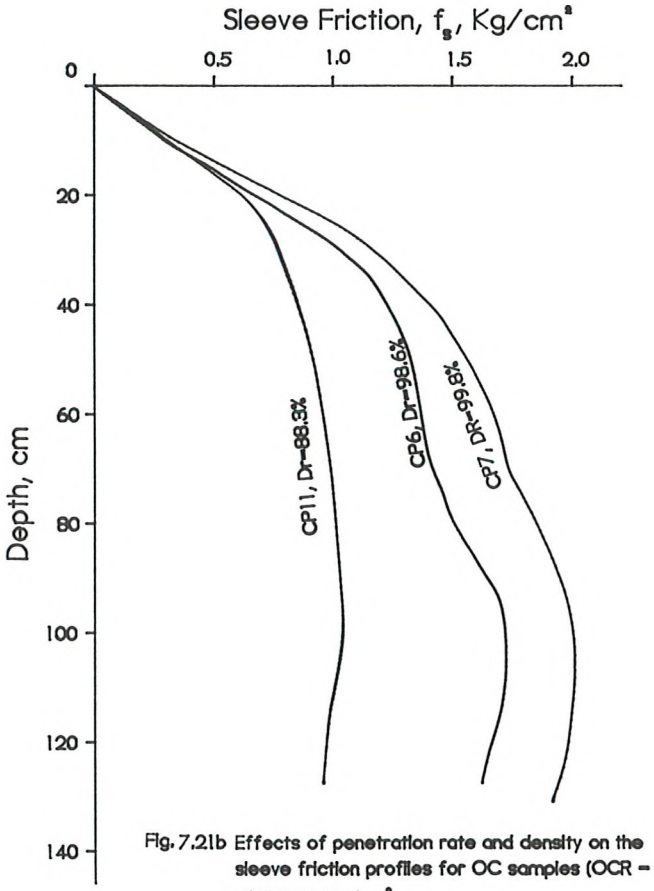

Fig. 7.21b Effects of penetration rate and density on the sleeve friction profiles for OC samples (OCR = 4) $\sigma'_v \simeq$ 1.00 Kg/cm²

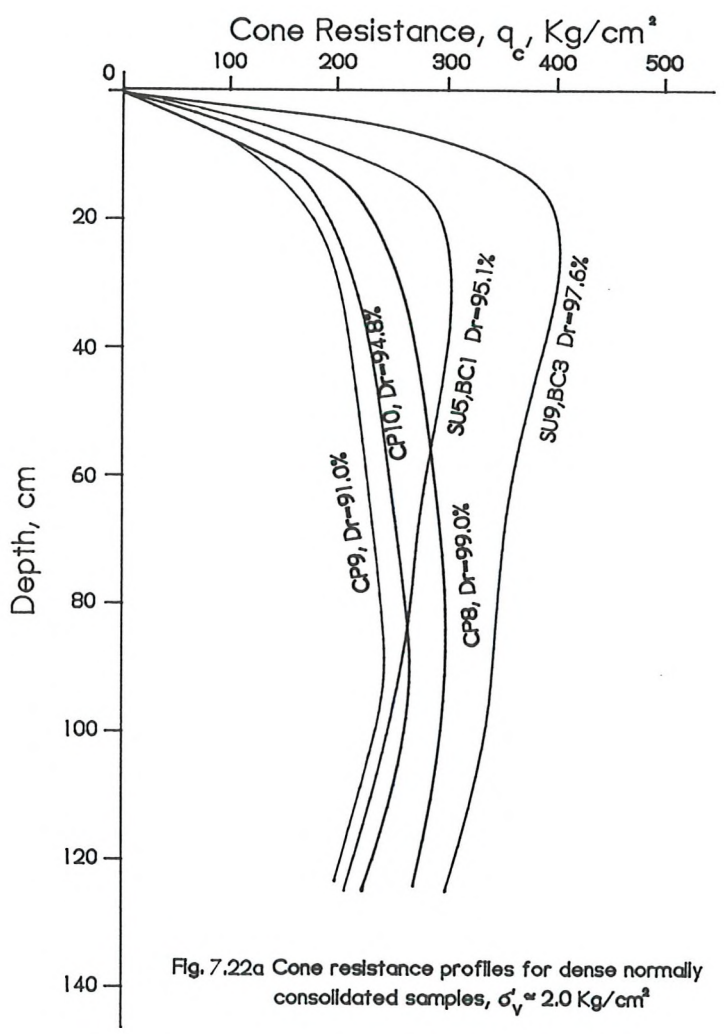

Fig. 7.22a Cone resistance profiles for dense normally consolidated samples, $\sigma'_v \simeq 2.0$ Kg/cm²

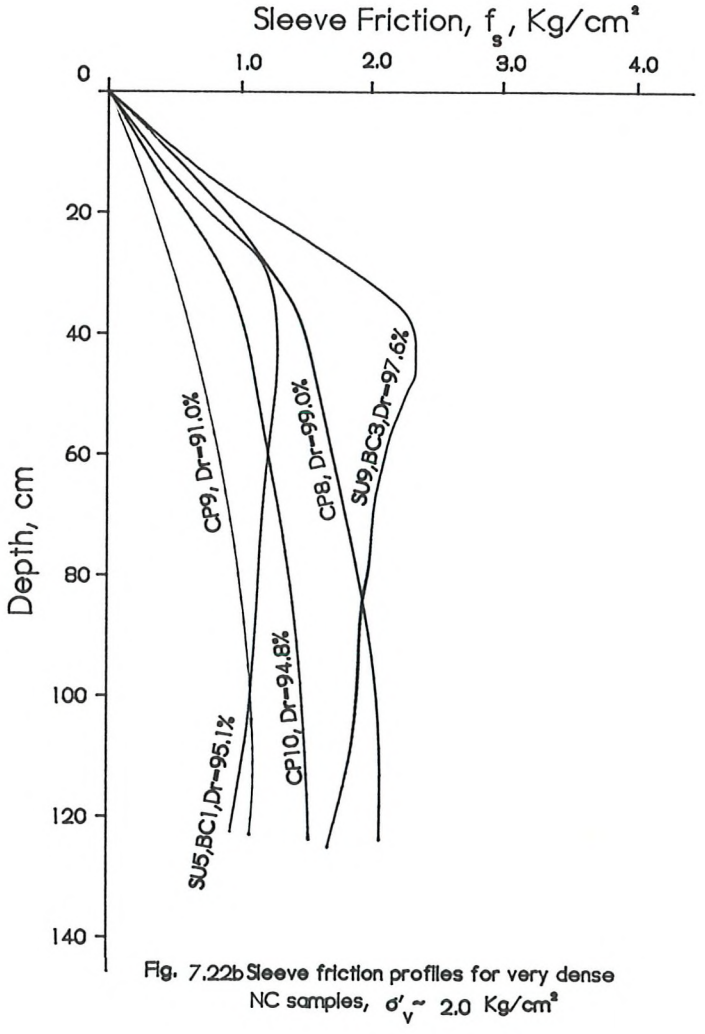

Fig. 7.22b Sleeve friction profiles for very dense NC samples, $\sigma'_v \sim$ 2.0 Kg/cm²

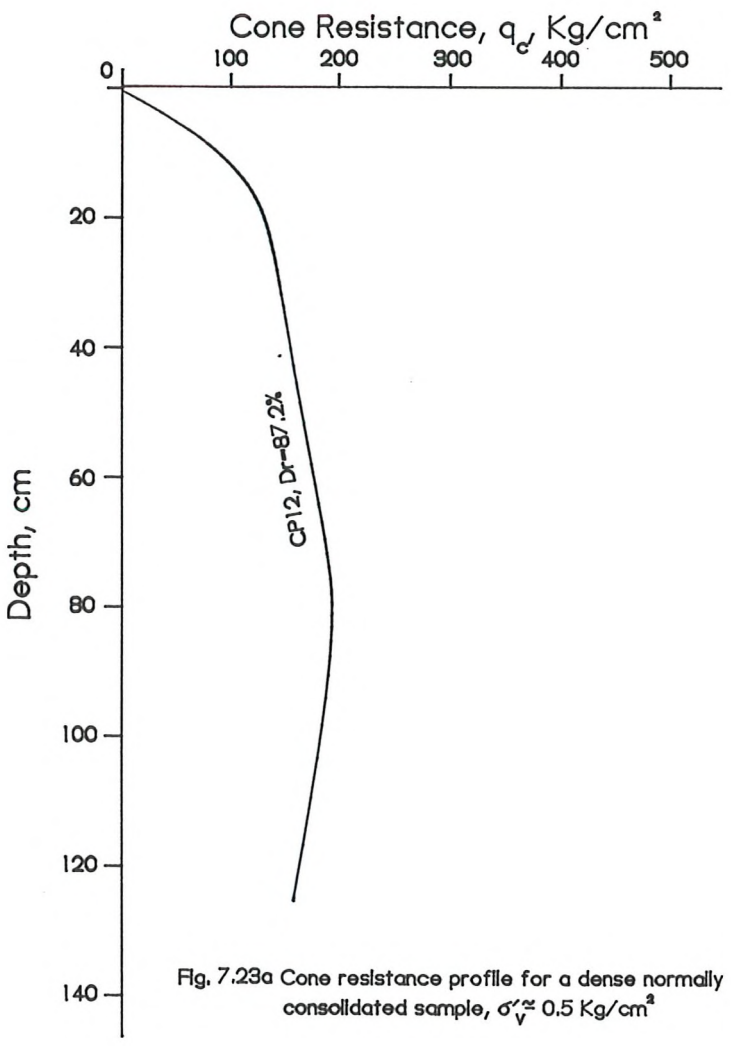

Fig. 7.23a Cone resistance profile for a dense normally consolidated sample, $\sigma'_v \simeq 0.5$ Kg/cm²

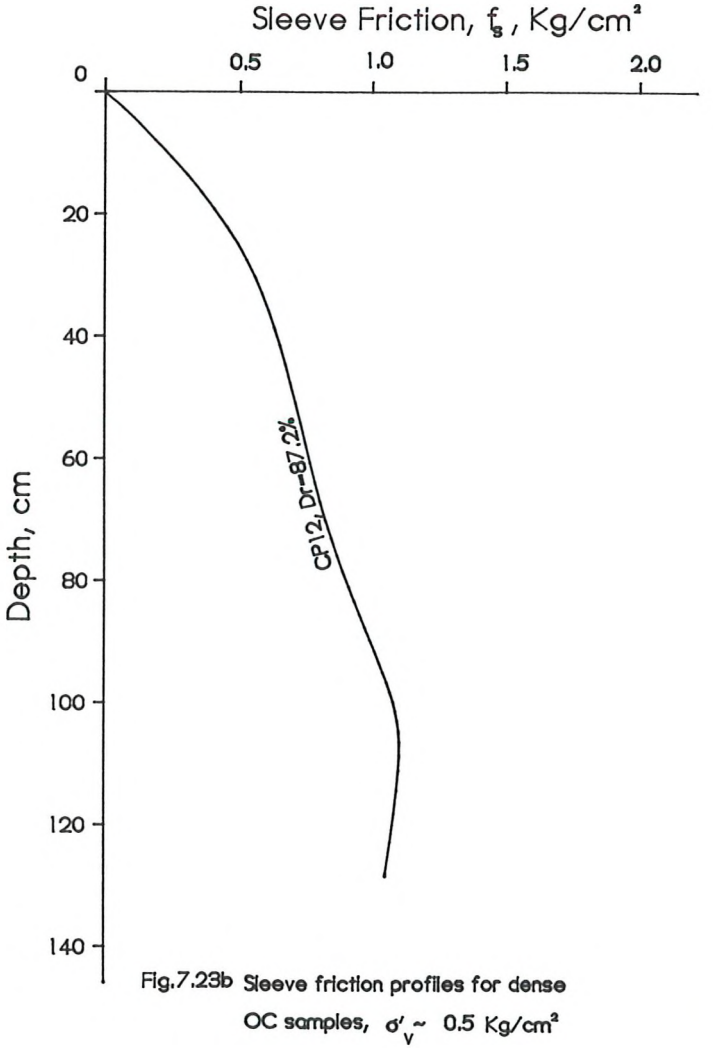

Fig.7.23b Sleeve friction profiles for dense OC samples, $\sigma'_v \sim 0.5$ Kg/cm²

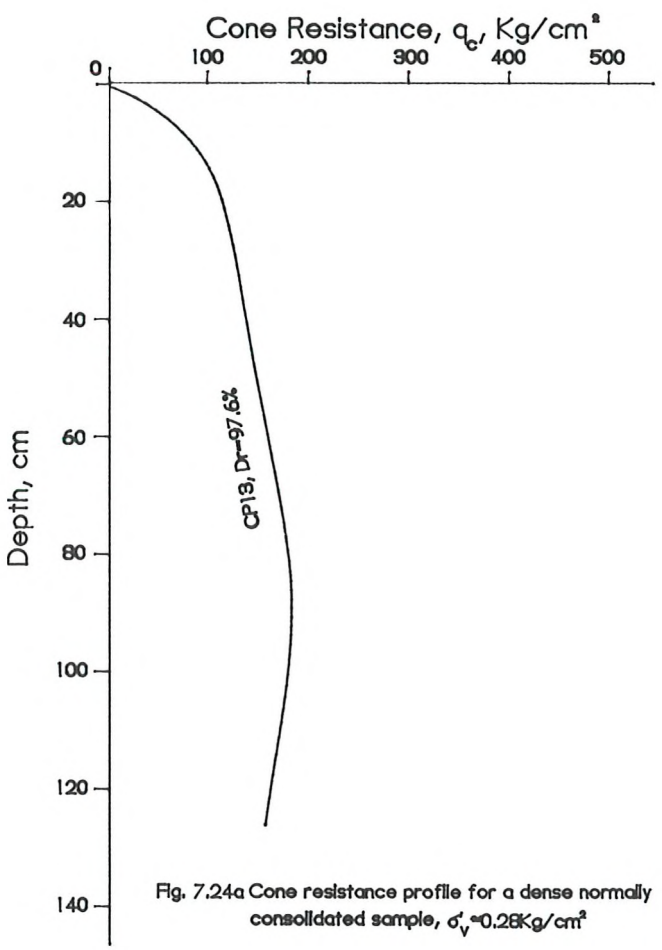

Fig. 7.24a Cone resistance profile for a dense normally consolidated sample, σ'_v=0.26Kg/cm²

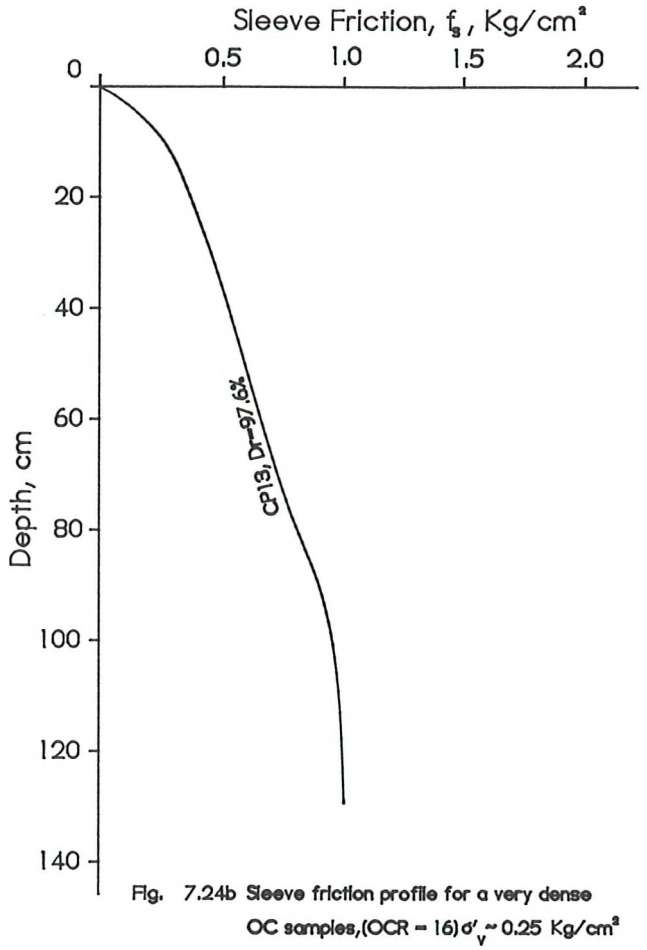

Fig. 7.24b Sleeve friction profile for a very dense OC samples,(OCR = 16) σ'_v = 0.25 Kg/cm²

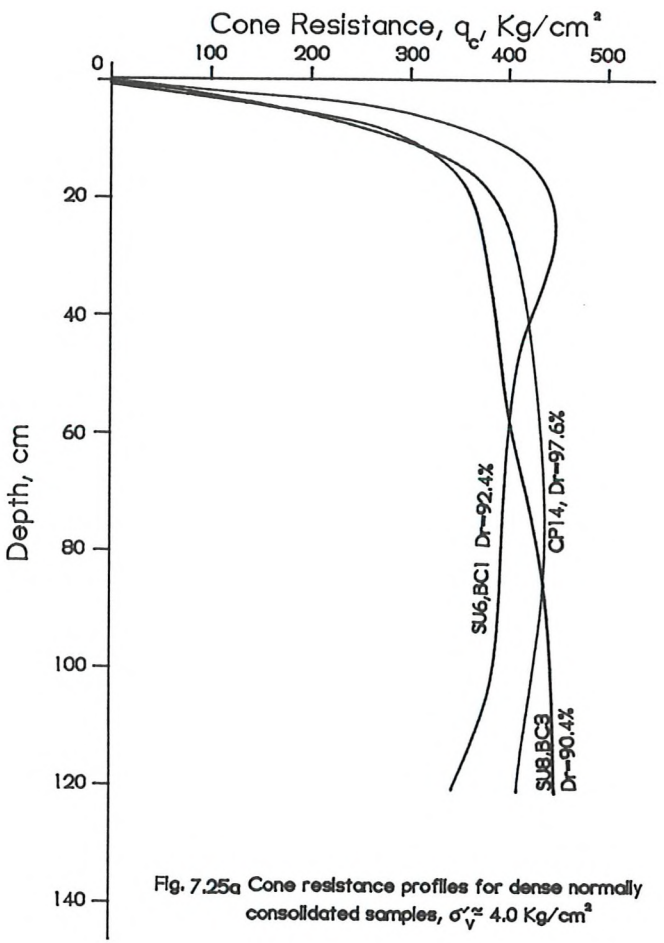

Fig. 7.25a Cone resistance profiles for dense normally consolidated samples, $\sigma'_v \simeq$ 4.0 Kg/cm²

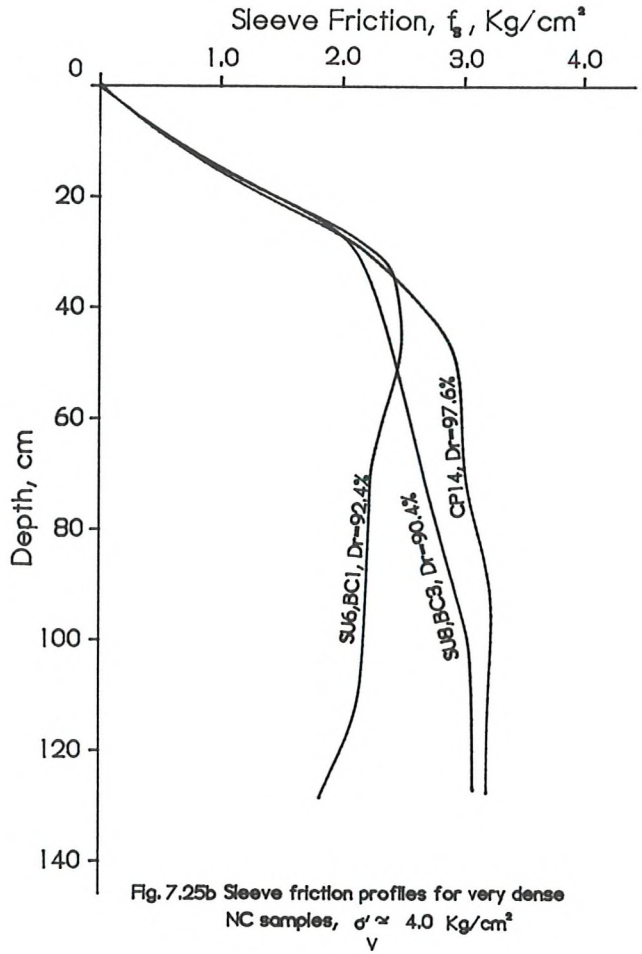

Fig. 7.25b Sleeve friction profiles for very dense NC samples, $\sigma'_v \simeq$ 4.0 Kg/cm²

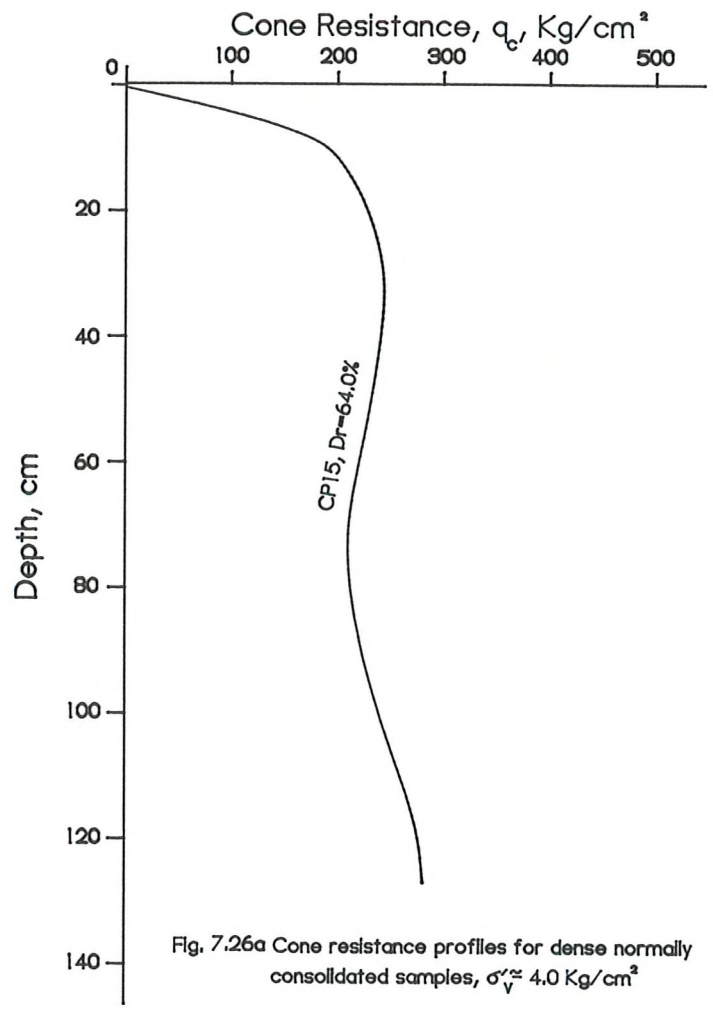

Fig. 7.26a Cone resistance profiles for dense normally consolidated samples, $\sigma'_v \simeq 4.0$ Kg/cm²

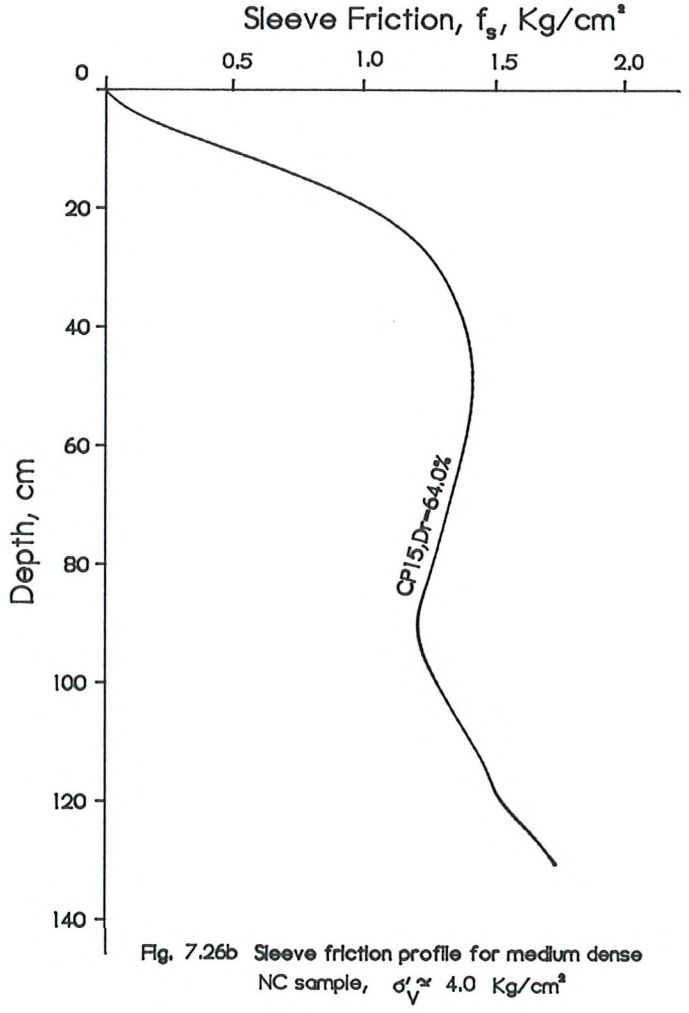

Fig. 7.26b Sleeve friction profile for medium dense NC sample, $\sigma'_v \simeq 4.0$ Kg/cm²

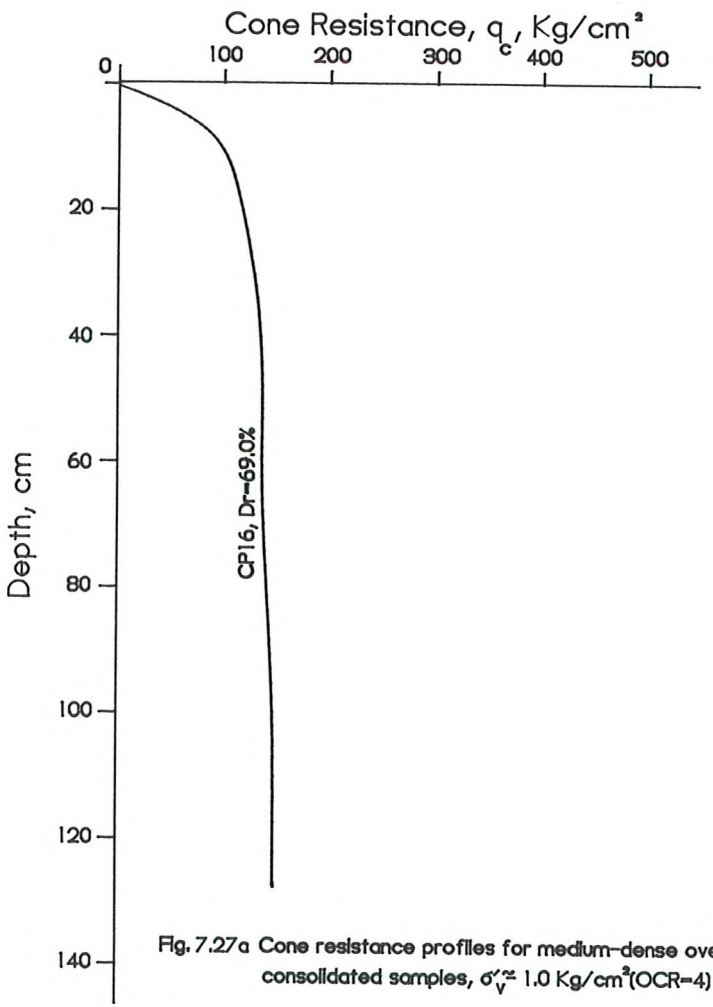

Fig. 7.27a Cone resistance profiles for medium-dense over-consolidated samples, $\sigma'_v \simeq$ 1.0 Kg/cm²(OCR=4)

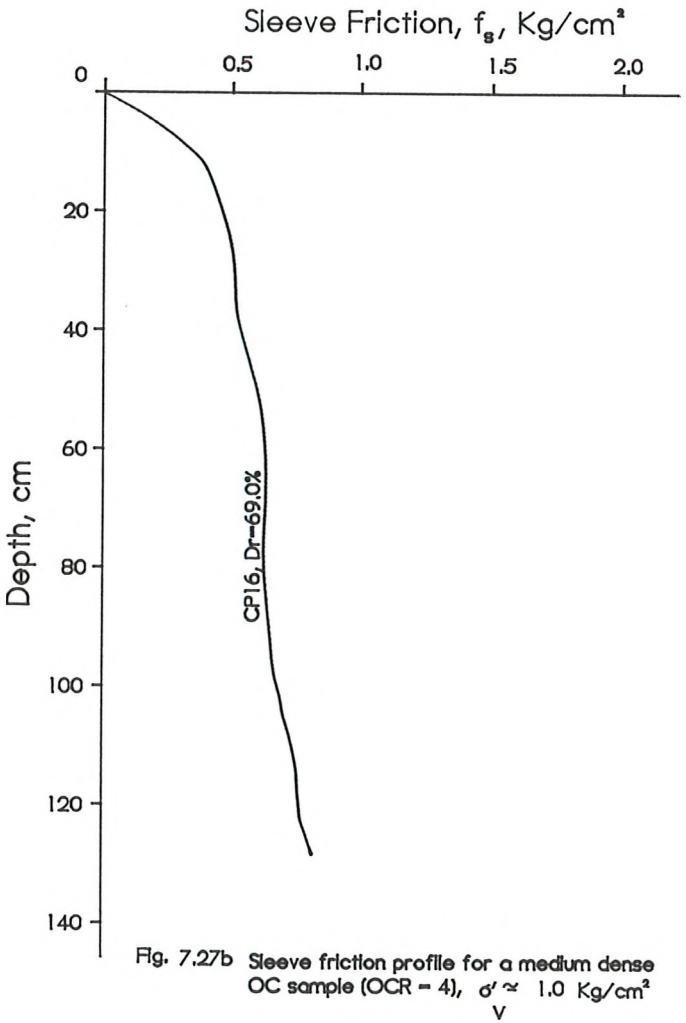

Fig. 7.27b Sleeve friction profile for a medium dense OC sample (OCR = 4), $\sigma'_v \simeq$ 1.0 Kg/cm²

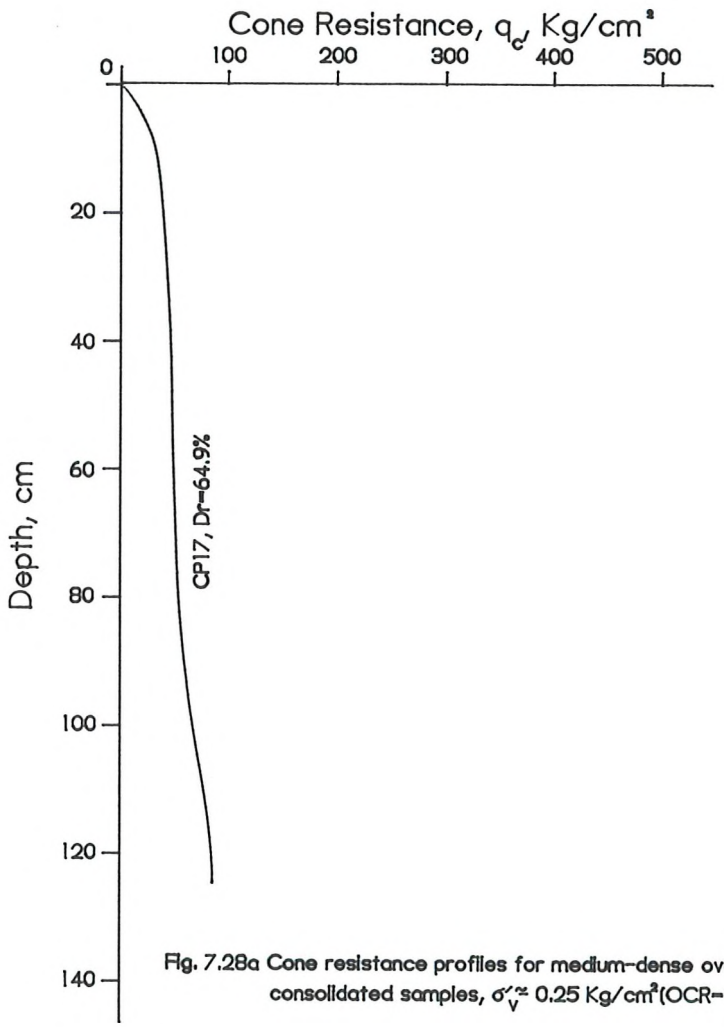

Fig. 7.28a Cone resistance profiles for medium-dense over-consolidated samples, $\sigma'_v \simeq 0.25$ Kg/cm² (OCR=16)

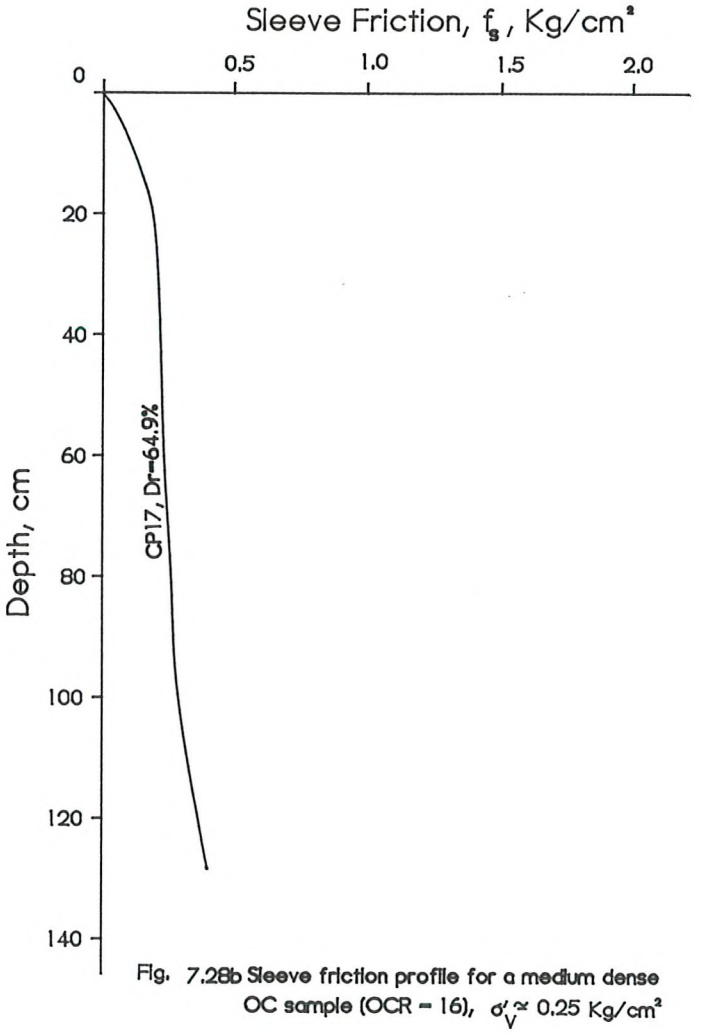

Fig. 7.28b Sleeve friction profile for a medium dense OC sample (OCR = 16), $\sigma'_v \simeq 0.25$ Kg/cm²

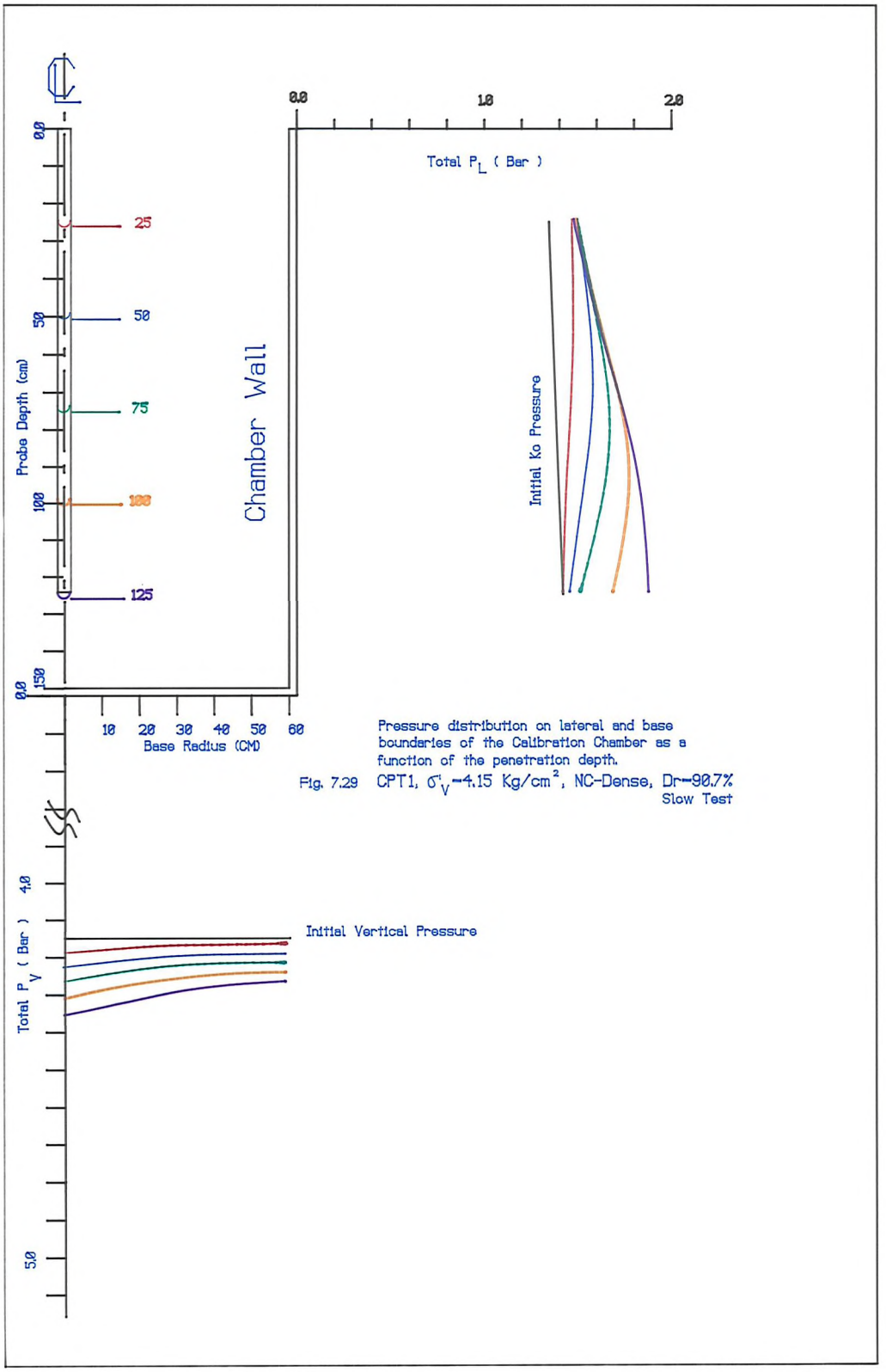

Pressure distribution on lateral and base boundaries of the Calibration Chamber as a function of the penetration depth.

Fig. 7.29 CPT1, σ'_V=4.15 Kg/cm^2, NC-Dense, Dr=90.7% Slow Test

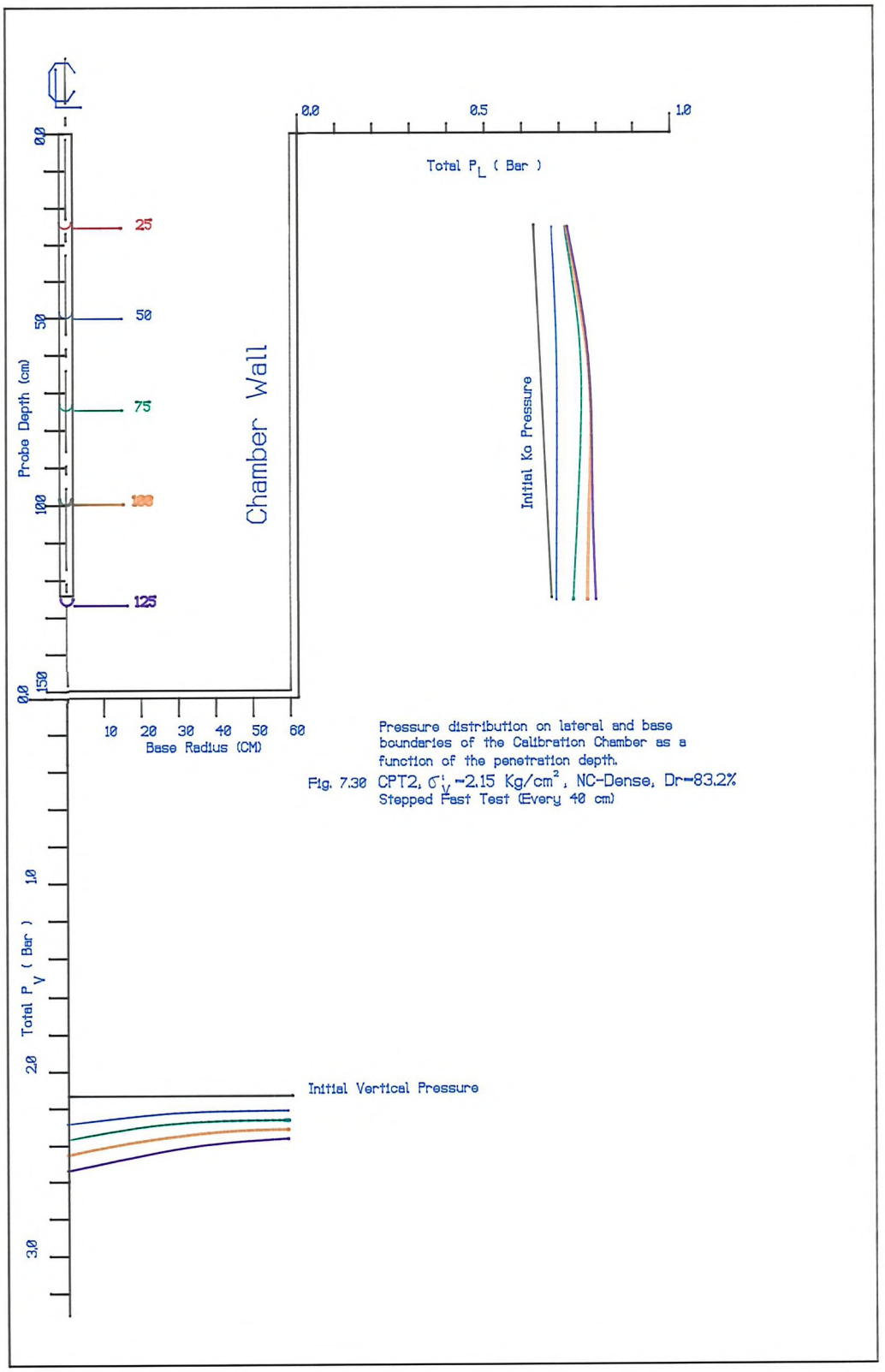

Pressure distribution on lateral and base boundaries of the Calibration Chamber as a function of the penetration depth.

Fig. 7.30 CPT2, σ'_V =2.15 Kg/cm^2, NC-Dense, Dr=83.2% Stepped Fast Test (Every 40 cm)

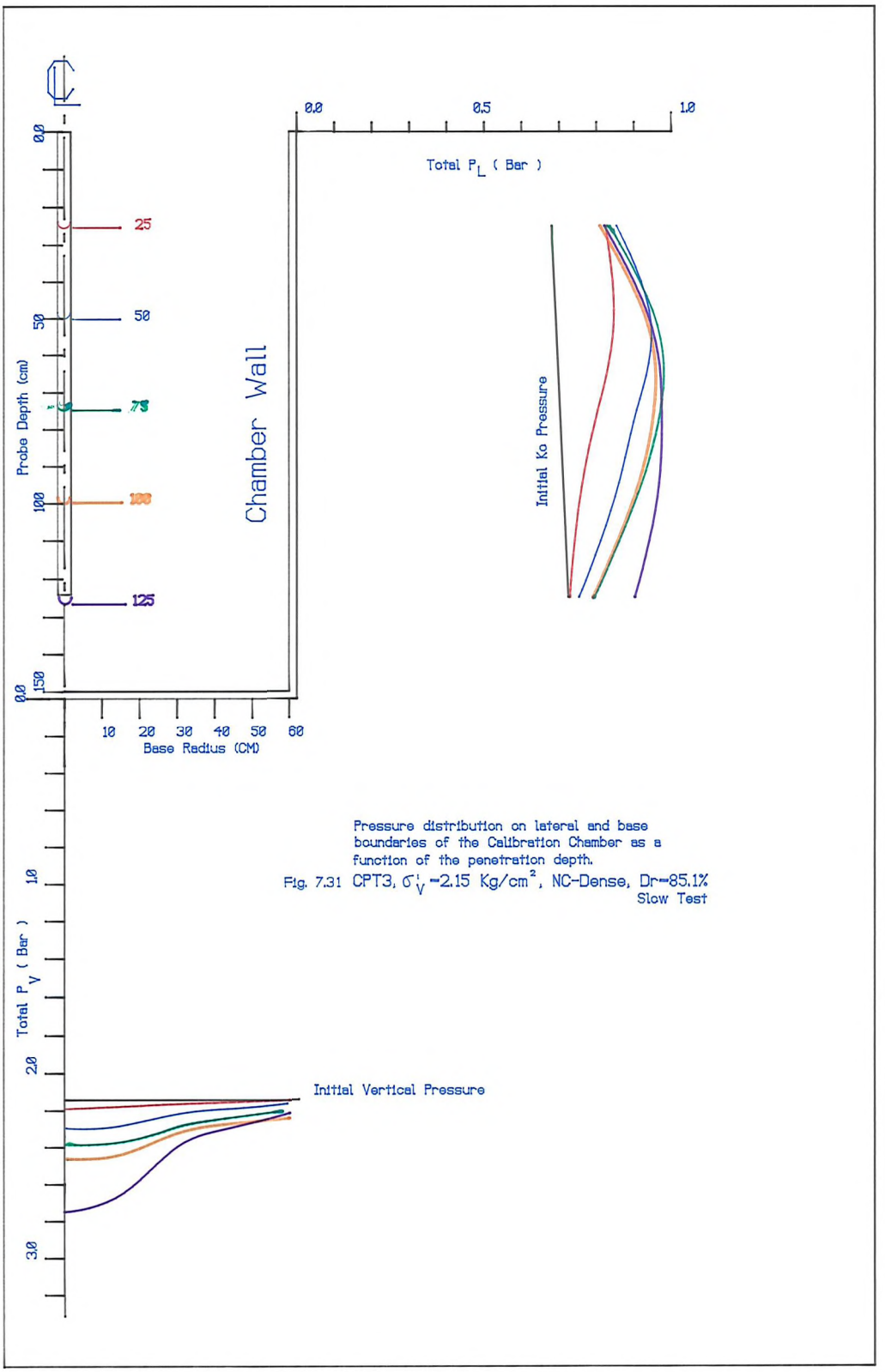

Pressure distribution on lateral and base boundaries of the Calibration Chamber as a function of the penetration depth.

Fig. 7.31 CPT3, σ'_V =2.15 Kg/cm^2, NC-Dense, Dr=85.1%
Slow Test

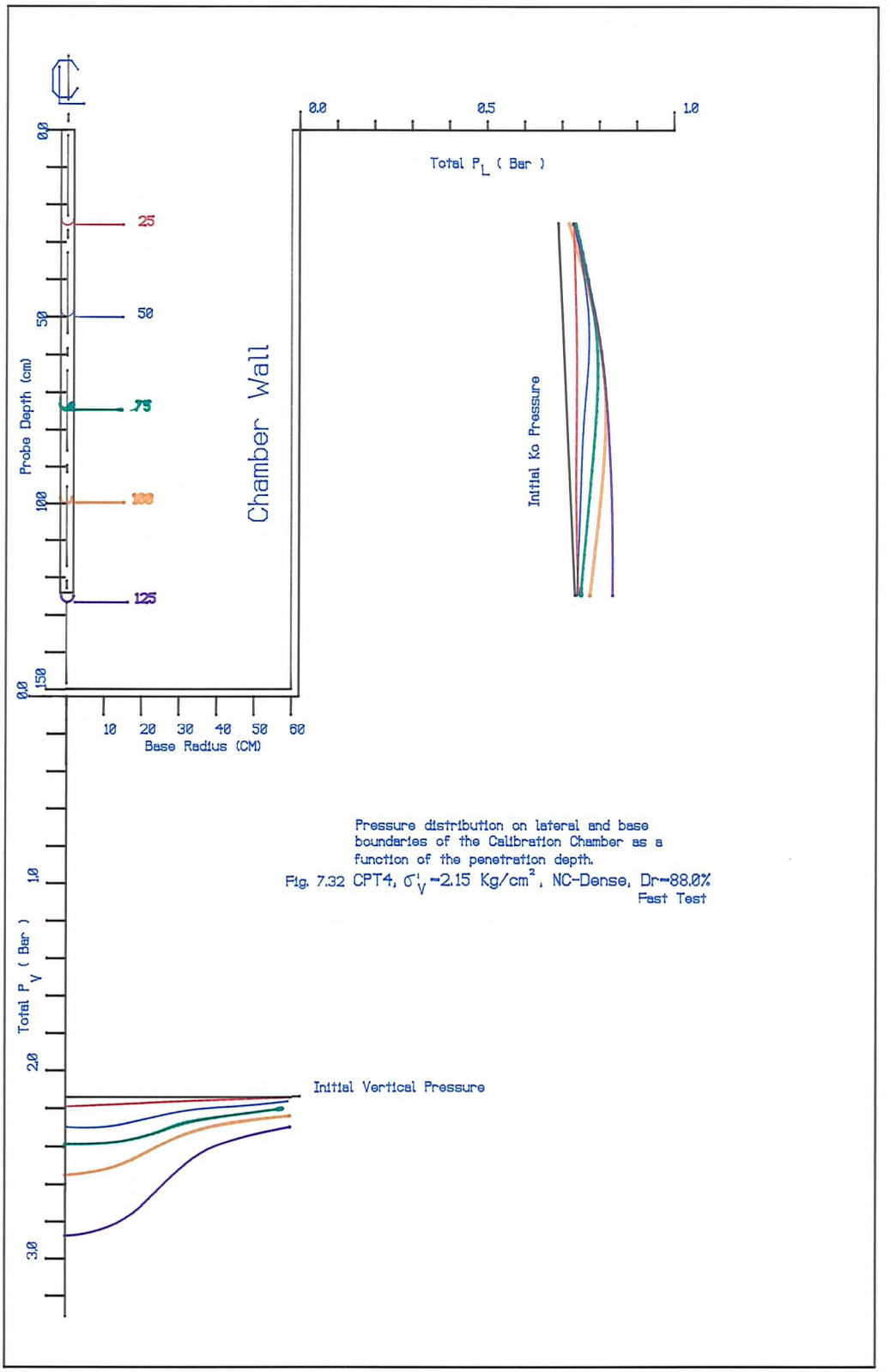

Pressure distribution on lateral and base boundaries of the Calibration Chamber as a function of the penetration depth.

Fig. 7.32 CPT4, σ'_V=2.15 Kg/cm^2, NC-Dense, Dr=88.0%
Fast Test

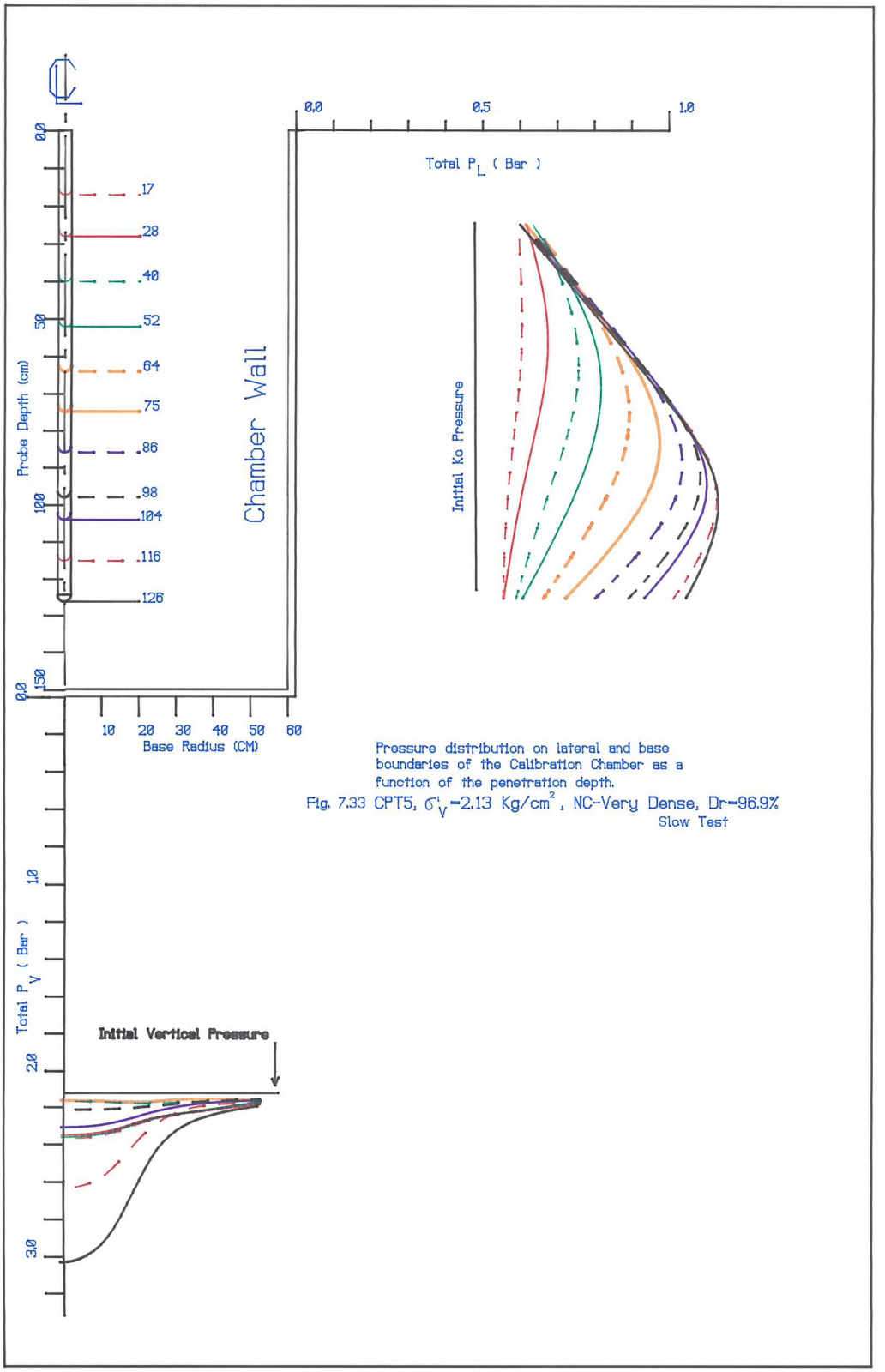

Pressure distribution on lateral and base boundaries of the Calibration Chamber as a function of the penetration depth.

Fig. 7.33 CPT5, σ'_V=2.13 Kg/cm^2, NC-Very Dense, Dr=96.9%
Slow Test

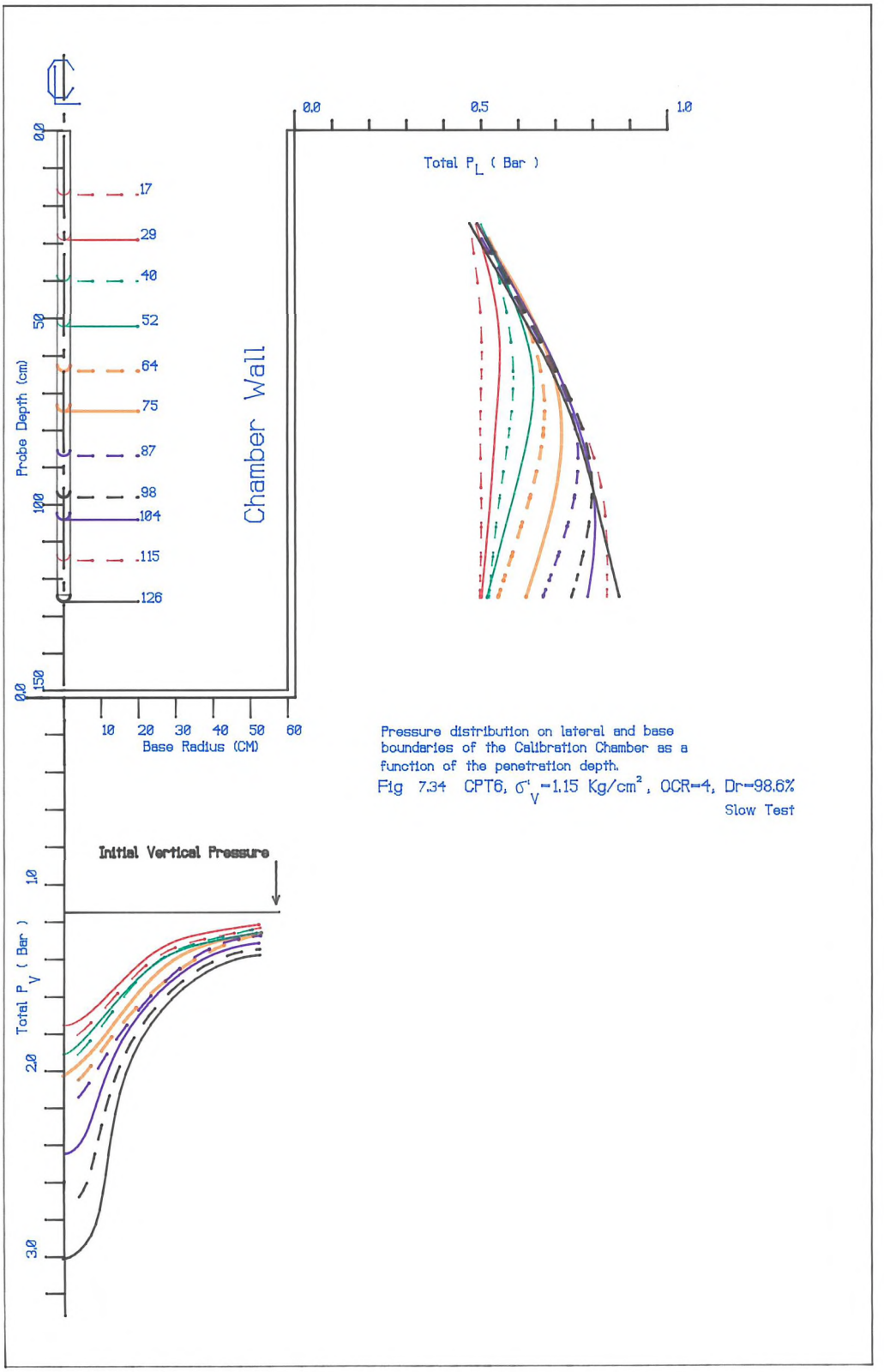

Pressure distribution on lateral and base boundaries of the Calibration Chamber as a function of the penetration depth.

Fig 7.34 CPT6, σ'_V=1.15 Kg/cm^2, OCR=4, Dr=98.6%
Slow Test

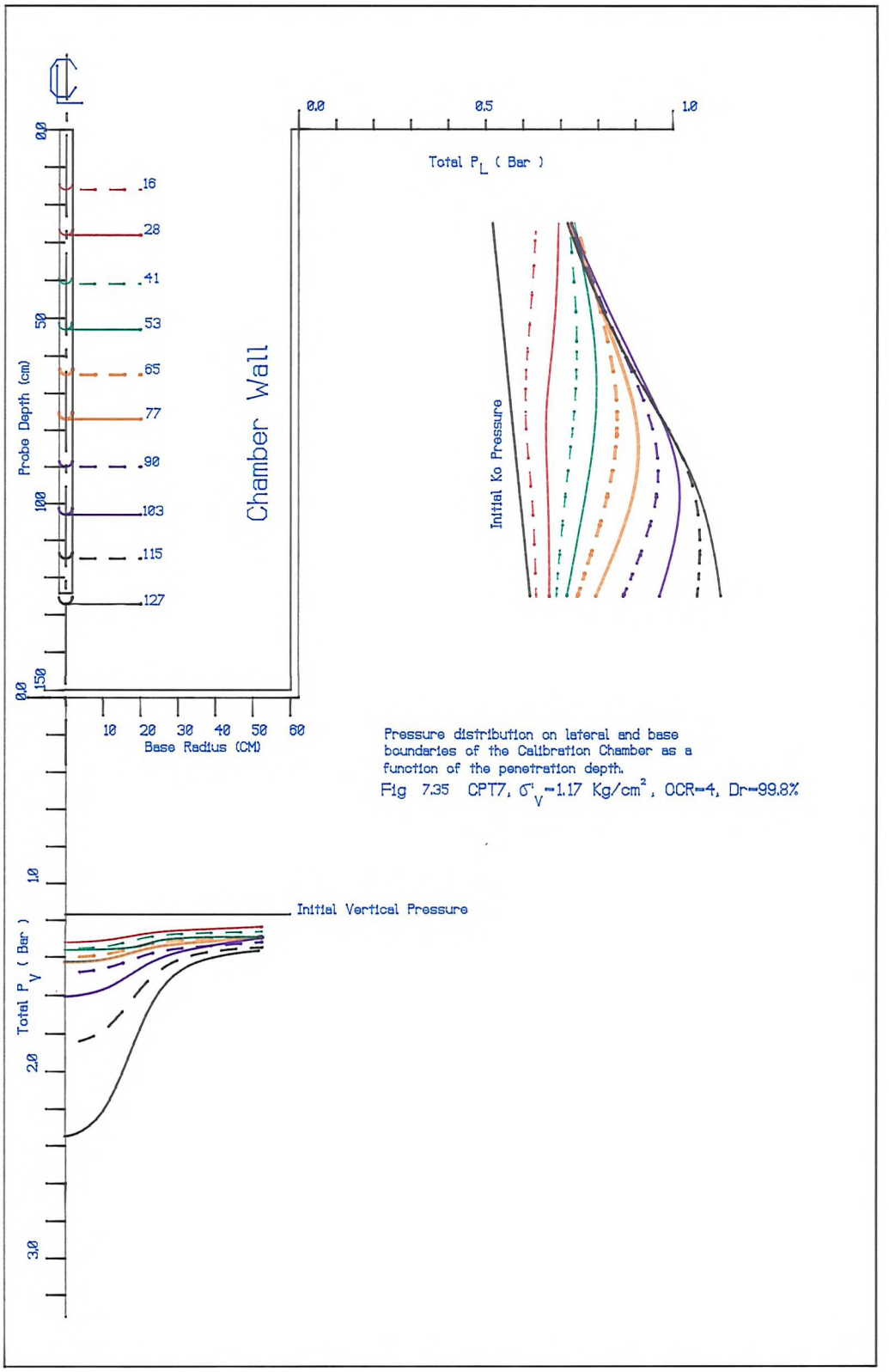

Pressure distribution on lateral and base boundaries of the Calibration Chamber as a function of the penetration depth.

Fig 7.35 CPT7, σ'_V=1.17 Kg/cm^2, OCR=4, Dr=99.8%

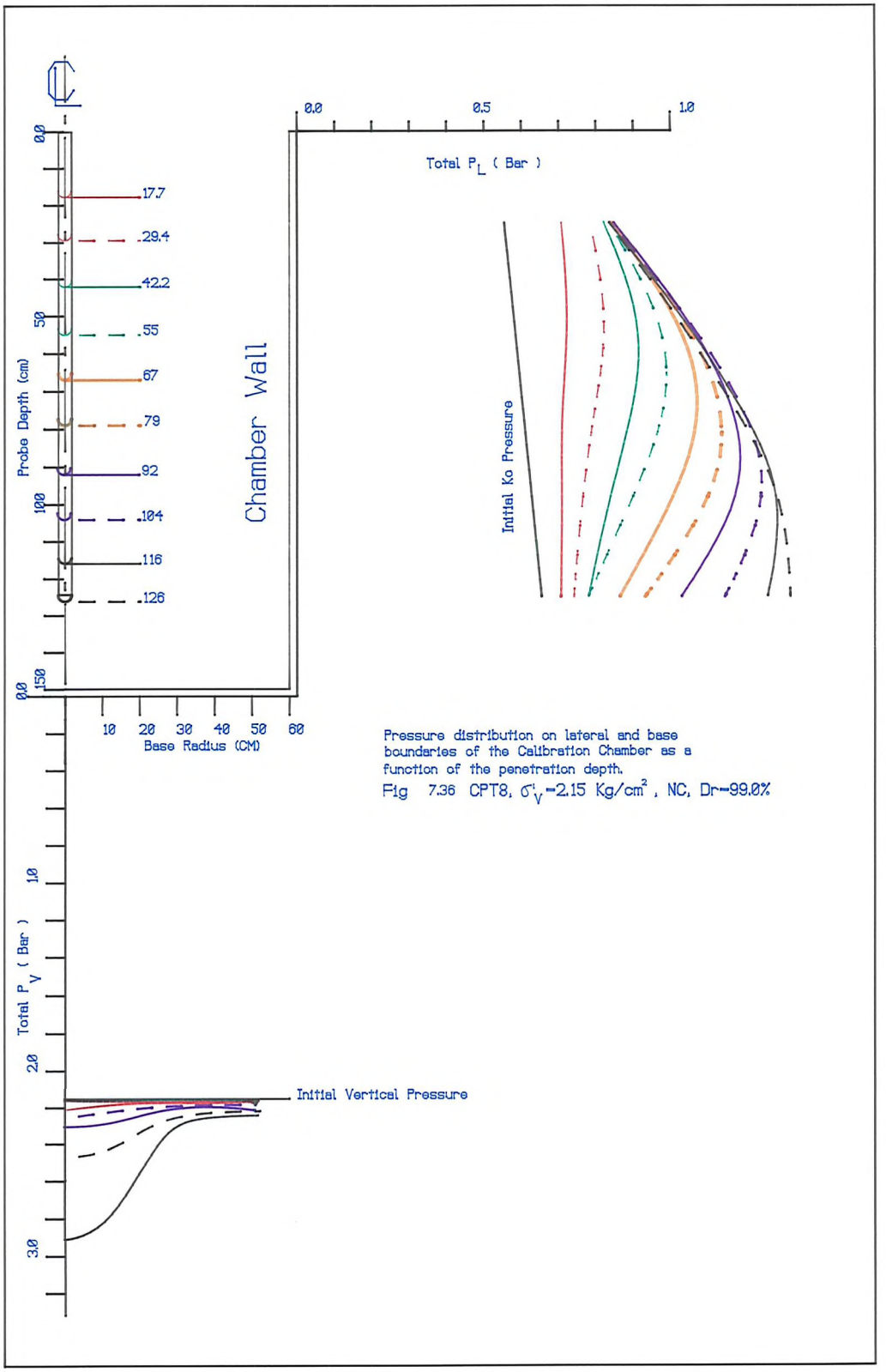

Pressure distribution on lateral and base boundaries of the Calibration Chamber as a function of the penetration depth.

Fig 7.36 CPT8, σ'_V=2.15 Kg/cm^2, NC, Dr=99.0%

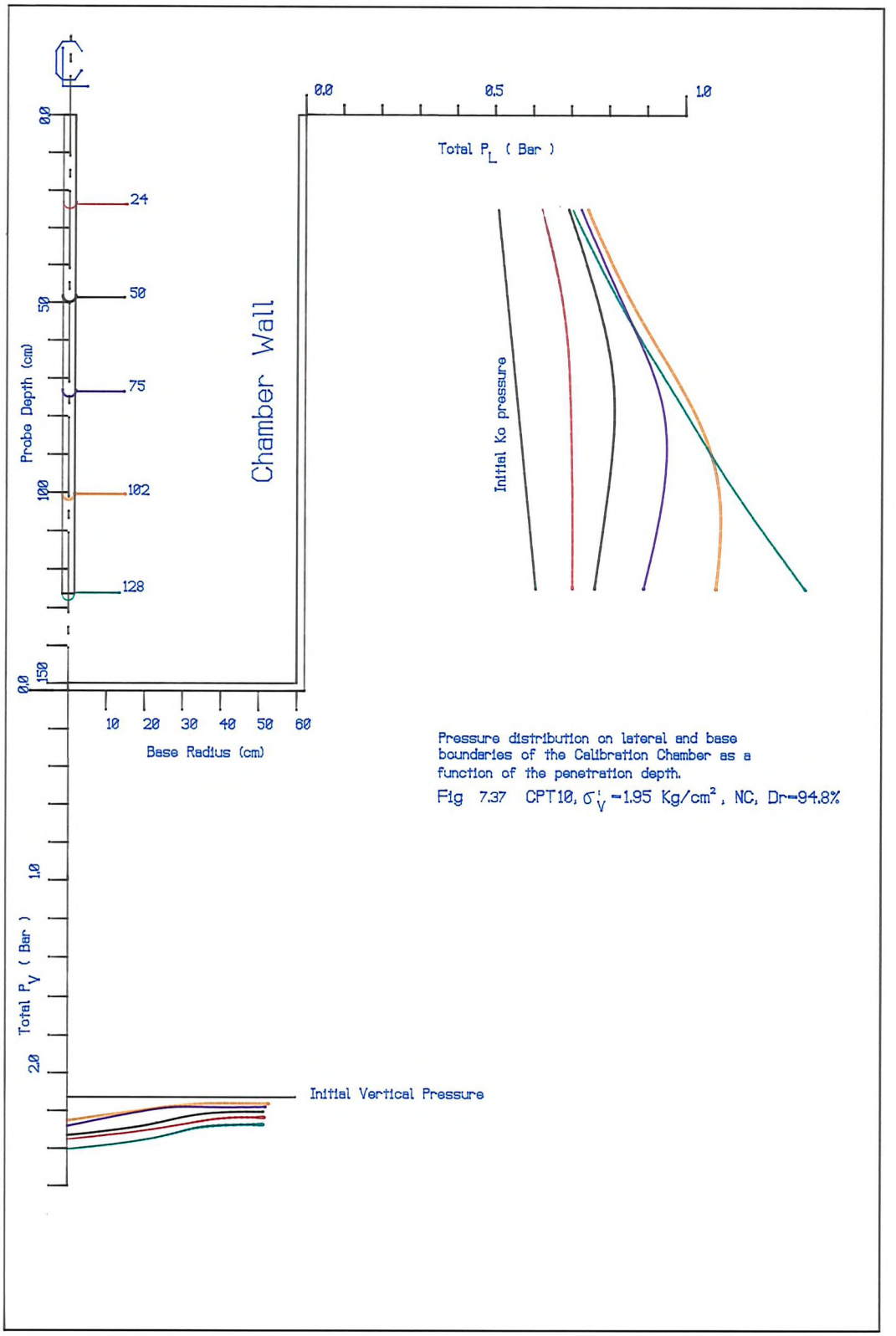

Pressure distribution on lateral and base boundaries of the Calibration Chamber as a function of the penetration depth.

Fig 7.37 CPT10, σ'_V =1.95 Kg/cm^2, NC, Dr=94.8%

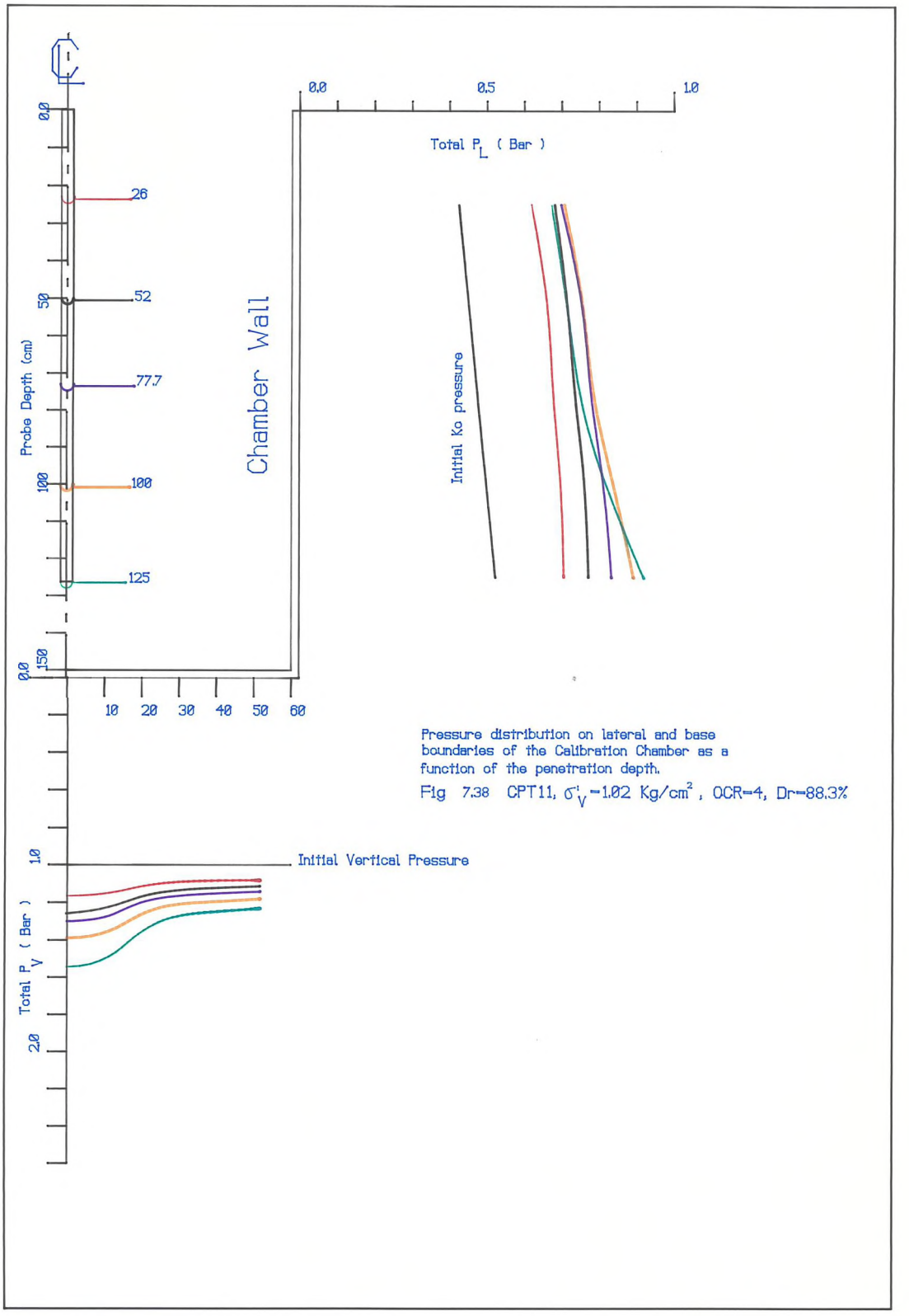

Pressure distribution on lateral and base boundaries of the Calibration Chamber as a function of the penetration depth.

Fig 7.38 CPT11, σ'_V=1.02 Kg/cm^2, OCR=4, Dr=88.3%

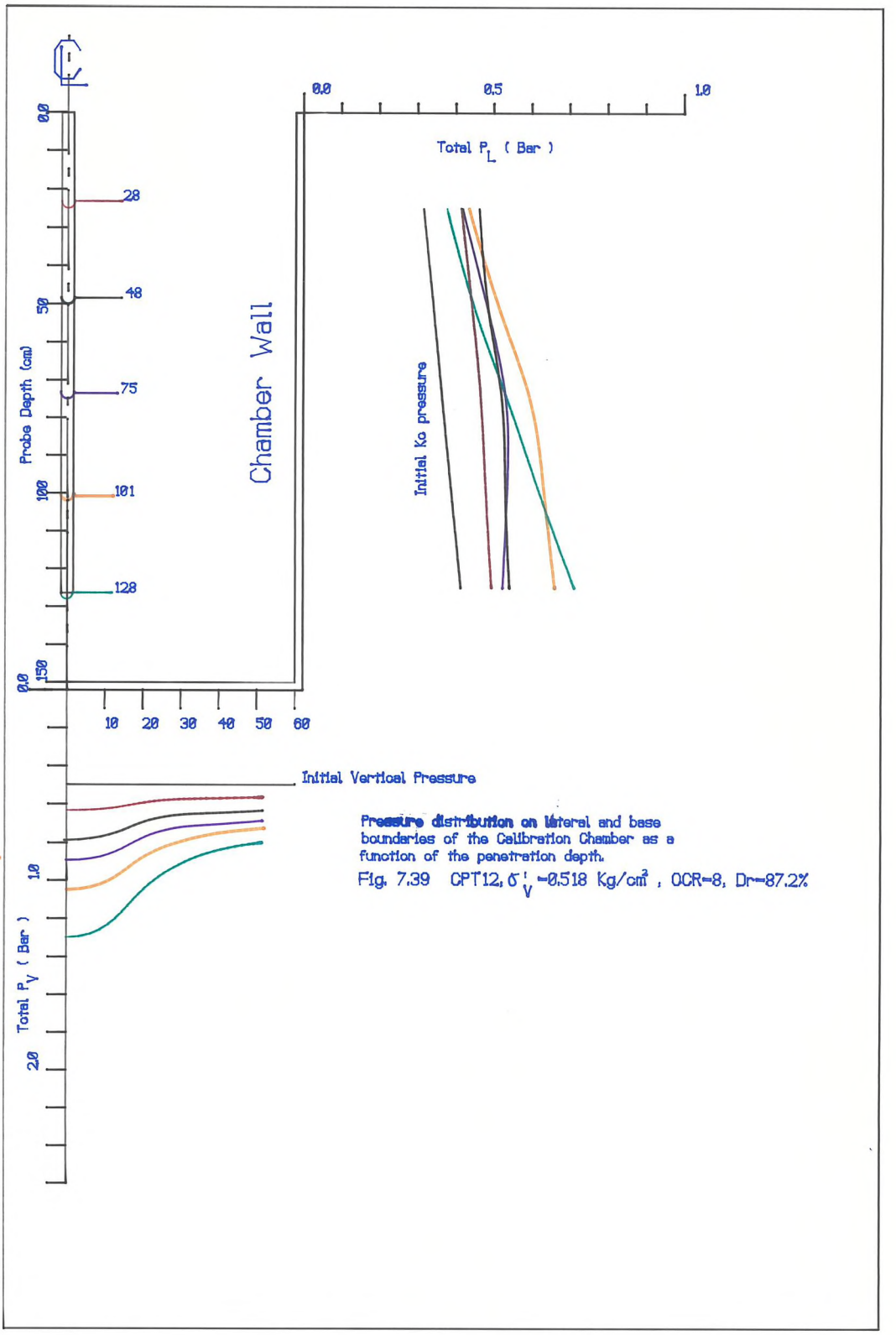

Pressure distribution on lateral and base boundaries of the Calibration Chamber as a function of the penetration depth.

Fig. 7.39 CPT12, σ'_V =0.518 Kg/cm^2 , OCR=8, Dr=87.2%

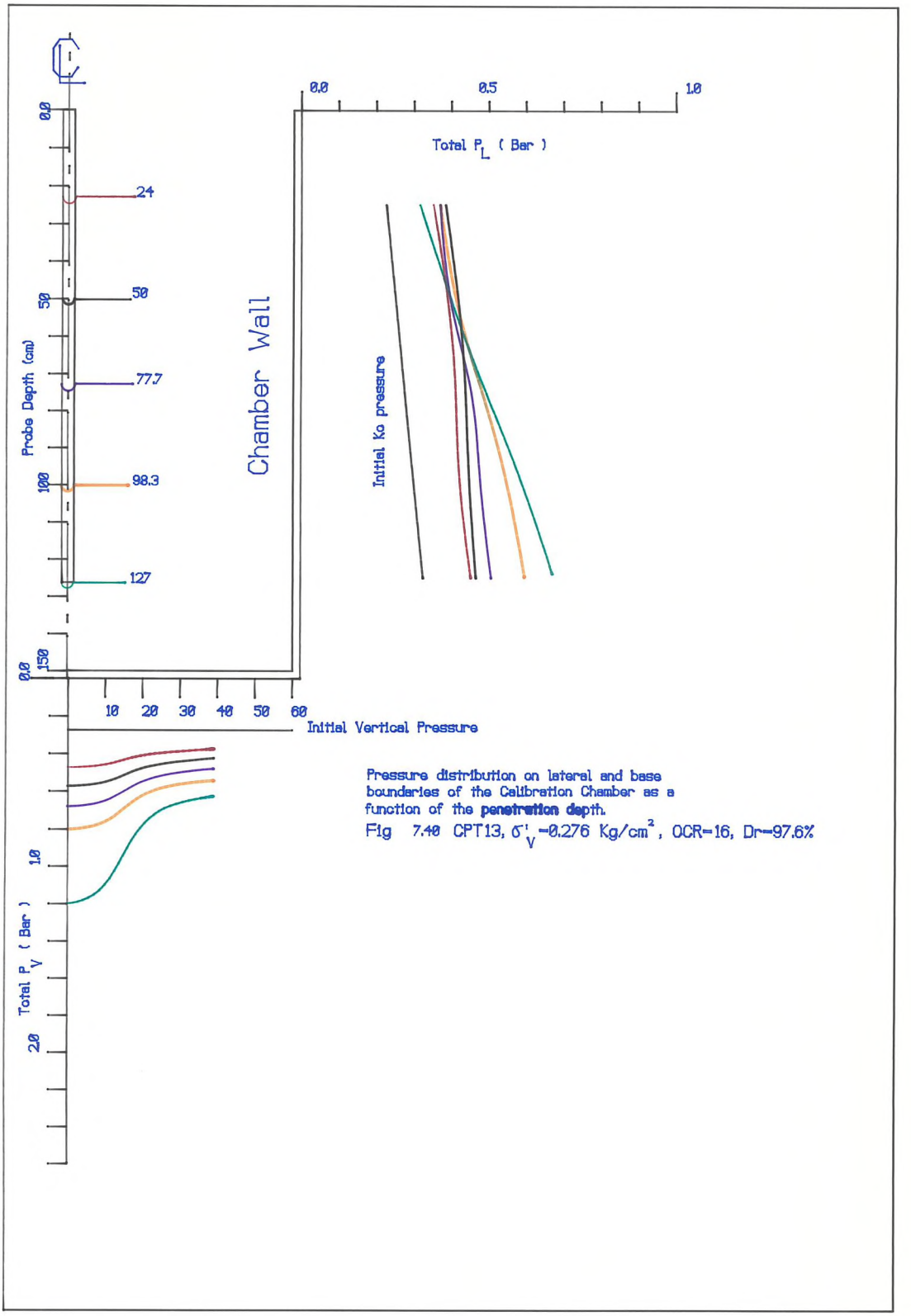

Pressure distribution on lateral and base boundaries of the Calibration Chamber as a function of the **penetration depth**.

Fig 7.40 CPT13, σ'_V=0.276 Kg/cm^2, OCR=16, Dr=97.6%

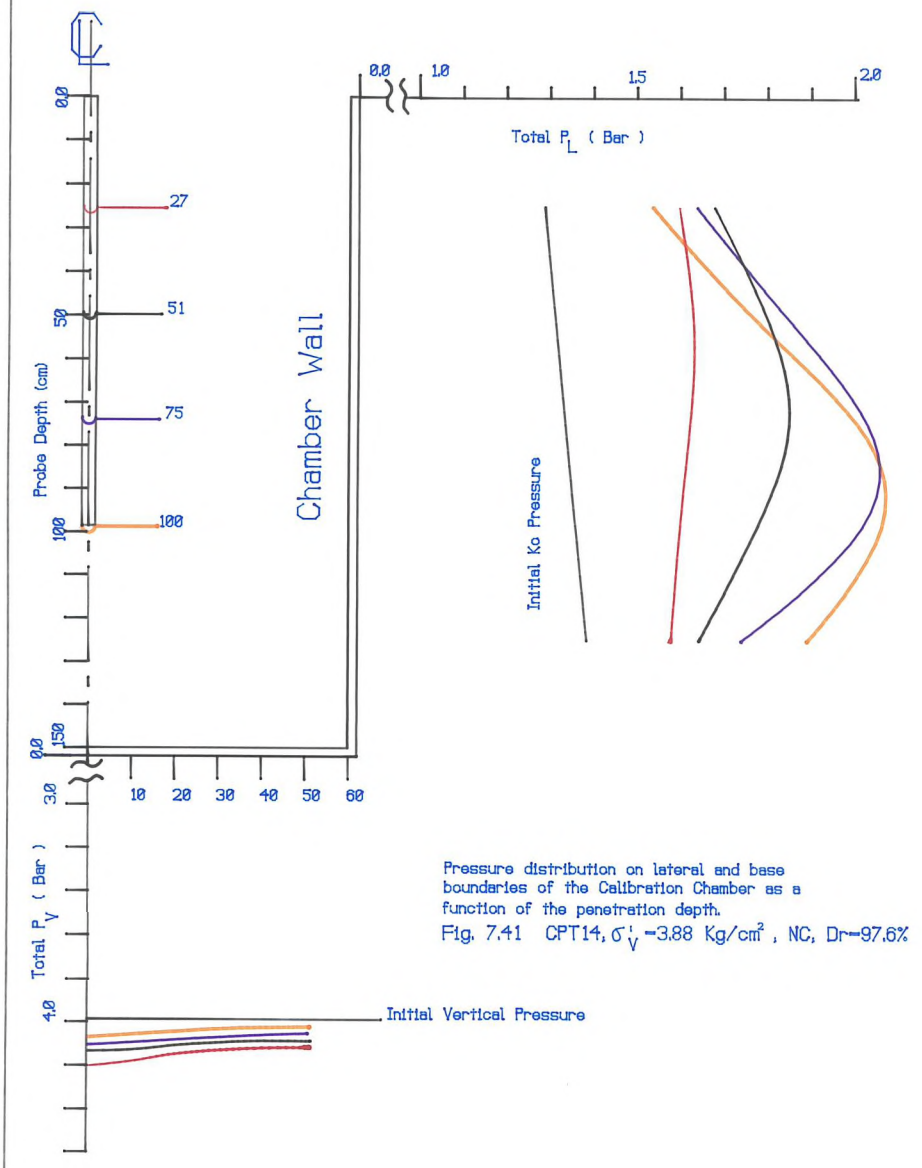

Pressure distribution on lateral and base boundaries of the Calibration Chamber as a function of the penetration depth.

Fig. 7.41 CPT14, σ'_V =3.88 Kg/cm^2 , NC, Dr=97.6%

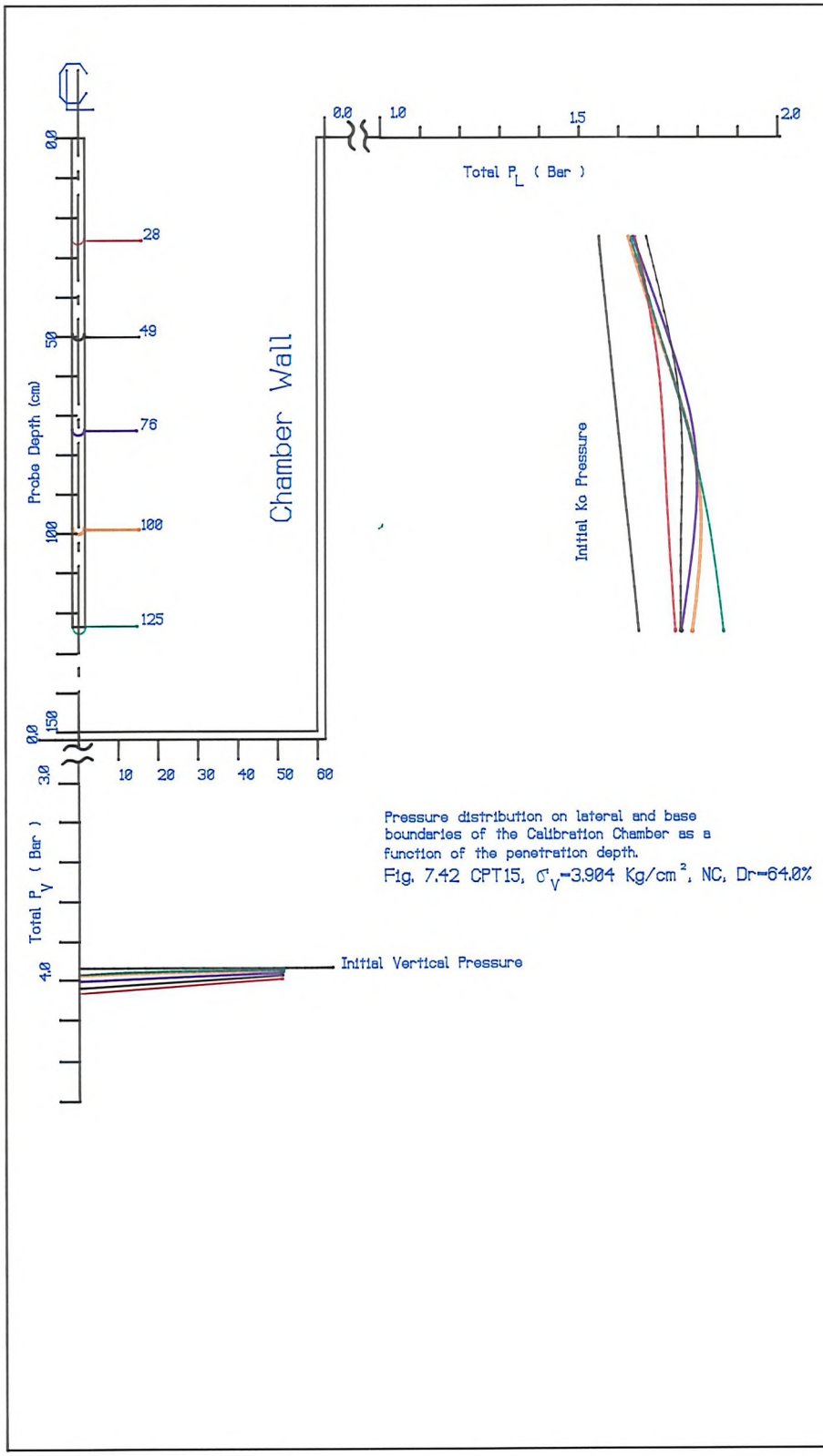

Pressure distribution on lateral and base boundaries of the Calibration Chamber as a function of the penetration depth.

Fig. 7.42 CPT15, σ'_V=3.904 Kg/cm^2, NC, Dr=64.0%

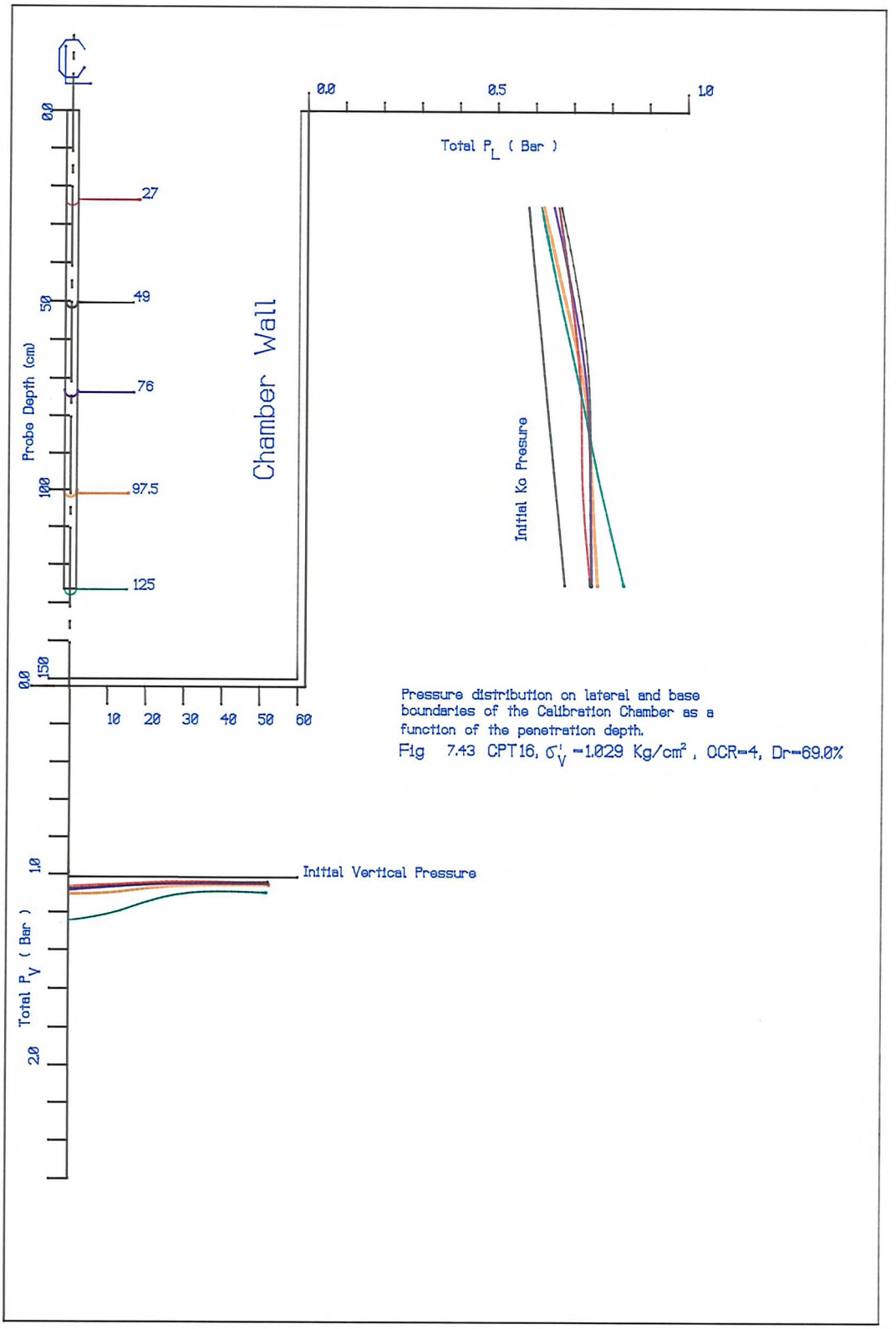

Pressure distribution on lateral and base boundaries of the Calibration Chamber as a function of the penetration depth.

Fig 7.43 CPT16, σ'_V =1.029 Kg/cm^2 , OCR=4, Dr=69.0%

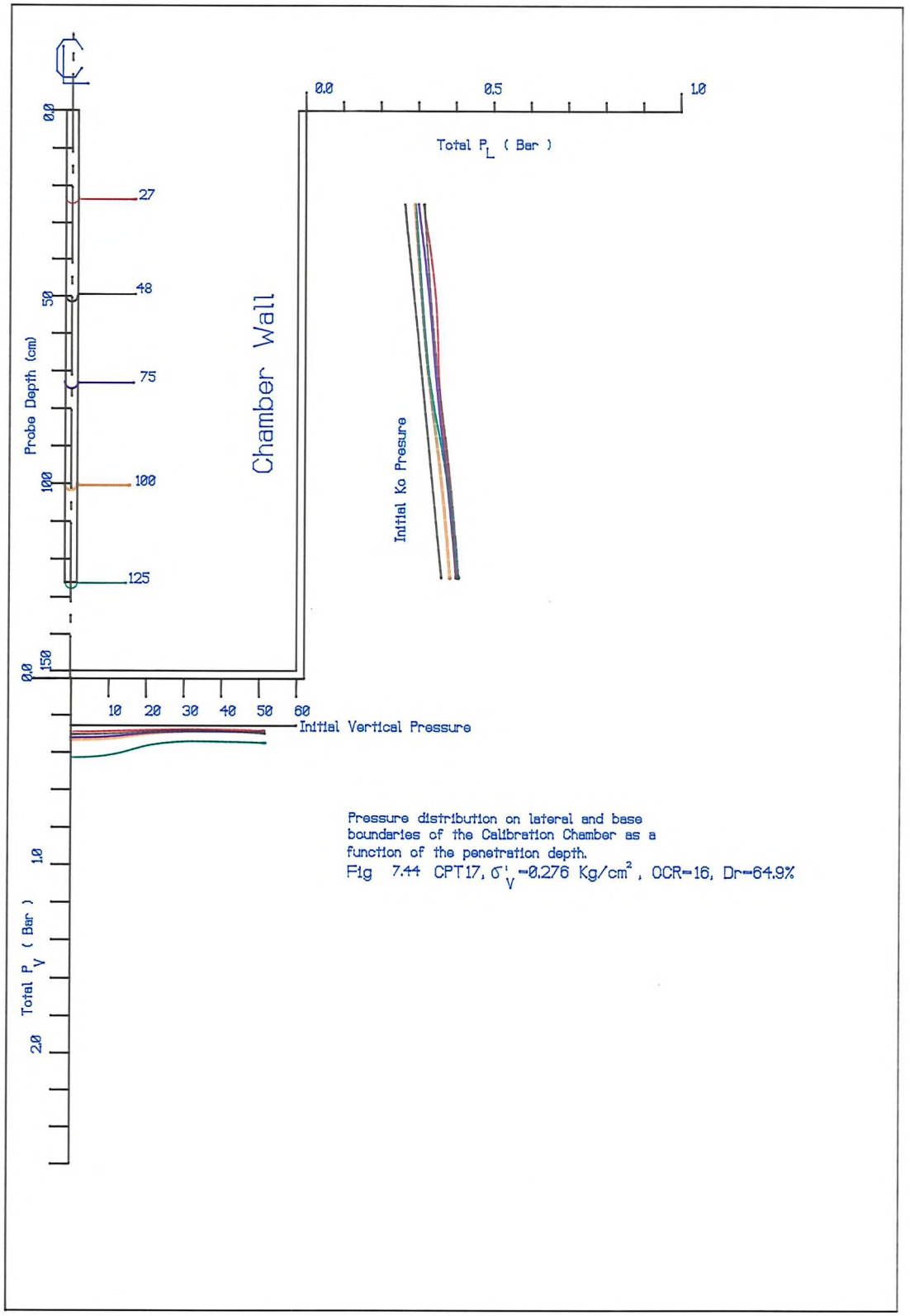

Pressure distribution on lateral and base boundaries of the Calibration Chamber as a function of the penetration depth.

Fig 7.44 CPT17, σ'_V=0.276 Kg/cm^2, OCR=16, Dr=64.9%

Fig. 7.45 Particle size distribution curves for Hokksund sand from selective test series

*NGI-REPORT NO. 51505-14 (1976)
†SU26 (1984)
Location of sample UNIV. OF SOTON
Date of sampling NOV., 1991
Date of test NOV., 1991

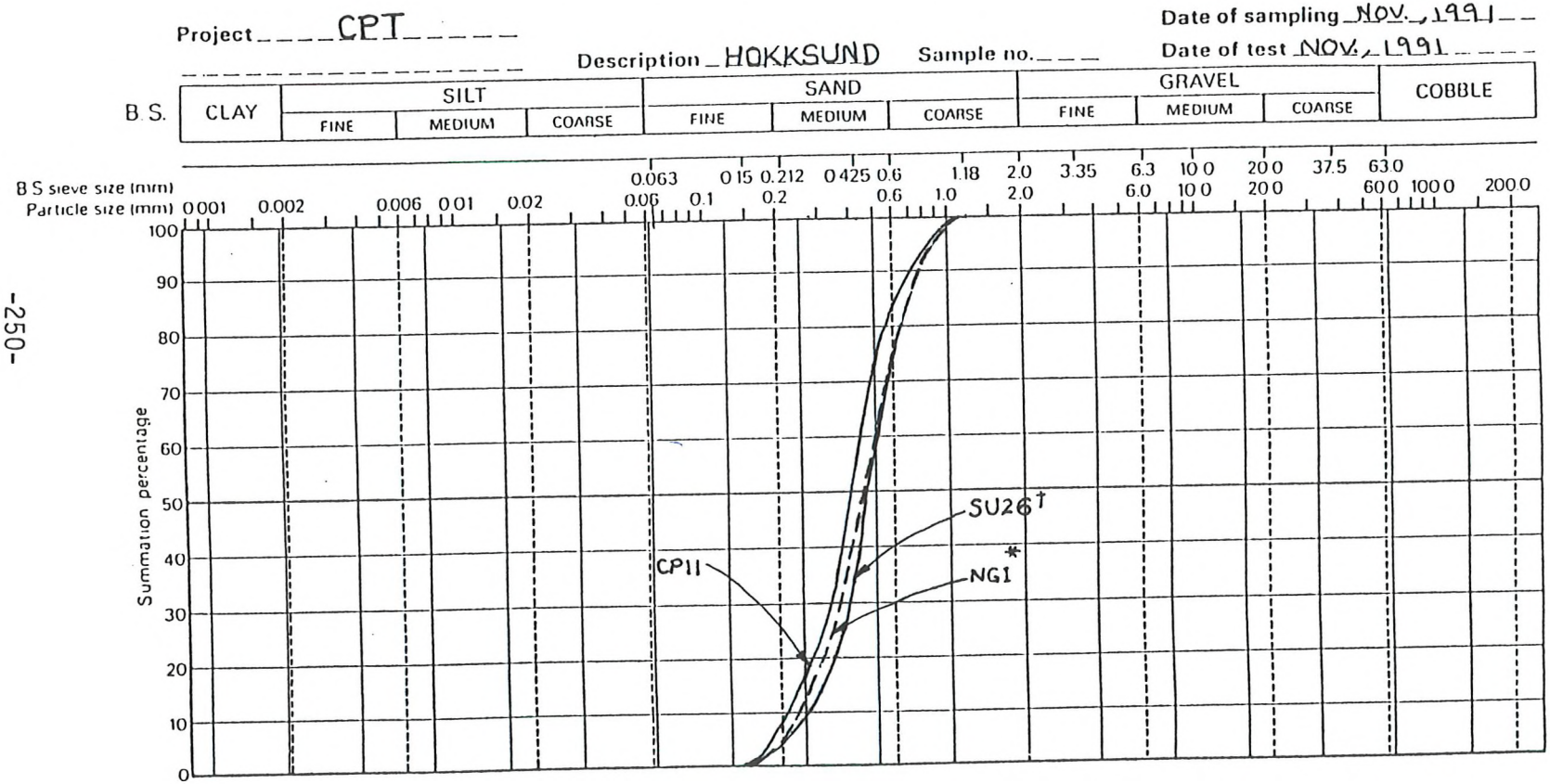

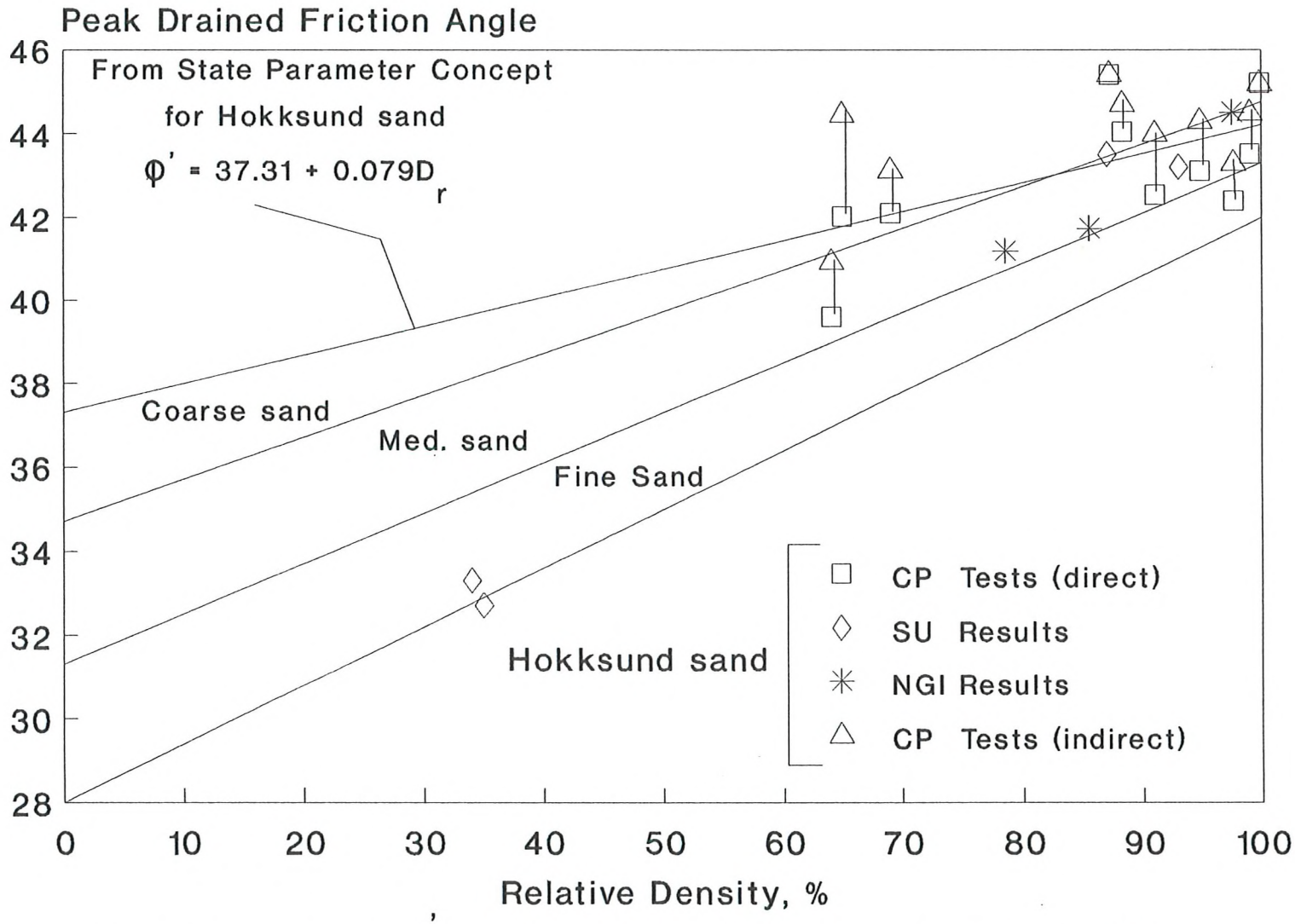

Fig. 7.46 Relation Between φ and D_r (Suggested by Schmertmann, 1978)

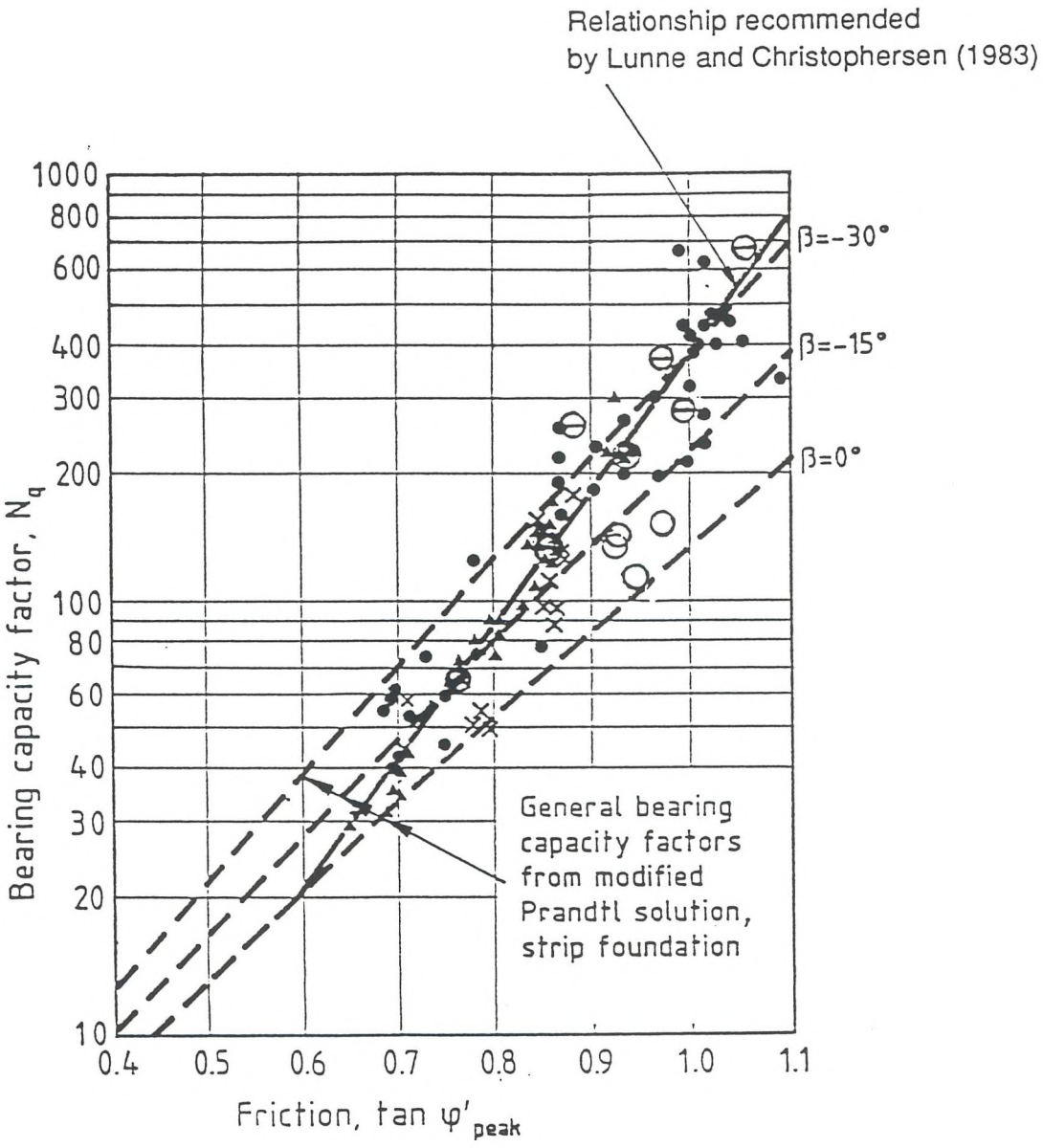

Fig. 7.47 N_q versus tanϕ' from other CC studies and from new boundary tests

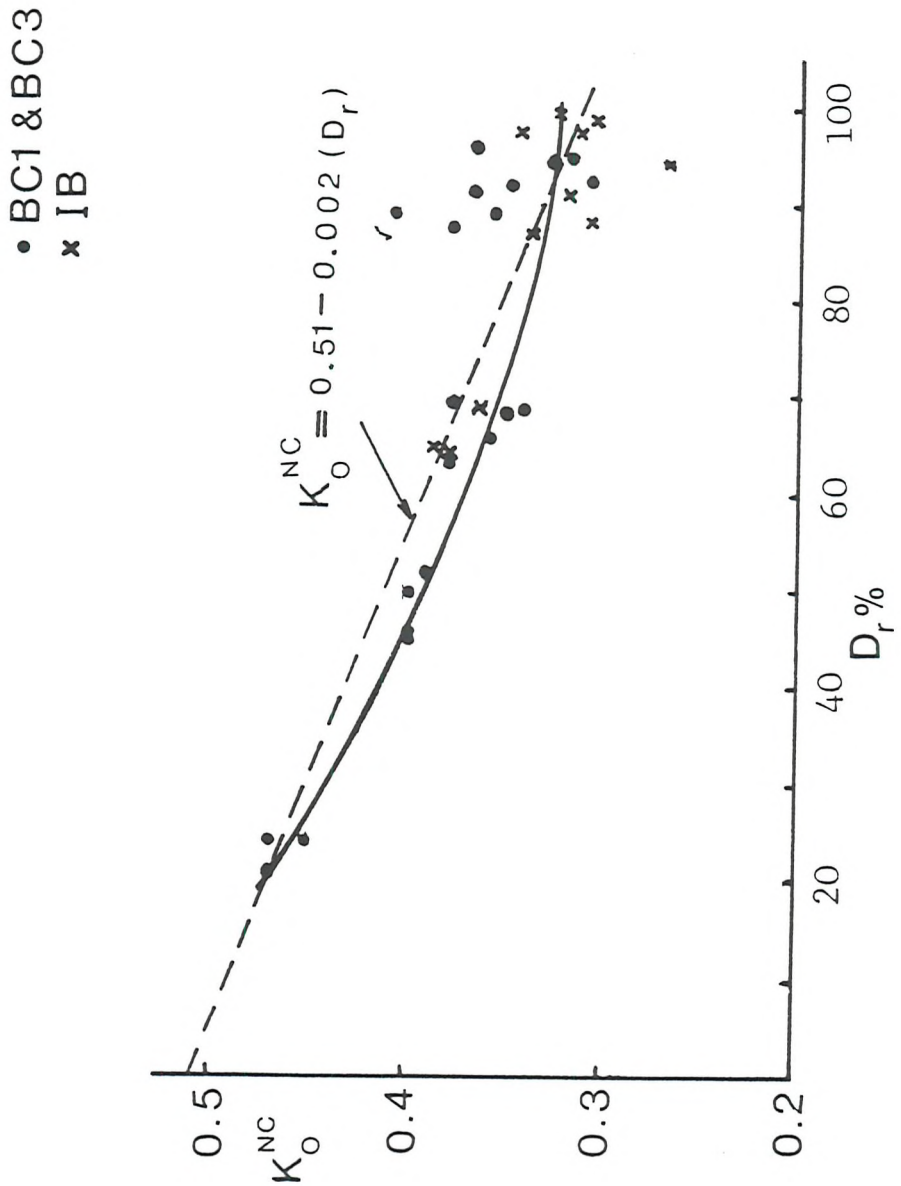

Fig. 7.48 K_o and D_r relationship for NC Hokksund sand

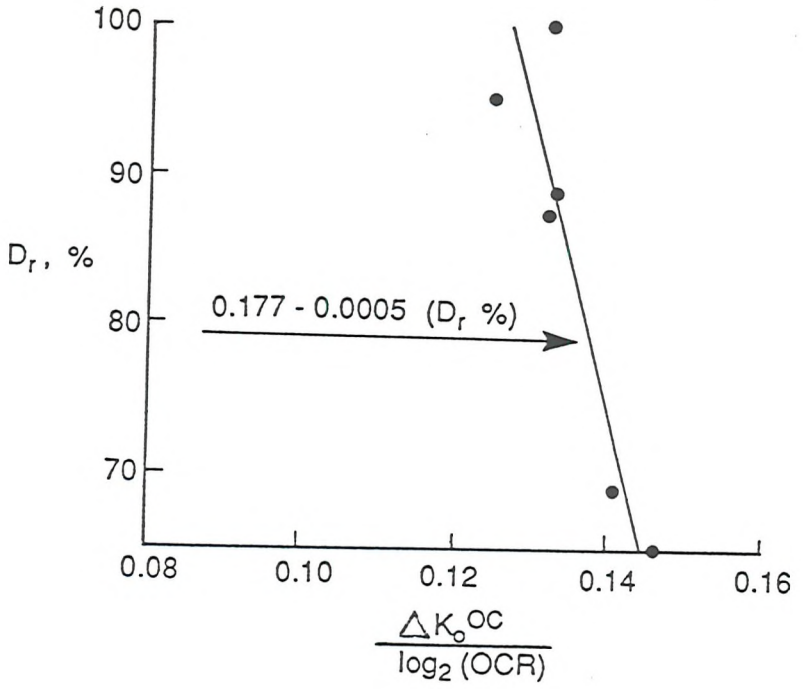

$$K_o^{OC} = K_o^{NC} + (0.177 - 0.0005\ D_r)\ \log_2(OCR)$$

(D_r in %)

Fig. 7.49 K_o – OCR – D_r relationship for Hokksund sand

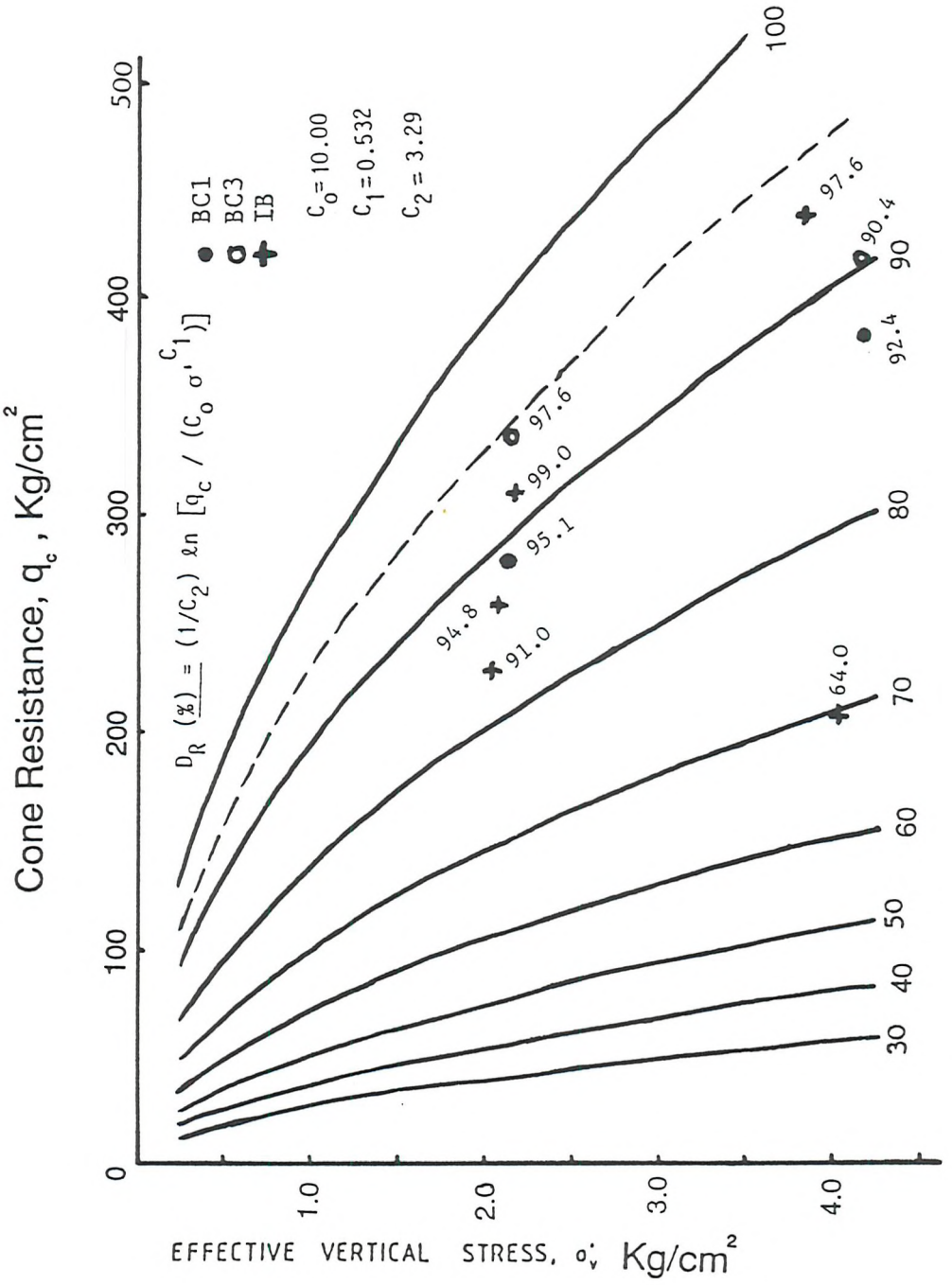

Fig. 7.50 q_c – D_r – σ'_v plot for NC Hokksund sand

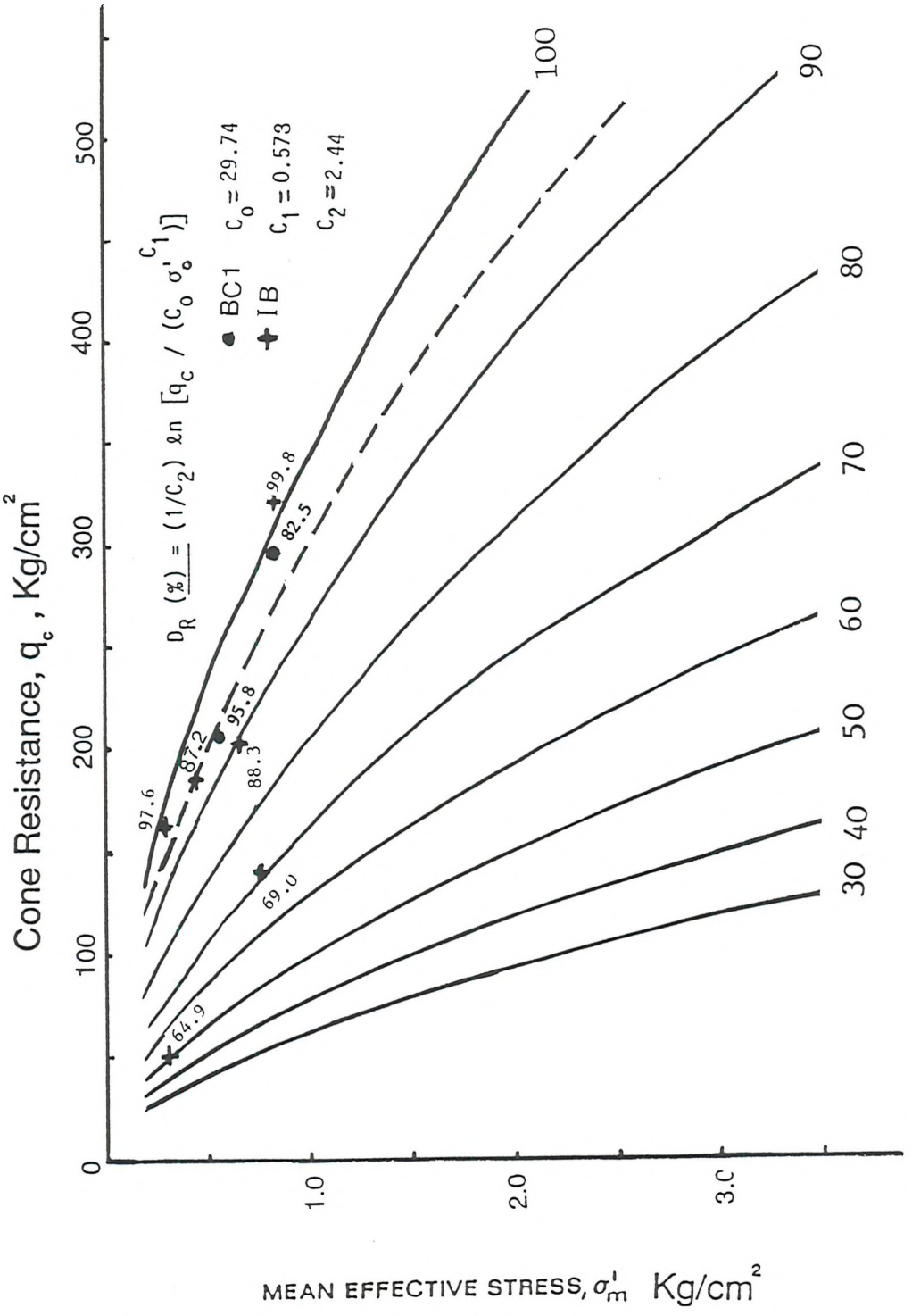

Fig. 7.51 $q_c - D_r - \sigma'_m$ plot for OC Hokksund sand

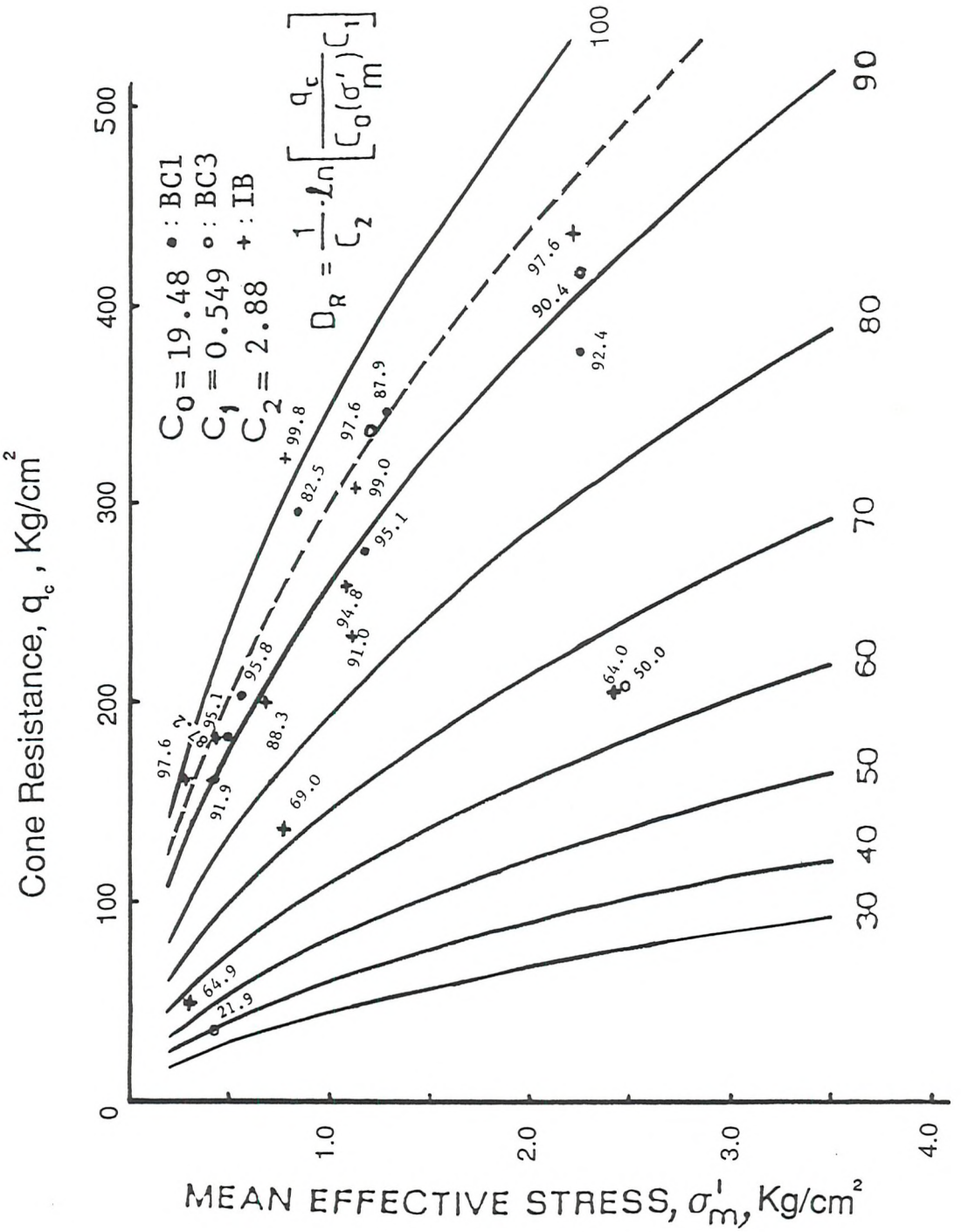

Fig. 7.52 $q_c - D_r - \sigma'_m$ plot for NC & OC Hokksund sand

Fig. 7.53 Evaluation of relative density from cone resistance for NC sand

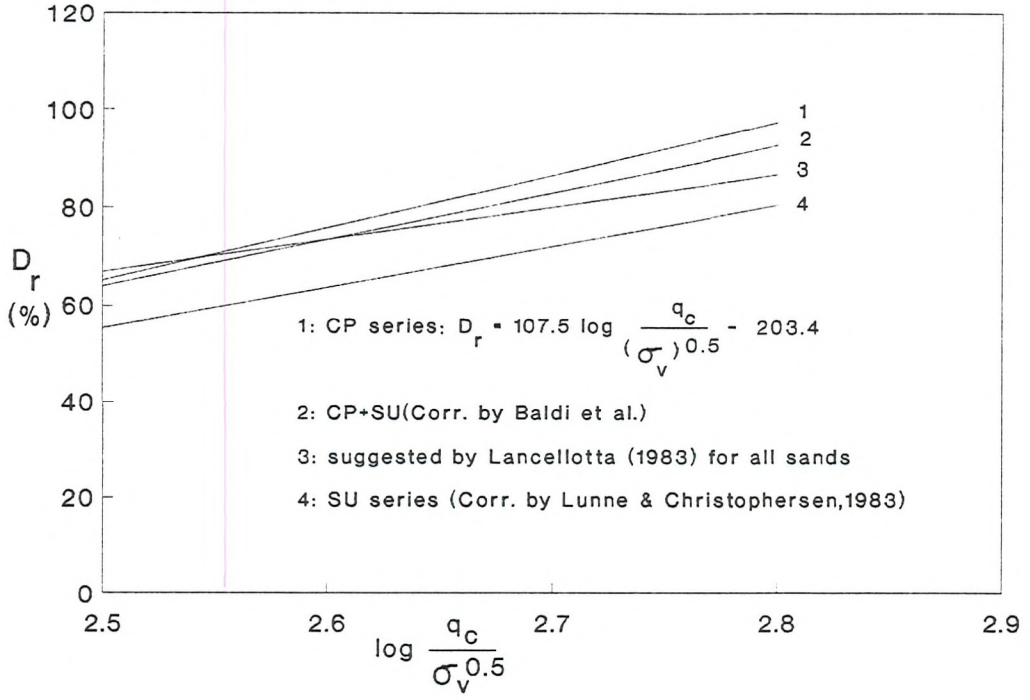

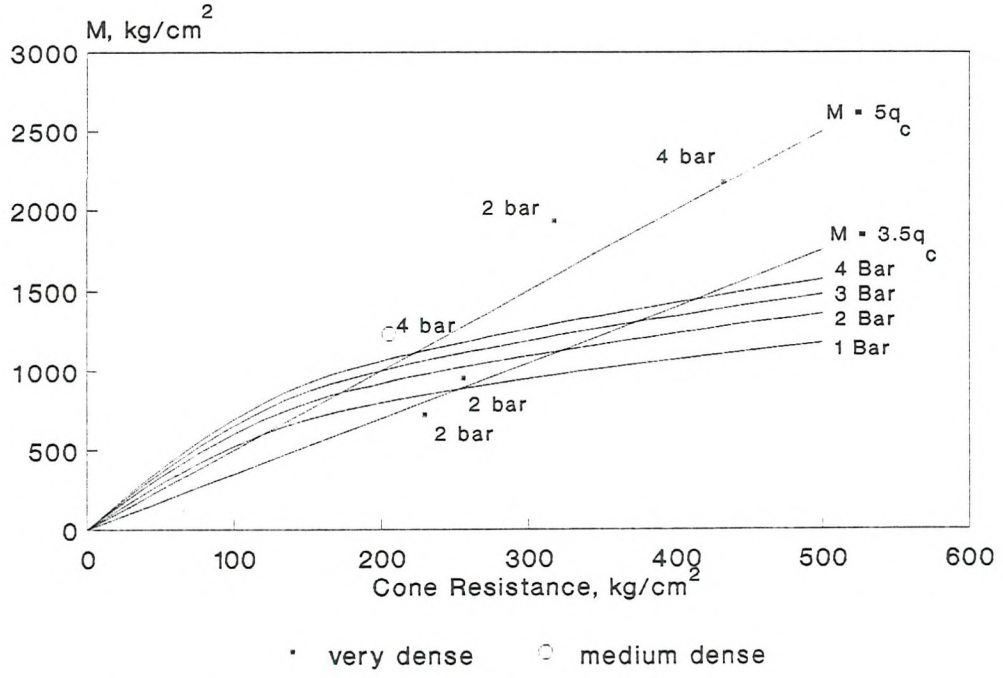

Fig. 7.54 Evaluation of constrained modulus from q_c and σ_v

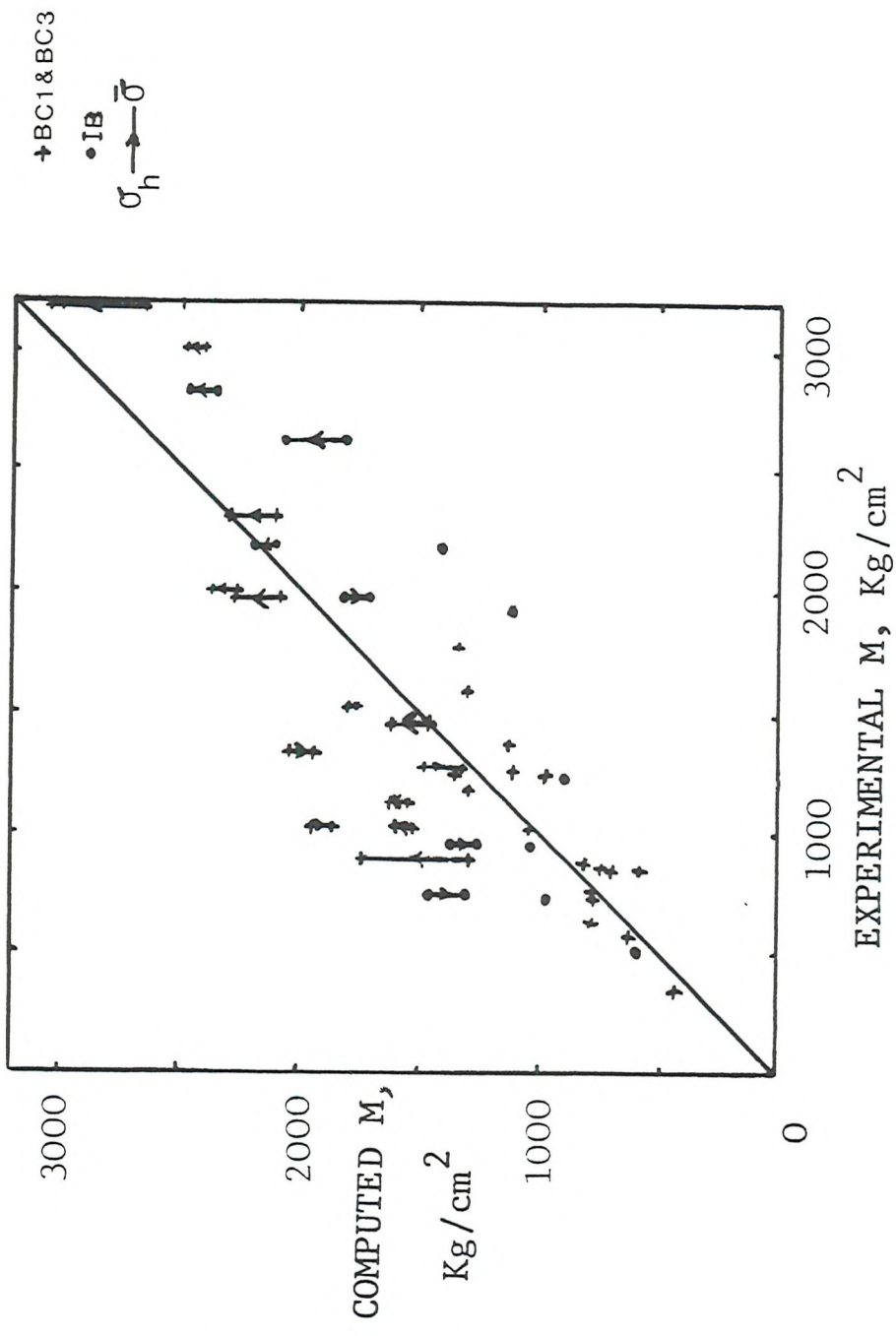

Fig. 7.55 Measured vs. computed constrained modulus for Hokksund sand

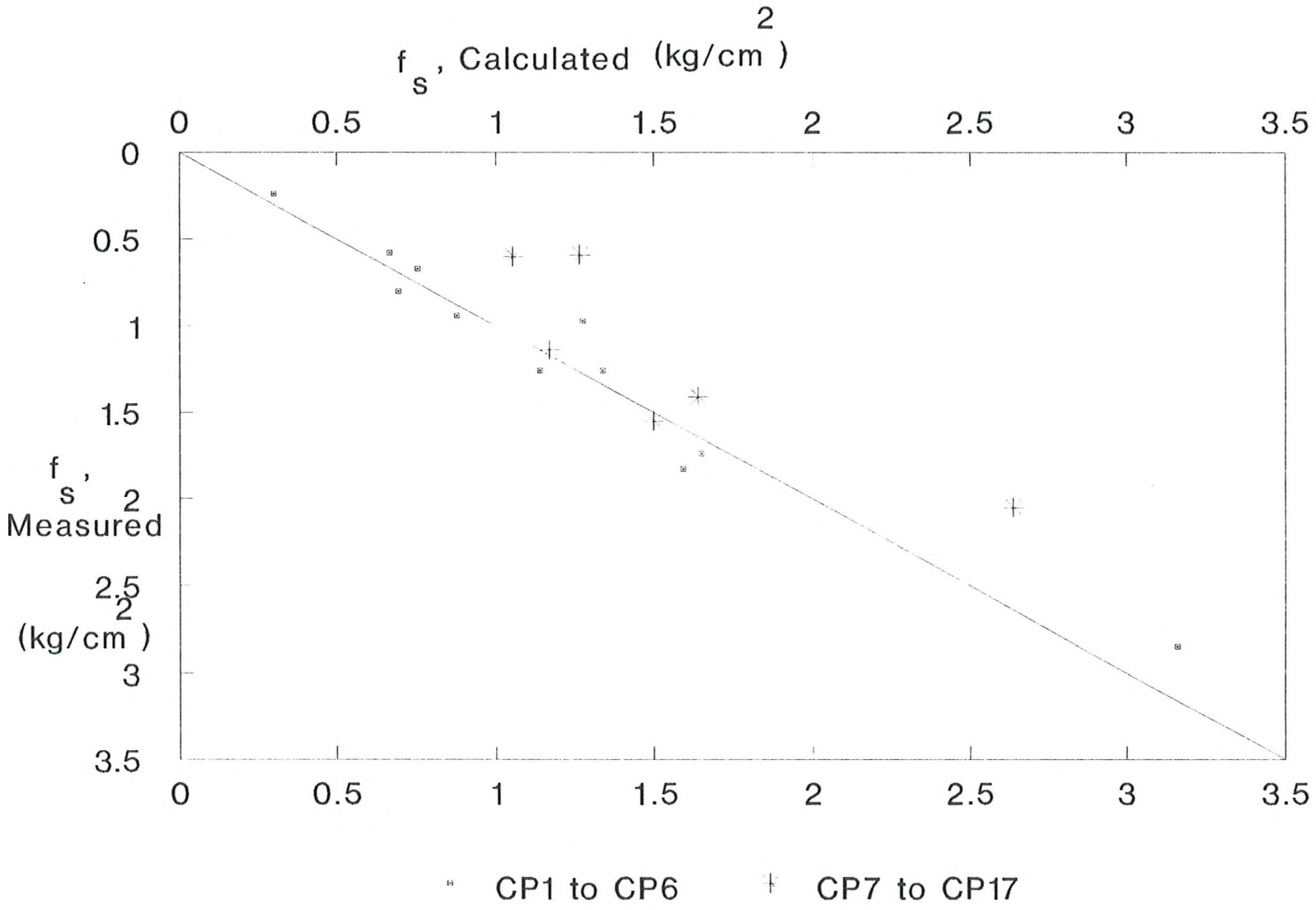

Fig. 7.56 Measured vs. calculated sleeve friction

CHAPTER 8

ELASTIC CPT MODEL

8.1. Introduction

In this chapter a theoretical analysis is given for the penetration mechanism that occurs during CPT. Soil is assumed to have anisotropic properties with transverse isotropy in the horizontal plane. It is believed that the penetration of a probe into a granular material involves three separate **phenomena:**

- a spheroidal cavity expansion at the point of the cone continually added to as penetration proceeds;
- a sleeve load that is also continually added to as penetration proceeds.
- and a vertical point load.

One of the main components of this model is the development of a spheroidal cavity expansion solution in a transversely-isotropic material. The same approach is used as for the isotropic case. The solutions for a cylindrical plane strain case and for semi-infinite penetration are, then, obtained by integration.

The derived solution is particularised for the case of isotropic soil properties. The components of the model that account for the three separate mechanisms outlined above are discussed at the end.

In the next section, the method used for the development of the stresses due to a spherical cavity expansion in an infinite isotropic medium is discussed. An analogous method will then be used to develop a solution for the anisotropic case.

8.2. Spherical Cavity Expansion in an Isotropic Medium

The cavity expansion solution, so far, exists only for an isotropic case. The task of this section is to show that the approach used in this solution can be used to develop the solution for an anisotropic elastic medium.

We assume that two equal and opposite forces, a small distance d apart, are applied to an infinitely extended isotropic elastic medium. The stresses produced by a force P applied at the origin O in the z direction within an infinite medium are given by Poulos and Davis (1974) [the Kelvin solution in cylindrical coordinates] as follows:

$$\sigma_r = B\left[(1-2\nu)z\left(r^2+z^2\right)^{-\frac{3}{2}} - 3r^2z\left(r^2+z^2\right)^{-\frac{5}{2}}\right] \qquad (1)$$

$$\sigma_\theta = B(1-2\nu)z\left(r^2+z^2\right)^{-\frac{3}{2}} \qquad (2)$$

$$\sigma_z = -B\left[(1-2\nu)z\left(r^2+z^2\right)^{-\frac{3}{2}} + 3z^3\left(r^2+z^2\right)^{-\frac{5}{2}}\right] \qquad (3)$$

$$\tau_{rz} = -B\left[(1-2\nu)z\left(r^2+z^2\right)^{-\frac{3}{2}} + 3rz^2\left(r^2+z^2\right)^{-\frac{5}{2}}\right] \qquad (4)$$

where $B = \dfrac{P}{8\pi(1-\nu)}$ [P is taken positive in tension]

By using the same equations, the stresses produced by the force P at O_1 (δ distance away from O) in the opposite direction can also be calculated. Considering the distance δ as an infinitely small quantity, any term f(r,z) in the above expressions should be replaced by $-[f + (\partial f/\partial z)\delta]$. Superimposing the stresses produced by the two opposite forces and using the symbol Δ for the product $B\delta$, one finds

$$\sigma_z = \Delta \frac{\partial}{\partial z}\left[(1 - 2\nu)z\left(r^2 + z^2\right)^{-\frac{3}{2}} + 3z^3\left(r^2 + z^2\right)^{-\frac{5}{2}}\right] \qquad (6)$$

$$\sigma_r = -\Delta \frac{\partial}{\partial z}\left[(1 - 2\nu)z\left(r^2 + z^2\right)^{-\frac{3}{2}} - 3r^2z\left(r^2 + z^2\right)^{-\frac{5}{2}}\right] \qquad (7)$$

$$\sigma_\theta = -\Delta \frac{\partial}{\partial z}(1 - 2\nu)z\left(r^2 + z^2\right)^{-\frac{3}{2}} \qquad (8)$$

$$\tau_{rz} = \Delta \frac{\partial}{\partial z}\left[(1 - 2\nu)z\left(r^2 + z^2\right)^{-\frac{3}{2}} + 3rz^2\left(r^2 + z^2\right)^{-\frac{5}{2}}\right] \qquad (9)$$

At a spherical radius R, the state of stress on an element perpendicular to R is

$$\sigma_R = \sigma_r \sin^2\omega + \sigma_z \cos^2\omega + 2\tau_{rz} \sin\omega \cos\omega \qquad (10)$$

$$\tau_{Rz} = (\sigma_r - \sigma_z) \sin\omega \cos\omega - \tau_{rz} (\sin^2\omega - \cos^2\omega) \qquad (11)$$

where ω is the angle from the vertical (z) axis.

The distribution of these stresses is symmetrical with respect to the z-axis and with respect to the coordinate plane perpendicular to z.

Supposing that, in addition to the force doublet $P\delta$ acting along the z-axis, an identical system acts along the r-axis and another one along the axis perpendicular to the rz-plane. In this way a stress distribution symmetrical with respect to the origin will be produced. Now if a sphere is considered with the centre at the origin, there will be only a normal uniformly distributed stress acting on the surface of this sphere. Considering the stress at points on the circle on the rz-plane, Eqn.(10) gives the part of this stress due to the force doublet along the z-axis [called the z-z doublet]. By interchanging $\sin\omega$ and $\cos\omega$, the normal stress round the same circle produced by the r-r doublet can be obtained. The normal stress due to the doublet along

the rz-plane is obtained by substituting $\omega = \pi/2$ in Eqn. (10). Combining the actions of the three perpendicular doublets the following normal stress acting on the surface of the sphere can be found:

$$\sigma_R = - \frac{4(1 - 2\nu)\Delta}{R^3} \tag{12}$$

This combination can be used to calculate the stresses in a spherical container submitted to the action of internal or external pressure.

A similar approach is now used to obtain the solution for an anisotropic medium.

8.3. Spheroidal Cavity in an Anisotropic Medium

8.3.1. Solution to a Point force Normal to the Plane of Isotropy

The solution for a point force applied normal to the plane of transverse isotropy at the interior of an infinite solid was obtained by Pan and Chou (1976) using three potential functions to govern the displacements. The displacement functions in x, y, and z directions, respectively, are

$$U_x = \sum_{i=1}^{2} \left[\nu_i A_i \frac{x}{R_i R_i^*} - \nu_i (A_i + B_i) \frac{xz_i}{R_i^3} \right] \tag{13}$$

$$U_y = \sum_{i=1}^{2} \left[\nu_i A_i \frac{y}{R_i R_i^*} - \nu_i (A_i + B_i) \frac{yz_i}{R_i^3} \right] \tag{14}$$

$$U_z = \sum_{i=1}^{2} \left[- \left(\frac{C_{11}B_i + C_{44}\nu_i^2 A_i}{C_{13} + C_{44}} \right) \frac{1}{R_i} - \frac{(A_i + B_i)\,\nu_i^2}{C_{13} + C_{44}} \left(\frac{C_{44}r^2 + C_{11}z^2}{R_i^3} \right) \right] \quad \ldots\ldots (15)$$

where C_{ij} is the elastic stiffness constant given as

$$C_{11} = C_{22} = \frac{E(1 - \rho\nu'^2)}{(1 + \nu)(1 - \nu - 2\rho\nu'^2)}$$

$$C_{12} = \frac{E(\nu + \rho\nu'^2)}{(1 + \nu)(1 - \nu - 2\rho\nu'^2)}$$

$$C_{13} = C_{23} = \frac{E\nu'}{(1 - \nu - 2\rho\nu'^2)}$$

$$C_{33} = \frac{E'(1 - \nu)}{1 - \nu - 2\rho\nu'^2} = M \quad \text{[Constrained Modulus]}$$

$$C_{66} = C_{11} - C_{12} = \frac{E}{1 + \nu}$$

$$C_{44} = G'$$

$$\tilde{C}_{13} = \left(C_{11}C_{33}\right)^{\frac{1}{2}}$$

and

$$\nu_1 = \left(\frac{(\tilde{C}_{13} - C_{13})(\tilde{C}_{13} + C_{13} + 2C_{44})}{4C_{33}C_{44}} \right)^{\frac{1}{2}} + \left(\frac{(\tilde{C}_{13} + C_{13})(\tilde{C}_{13} - C_{13} - 2C_{44})}{4C_{33}C_{44}} \right)^{\frac{1}{2}}$$

$$\nu_2 = \left(\frac{(\tilde{C}_{13} - C_{13})(\tilde{C}_{13} + C_{13} + 2C_{44})}{4C_{33}C_{44}} \right)^{\frac{1}{2}} - \left(\frac{(\tilde{C}_{13} + C_{13})(\tilde{C}_{13} - C_{13} - 2C_{44})}{4C_{33}C_{44}} \right)^{\frac{1}{2}}$$

$$\nu_3 = \left(C_{66}/C_{44}\right)^{\frac{1}{2}}$$

$$z_1 = \nu_1 z$$

$$z_2 = \nu_2 z$$

$$z_3 = \nu_3 z$$

$$R_i^* = R_i + z_i \quad (i = 1, 2)$$

$$R_i^2 = r^2 + z_i^2$$

and $r^2 = x^2 + y^2$

From the positiveness of the strain energy

$$\tilde{C}_{13} \rangle\ |C_{13}| \rangle\ 0$$

A degenerate case occurs when $\tilde{C}_{13} - C_{13} - 2C_{44} = 0$ which leads to $\nu_1 = \nu_2$. This can further be simplified to obtain the spherical solution.

The constants A_i and B_i can be found from the following equations:

(i) $\tilde{C}_{13} - C_{13} - 2C_{44} \neq 0$

$$\nu_1 A_1 = -\nu_2 A_2 = \frac{P(C_{13} + C_{44})}{4\pi C_{33} C_{44} (\nu_2^2 - \nu_1^2)}$$

and $A_i + B_i = 0$

(ii) $\tilde{C}_{13} - C_{13} - 2C_{44} = 0$

$$A_1 = A_2 = 0$$

$$B_1 = B_2 = -\frac{P(C_{13} + C_{44})}{16\pi C_{11} C_{44}}$$

Letting

$$k_i = \frac{C_{11} / \nu_i^2 - C_{44}}{C_{13} + C_{44}}$$

the stress field due to the point force is given as

$$\sigma_x = \sum_{i=1}^{2} \left\{ \left[\left(C_{11} - C_{13}\nu_i^2 k_i \right)(2A_i + B_i) + 2\left(C_{66} + \frac{C_{13}C_{44}\nu_i^2}{C_{13} + C_{44}} \right)(A_i + B_i) \right] \frac{\nu_i z_i}{R_i^3} \right.$$

$$- 3\left(C_{11} - C_{13}\nu_i^2 k_i \right)(A_i + B_i) \frac{\nu_i z_i^3}{R_i^5} - 2C_{66}(A_i + B_i) \frac{3\nu_i z_i y^2}{R_i^5}$$

$$\left. - 2C_{66}\nu_i A_i \left(\frac{1}{R_i R_i^*} - \frac{y^2}{R_i^3 R_i^*} - \frac{y^2}{R_i^2 R_i^{*2}} \right) \right\} \qquad \ldots\ldots (16)$$

$$\sigma_y = \sum_{i=1}^{2} \left\{ \left[\left(C_{11} - C_{13}\nu_i^2 k_i \right)(2A_i + B_i) + 2 \left(C_{66} + \frac{C_{13}C_{44}\nu_i^2}{C_{13} + C_{44}} \right)(A_i + B_i) \right] \frac{\nu_i z_i}{R_i^3} \right.$$

$$- 3\left(C_{11} - C_{13}\nu_i^2 k_i \right)(A_i + B_i) \frac{\nu_i z_i^3}{R_i^5} - 2C_{66}(A_i + B_i) \frac{3\nu_i z_i x^2}{R_i^5}$$

$$\left. - 2C_{66}\nu_i A_i \left(\frac{1}{R_i R_i^*} - \frac{x^2}{R_i^3 R_i^*} - \frac{x^2}{R_i^2 R_i^{*2}} \right) \right\} \qquad \ldots\ldots (17)$$

$$\sigma_z = \sum_{i=1}^{2} \left\{ \left[\left(C_{13} - C_{33}\nu_i^2 k_i \right)(2A_i + B_i) + \frac{2C_{33}C_{44}\nu_i^2}{C_{13} + C_{44}} (A_i + B_i) \right] \frac{\nu_i z_i}{R_i^3} \right.$$

$$\left. -3\left(C_{13} - C_{33}\nu_i^2 k_i \right)(A_i + B_i) \frac{\nu_i z_i^3}{R_i^5} \right\} \qquad \ldots\ldots (18)$$

8.3.2. Solution to a Point Force Parallel to the Plane of Isotropy

Pan and Chou also obtained the displacement and stress functions for a point force in the plane of transverse isotropy. The displacement functions are

$$U_x = \sum_{i=1}^{2}\left[(A_i' - B_i')\left(\frac{\nu_i}{R_i} - \frac{\nu_i x^2}{R_i^3}\right) + 2\nu_i B_i'\left(\frac{1}{R_i^*} - \frac{x^2}{R_i R_i^{*2}}\right)\right] + D\left[\frac{1}{R_3^*} - \frac{y^2}{R_3 R_3^{*2}}\right] \quad \ldots\ldots (19)$$

$$U_y = \sum_{i=1}^{2}\left[-\nu_i(A_i' - B_i')\frac{xy}{R_i^3} - 2\nu_i B_i' \frac{xy}{R_i R_i^{*2}}\right] + D\frac{xy}{R_3 R_3^{*2}} \quad (20)$$

$$U_z = \sum_{i=1}^{2}\left[-\nu_i^2 k_i(A_i' - B_i')\frac{xz_i}{R_i^3} - \frac{C_{11}A_i' - C_{44}\nu_i^2 B_i'}{C_{13} + C_{44}} \frac{2x}{R_i R_i^{*2}}\right] \quad (21)$$

R_i, R_i^* and z_i are defined as before. The constants A_i' and B_i' and D can be found from the following equations

$$D = \frac{P}{4\pi C_{33}\nu_3}$$

(i) $\tilde{C}_{13} - C_{13} - 2C_{44} \neq 0$

$$A_1' = B_1' = -\frac{P(C_{44} - C_{33}\nu_1^2)}{8\pi C_{33}C_{44}(\nu_1^2 - \nu_2^2)\nu_1^2}$$

$$A_2' = B_2' = \frac{P(C_{44} - C_{33}\nu_2^2)}{8\pi C_{33}C_{44}(\nu_1^2 - \nu_2^2)\nu_2^2}$$

(ii) $\tilde{C}_{13} - C_{13} - 2C_{44} = 0$

$$A_1' = A_2' = \frac{P}{16\pi C_{11}} \quad \text{and} \quad B_1' = B'_2 = \frac{P}{16\pi C_{44}\nu_1^2}$$

The stress field due to the point force is

$$\sigma_x = \sum_{i=1}^{2} \left\{ \left[\left[\left(2C_{66} - \frac{C_{44}(C_{11} - C_{13}\nu_i^2)}{C_{13} + C_{44}} \right) (A_i' - B_i') - 2C_{44}\nu_i^2 (1 + k_i) B_i' \right] \frac{\nu_i x}{R_i^3} \right.\right.$$

$$- C_{44}\nu_i^2 (1 + k_i)(A_i' - B_i') \frac{3\nu_i x z_i^2}{R_i^5} - 6C_{66}(A_i' - B_i') \frac{\nu_i x y^2}{R_i^5}$$

$$\left.\left. - 2C_{66} B_i' \left(- \frac{2\nu_i x}{R_i R_i^{*2}} + \frac{2\nu_i x y^2}{R_i^3 R_i^{*2}} + \frac{4\nu_i x y^2}{R_i^2 R_i^{*3}} \right) \right] \right\} - 2C_{66} D \left(\frac{x}{R_3 R_3^{*2}} - \frac{x y^2}{R_3^3 R_3^{*2}} - \frac{2x y^2}{R_3^2 R_3^{*3}} \right)$$

..... (22)

$$\sigma_y = \sum_{i=1}^{2} \left\{ \left[\left[\left(6C_{66} - \frac{C_{44}(C_{11} - C_{13}\nu_i^2)}{C_{13} + C_{44}} \right) (A_i' - B_i') - 2C_{44}\nu_i^2 (1 + k_i) B_i' \right] \frac{\nu_i x}{R_i^3} \right.\right.$$

$$- C_{44}\nu_i^2 (1 + k_i)(A_i' - B_i') \frac{3\nu_i x z_i^2}{R_i^5} - 6C_{66}(A_i' - B_i') \frac{\nu_i x^3}{R_i^5}$$

$$\left.\left. - 2C_{66} B_i' \left(- \frac{6\nu_i x}{R_i R_i^{*2}} + \frac{2\nu_i x^3}{R_i^3 R_i^{*2}} + \frac{4\nu_i x^3}{R_i^2 R_i^{*3}} \right) \right] \right\} + 2C_{66} D \left(\frac{x}{R_3 R_3^{*2}} - \frac{x y^2}{R_3^3 R_3^{*2}} - \frac{2x y^2}{R_3^2 R_3^{*3}} \right)$$

..... (23)

$$\sigma_z = \sum_{i=1}^{2} - \left\{ \left[\left[\left(C_{13} - \frac{C_{33}(C_{11} + C_{44}\nu_i^2)}{C_{13} + C_{44}} \right) (A_i' - B_i') + 2(C_{13} - C_{33}\nu_i^2 k_i) B_i' \right] \frac{\nu_i x}{R_i^3} \right.\right.$$

$$\left.\left. + (C_{13} - C_{33}\nu_i^2 k_i)(A_i' - B_i') \frac{3\nu_i x z_i}{R_i^5} \right] \right\} \qquad (24)$$

The solution for a point force lying in the y-direction can be obtained by interchanging x and y in equations (19) to (24).

All of these equations can be reduced to the isotropic case by noting that

$$C_{11} = C_{33} = (\lambda + 2\mu)$$

$$C_{12} = C_{13} = \lambda$$

$$C_{44} = C_{66} = \mu$$

where λ and μ are the Lame' constants.

8.3.3. Doublets for a Transversely Isotropic Medium

It was shown in section 8.2. that the three force doublets could be added in equal proportions in order to develop the isotropic solution. For the transversely isotropic case, where expansion is assumed to be in the form of either an oblate or prolate spheroid [in which the major axes may lie along the r- or z-axes, respectively, and depend on the relative material properties, e.g., as determined by the over-consolidation ratio (OCR) and the consolidation stress level], x-x and y-y doublets are added equally, due to radial symmetry, but the z-z doublet needs to be proportioned as determined in the next section.

In this section the solution for the individual doublets is given for all the displacement and stress functions. Also given are the transverse 'doublet' solutions in terms of r obtained by appropriate addition of the xx and yy doublets.

The z-z Doublet

Assuming that the distance between the two equal and opposite forces that form the doublet is δ and redefining the the parameters A_i, B_i, A'_i and B'_i to include the $P\delta$ term as

$$\bar{A}_i = \delta \cdot A_i \quad \text{and} \quad \bar{B}_i = \delta \cdot B_i$$

and also

$$\bar{A}'_i = \delta \cdot A'_i \qquad \bar{B}'_i = \delta \cdot B'_i \quad \text{and} \quad \bar{D} = \delta \cdot D$$

Then, the individual doublet equations for both displacements and

stresses can be set up as

$$U_r\Big|_{(zz)} = \sum_{i=1}^{2} \left\{ \left[\bar{A}_i \nu_i^2 r \left[\frac{z_i}{R_i^3 R_i^*} + \frac{1}{R_i^2 R_i^*} \right] \right. \right. \tag{25}$$

$$U_z\Big|_{(zz)} = \sum_{i=1}^{2} \left(\bar{A}_i \nu_i^3 k_i \frac{z_i}{R_i^3} \right) \tag{26}$$

$$\sigma_r\Big|_{(zz)} = \sum_{i=1}^{2} - \bar{A}_i \nu_i^2 \left[\left(C_{11} - C_{13} \nu_i^2 k_i \right) \left(\frac{1}{R_i^3} - \frac{3z_i^2}{R_i^5} \right) + 2C_{66} \left(\frac{z_i}{R_i^3 R_i^*} + \frac{1}{R_i^2 R_i^*} \right) \right] \tag{27}$$

$$\sigma_\theta\Big|_{(zz)} = \sum_{i=1}^{2} -\bar{A}_i \nu_i^2 \left\{ \left[\left(C_{11} - C_{13} \nu_i^2 k_i \right) \left(\frac{1}{R_i^3} - \frac{3z_i^2}{R_i^5} \right) + 2C_{66} \left[\frac{z_i}{R_i^3 R_i^*} + \frac{1}{R_i^2 R_i^*} \right. \right. \right.$$

$$\left. \left. \left. - r^2 \left(\frac{3z_i}{R_i^5 R_i^*} + \frac{1}{R_i^4 R_i^*} + \frac{4z_i}{R_i^4 R_i^{*2}} + \frac{2}{R_i^3 R_i^{*2}} \right) \right] \right] \right\} \tag{28}$$

$$\sigma_z\Big|_{(zz)} = \sum_{i=1}^{2} - \bar{A}_i \nu_i^2 \left(C_{13} - C_{33} \nu_i^2 k_i \right) \left(\frac{1}{R_i^3} - \frac{3z_i^2}{R_i^5} \right) \tag{29}$$

x-x Doublet

$$U_x\Big|_{(xx)} = \sum_{i=1}^{2} 2\nu_i \bar{B}_i' x \left[\frac{3}{R_i R_i^{*2}} + \frac{x^2}{R_i^3 R_i^{*2}} + \frac{2x^2}{R_i^2 R_i^{*3}} \right] - \bar{D}x \left[\frac{-1}{R_3 R_3^{*2}} + \frac{y^2}{R_3^3 R_3^{*2}} + \frac{2y^2}{R_3^2 R_3^{*3}} \right]$$

..... (30)

$$U_y\Big|_{(xx)} = \sum_{i=1}^{2} 2\nu_i \bar{B}'_i x\left[\frac{1}{R_i R_i^{*2}} - \frac{y^2}{R_i^3 R_i^{*2}} - \frac{2y^2}{R_i^2 R_i^{*3}}\right] + \bar{D}x\left[\frac{-1}{R_3 R_3^{*2}} + \frac{x^2}{R_3^3 R_3^{*2}} + \frac{2x^2}{R_3^2 R_3^{*3}}\right] \quad \ldots\ldots \quad (31)$$

$$U_z\Big|_{(xx)} = \sum_{i=1}^{2} 2\nu_i B'_i \bar{k}_i\left[\frac{1}{R_i R_i^*} - \frac{x^2}{R_i^3 R_i^*} - \frac{x^2}{R_i^2 R_i^{*2}}\right] \quad (32)$$

$$\sigma_x\Big|_{(xx)} = \sum_{i=1}^{2} 2\bar{B}'_i \nu_i\left[C_{44}\nu_i^2(1 + k_i)\left(\frac{1}{R_i^3} - \frac{3x^2}{R_i^5}\right) + 2C_{66}\left(\frac{-1}{R_i R_i^{*2}} + \frac{x^2}{R_i^3 R_i^{*2}} + \frac{2x^2}{R_i^2 R_i^{*3}}\right)\right.$$

$$+ 2C_{66}y^2\left(\frac{1}{R_i^3 R_i^{*2}} - \frac{12x^2}{R_i^4 R_i^{*3}} - \frac{3x^2}{R_i^5 R_i^{*2}} + \frac{4}{R_i^2 R_i^{*3}} - \frac{12x^2}{R_i^3 R_i^{*4}}\right)\Big]$$

$$- 2C_{66}\bar{D}\left(-\frac{1}{R_3 R_3^{*2}} + \frac{x^2}{R_3^3 R_3^{*2}} + \frac{2x^2}{R_3^2 R_3^{*3}}\right)$$

$$- 4C_{66}Dy^2\left(\frac{1}{R_3^3 R_3^{*2}} - \frac{12x^2}{R_3^4 R_3^{*3}} - \frac{3x^2}{R_3^5 R_3^{*2}} + \frac{4}{R_3^2 R_3^{*3}} - \frac{12x^2}{R_3^3 R_3^{*4}}\right) \quad (33)$$

$$\sigma_y\Big|_{(xx)} = \sum_{i=1}^{2} 2\bar{B}'_i \nu_i\left[C_{44}\nu_i^2(1 + k_i)\left(\frac{1}{R_i^3} - \frac{3x^2}{R_i^5}\right) + 6C_{66}\left(\frac{-1}{R_i R_i^{*2}} + \frac{2x^2}{R_i^3 R_i^{*2}} + \frac{4x^2}{R_i^2 R_i^{*3}}\right.\right.$$

$$\left.\left. - \frac{-x^4}{R_i^5 R_i^{*2}} - \frac{2x^4}{R_i^4 R_i^{*3}} - \frac{2x^4}{R_i^3 R_i^{*4}}\right)\right] - 2C_{66}\bar{D}\left(\frac{1}{R_3 R_3^{*2}} - \frac{x^2}{R_3^3 R_3^{*2}} - \frac{2x^2}{R_3^2 R_3^{*3}}\right)$$

$$+ 4C_{66}Dy^2\left(\frac{1}{R_3^3 R_3^{*2}} - \frac{12x^2}{R_3^4 R_3^{*3}} - \frac{3x^2}{R_3^5 R_3^{*2}} + \frac{4}{R_3^2 R_3^{*3}} - \frac{12x^2}{R_3^3 R_3^{*4}}\right) \quad (34)$$

$$\sigma_z\Big|_{(xx)} = \sum_{i=1}^{2}\left[2(C_{13} - C_{33}\nu_i^2 k_i)\bar{B}_i'\nu_i\left(\frac{1}{R_i^3} - \frac{3x^2}{R_i^5}\right)\right] \qquad (35)$$

Transverse 'Doublets'

Since there exists a radial symmetry in a transversely isotropic stress state, Eqns. (30) to (35) are the same for y-y doublet (with x and y interchanged) and the two doublets can be added together to give radially symmetric expressions in terms of r [x being replaced by r and y set to zero] in the r-z plane:

(a) Displacement Equations

$$U_r\Big|_{(xy)} = \sum_{i=1}^{2} - 2\nu_i\bar{B}_i' r\left[\frac{-4}{R_i R_i^{*2}} + \frac{r^2}{R_i^3 R_i^{*2}} + \frac{2r^2}{R_i^2 R_i^{*3}}\right] \qquad (36)$$

$$U_z\Big|_{(xy)} = \sum_{i=1}^{2} - 4\nu_i\bar{B}_i' k_i\left[\frac{-1}{R_i R_i^{*}} + \frac{r^2}{R_i^3 R_i^{*}} + \frac{r^2}{R_i^2 R_i^{*2}}\right] \qquad (37)$$

(b) Stress Equations

$$\sigma_r\Big|_{(xy)} = \sum_{i=1}^{2} 2\bar{B}_i'\nu_i\left[C_{44}\nu_i^2(1 + k_i)\left(\frac{2}{R_i^3} - \frac{3r^2}{R_i^5}\right) - 2C_{66}\left(\frac{4}{R_i R_i^{*2}} - \frac{r^2}{R_i^3 R_i^{*2}} - \frac{2r^2}{R_i^2 R_i^{*3}}\right)\right]$$

.....(38)

$$\sigma_\theta\Big|_{(xy)} = \sum_{i=1}^{2} 2\bar{B}'_i \nu_i \left[C_{44}\nu_i^2(1+k_i)\left(\frac{2}{R_i^3} - \frac{3r^2}{R_i^5}\right) - 2C_{66}\left(\frac{4}{R_i R_i^{*2}} - \frac{7r^2}{R_i^3 R_i^{*2}} - \frac{14r^2}{R_i^2 R_i^{*3}} + \frac{3r^4}{R_i^5 R_i^{*2}} + \frac{6r^4}{R_i^4 R_i^{*3}} + \frac{6r^4}{R_i^3 R_i^{*4}}\right)\right] \qquad (39)$$

$$\sigma_z\Big|_{(xy)} = \sum_{i=1}^{2} 2\bar{B}'_i \nu_i (C_{13} - C_{33}\nu_i^2 k_i)\left(\frac{2}{R_i^3} - \frac{3r^2}{R_i^5}\right) \qquad (40)$$

8.3.4. Solution for a Cavity Expansion in a Transversely-Isotropic Medium (Non-degenerate Solution)

It is not known in advance what proportion of the zz doublet should be added to the transverse (xy) doublet in order that the combination has useful properties. However, we need to have a combination which will define a spheroidal shape on the surface of which the stress is normal and uniform so as to give the equivalent of a Lame' stress distribution. It is also intuitively apparent that strains resulting from a pressure increase in the cavity should not affect the shape of these spheroidal surfaces. The latter requirement means that the displacement of this surface is proportional to its distance from the centre. At the expense of some rigor (but with greater simplicity of expression) this requirement can be satisfied by comparing a point on the axis with one on a transverse diameter with the assumption that it will apply elsewhere on the spheroidal surface.

Thus we require

$$\left(\frac{U_r(r)}{r}\Big|_{(xy)} + \alpha\cdot\frac{U_r(r)}{r}\Big|_{(zz)}\right)_{z=0} = \left(\frac{U_z(r)}{z}\Big|_{(xy)} + \alpha\cdot\frac{U_z(r)}{z}\Big|_{(zz)}\right)_{r=0,\ z=r/\beta} \qquad (41)$$

and,

$$\left[\sigma_r\Big|_{(xy)} + \alpha\cdot\sigma_r\Big|_{(zz)}\right]_{z=0} = \left[\sigma_z\Big|_{(xy)} + \alpha\cdot\sigma_z\Big|_{(zz)}\right]_{r=0,\ z=r/\beta} \tag{42}$$

The simplified expressions for these two points are:

$$U_r\Big|_{(xy)} = \frac{1}{r^2}\sum_{i=1}^{2} 2\bar{B}_i'\nu_i \tag{43}$$

$$U_r\Big|_{(zz)} = \frac{1}{r^2}\sum_{i=1}^{2} \bar{A}_i\nu_i^2 \tag{44}$$

and, similarly, for depth z

$$U_z\Big|_{(xy)} = \frac{1}{z^2}\sum_{i=1}^{2} 2k_i\bar{B}_i' \tag{45}$$

$$U_z\Big|_{(zz)} = \frac{1}{z^2}\sum_{i=1}^{2} \bar{A}_i\nu_i k_i \tag{46}$$

The stress functions are simplified in the same way:

$$\sigma_r\Big|_{(xy)} = \frac{1}{r^3}\sum_{i=1}^{2} -2\bar{B}_i'\nu_i\left(C_{44}\nu_i^2(1 + k_i) + 2C_{66}\right) \tag{47}$$

$$\sigma_r\Big|_{(zz)} = \frac{1}{r^3} \sum_{i=1}^{2} - \bar{A}_i \nu_i^2 \left(\left(C_{11} - C_{13} \nu_i^2 k_i \right) + 2C_{66} \right) \tag{48}$$

and similarly

$$\sigma_z\Big|_{(xy)} = \frac{4}{z^3} \sum_{i=1}^{2} \left((C_{13} - C_{33} \nu_i^2 k_i) \frac{\bar{B}_i'}{\nu_i} \right) \tag{49}$$

$$\sigma_z\Big|_{(zz)} = \frac{2}{z^3} \sum_{i=1}^{2} \left((C_{13} - C_{33} \nu_i^2 k_i) \frac{\bar{A}_i}{\nu_i} \right) \tag{50}$$

These functions now depend on material properties and it is necessary to obtain the 5 elastic constants for the tranversely isotropic material and hence the stiffness constants, C_{ij}. These may be taken as G [G_{23}], G′ [G_{31}], ν [ν_{23}], ν' [ν_{13}], and ρ [= E/E',]. Gazetas (1981) has shown that for many sands a good estimate of G′ may be obtained using the relationship proposed by Carrier (1946) between G′ and the other four cross anisotropic parameters as

$$G' = C_{44} = \frac{C_{11}C_{33} - C_{13}^2}{C_{11} + 2C_{13} + C_{33}} \tag{51}$$

The other four have been calculated in Appendix III based on special laboratory results and relevant theoretical relationships.

Assigning the anisotropic elastic parameters for the three expanding cylinder tests (2, 4, and 5 – see Tables 5.1 and 5.2) gave α and β values as shown in Table 8.1. It is clear from this table that

the greater vertical to horizontal stiffness ratio (C_{33}/C_{11}) for the OC test requires a much higher value of α than the NC tests. The shape of the spheroid is not so clearly differentiated.

The general σ_r, σ_θ and σ_z solutions for the spheroidal expansion can, in any case, be written as the sum of the three doublets [with α proportion of the zz doublet] as follows:

$$\sigma_r\Big|_{(xyz)} = \sum_{i=1}^{2}\Bigg\{\Bigg[2\bar{B}_i'\nu_i\Bigg[C_{44}\nu_i^2(1+k_i)\left(\frac{2}{R_i^3}-\frac{3r^2}{R_i^5}\right)+2C_{66}\left(\frac{-4}{R_iR_i^{*2}}+\frac{r^2}{R_i^3R_i^{*2}}+\frac{2r^2}{R_i^2R_i^{*3}}\right)\Bigg]$$

$$-\alpha\bar{A}_i\nu_i^2\Bigg[\left(C_{11}-C_{13}\nu_i^2k_i\right)\left(\frac{1}{R_i^3}-\frac{3z_i^2}{R_i^5}\right)+2C_{66}\left(\frac{z_i}{R_i^3R_i^*}+\frac{1}{R_i^2R_i^*}\right)\Bigg]\Bigg]\Bigg\} \qquad (52)$$

$$\sigma_\theta\Big|_{(xyz)} = \sum_{i=1}^{2}\Bigg\{\Bigg[2\bar{B}_i'\nu_i\Bigg[C_{44}\nu_i^2(1+k_i)\left(\frac{2}{R_i^3}-\frac{3r^2}{R_i^5}\right)-2C_{66}\left(\frac{4}{R_iR_i^{*2}}-\frac{7r^2}{R_i^3R_i^{*2}}-\frac{14r^2}{R_i^2R_i^{*3}}+\frac{3r^4}{R_i^5R_i^{*2}}+\frac{6r^4}{R_i^4R_i^{*3}}+\frac{6r^4}{R_i^3R_i^{*4}}\right)\Bigg]$$

$$-\alpha\bar{A}_i\nu_i^2\Bigg\{\Bigg[\left(C_{11}-C_{13}\nu_i^2k_i\right)\left(\frac{1}{R_i^3}-\frac{3z_i^2}{R_i^5}\right)+2C_{66}\Bigg[\frac{z_i}{R_i^3R_i^*}+\frac{1}{R_i^2R_i^*}$$

$$-r^2\left(\frac{3z_i}{R_i^5R_i^*}+\frac{1}{R_i^4R_i^*}+\frac{4z_i}{R_i^4R_i^{*2}}+\frac{2}{R_i^3R_i^{*2}}\right)\Bigg]\Bigg]\Bigg\}\Bigg]\Bigg\} \qquad (53)$$

$$\sigma_z\Big|_{(xyz)} = \sum_{i=1}^{2}-\left(C_{13}-C_{33}\nu_i^2k_i\right)\left(2\bar{B}_i'\nu_i+\alpha A_i\nu_i\right)\left(\frac{1}{R_i^3}-\frac{3z_i^2}{R_i^5}\right) \qquad (54)$$

8.3.5. Degenerate Solution

The non-degenerate solution breaks down when

$$C_{44} \text{ (or } G') = \frac{\tilde{C}_{13} - C_{13}}{2} \tag{55}$$

and a new solution must be found. This is necessary, in particular, if the isotropic equations are to be derived from the more general anisotropic ones. In the new solution $\nu_1 = \nu_2$, $R_1 = R_2$, and $k_1 = k_2$. In this solution, Eqns. (16), (22), and (23) are used again to form the doublets for radial stresses in the three planes. The z-z doublet will still need to be proportioned in the manner discussed for the non-degenerate case. The results are summarised in the next equation for a spheroidal cavity expansion for the radial stress as a function of radius r and depth z:

$$\sigma_r\Big|_{(xyz)} = \frac{-2\nu_1}{R_1^3}\left[\left(4C_{66} - \frac{C_{44}(C_{11}-C_{13}\nu_1^2)}{C_{13}+C_{44}}\right)(\bar{A}_1' - \bar{B}_1') - 2C_{44}\nu_1^2(1+k_1)\bar{B}_1'\right]\left(2 - \frac{3r^2}{R_1^2}\right)$$

$$+ 6C_{44}\nu_1^3(1+k_1)(\bar{A}_1' - \bar{B}_1')\frac{z_1^2}{R_1^5}\left(2 - \frac{5r^2}{R_1^2}\right) - 8C_{66}\nu_1\bar{B}_1'\left(\frac{4}{R_1 R_1^{*2}} - \frac{r^2}{R_1^3 R_1^{*2}} - \frac{2r^2}{R_1^2 R_1^{*3}}\right)$$

$$- 2\bar{B}_1\alpha\nu_1^2\frac{1}{R_1^3}\left[\left(C_{11} - C_{13}\nu_1^2 + 2C_{66} + \frac{2C_{13}C_{44}}{C_{13}+C_{44}}\right)\left(1 - \frac{3z_1^2}{R_1^2}\right)\right.$$

$$\left. - 3(C_{11} - C_{13}\nu_1^2 k_1)\left(\frac{3z_1^2}{R_1^2} - \frac{5z_1^4}{R_1^4}\right)\right] \tag{56}$$

The vertical stress distribution can also be obtained using Eqns. (18) and (24) as a function of radius r and depth z as follows:

$$\sigma_z\Big|_{(xyz)} = -\frac{2}{R_1^3}\Bigg\{\bar{B}_1\nu_1^2\alpha\Bigg[\left(C_{13} - C_{33}\nu_1^2k_1 + \frac{2C_{33}C_{44}\nu_1}{C_{13}+C_{44}}\right)\left(1 - \frac{3z_1^2}{R_1^2}\right)$$

$$- 3\nu_1(C_{13} - C_{33}\nu_1^2k_1)\left(\frac{3z_1^2}{R_1^2} - \frac{5z_1^4}{R_1^4}\right)\Bigg]$$

$$- 2\nu_1\Bigg[\left(C_{13} - \frac{C_{33}(C_{11}+C_{44}\nu_1^2)}{C_{13}+C_{44}}\right)(\bar{A}_1' - \bar{B}_1') + 2(C_{13} - C_{33}\nu_1^2k_1)\bar{B}_1'\Bigg]\left(2 - \frac{3z_1^2}{R_1^2}\right)$$

$$+ \frac{3z_1^2}{R_1^2}\left(\left(C_{13} - C_{33}\nu_1^2k_1\right)(\bar{A}_1' - \bar{B}_1')\left(4 - \frac{5z_1^2}{R_1^2}\right)\right)\Bigg\} \qquad (57)$$

8.4. Extension of Spheroidal cavity Equations to Give Semi-infinite Cylindrical Cavity

It is possible to integrate Eqns. (52) to (54) or Eqns. (56) and (57) from depth z up to $+\infty$ in order to obtain the stress distributions as a function of depth and radius for a semi-infinite penetration problem. The integration element should correspond to a short cylinder whose height gives the same volume as the expanding spheroid. Thus

$$V = \frac{4\pi a^3}{3\beta} = \pi a^2 h \quad \text{for a cylinder with same transverse radius, a to give } h = 4a/3\beta$$

Therefore, for a stress point at z = 0 (with the penetrometer 'cylinder' stretching from +z to $+\infty$)

$$\sigma_r(r)\Big|_{z=0} = \int_{+z}^{+\infty}\sigma_r(r,z)\cdot dz/h \qquad (58)$$

$$\sigma_z(r)\Big|_{z=0} = \int_{+z}^{+\infty}\sigma_z(r,z)\cdot dz/h \qquad (59)$$

8.4.1. Non-degenerate case

Eqns. (58) and (59) are integrated using Eqns. (52) and (54), respectively, to give

$$\sigma_r\Big|_{(xyz)} = -\frac{3\beta}{4a}\sum_{i=1}^{2}\left[\alpha\bar{A}_i\nu_i\left(\left(C_{11}-C_{13}\nu_i^2k_i\right)\frac{z_i}{R_i^3}+2C_{66}\frac{1}{R_iR_i^*}\right)\right.$$
$$\left.+2\bar{B}_i'\nu_i\left(C_{44}\nu_i^2(1+k_i)\frac{z}{R_i^3}+2C_{66}\frac{z}{r^2R_i}\right)\right]_{+z}^{+\infty} \qquad (60a)$$

$$=\frac{3\beta}{4a}\sum_{i=1}^{2}\left\{\left[\alpha\bar{A}_i\nu_i\left(\left(C_{11}-C_{13}\nu_i^2k_i\right)\frac{z_i}{R_i^3}+2C_{66}\frac{1}{R_iR_i^*}\right)\right.\right.$$
$$\left.\left.+2\bar{B}_i'\nu_i\left(C_{44}\nu_i^2(1+k_i)\frac{z}{R_i^3}-2C_{66}\frac{1}{\nu_iR_iR_i^*}\right)\right]\right\} \qquad (60b)$$

$$\sigma_z\Big|_{(xyz)} = \frac{3\beta}{4a}\sum_{i=1}^{2}\left(C_{13}-C_{33}\nu_i^2k_i\right)\left(2\bar{B}_i'\nu_i+\alpha\bar{A}_i\nu_i^2\right)\left(\frac{z}{R_i^3}\right) \qquad (61)$$

The lower limit of integration implies that σ_r and σ_z are at z below the penetrometer level. Hence, the stresses at the penetrometer level are obtained by setting $z = 0$. In this solution the radial stress on a cylinder co-axial with the penetrometer is skew-symmetric about the mean stress value on the cylinder at the same level as the penetrometer tip. That is, below the level of the tip the stress reduces asymptotically to zero whilst above the level of the tip it increases to an asymptotic value twice that of the mean. The vertical stress, on the other hand, is zero at the level of the tip and behaves exactly similarly to a point load distribution [see section 8.3.1 and 8.6 later] within an elastic medium undergoing tension above the tip

along the shaft whilst compressing the soil beneath the tip. The effect, of course, decays to zero at both $+\infty$ and $-\infty$.

If two semi-infinite cylinders (one from z = 0 to z = $+\infty$, the other from z = 0 to z = $-\infty$) are added together, the sum of the two σ_r distributions will give the solution for a complete infinite cylinder - at twice the mean value of each. The expression for σ_r is that for plane-strain expansion (as for the elastic part of the expanding cylinder tests of Chapter 5):

$$\sigma_r = -\frac{3\beta}{4a}\sum_{i=1}^{2}\frac{8C_{66}\bar{B}_i'}{r^2} \tag{62}$$

Replacing for $\bar{B}_i'$ in this equation and simplifying gives

$$\sigma_r = \frac{3\beta P\delta}{4\pi a r^2}\left(\frac{1-\nu-2\rho\nu'^2}{1-\rho\nu'^2}\right) \tag{63}$$

where $P\delta$ is that for the horizontal doublets of the anisotropic medium.

This has been obtained directly in Appendix VI for an anisotropic material. In that solution, a known radial stress, P_i, is applied at a cylindrical radius, a, in an infinite material. The results show that, despite the anisotropy, the radial stress is not related to any anisotropic parameter but is inversely proportional to the square of the radius, r, as is the case for an isotropic material.

$$\sigma_r = \frac{a^2}{r^2}P_i \tag{64}$$

To make Eqn. (63) compatible to Eqn. (64), $P\delta$ can be replaced by:

$$P\delta = \frac{4\pi a^3}{3\beta}\left(\frac{1-\rho\nu'^2}{1-\nu-2\rho\nu'^2}\right)\cdot P_i \tag{65}$$

Since the cylindrical solution was obtained by integration of the single spheroidal solution, the $P\delta$ value just obtained for the former must apply to the latter as well.

8.4.2. Degenerate case

Eqn. (56) is integrated using Eqn. (58) [from $-\infty$ to $+\infty$] to give the cylindrical solution of σ_r for the degenerate case leading to:

$$\sigma_r = \frac{3\beta P\delta}{4\pi a r^2} \frac{C_{66}}{\nu_1^2 C_{44}} \tag{66}$$

This stress has the same form as that given directly by Eqn. (64). Hence, $P\delta$ should be replaced by

$$P\delta = \frac{4\pi a^3 \nu_1^2 C_{44}}{3\beta C_{66}} P_i \tag{67}$$

in which P_i is the radial stress at radius a in the transverse plane.

8.5. The Degenerate Case leading to an Isotropic Solution

The stress distribution equations for the anisotropic case using the degenerate solution to define G′ can be reduced to the isotropic solutions by setting

$C_{11} = C_{33} = \lambda + 2\mu$, $C_{44} = C_{66} = \mu$, and $C_{13} = C_{12} = \lambda$

Hence, the following simplifications are made in the different constants used:

$$P\delta = \frac{4}{3}\pi a^3 P_i$$

Also

$$\bar{A}_i = 0 \text{ and } \bar{B}_1 = \bar{B}_2 = \bar{B} = \frac{-a^3(\lambda + \mu)P_i}{12\mu(\lambda + 2\mu)} = \bar{A}' - \bar{B}'$$

and similarly

$$\bar{A}' = \frac{a^3 P_i}{12(\lambda + 2\mu)} \quad \text{and} \quad \bar{B}' = \frac{a^3 P_i}{12\mu} \quad \text{and} \quad \bar{D} = \frac{a^3 P_i}{3\mu}$$

with $k_1 = k_2 = 1$

The stress functions in Eqns. (54) and (55) are simplified on the axial and transverse diameters to give

$$\sigma_r = -\frac{16(\bar{B} + \bar{B}')\mu}{r^3} = \frac{-4\nu a^3 P_i}{(1-\nu)r^3} \tag{68}$$

$$\sigma_z = -\frac{16(\bar{B} + \bar{B}')\mu}{z^3} = \frac{-4\nu a^3 P_i}{(1-\nu)z^3} \tag{69}$$

The displacement functions can also be set up in the same manner as the stress functions for both spherical and cylindrical cavities. These functions, after simplification and having been added in equal proportions to each other, give the solutions for the displacements of the spherical type cavity expansion at the two previously mentioned points:

$$U_r = \frac{2}{r^2}\bar{A}' = \frac{P_i(1 - 2\nu)(1 + \nu)a^3}{3(1 - \nu)Er^2} \tag{70}$$

$$U_z = \frac{2}{z^2}\bar{A}' = \frac{P_i(1 - 2\nu)(1 + \nu)a^3}{3(1 - \nu)Ez^2} \tag{71}$$

This shows that for equal r and z the displacements and stresses are equal as must be so for a spherical expansion in an isotropic material.

8.6. Point Force Effect at the Penetrometer Level

The forces acting on any one spheroid along the vertical direction are equal but in opposite directions. When any two such spheroids are integrated vertically, the forces at the contact surfaces will cancel each other but still leave two equal and opposite forces at the extreme vertical ends. For a penetrometer approaching from infinity, there will exist an unbalanced force at the penetrometer level, with the assumption that the same at infinity will not affect the stresses. Hence, the distribution of stress in the vicinity of the penetrometer will include the effect of a point force at the penetration level. This point force is due to expansion but is otherwise similar to the additional point force required for penetration. Assuming that the stresses are uniform along the surface of the bottom semi-spheroid containing the unbalanced force, a vertical point force that is equal to the normal force to the penetrometer at the tip can then be chosen.

The solution for a point force acting along the penetrometer axis is that given by Pan and Chou as in Section 8.3.1. The radial and vertical stresses in cylindrical coordinates are summarised as follows which can be particularised for either of the degenerate or the non-degenerate cases:

$$\sigma_r = \sum_{i=1}^{2} \left\{ \left[\left(C_{11} - C_{13}\nu_i^2 k_i \right)[2A_i + B_i] + 2 \left(C_{66} + \frac{C_{13}C_{44}\nu_i^2}{C_{13} + C_{44}} \right)(A_i + B_i) \right] \frac{\nu_i z_i}{R_i^3} \right.$$

$$\left. - 3\left(C_{11} - C_{13}\nu_i^2 k_i \right)[A_i + B_i] \frac{\nu_i z_i^3}{R_i^5} - 2C_{66}A_i\nu_i \frac{1}{R_i R_i^*} \right\} \qquad (72)$$

$$\sigma_z = \sum_{i=1}^{2} \left\{ \left[\left(C_{13} - C_{33}\nu_i^2 k_i \right)[2A_i + B_i] + \frac{2C_{33}C_{44}\nu_i^2}{C_{13} + C_{44}} (A_i + B_i) \right] \frac{\nu_i z_i}{R_i^3} \right.$$

$$\left. -3\left(C_{13} - C_{33}\nu_i^2 k_i \right)[A_i + B_i] \frac{\nu_i z_i^3}{R_i^5} \right] \qquad (73)$$

8.7. Sleeve Friction Effect on Penetration

Another mechanism that is involved in deep penetration is sleeve friction. This can be treated as a line load approaching from infinity and can be solved by integrating the stress equations (72) and (73) from +z to +∞ (for a stress point at z = 0) with the point force P replaced by p·dz as follows:

8.7.1. Non-degenerate case

$$\sigma_{r_{sleeve}} = \sum_{i=1}^{2} \frac{p(C_{13}+ C_{44})}{4\pi C_{33}C_{44}(\nu_2^2 - \nu_1^2)\nu_i}\left[\left(C_{11} - C_{13}\nu_i^2 k_i\right)\frac{1}{R_i} - 2\,C_{66}\frac{1}{R_i^*}\right] \quad \ldots\ldots (74)$$

$$\sigma_{z_{sleeve}} = \sum_{i=1}^{2} \frac{p(C_{13}+ C_{44})}{4\pi C_{33}C_{44}(\nu_2^2 - \nu_1^2)\nu_i}\left(C_{13} - C_{33}\nu_i^2 k_i\right)\frac{1}{R_i} \quad (75)$$

8.7.2. Degenerate case

$$\sigma_{r_{sleeve}} = \frac{p(C_{13}+ C_{44})}{8\pi C_{11}C_{44}R_1}\left[\left(C_{11} - C_{13}\nu_1^2 k_1\right)\left(2 - \frac{r^2}{R_1^2}\right) - 2\left(C_{66}+ \frac{C_{13}C_{44}\nu_1^2}{C_{13}+ C_{44}}\right)\right] \quad \ldots\ldots (76)$$

$$\sigma_{z_{sleeve}} = \frac{p(C_{13}+ C_{44})}{8\pi C_{11}C_{44}R_1}\left[\left(C_{13} - C_{33}\nu_1^2 k_1\right)\left(2 - \frac{r^2}{R_1^2}\right) - \frac{2C_{33}C_{44}\nu_1^2}{C_{13}+ C_{44}}\right] \quad (77)$$

Eqns. (75) and (77) indicate that the vertical and horizontal normal stresses are not affected by the direction of z.

The degenerate solution for the sleeve friction can, in any case, be particularised for an isotropic solution with the stiffness

constants being replaced with their equivalent isotropic terms as follows:

$$\sigma_r = \frac{p}{8\pi(1 - \nu)R}\left(1 - 2\nu - \frac{r^2}{R^2}\right) \tag{78}$$

$$\sigma_z = \frac{-p}{8\pi(1 - \nu)R}\left(4 - 2\nu - \frac{r^2}{R^2}\right) \tag{79}$$

where p is the vertical force per unit height (positive in tension) and R is the spherical distance from point of the tip. These equations could also be obtained by integrating Eqns. (1) and (3) [Kelvin solution] directly.

8.8. Conclusion

The three separate mechanisms contributing to the stress distribution around a semi-infinite penetrating cylinder have been presented for a transversely isotropic medium. The combination of the three mechanisms will be considered at the end of Chapter 9 for the three testing conditions shown in Table 8.1.

Test No.	σ'_v bar	OCR	C_{11}	C_{13}	C_{33}	C_{44}	C_{66}	$\tilde{C}_{13}$	ν_1	ν_2	α	β
			bars									
CPT2	4.00	1	2374	647	3500	1100	1666	2883	1.003	0.821	1.077	1.106
CPT4	1.00	4	1207	332	2500	665	833	1737	.9420	.7529	1.062	1.720
CPT5	2.00	1	1309	340	2000	627	1000	1618	1.001	.8079	1.099	1.095

Table 8.1. Values of the elastic stiffness constants and other parameters used in the development of the spheroidal cavity expansions solution

CHAPTER 9

ELASTO/PLASTIC CPT MODEL

9.1. Introduction

It was very clear from the expanding cylinder test series that the expansion required for the penetration of the penetrometer and its drill shaft puts the soil into the plastic range of deformation up to the order of the diameter of the chamber itself. The elastic analysis of the last chapter could only, therefore, be relevant to the distortion the soil would have to undergo beyond about 60 cm radius. Indeed, since the net volume change in the plastic region is approximately zero, one could infer from the elastic analysis the likely stresses that soil-to-infinity should exert at the chamber boundary for the volume change required. With such elastic stresses as input for the boundary stresses of a plastically expanding cylinder analysis (the chamber soil being regarded as a stack of independent (2-D) discs each acting in plane strain), a revised stress distribution (as a function of radius) could be obtained. At the radius of the penetrometer the new radial stress would be multiplied by an assumed coefficient of friction against the steel casing of the penetrometer's shaft to give a new predicted sleeve stress with which to compare with that measured in the CPT itself. In fact, the results of the expanding cylinder tests can be used directly and the actual stress-strain behaviour as measured in these tests is used - modified by elastic theory only to the extent of predicting the variation with depth relative to the level of the penetrometer tip.

The following sections discuss in more detail, firstly, the prediction of sleeve friction from expanding cylinder test data (and its related theory), and, secondly, the effect of the accumulated sleeve friction in the overall stress distribution and its combination with the remnant requirement for a point load additional to that

already implied by the semi-infinite cylindrical expansion.

9.2. Prediction of Sleeve Friction from the Expanding Cylinder Test Data

The anisotropic model in the last chapter indicated that the distribution of elastic radial stresses along the lateral boundary of the calibration chamber [Eqn. 8.60b] was skew-symmetric about a mean value at the penetrometer level. It is clear, therefore, that the total volume change on the boundary for equal distances above and below the penetrometer tip due to the semi-infinite expanding cylinder will correspond to this mean value - or to the full value for the half distance. Hence, the total measured volume change for 75 cm of penetration (half the depth of the chamber) must correspond (in the elastic analysis) to the full expansion of 75 cm of 2-D cylinder.

Now the expanding cylinder tests give stress/strain data from the outer boundary to the 8 cm radius of the expanding cylinder. Further, they all indicate a constant dilation angle, ψ, from relatively small strains to about twice those required for the CPT's at this radius. It would seem reasonable, then, to use those dilation values (about 6° for the 2 bar NC and 1 bar OC tests and 5° for the 4 bar NC test) for the soil behaviour from 8 cm radius in towards the penetrometer itself. A further assumption, that this dilation should stop at approximately 2.5 cm radius, is based on the realisation that the displaced soil must occupy a region of approximated 10 cm^2 immediately beyond the 10 cm^2 of the penetrometer itself and is likely to have been crushed sufficiently to have suffered no net dilation in the intense shearing process about the tip.

The displacements within the 8 cm range are related as [Eqn. A.II. 30]

$$u_r = u_r|_{r=8cm} \cdot \left(\frac{8}{r}\right)^{1/N_\psi} \qquad (1)$$

where the N_ψ is the net dilation of the soil as obtained from the slope of the relevant volumetric strain versus the shear strain plots of Fig. 5.20. This equation can be re-arranged to convert the displacements into their corresponding volume changes as follows:

$$\text{Vol.}_r = \text{Vol.}_r\Big|_{r=8cm} \cdot \left(\frac{r}{8}\right)^{1 - 1/N_\psi} \qquad (2)$$

For a 10 cm^3 volume change at the 2.5 cm radius it is possible to obtain the dilated volume at the 8 cm radius from Eqn. (2) which can then be used to determine the state of stress at this radius from Col.#3 of Tables 5.1 to 5.3.

The stresses at different radii within the inner plastic zone ($r < 8$ cm) are related in a manner similar to the displacements and take the form [Eqn. A.II.25]:

$$\sigma_r = \sigma_r\Big|_{r=8cm} \cdot \left(\frac{8}{r}\right)^{1 - 1/N_\phi} \qquad (3)$$

The friction angle used in this equation is that for the plastic strains, as quoted in Col.#7 of Tables 5.1 to 5.3. In this way, the radial stress at the 2.5 cm radius is obtained.

When the stress distribution of the severely disturbed soil inside 2.5 cm radius is considered, it is realized that the radial stress is no longer (even approximately) a principal stress and that the circumferential stress, though a principal stress, is now intermediate (since the most recent shear in the soil - as it rounded the tip of the penetrometer - must have been in a vertical, radial, plane). There is no need to assume a continuity in circumferential stress across the 2.5 cm 'boundary' between the two separate mechanisms of soil distortions and - for lack of any evidence to the contrary - it might (and will) be assumed that inside this radius the radial and circumferential stresses

are equal. This immediately implies that the radial stress is constant with radius from the penetrometer surface up to the 2.5 cm radius.

The friction angle between the sand and the penetrometer, δ, is normally given as a fraction of the internal friction angle, ϕ'. Last (1982) suggested that a value of $^{\delta}/_{\phi} = 0.5$ is suitable for a steel cone in sand. However, the tests by Andrawes (1970) showed that the kinematic angle of friction between steel and sand is even lower and suggests that $^{\delta}/_{\phi} = 0.33$ gives a suitable value of the kinematic angle of friction. For a $\phi'_{cv} = 36°$, the kinematic angle of friction would then be 12°.

It is now possible to predict the normal stress on the penetrometer and thus the sleeve friction for full 2-D expansion to a fully penetrated penetrometer: with 10 cm^2 expansion at the penetrometer and continued to 2.5 cm radius, the dilation of the soil beyond this to 8 cm radius gives a volume expansion (slightly different for the 4 bar test from the other two) of about 12 cm^2. This is compared with the relevant expansion tests to give a radial stress for each test at 8 cm radius. Eqn. (3) then gives the stress at 2.5 cm and thus the normal stress at the penetrometer surface. A 12° friction angle then gives the surface friction stress to be used for the semi-infinite line load and the corresponding elastic stress distribution for side friction.

In order to obtain values for sleeve friction to compare with those measured in the CPT's, it is necessary to allow for the variation in expansion with height as predicted by the elastic analysis at the 60 cm radius boundary. Here, at the mean height of the measuring sleeve above the tip level (7 cm), it is found that the expansion is 47.5 % above the mean level. Using these reduced values in Tables 5.1 to 5.3 of the expanding cylinder tests allows a revised stress at 8 cm radius to be obtained for each test and thus revised normal and shear stresses at the penetrometer measuring sleeve.

The results of the predictions together with the actual sleeve friction measurements are shown in Table 9.1. This Table shows two different radial stress and sleeve friction values that correspond to the full (cylindrical) and penetrometer sleeve level values. It shows that the measured and the calculated sleeve frictions can be made identical if δ is set at 12° for both the 2.0 bar NC and the 1.0 bar (OCR = 4) tests and at 10° for the 4.0 bar NC test.

The sleeve friction for the 2.0 bar NC test appears to be about 10 % greater than that for the 1.0 bar (OCR = 4) test. It is interesting to note that the same ratio also exists between their starting K_o lateral pressures indicating the close link between the sleeve friction and the in-situ lateral stress, as shown in Chapters 3 and 7. This will be further investigated at the end of the next section by studying the sleeve friction profiles of selected tests as related to the lateral stress opposite to the penetrometer as well as to the lateral stress at an angle below the penetrometer tip.

9.3. Components of the Elastic CPT Model

It was pointed out in Chapter 8 that penetration into a dense sand involves three separate mechanisms: an expansion, a point force, and a sleeve force. The combination of the first two, vertically, should ideally add up to the measured cone resistance force for a particular test. These components, as discussed below, will be combined in order to obtain the radial stress distribution at the outer soil boundary as a function of depth for a penetration depth of 75 cm.

The elastic analysis could only define the state of soil distortion beyond about 60 cm radius. The elastic lateral pressure distribution with depth due to expansion beyond this radius could be obtained from the integrated spheroidal expansion [Eqn. (8.60b)]. This distribution was shown to be skew-symmetric about the mean stress at the penetrometer level. The total lateral pressure measured at the lateral boundary at the 75 cm penetration is matched against the cylindrical value of the pressure from the above distribution and the

ratio is used to adjust the entire pressure profile due to expansion.

The sleeve friction is taken from the cylindrical f_s values as given in Table 9.1. The stresses due to the resulting line load are assumed to distribute elastically within the chamber to provide corrections to the radial stress (and displacement) at the 60 cm boundary as obtained from Eqn. (8.74).

As also pointed out in Chapter 8, the semi-infinite cylindrical expansion has a vertical point force component which is assumed to act on a 20 cm^2 cross-sectional area. From the equilibrium conditions at the penetrometer tip between this force and the cone force, the net vertical point force is obtained. It is also assumed that the stresses within the chamber change elastically according to Eqn. (8.72) to provide a further correction to the boundary stresses and strains at the 60 cm boundary.

The assumption of elastic stress distribution due to a point force within the chamber is rather a gross one. A proper lateral stress distribution due to a point force in a frictional material would require an elasto/plastic analysis of the soil in 3-D and would need to be carried out in conjunction with that for the expanding cylinder analysis as both of them are non-linear and their individual behaviours could not be superimposed. As input to a 3-D analysis the volume change measurements made at the base of the sample during penetration could have been used. However, it was quite clear that the actual volume change measurements in the base pockets lacked the degree of sensitivity required for any corroboration of such an analysis and the latter was not attempted.

The sum of the component distributions at the outer boundary add up to a single lateral stress distribution that should, ideally, look like the measured stress distribution deduced from the strain gauges. The shape of the final distribution is largely governed by the shape of the expansion component due to its controlling role in the penetration process. The two sets of curves are shown in Figs. 9.1 to 9.3 for the

three tests considered. Figs. 9.1a to 9.1c show the components of the theoretical curves for the 4.0 bar NC test for both an infinite medium and one limited by the chamber boundaries.

It is clear that, although the theoretical predictions have much the same shape and peak values, they are displaced vertically in relation to the observed values. In particular, the predicted peak occurs behind the penetrometer tip whilst the observed peak is always ahead of the tip. It is possible that the radial stress at the shaft decreases with distance from the tip to a lower value than that predicted for the theoretical expansion, though confirmation would require further stress sensors along the shaft (or, indeed, a measurement of the total load on the penetrometer and shaft). It has been noted in the earlier chapters that the sand density at the shaft is less than might have been expected and might, indeed, indicate a lower stress than that measured immediately behind the tip. The stress-strain curves from which the theoretical distributions have been deduced were obtained from the monotonic expanding cylinder tests and would require modification if the distortion mechanism around the penetrometer allowed a relaxation of radial stress behind the tip. This would result in an increase in the predicted value of the boundary radial deflection and the accompanying stress at the level of the penetrometer tip and a reduced value above this level to keep the total volume of expansion consistent with the displaced volume at the penetrometer. This would shift the predicted peak closer to that observed.

This is further studied in the next section by relating both cone resistance and sleeve friction values, measured at the tip level, to the stresses developed along the lateral wall.

9.4. Correlations between the Cone Stresses and the lateral Stress Distributions

The analysis of sleeve friction data in Chapter 7 showed a remarkable relationship between the measured sleeve frictions at the chamber mid-height and the lateral outer soil stresses developed at the same height. This was not, however, so well established in the case of the cone resistance. The sleeve friction profiles of selected tests have been related to the lateral stress developed opposite to the penetrometer in Fig. 9.4. The ratio of f_s to the lateral pressure appears to be constant along the depth for these tests. The cone resistance profiles for the same tests, on the other hand, seem to show a constant ratio to the lateral stresses that develop 25 cm below the penetrometer level, as shown in Fig. 9.5. This is further investigated using the results of CP3 which had non-uniform density along the depth (Fig. 9.6). This figure shows that the unconventional cone resistance profile developed due to this non-uniformity matches the profile obtained from the lateral pressure points some 25 cm below the penetrometer level corresponding to a cone angle from the horizontal at the penetrometer tip of about 22.5°. The lateral pressure distribution deduced from the strain gauges also shows that the peak occurs about 25 cm ahead of the tip level.

σ_v bar	OCR	$\psi°$		Δv at r=8 cm (cc)	σ_r(r=2.5 cm), bar		* $\delta°$	calculated f_s*, bar	
		plas	net		cylind.	at sleeve		cylind.	meas.sleeve
4.0	1	7.6	5	12.00	19.10	16.85	10	3.37	2.90
2.0	1	7.7	6	12.44	9.86	8.66	12	2.10	1.84
1.0	4	7.6	6	12.44	9.44	8.28	12	2.01	1.75

* δ values required to make calculated f_s values at sleeve correspond to those measured

Table 9.1 Comparison of the analytic results with the experimental CPT ones for sleeve friction

Fig. 9.1a Normal stress distribution at chamber boundary due to semi-cylindrical (integrated spheroidal) expansion

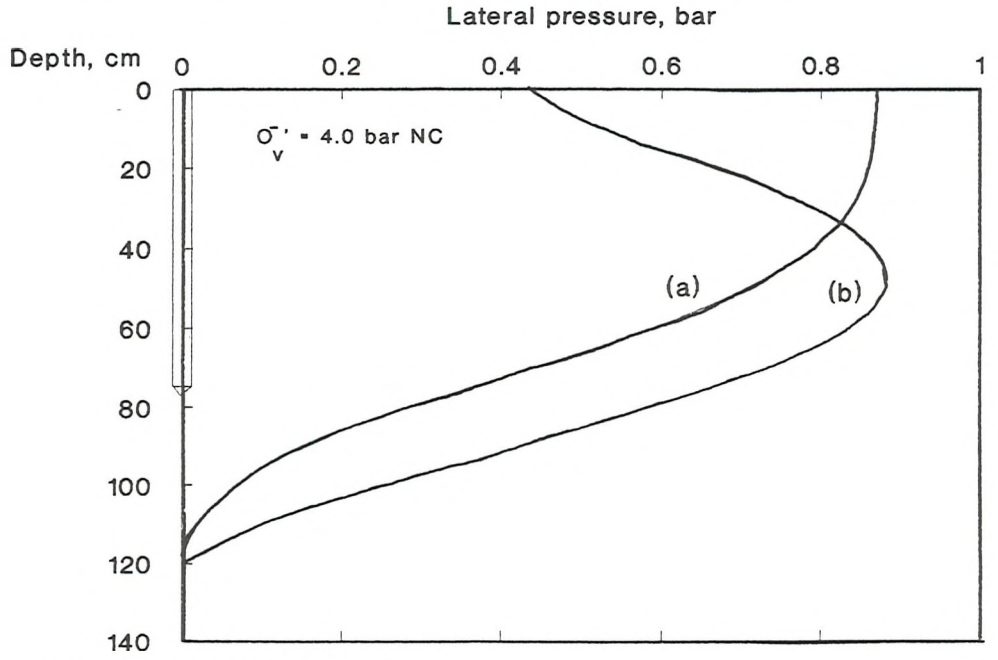

(a) Penetrometer from infinity

(b) Penetrometer from top of chamber in infinite soil mass

Fig. 9.1b Normal (anisotropic elastic) stress distributions at chamber boundary due to vertical point and sleeve load components (b & c)

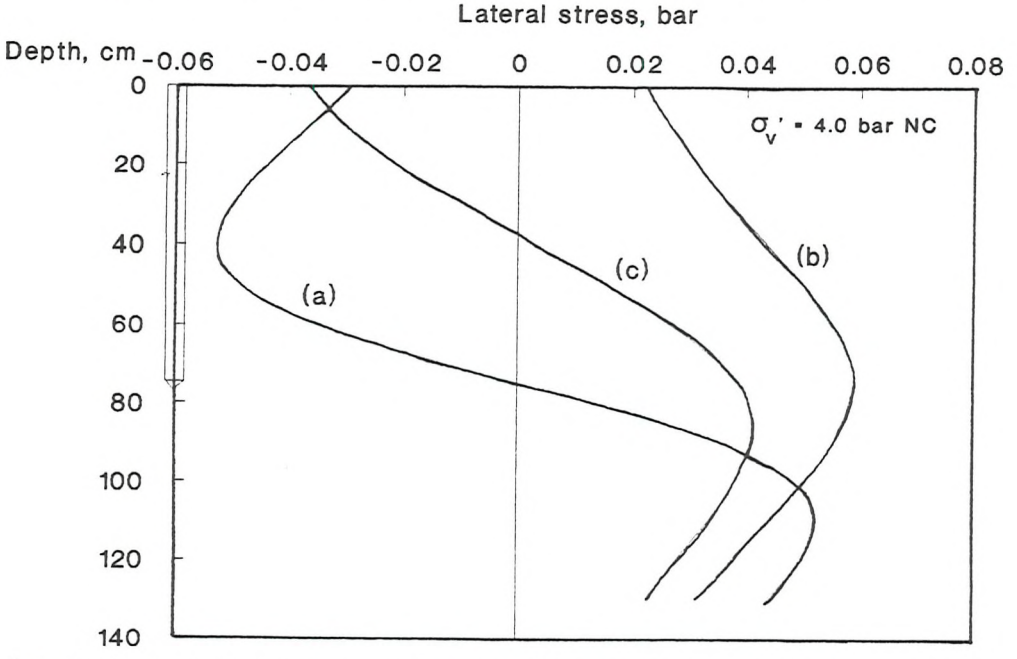

(a) Point load at tip in infinite soil mass; (b) Penetrometer from infinity

(c) Penetrometer from chamber top in infinite soil mass

Fig. 9.1c Predicted vs. experimental lateral stress distribution at chamber boundary

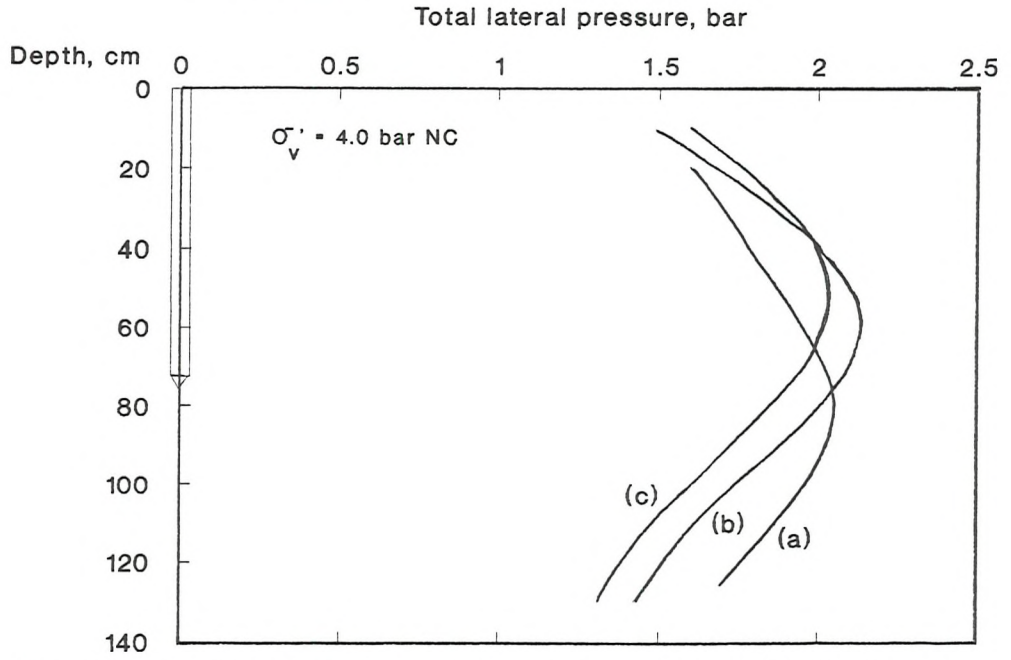

(a) Experimental, (b) Predicted - totally elastic, (c) Predicted - line and point load components from penetrometer measurements

Fig. 9.2. Predicted vs. experimental lateral stress distribution for 2 bar NC test at chamber boundary

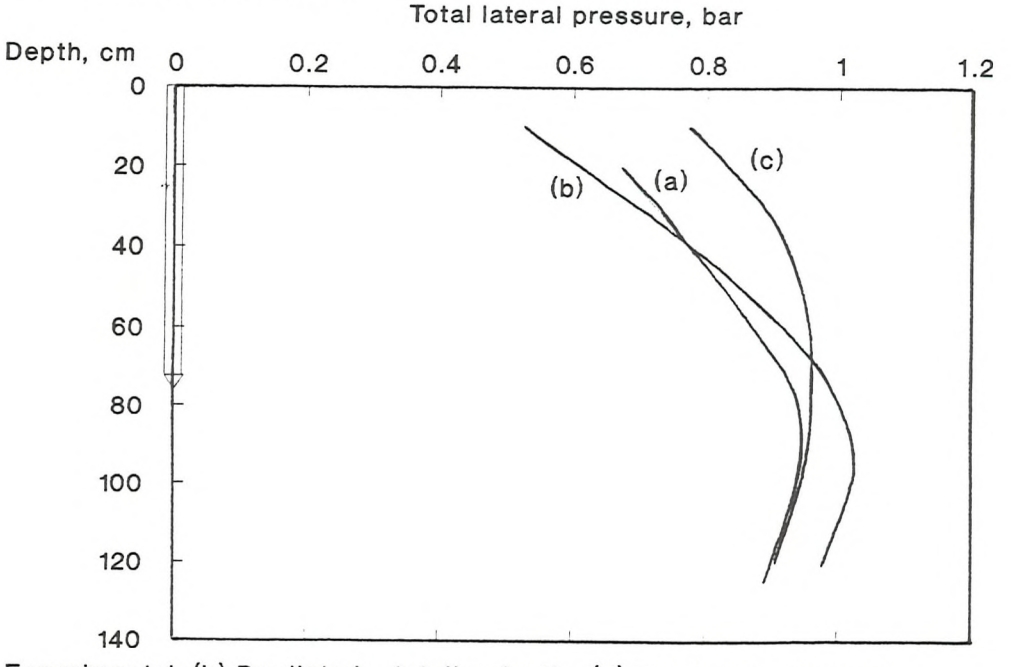

(a) Experimental, (b) Predicted - totally elastic, (c) Predicted - line and point load components from penetrometer measurements

Fig. 9.3 Predicted vs. experimental lateral stress distribution for 1 bar (OCR = 4) test at chamber boundary

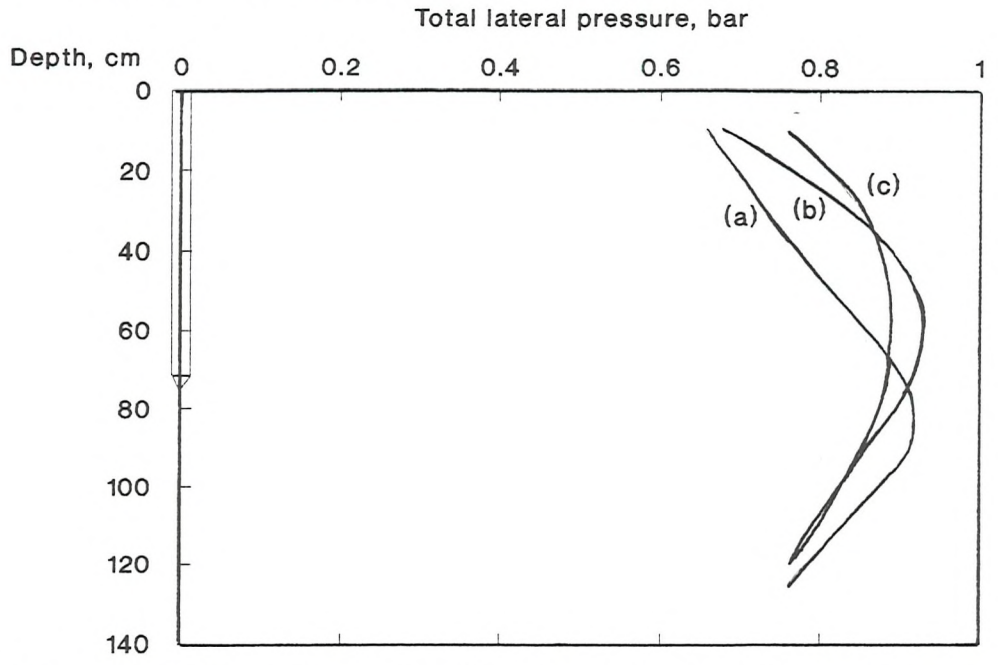

(a) Experimental, (b) Predicted - totally elastic, (c) predicted - line and point load components from penetrometer measurements

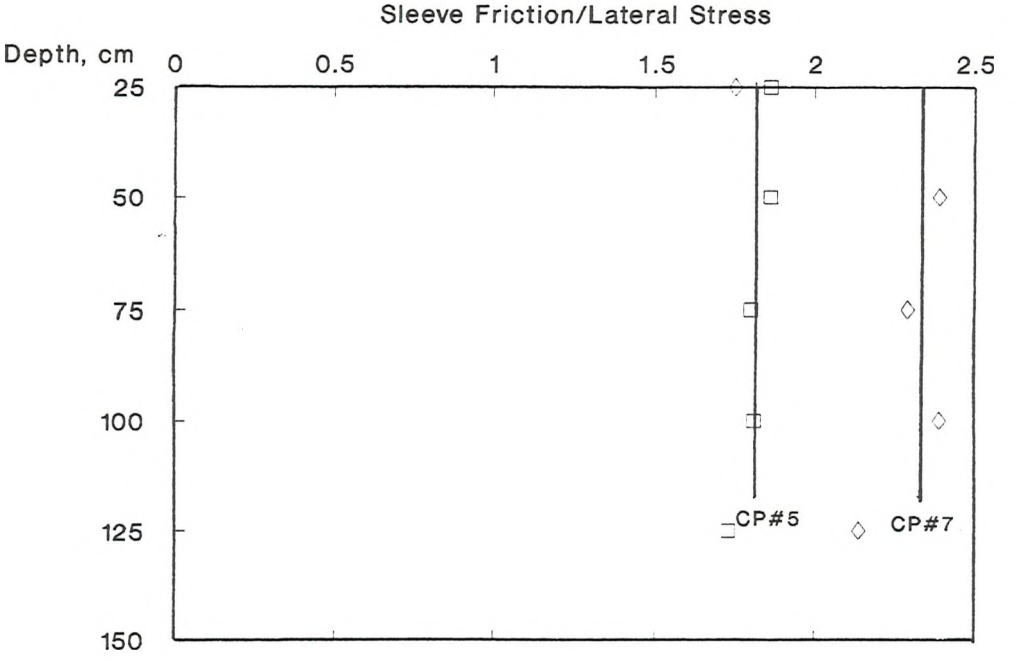

Fig. 9.4. f_s/P_L (at the Penetrometer Level) vs. Depth

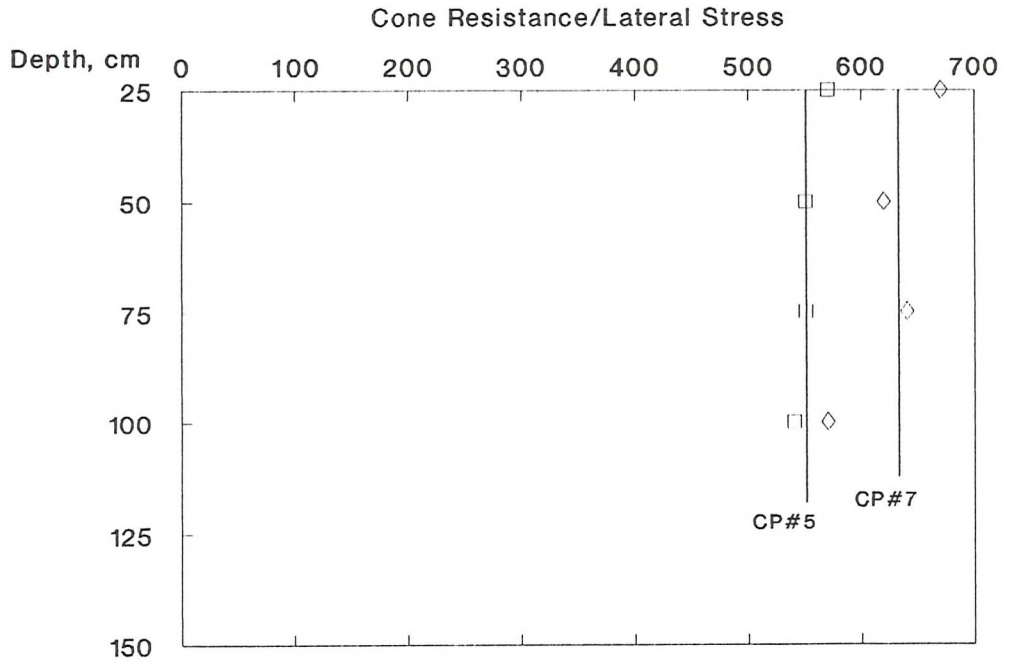

Fig. 9.5. q_c/P_L (25 cm Below Penetrometer Level) vs. Depth

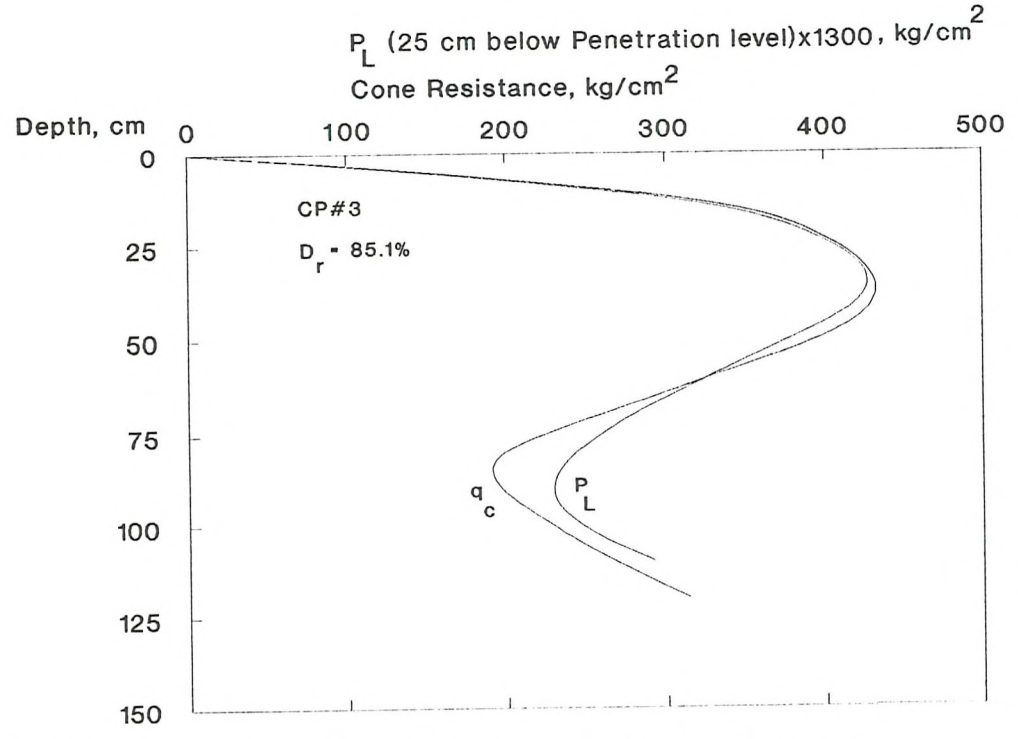

Fig. 9.6. q_c and P_L Profiles vs. Depth for a Non-uniform Dense Sand

CHAPTER 10

SUMMARY, CONCLUSIONS AND RECOMMENDATIONS FOR FUTURE WORK

Over the past 20 years large scale calibration chambers with flexible lateral walls have been used to obtain correlations between results of CPTs and engineering parameters in sand.

From the results of a total of 84 relevant cone penetration tests in Hokksund sand at Norway, Italy, and Southampton, which involved both full scale and half scale penetrometers under BC1 and BC3 boundary conditions over a range of stress histories, it was shown that calibration chamber tests on dense samples are affected by the size of the chamber (Chapters 3 and 4). It was concluded that the chamber would need to be at least 1.8 m in diameter (when using the standard penetrometer) if any boundary and size effects were to be substantially eliminated and thus allow the cone stresses obtained in the calibration chamber to be applied directly in the field. The cone stresses measured in actual calibration chamber tests were considered to under-estimate field conditions in both BC1 and BC3 cases.

Two sets of correction factors to the measured cone resistance values for both NC and OC dense samples have been proposed for the two boundary conditions:

- Lunne and Christophersen (1983) of NGI suggest an increase of 25 % and 7 % to the measured q_c of NC samples under BC1 and BC3, respectively, while the q_c of OC samples need to be increased by 24 % for both boundary conditions.

- Baldi et al. (1982) [Italian group] suggested an increase of 8 % and 18 % for dense and very dense NC samples, respectively, (presumably under BC1) and a corresponding increase for OC

samples of at least 39 %.

To achieve a more natural boundary behaviour in calibration chamber tests, the boundaries of a large calibration chamber (on loan from NGI) were modified by using 6 mm^2 rubber strips placed at 14 mm (centre-to-centre) intervals and covered with a thick layer of solid rubber. This produced a linear stiffness of 1 bar per millimetre of radial compression and corresponded to the stiffness indicated by a series of full length expanding cylinder tests for the outer soil stress-strain behaviour of 2.0 bar NC and 1.0 bar (OCR = 4) tests in dense sand. Additional tests under different stress conditions were performed to study the scale effects.

For an assumed infinite boundary the stress-strain behaviour of the homogeneous soil at any radius must follow the same curve, though at any instant the distance along the curve will be greater for a smaller radius. Thus to simulate an infinite boundary in the chamber it was necessary to force the outer cylindrical boundary of the soil to follow the same stress-strain behaviour as given at an earlier stage of the test by the expansion of the inner cylindrical cavity. When water was allowed to flow out of the lateral cell of the chamber, the pressure would drop and this increase in strain and decrease in pressure could be adjusted so that the combination did, indeed, fall on the previously established stress-strain curve for each step in the expansion process.

The same argument could, of course, be used to apply at any radius. This gave the opportunity of analysing the distribution of stress with radius as well as with time and could be commenced by assuming an elastic distribution for the first increment and allowing the strain value at the inner boundary to be propagated towards the outer boundary as the former was subjected to progressively increasing pressure. For the analysis the soil was assumed to be composed of 11 annuli all having geometric similarity (the same thickness-to-radius ratio) so that when a stress/strain state at one boundary propagated to the next, the same would happen at all other annuli boundaries.

The initial elastic stiffness was obtained by unload-reload at small strains as well as from the initial slope of the stress-strain curve. The latter, however, departed very quickly from this tangent value and would have been less than reliable by itself. This elastic stiffness (in the horizontal plane) was approximately proportional to the starting lateral stress.

It was decided to treat the soil as anisotropic: elastic constants were obtained from the last stage of the consolidation process as well as from a special test in which the soil in the chamber was subjected to perturbations in the lateral cavity pressure.

In the analysis, the soil was assumed to yield plastically in the plane of extreme principal stresses - initially vertical and eventually the more conventional horizontal. Vertical plastic yielding was accompanied by elastic unloading so that the net vertical strain remained zero. The plastic behaviour of the soil was assumed to follow Rowe's dilatancy theory.

With the above assumptions it proved possible to analyse the elastic/plastic behaviour of the soil as exhibited at the soil boundaries during the expansion tests and thus to obtain stress/strain (including dilatancy) values for the whole test as a function both of space and time. This analysis was performed for three testing conditions: two NC samples at 2 bar and 4 bar with an OC sample at 1 bar (OCR = 4). The following points can be summarised from the results of the analysis:

- The transitional plastic phase (i.e., vertical stress as the major principal stress) could stretch as far as the whole soil radius within the chamber before the second plastic phase (yielding in the horizontal plane) started in the first annulus.

- The 4.0 bar NC test experienced considerable volumetric compression, as compared to the 2.0 bar NC and 1.0 bar OC tests, before dilation at the cavity began. In fact, the sand in the 4

bar test at the end of expansion was still in a state of overall compression.

- All three tests gave similar plastic dilation angles at the limiting obliquities. The net dilation angle of the 2 bar NC and 1 bar OC tests was 1° higher than the 4 bar NC test showing the effect of overall compression during the cylindrical expansion. A theoretical approach to the elastic/plastic analysis of cylindrical expansion in an infinite homogeneous medium is given in Appendix II and includes the effects of dilation.

- The 2 bar NC and the 1 bar OC tests exhibited similar behaviours in the second plastic phase (despite their different behaviour in the transitional phase) and this is believed to be linked with their similar starting horizontal stress and their similar shear modulus values.

Theoretical Results

It was possible to use the spherical cavity expansion analogy in an elastic isotropic medium to develop a solution in a transversely isotropic medium. The expanded shape, which was a function of consolidation stress and stress history, appeared to be in the form of a spheroid: oblate spheroids for the NC tests and prolate spheroids for the OC one.

It is assumed that penetration into dense sand involves three separate mechanisms: a cylindrical expansion, a point force, and a line sleeve force. The combination of these forces at the penetrometer tip were determined and used to obtain a distribution of lateral pressure at the outer soil boundary. The shape of the obtained curves corresponded to the curves deduced from the strain gauge measurements.

The analysis of selected CPT results showed that sleeve friction could be related closely to the lateral pressure that developed opposite to the penetrometer. The cone resistance profiles, however, seemed to show a better correlation to the lateral stresses that

developed 25 cm below the penetrometer level. This further justifies the lateral pressure distributions obtained both experimentally and theoretically in which the peak occurs about 25 cm below the penetrometer level.

The base pockets in the designed base boundary failed to give accurate measurements of volume changes during penetration. A more sensitive measuring method might have allowed the data to be used to perform an elasto/plastic analysis of soil deformation in the anisotropic, radial, plane similar to the one carried out for the transverse plane.

The results of previous studies (Chapter 2) showed that during penetration into dense sand a band of looser material develops around the penetrometer shaft. In this study it has been assumed that a volume of sand equal to the penetrometer volume is crushed and displaced around the penetrometer to create a stress relief zone over which sand is assumed to shear at constant volume and to stay at constant stress. Hence, from the results of the expansion test, it was possible to predict normal stresses at the penetrometer and the corresponding sleeve frictions developed on the shaft. The results of the three tests analysed indicate the predicted sleeve friction values to be very close to the calculated ones.

Cone Penetration Tests

The analysis of the results gave a unique relationship between q_c and f_s of the CP set through K_o. This led the author to explore the possibility that from a single CPT one would be able to obtain the necessary information to establish the K_o state of the soil in the field. The K_o effect, however, appeared to be very small and would, in practice, be masked by uncertainties of local soil properties in the field.

On the assumption that the infinite boundary tests represent real field conditions, the interpretation procedures of Lunne and Christophersen (1983), as far as the penetration tests are concerned, appear to underpredict relative density of the very dense sand by 12 - 17 % and by 5 % or less for medium dense sand. The Baldi et al. (1982 and 1986) method also underpredicts D_r by 2 - 11 % for very dense sand: for medium dense sand the predicted values are similar to those measured.

A study of the original SU results and their comparison with the later, infinite boundary tests showed that sleeve friction under BC1 should be increased by about 26 % for a 2.0 bar NC test whilst an OC test under either boundary conditions requires an increase of at least 14 %.

Similar correction factors were developed for cone resistance values of the SU results: for a typical 2.0 bar NC test, the q_c of BC1 needs to be increased by 12% but that BC3 results do not appear to require any correction factors. For higher lateral stresses (σ_h = 1.25 bar), the original OC results are similar to those for infinite boundaries: results of 1.0 bar, OCR = 4, tests under either BC1 or BC3 needed to be increased by 7 %. This suggests that CP results give q_c values that are 13 % and 17 % smaller for NC and OC, respectively, than the field values suggested by Lunne and Christophersen. Of course, it needs to be borne in mind that whereas their method was for a range of sands, the CP series were for dense Hokksund sand only. The Baldi et al. method, also, was based on Ticino sand which is rather similar to but still different from Hokksund sand as is indicated by their different behaviour in terms of state parameters.

In conclusion, the author believes that the following points might be worthwhile considering for calibration chamber testing in future research works:

- more attention given to the ease of de-airing the lateral cell.

- possibility of providing choice of lateral stiffness perhaps by using easily replaceable curtains of different compressibilities.

- further study in the design and function of end discs in the calibration chamber.

- extend the range of expanding cylinder tests with the aim of studing the relationship between stress levels/stress history and the elasto/plastic description of sand behaviour for a range of sands.

REFERENCES

ADDO, G. D. (1983). Penetration of Sand on Confined Conditions". PhD Thesis, King's College, London.

AL AWKATI, A. (1975). "On Problems of Soil Bearing Capacity at Depth". PhD. Thesis, Duke University, Durham, N.C., USA.

ALPAN, I. (1967). "The Empirical Evaluation of the Coefficients K_o and $K_{o_{oc}}$". Soils and Foundations, 7, No. 1.

ANDRAWES, K. Z. (1970). "A contribution to Plane Strain Model Testing of Granular Soils". PhD Thesis, University of Southampton.

ASTM (1973). "Evaluation of Relative Density and Its Role in Geotechnical Projects Involving Cohesionless Soils". STP 523.

ASTM (1979). "Standard Method for Deep Quasi-Static, Cone and Friction-Cone Penetration Tests of Sands. D3441.

ATKINSON, J. H. and BRANSBY, P. L. (1978). "The Mechanics of Soils - An Introduction to Critical State Soil Mechanics. Mc Graw-Hill Inc., London.

BALDI, G., BELLOTTI, R., GHIONNA, V., JAMIOLKOWSKI, M. and PASQUALINI, E. (1981). "Cone resistance in Dry N.C. and O.C. Sands". Proc. Session Sponsored by Geotech. Engng. Div. of ASCE., National Convention, St. Louis, Mo., USA, Oct. 1981, 145-177.

BALDI ET AL.——— (1982). "Design Parameters for Sands from CPT". Proc. of the Second European Symposium on Penetration Testing, ESOPT II, Amsterdam, May 1982, 2, 425-438.

BALDI ET AL.——— (1983). "Correlations between Cone Resistance q_c and Relative Density D_r". Discussion, Proc. of the VIII ECSMFE, Helsinki.

BALDI ET AL.——— (1985). "Penetration Resistance and Liquefaction of Sands". Eleventh International Congress on Soil Mechanics and Foundation Engineering, XI ICSMFE, San Francisco.

BALDI ET AL.——— (1986). "Interpretation of CPT's and CPTU's. Part 2: Drained Penetration of Sands". 4th Int. Geotech. Seminar, Singapore.

BALDI ET AL.——— (1988). "Stiffness of Sands from CPT, SPT and DMT- A Critical Review". Inst. of Civil Engrs. Geotechnology Conf. on Penetration Testing in the U.K., July 1988, Univ. of Birmingham.

BALIGH, M. M. (1975). "Theory of Deep Site Static Cone Penetration Resistance". Rep. No. R-75-76, Massachussetts Institute of Technology (MIT).

BALIGH, M. M. (1976). "Cavity Expansion in Sands with Curved Envlopes". J. of Geotech. Engng. Div., ASCE, GT11.

BALIGH, M. M. (1984). "The Simple Pile Approach to Pile Installation in Clay". Proc. Symp. on Analysis and Design of Pile Foundations, GED., ASCE National Convention, San Francisco, Oct. 1984, 310-330.

BALIGH, M. M., VIVATRAT, V., and LADD, C. C. (1980). "Cone Penetration for Soil Profiling". JGED, ASCE, GT. 4, April.

BASSETT, R. H. (1964). "Granular Materials in the SSA". Phd Thesis, University of Cambridge.

BCP Committee, Japan (1971). "Field Tests on Piles in Sand". Soils and Foundations, Vol. 11, No. 2, June.

BEEN, K., CROOKS, J. H. A., BECKER, D. E. and JEFFERIES, M. G. (1986). "The Cone Penetration Test in Sands, Part 1: State Parameter Interpretation". Geotechnique 36, No. 2, 239-249.

BEEN, K., CROOKS, J. H. A. and JEFFERIES, M. G. (1988). "Interpretation of Material State from the CPT in Sands and Clays". Inst. of Civil Engrs. Geotechnology Conf. on Penetration Testing in the U.K., July 1988, Univ. of Birmingham.

BEEN, K. and JEFFERIES, M. G. (1985). "A state Parameter for Sands". Geotechnique 35, No. 2, 99-112.

BEEN, K., JEFFERIES, M. G., CROOKS,J. H. A., and ROTHENBURG, L. (1987a). "The Cone Penetration Test in Sands, Part II: General Inference of State". Geotechnique 37, No. 3, 285-299.

BEEN, K., LINGNAU, B. E., CROOKS, J. H. A. and LEACH, B. (1987b). "Cone Penetration Test Calibration for Erksak (Beaufort Sea) Sand". Can. Geotech. J., 24, 601-610.

BEGEMAN, H. K. S. (1965). "The Friction Cone as An Aid in Determining The Soil Profile". Proc. ISSMFE. Vol. 1, 17-20.

BELLOTTI ET AL., BALDI ET AL. and GHIONNA ET AL. (1985). "Laboratory Validation of In-Situ Tests". Draft of the Paper to Be Included in Italian Geotechnical Society. Jubilee Vol. for XI ICSMFE, San Francisco.

BEREZANTSEV, V. G. and YAROSHENKO, V. A. (1957). "The Bearing Capacity of Sands under deep Foundations". Proc IV ICSMFE, London, V.1, 283-286.

BISHOP, R. F., HILL, R. and MOTT, N. F. (1945). "The Theory of Indentation and Hardness Test". Proc. of the Physical Society 57, 147-159.

BOLTON, M. (1986). "The Strength and Dilatancy of Sands". Geotechnique, 36, No. 1, 65-78.

BRINCH-HANSEN, J. (1961). "A General Formula for Bearing Capacity"., Danish Geotech. Inst., Bulletin No. 11, Copenhagen, 38-46.

BRINCH-HANSEN, J. (1966). "Notes Concerning DGI Bulletin No. 11". Bulletin No. 21, Danish Geotech. Inst., p.13.

BUDHU, M. (1979). "Simple Shear Deformation of Sands". PhD Thesis, University of Cambridge.

BUISMAN, A. S. K. (1935). "De Weerstand van Paalpunten in Zand, De Ingenieur 50, 25-28 & 31-35.

BUTTERFIELD, R., HARKNESS, R. M. and ANDRAWES, K. Z. (1970). "A Stereo Photogrametric Technique for Measuring Displacement Field". Geotechnique, 20, No. 3, 308-314.

BUTTERFIELD, R. and HARKNESS, R. M. (1972). "The Kinematics of Mohr-Coulomb Materials' In 'Stress-Strain Behaviour of Soils'". Foulis; Proc. of the Roscoe Memo. Symp., Cambridge University, 220-233.

BYRNE, P. M. and ELDRIDGE, T. L. (1982). "A Three Parameter Dilatant Elastic Stress-Strain Model for Sands". Civil Engng. Dept. Soil Mechanics Series No. 57, Univ. of British Columbia, Vancouver, B.C., Canada.

CAMPANELLA, R. G. and ROBERTSON, P. K. (1982). "State-of-the-Art in In-Situ Testing Of Soils: Developments since 1978". Engng. Found. Conf. on Updating Subsurface Sampling of Soils and Rocks and Their In-Situ Testing, Santa Barbara, CA, USA, Jan. 1982.

CAMPANELLA, R. G. and ROBERTSON, P. K. (1988). "Current Status of the Piezocone Test". Draft Submitted for Publication in Proc. of ISOPT I, Disney World, FL., USA.

CAQUOT, A. (1934). "Equilibre des Massifs a Frottement Interne, Paris (Gauthier-Villars).

CARRIER, G. F. (1946). "Propagation of waves in Orthotropic Media". Q. Appl. Math. 4, 160-165.

CASAGRANDE, A. (19750. "Liquefaction and Cyclic Deformation of Sands, A Critical Review". Proc. Fifth Pan American Conf. on Soil Mech. and Found. Engng., Buenos Aires 5, 80-113.

CASTRO, G. (1969). "Liquefaction of Sand". PhD Thesis, Div. of Engng & Applied Physics, Harvard University.

CASTRO, G. and POULOS, S. J. (1977). "Factors Affecting liquefaction and Cyclic Mobility". J. of Geotech. Engng. Div., ASCE, GT6, 501-505.

CHAPMAN, G. A. (1975). "A Calibration chamber for Field Test Equipment". Proc. European Symp. Penetration Testing, Stockholm 1974, Vol. 2.2, 59-65.

CHAPMAN, G. A. and DONALD, I. B. (1981). " Interpretation of Static Penetration Tests in Sand". X ICSMFE, Stockholm, V.2, 455-458.

CHEN P. K. H. (1986). "Axisymmetric Deformation during Cone Penetration Testing on Sand". PhD Thesis, King's College, London.

CHONG, M. K. (1983). "A New Site Investigation Tool Based on Quasi Static Cone Penetrometer". PhD Thesis, University of Leeds.

CHONG, M. K. (1988). "Density Changes of Sand on Penetration resistance". ISOPT-1, 707-714.

COLE, E. R. L. (1967). "The behaviour of Soils in the Simple Shear Apparatus". Phd Thesis, University of Cambridge.

COUMOULOS, D. G. (1967). "A Radiographic Study of Soils". PhD Thesis, University of Cambridge.

CPTE (1981). Proc. of ASCE Convention, Session 35 on Cone Penetration Testing and Experience, St. Louis, MO., Oct. 1981, 1-48.

DAHLBERG, R. (1974). "Penetration, Pressuremeter and Screw Plate Tests in a Preloaded natural sand Deposit". Proc. of the European Symp. on Cone Penetration testing and Experience". Geotech. Engng. Div., ASCE, Oct. 1981, 49-75.

DAYAL, U. and ALLEN, J. H. (1975). " The Effect of Penetration Rate on the strength of Remoulded Clay and sand samples". Canad. Geotech. J., Vol. 12, No. 3.

DE BEER, E. E. (1945). "Etude des Fondations sur Pilotis et des fondations directes". Annales des Travaux Publics de Belguique, Brussels, Belgium, 46, 1-78.

DE BEER, E. E. (1967). "Bearing Capacity and Settlements of Shallow Foundations on Sands". Proc. Symp. on Bearing Capacity and settlement of Foundations, Duke University, 15-33.

DE RUITER, J. and RICHARDS, A. F. (1983). "Marine Geotechnical Investigations, A Mature Technology". Proc. ASCE, Conf. on Geotechnical Practice in Offshore Engineering, Austin, Texas, USA.

DOUGLAS, B. J. and OLSEN, R. S. (1981). "Soil Classification Using Cone Penetrometer (in Cone Penetration and Testing, Editted by G. M. Norris and R. D. Holtz)". Proc. of ASCE Convention, St. Louis, MO., Oct. 1981, 209-227.

DURGANOGLU, H. T. (1972). "Static Penetration Resistance of Soils". PhD Thesis, University of California, Berkeley.

DURGANOGLU, H. T. and MITCHELL, J. K. (1973). "Static Penetration Resistance of Soils". Research Report Prepared for NASA Headquarters, Washingtonn DC, Univ. of California, Berkeley.

DURGANOGLU, H. T. and MITCHELL, J. K. (1975). "Static Penetration Resistance of Soils, Part I: Analysis". Proc. ASCE, Spec. Conf. on In-Situ Measurement of Soil Parameters, Raleigh, N.C., V.1.

EGGESTAD, A. (1974). "A New Method for Compaction Control of Sand". NGI Pub. No. 104, 1-13.

ESOPT I (1974). European Symposium on Penetration Testing, Stockholm, Proc. in 3 Volumes.

ESOPT II (1982). European Symposium on Penetration Testing, Amsterdam, Proc. in 2 Volumes.

FAHEY, M. (1980). "A Study of the Pressuremeter Test in Dense Sand". PhD Thesis, University of Cambridge.

FAHEY, M. (1986). "Expansion of A Thick Cylinder of Sand: A Laboratory Simulation of the Pressuremeter Test". Geotechnique 36, No.3, 397-424.

GAZETAS, G. (1981). "Strip Foundations on a Cross-Anisotropic Soil Layer subjected to Dynamic Loading". Geotechnique, 31, No. 2, 161-179.

GHIONNA, V. (1984). "Influence of Chamber Size and Boundary Conditions on the Measured Cone resistance". Seminar on Cone Penetration Testing in the Laboratory, University of Southampton.

GIBSON, R. E. and ANDERSON, W. F. (1961). "In-Situ Measurement of Soil Properties with the Pressuremeter". Civ. Engng. Publ. Wks. Rev. 56, No. 658, 615-618.

GREEUW, G., SMITS, F. P. and DRIEL, P. van (1988). "Cone Penetration Tests in Dry Oosterschelde Sand and the Relation with A Cavity Expansion Model". Proc., ISOPT- I, Orlando, Florida.

HANSEN, B. and CHRISTENSEN, N. H. (1969). "Discussion on 'Theoretical Bearing Capacity of very Shallow Footings', by Larkin, L. A.". J. of Soil Mech. and Found. Engng. Div., ASCE, 95, SM6, 1568-1572.

HARDIN, B. O. and DRNEVICH, V.P. (1972). "Shear Modulus and Damping in Soils: Design Equations and Curves". J. Soil Mech. and Found. Div., ASCE, 98, SM7, 667-692.

HARMAN, D. E. (1976). "A Statistical Study of static Cone Bearing Capacity, Vertical Effective Stress, and Relative Density of Dry and Saturated Fine sands in a Large Triaxial Test Chamber". M.Sc. Thesis, University of Florida.

HOLDEN, J. C. (1976). "The Calibration of Electrical Penetrometers in Sand". Final Report, Norwegian Geotech. Inst. (NGI), Oslo.

HOLDEN, J. C. (1991). "History of Calibration Chamber Testing". ISOCCT 1.

HUGHES, J. M. O., WROTH, C. P., and WINDLE, D. (1977). "Pressuremeter Tests in Sands". Geotechnique 27, No. 4, 455-477.

ISOCCT 1 (1991). Int. Symp. on Calibration Chamber Testing, Clarkson University, June 27-29, 1991.

ISOPT I (1988). Int. Symposium on Penetration Testing, De Ruiter (Ed.), Balkema, Rotterdam, 1988.

JACOBSEN (1976). "On Pluvial Compaction of Sand". Rep. No. 9, Labratoriet for Fundering, Aalborg University Centre, Denmark

JAMES, R. G. and BRANSBY, P.L. (1970). "Experimental and Theoretical Investigations of a Passive Earth Pressure Problem". Geotechnique 20, No. 1, 17-37.

JAMIOLKOWSKI, M., GHIONNA, V. N., LANCELLOTTA, R. and PASQUALINI, E. (1988). New Correlations of Penetration Tests for Design Practice". Proc. ISOPT-I,Orlando, Florida.

JAMIOLKOWSKI, M., LADD, C. C., GERMAINE, J. T. and LANCELLOTTA, R. (1985). "New Developments in Field and Laboratory Testing of Soils". Proc. XI ICSMFE, San Francisco, V.1, 57-153.

JAMIOLKOWSKI, M. and ROBERTSON, P. K. (1988). "Closing Address. Future Trends for Penetration Testing". Proc. Geotechnology Conf. on 'Penetration Testing in the U.K.' Organised by Inst. of Civil Engrs., Birmingham, July, 1988.

JANBU, N. (1963). "Soil Compressibility as Determined by Oedometer and Triaxial Tests". 3rd European Conf. on Soil Mech. and Found. Engng., Wiesbaden, Germany, V.1, 19-25.

JARDINE, R. J., SYMES, M. J. and BURLAND, J. (1984). "The Measurement of Soil Stiffness in the Triaxial Apparatus". Geotechnique, 34, No. 3

JANBU, N. and SENNESET, K. (1974). "Effective Stress Interpretation of In-Situ Static Penetration Tests". Proc., ESOPT I, V.2.2, 181-193.

JEWELL, R. J., FAHEY, M. and WROTH, C. P. (1980). "Laboratory Studies of the Pressuremeter Test in Sand". Geotechnique 30, No.4, 507-531.

JONES, G. A. and RUST, E. A. (1982). "Piezometer Penetration Testing CUPT." Proc., ESOPT II, V.2, 607-613.

KEAVENY, J. (1985). "In-Situ Determination of Drained and Undrained Soil Strength Using the Cone Penetration Test". PhD Thesis, Univ. of Cal., Berkeley.

KERISEL, J. (1961). " Fondations Profondes en Milieu Sableux". Proc. 5th Int. Conf. Soil. Mech., Paris, France. Vol. 2., 73-83.

KILDALEN, S. LAST, N., LUNNE, T. & PARKIN, A. (1982). "Results of Triaxial Tests on Hokksund Sand". NGI Rep. No. 52108-12, NGI, Oslo

KOUMOTO, T. (1988). "Ultimate Bearing Capacity of Cones in Sand". Proc., ISOPT I, 809-813.

LADANYI, B. (1963). "Evaluations of Pressuremeter Tests in Granular Soils". 2 nd Panamerican Conf. Soil Mech. Found. Engng 1, 3-20.

LADE, P. V. (1972). "The Stress-Strain and Strength Characteristics of Cohesionless Soils". PhD Thesis, University of California, Berkeley.

LAMBRECHTS, J. K. and LEONARDS, G. A. (1978). "Effects of Stress History on Deformation of Sand". J. of Geotech. Engng. Div., ASCE, GT11, 1371-1387.

LANCELLOTTA, R. (1983). "Analisi di Affidabilita in Ingegneria Geotecnica". Atti Instituto Scienza Construzioni. No. 625, Politecnico di Torino.

LAST, N. C. (1979). "The Use of Calibration Chambers to Study Cone Penetration Behaviour in Dry Samples of Hokksund Sand". NGI Rep. No. 52108-6, NGI, Oslo.

LAST, N. C. (1982). "The Cone Penetration Tests in Granular Soils". PhD Thesis, Univ. of London, King's College.

LAST, N. C. (1984). Compiled Notes of 'Seminar on Cone Penetration Testing in the Laboratory', Held at Southampton University, Nov. 1984.

LAST, N. C. (1985). "An Investiogation of Full Scale Penetrometers in A Large Triaxial Calibration Chamber - Progress Report to SERC & NGI". Civil Engng Dept., Univ. of Southampton.

LAST, N. C., BUTTERFIELD, R. and HARKNESS, R. M. (1987). "An Investigation of Full-Scale Penetrometers in A Large Triaxial Calibration Chamber: Mar. 1983 to Feb. 1986". Civil Engng Dept., Univ. of Southampton.

LEE, K. L. (1966). "Stress Dilatancy Performance of Feldspars". ASCE J. of Soil Mech. and Found. Div. , Vol. 92, NO. SM2, 79-103.

LEE, K. L. (1965). "Triaxial Compressive Strength of Saturated Sands under Siesmic Loading Conditions". PhD Thesis, Univ. of Cal., Berkeley.

LO PRESTI, D. (1987). "Behaviour of Ticino Sand During Resonant Column Test". PhD Thesis, Technological University of Turin.

LUNNE, T. (1991). "Practical use of CPT correlations in Sand Based on Calibration Chamber Tests". ISOCCT-1 and also NGI Int. Rep. No. 521550-57.

LUNNE, T. and CHRISTOFFERSEN, H. P. (1983). "Interpretation of Cone Penetration Data for Offshore Sands". Proc., 15th Annual Offshore Technology Conf., Houston, Texas, V.1, 181-192.

LUNNE, T., CLAUSEN, C. J. F. and KJEKSTAD, D. (1976). "Comparison between Cone Penetration Tests and Borings at Some North Sea Locations". NGI Internal Rep. No. 52155-6.

LUNNE, T., EIDSMOEN, T., GILLESPIE, D. and HOWLAND, J. D. (1986). "Laboratory and Field Evaluation of Cone Penetrometers".

LUNNE, T. and KLEVEN, A. (1981). "Role of CPT in North Sea Foundation Engineering". Symp. on Cone Penetration Testing & Experience, Geotech. Engng. Div., ASCE, Oct.1981, 49-75.

MAHMOOD, M. A. (1985). "Continuously Penetrating Bodies in Granular Materials". PhD Thesis, University of southampton.

MAIR, R. J. and WOOD, D. M. (1987). "Pressuremeter Testing: Methods and Interpretation". CIRIA Ground Engineering Report: In-Situ Testing, Butterworths (Pub.), London, 160p.

MARCHETTI, S. (1982). "Dilation of Liquifiable Sand Layers by Means of Quasi-Static Penetration Test". ESOPT II, Vol. 2, 689-695.

MEIGH, A. C. and NIXON, I. K. (1961). "Comparison of In-Situ Tests of Granular Soils". Proc. 5^{th} ICSMFE.

MESRI, G. and CASTRO, A. (1987). "C_α/C_c Concept and K_o during Secondary Compression". JGED, ASCE, GT3.

MEYERHOF, G. G. (1951). "The Ultimate Bearing Capacity of Foundations". Geotechnique, 2, 301-332.

MEYERHOF, G. G. (1961). "The Ultimate Bearing Capacity of Wedge Shaped Foundations". V ICOSMFE, V.2, 105-109.

MITCHELL, J. K. (1988). "Horizontal Stress In-Situ by Cone Penetrometers and Related Studies". NGI Seminar on Calibration of In Situ Tests in Laboratory and Field, Oslo, 28-29 Jan., 1988.

MITCHELL, J. K. and DURGUNOGLU, H. T. (1978). "In-Situ Strength by Static Cone Penetration Test". VIII ICOSMFE, V.1.2, 279-286.

MITCHELL, J. K. and GARDNER, W. S. (1975). "In-Situ Measurements of Volume Change Characteristics". Proc., ASCE Spec. Conf. on 'In-Situ Measurements of Soil Properties'", Rayleigh, N.C., 2, 279-235.

MITCHELL, J. K. and KEAVENY, J. M. (1986). "Determining Sand Strength by Cone Penetrometer". Proc., In-Situ '86, ASCE, Specialty Conf., Blacksburg, Virginia, USA.

MITCHELL, J. K. and LUNNE, T. (1978). "Cone Resistance as A Measure of Sand Strength". Proc., ASCE, 104, GT7,995-1012 (also in NGI Pub. No. 123).

MIURA, S., TOKI, S. and TANIZAWA, F. (1984). "Cone Penetration Characteristics and Its Correlation to Static and Cyclic DeformationStrength Behaviour of Anisotropic sands". Soils and Foundations, 24, No. 2, 57-74.

NOWATZKI, E. A. and KARAFIATH, L. L. (1972). "The Effect of Cone Angle on Penetration Resistance". Presented at the 51st Annual Meeting of the Highway Research Board.

PAN, Y. C. and CHOU, T. W. (1976). "Point Force Solution for an Infinite Transversely Isotropic solid". Transactions of the ASME, Dec. 1976.

PARKIN, A.K. (1977). "The Friction Cone Penetrometer: Lab. Calib. for the Prediction of Sand Properties, NGI Int. Rep. 52108-5.

PARKIN, A. K. (1986). "Evaluation of Calibration Chamber Data". Southampton seminar on CPT Testing of 1984; also NGI Int. Rep. 52108-18.

PARKIN, A. K. (1988). "The Calibration of Cone Penetrometers". ISOPT-1, 221-243.

PARKIN, A. K., HOLDEN, J., AAMOT, K. LAST, N. and LUNNE, T. (1980). "Laboratory Investigations of CPT's in Sand". NGI Report No. 52108-9, Oslo.

PARKIN A. K. and LUNNE, T. (1982). "Boundary Effects in the Laboratory Calibration of a Cone Penetrometer for Sand". Proc., ESOPT II, 761-768.

PLANTEMA, G. (1953). "A Soil Pressure Cell and Calibration Equipment". Proc. 3rd Int. Conf. Soil Mech. Found. Eng., Zurich, Vol.1.

POULOS, S. J. (1981). "The Steady State of Deformation". J. of Geotech. Engng. Div., ASCE, 107, GT5, 553-562.

POULOS, S. J. and DAVIS, E. H. (1974). "Elastic Solutions for Soil and Rock Mechanics". Published by John Wiley and Sons, Inc.

PRANDTL, L. (1921). "On the Penetration Strength of Plastic Construction Materials and the Strength of Cutting Edges". Zeitschfift fur Angewandte Mathematic und Mechanik 1, No. 1, 15-20.

REISSNER, H. (1924). "Concerning the Earth Pressure Problems". Proc., 1st Int. Conf. Applied Mechanics, Delft, 295-311.

ROBERTSON P. K. (1982). "In-Situ Testing of Soil with Emphasis on Its Application to Liquefaction Assessment". PhD Thesis, Univ. of British Columbia, Vancouver, Canada.

ROBERTSON, P. K. and CAMPANELLA, R. G. (1983). "Interpretation of Cone Penetration Tests. Part 1: Sand". Canad. Geotech. J., V.20, 718-733.

ROBERTSON, P. K., CAMPANELLA, R. G., GILLESPIE, D. and GREIG, J. (1986). "Use of Piezometer Cone Data". Proc. of In-Situ '86, ASCE, Specialty Conf., Blacksburg, Virginia.

ROBINSKY, E. I. and MORRISON, C. F. (1964). "Sand Displacement and Compaction around Model Friction Piles". Can. Geotech. J., Vol. 1, No. 2, 81-93.

RODIN, S. (1961). "Experience with the Penetrometers with Particular Reference to the Standard Penetration Test". Proc. 5th ICSMFE, Paris.

ROSCOE, K. H. (1953). "An Apparatus for the Application of Simple Shear to Soil Samples". Proc. 3rd Int. Conf. Soil Mech., 1.

ROWE, P. W. (1971). "Theoretical Meaning and Observed values of Deformation Parameters for Soil". Proc. Roscoe Memorial Symp. (Ed. R. H. G. Parry), 143-194, Yeovil: Foulis.

SANGLERAT, G. (1972). "The Penetrometer and Soil Exploration". Elsevier Pub. Co., Amsterdam.

SCHMERTMANN, J. H. (1970). "Static Cone to Compute Static Settlement on Sand". J. of Geotech. Engng Div., ASCE, 96, SM3, 1011-1043.

SCHMERTMANN, J. H. (1975). "The Measurement of In-Situ Shear Strength". ASCE Special Con. on In-Situ Measurements of Soil Properties, Proc., V.2, 57-138.

SCHMERTMANN, J. H. (1976). "An Updated Correlation between Relative Density, Dr, and Fugro-Type Electric Cone Bearing, q_c". Waterways Experimental Station, Contract Rep. DACW 39-76-M6646.

SCHMERTMANN, J. H. (1978a). "Study of Feasibility of Using Wissa-Type Piezometer Probe to Identify Liquefaction Potential of Saturated Sands". U.S. Army Engineers Waterways Experiment Station, Rep. No. S-78-2.

SCHMERTMANN, J. H. (1978b). "Cone Penetration Test, Performance and Design". U.S. Dept. of Transportation, FHWA-TS-78-209.

SCHMERTMANN, J. H., HARMAN, J. D. and BROWN, P. R. (1978). "Improved Strain Influence Factor Diagrams". Technical Notes, J. Geotech. Engng. Div., ASCE, GT8.

SCHMIDT, B. C. (1966). "Discussion on Earth Pressure at Rest Related to Stress History". Can. Geotech. Journal, Vol. 3, No. 4.

SEED, H. B. and IDRISS, I. B.(1970). "Soil Moduli and Damping Factors for Dynamic Response Analysis". Rep. No. 70-10, Univ. of Cal., Berkeley.

SENNESET, K. and JANBU, N. (1984). "Shear Strength Parameters Obtained from Static Cone Penetration Tests". ASTM STP 883, Symp., San Diego.

SENNESET, K., JANBU, N. and SVANO, G. (1982). "Strength and Deformation Parameters from Cone Penetration Tests". Proc., ESOPT II, Amsterdam.

SKEMPTON, A. W., YASSIN, A. A. and GIBSON, R. E. (1953). "Theorie de la Force Portante des Pieux". Annales de L'Institut Technique du Batiment et des Travaux Publics 6, No.63-64,285-290.

SMITS, F. P. (1982). "Cone Penetration Tests in Dry Sand". Proc., ESOPT II, Amsterdam, 877-881.

SMOLIRA, M. (1955). "Analysis of Structures". Published by Concrete Publications ltd., London.

STROUD, M. A. (1971). "Sand at Low Stress Levels in the Simple Shear Apparatus". PhD Thesis, University of Cambridge.

TERZAGHI, K. (1943). "Theoretical Soil Mechanics". New York, John Wiley & Sons.

TORSTENSSON, B. A. (1977). "The Pore Pressure Probe". NGI Rep. No. 34, Oslo.

TORSTENSSON, B. A. (1982). "A Combined Pore Pressure and Point Resistance Probe". Proc. ESOPT II, Amsterdam.

TREADWELL, D. (1976). "Effect of Layering on the Cone Resistance of Soils". PhD Thesis, Univ. of Cal., Berkeley.

TRINGALE, P. T. (1983) "Soil Investigation In-Situ Using An Acoustic Penetrometer". PhD Thesis, University of California, Berkeley.

TROFIMENKOV, J. G. (1974). "Penetration Testing in USSR". Proc., ESOPT I, V.1, 147-154.

TUMAY, M. (1976). "Relative Density versus CPT Cone Bearing in Cohesionless Soils". Bogazici University.

VEISMANIS, A. (1974). "Laboratory Investigation of electrical Friction-Cone Penetrometers in Sand". Proc., ESOPT I, V.2.2.

VESIC, A. S. (1963). "Bearing Capacity of Deep Foundations in Sand". National Academy of Sciences, national Research Council, Highway Research Record 39, 112-153.

VESIC, A. S. (1970). "Tests on Instrumented Piles: Ogeechee River Site". Proc., ASCE, 96, SM2, 561-584.

VESIC, A. S. (1972). "Expansion of Cavities in Infinite Soil Mass". J. of Soil Mech. and Foun. Engng., ASCE, 98, SM3, 265-290.

VESIC, A. S. (1974). "Bearing Capacity of Shallow Foundations". Handbook of Found. Engng., Winterkorn, H. and Fang, H. Y. (Eds.), Van Nostrand, New York.

VESIC, A. S. (1975). "Principles of Pile Foundation Design". Duke Univ. Soil Mech. Series No. 38, Durham, N.C., USA.

VESIC, A. S. (1977). "Design of Pile Foundations". National Cooperative Highway Research Programme, Rep. No. 42, Trans. Research Board, Washington, D.C.

VILLET, W. C. B. (1981). "Acoustic Emissions During the Static Penetration of Soils". PhD Thesis, Univ. of California, Berkeley.

VILLET, W. C. B. and MITCHELL, J. K. (1981). Cone Resistance, Relative Density and Friction Angle". Symp. on Cone Penetration Testing and Experience, Geotech. Engng. Div., ASCE, Oct. 1981, 178-208.

WISSA, A. E. Z. ET AL. (1975). "The Piezometer Probe". Proc. ASCE Specialty Conf. on In-Situ Measurement of Soil Properties.

WROTH, C. P. (1984). "The Interpretation of In-Situ Soil Tests". XXIV Rankine Lecture, Geotechnique, 34, No. 4.

WOOD, D. M. (1981). "True Triaxial tests on Boston Blue Clay". Proc. 10th ICSMFE, Stockholm, 1981, A. A. Balkema (Rotterdam), Vol. 1, 825-830.

WOOD, D. M. and WROTH, C. P. (1977). "Some laboratory Experiments Related to the Results of the Pressuremeter Tests". Geotechnique, 27, No. 2.

WROTH, C. P. (1988). "Penetration testing - A More Rigorous Approach to Interpretation". Proc., ISOPT I, Orlando, Florida.

WROTH, C. P. and HOULSBY, G. T. (1985). "Soil Mechanics - Property Characterisation and Analysis Procedures. Theme Lecture". Proc., XI ICSMFE, San Francisco.

YU, P. and RICHART, F. E. Jr. (1984). "Stress Ratio Effects on Shear Modulus of Dry Sand". J. Geotech. Engng. Div., ASCE, GT3.

APPENDIX I

EXPANDING CYLINDER TESTS

Introduction

The tests described in this Appendix refer to Figs. 5.6 and 5.7. A total number of six expanding cylinder tests were performed under different boundary conditions and consolidation stress levels. The suitability of these tests are judged with particular reference to their linear stiffness values (pressure per mm of compression) as compared to that produced by the rubber strips at a pre-designed spacing.

Expansion Test Nos. 1 and 6

The first test was carried out on a dense sample normally consolidated under K_o conditions to a vertical pressure of $\sigma'_v = 4.0$ kg/cm^2. This produced a lateral pressure of $\sigma'_h = 1.28$ kg/cm^2, thus giving a $k_o = 0.32$. Test No. 6 was consolidated to a maximum past vertical pressure of 4.5 kg/cm^2 and then relaxed to a vertical of 1.5 kg/cm^2, thus producing an OCR = 3. The pressure in the central cavity during the consolidation phase was maintained equal to the K_o value measured at the sample outer boundary so that at the start of cylindrical expansion the inner pressure was equal to the transversely isotropic pressure throughout the sample. The expansion test itself was performed under constant lateral stress at the outer boundary which was achieved by lowering the lateral fluid pressure to maintain the pressure constant in the sealed cavity of the double-walled chamber. Clearly, if the pressure in this sealed cavity did not vary, then the inner shell could not have deformed and the pressure jump across it must have remained constant. Both total pressures had the same initial value and they would continue to have this value during the expansion

so that the sum of the lateral cell fluid pressure and the pressure due to compression of the rubber strips on the inside of the inner shell would also remain constant.

The volume of lateral cell water withdrawn during this process gave the volume change of the outer boundary of the soil.

The results of both the first test and of test No. 6 showed that the required boundary stiffness was greater than that of the rubber strips.

Expansion Test Nos. 2, 4, and 5

Apart from the difference in their consolidation stress levels and stress histories, expansion test Nos. 2, 4, and 5 were conducted under true infinite lateral outer boundary conditions. [Test No. 2 was consolidated to the same stress level as the first test. Test No. 4 was also consolidated to the same stress level but relaxed to 1 bar value to give an OCR = 4. Test No. 5, on the other hand, was normally consolidated to a stress level of only 2 bar]. In order to incorporate the chosen infinite field condition, first the lateral pressure was allowed to increase as the expansion pressure increased, the cavity pressure being made to follow the same rise. Then the lateral strain corresponding to the pressure rise (as indicated at an earlier stage of the central cavity expansion) was determined and partially allowed for by releasing water from the lateral cell. This latter operation resulted, of course in a drop in lateral pressure and the compatible final strain and pressure achieved by successive approximation. Since the expansion stages in the beginning were very small, only one adjustment was sufficient to give a stable lateral weight change. The larger pressure steps required more adjustments.

Unloading of expansion involved essentially the same procedure except that the pressure changes were negative.

It is evident from the results that the sample in test No. 2 required a stiffness that was greater than that of the rubber strips. This test condition would converge to the rubber stiffness at higher expansion pressures (a Pressure change, $\Delta p \rangle 1.7$ kg/cm^2).

The results of 2.0 bar NC and 1.0 bar (OCR = 4) tests showed a reasonable convergence with the stiffness produced by the rubber strips.

Expansion Test No. 3

The consolidation stress for this test was identical to that for the first two tests (σ'_v = 4.0 kg/cm^2). This test was performed under infinite boundary conditions approximated by the rubber stiffness only. This was achieved by keeping the lateral fluid pressure constant and applying the sum of the lateral pressure and the Δp due to the rubber strips (corresponding to the ΔW of the lateral cell using the rubber stiffness curve). In each step of the expansion the cavity pressure was adjusted to equal the sum of the deduced rubber pressure and the fluid pressure of the lateral cell so that the inner shell remained unstressed.

The same boundary pressure control was imposed during the unloading process. During the early stages of expansion, at very small strains, the pressure - expansion curve appears to be a lower bound to that of test No. 1 with the test No. 2 result lying in between. The maximum width of the pressure band is only 0.05 kg/cm^2 at a pressure change of 1.0 kg/cm^2 after expansion. This test shows a convergence towards the rubber stiffness at a pressure change of 1.5 kg/cm^2 after the start of expansion.

APPENDIX II

CYLINDRICAL CAVITY EXPANSION IN AN ELASTIC MOHR-COULOMB PLASTIC MATERIAL

When a cylindrical cavity, of radius 'a', is surrounded by a thick elastic, Mohr-Coulomb plastic, material of outer radius 'b', with initial inner and outer stresses equal at P_o, the radial and hoop stresses (σ'_r and σ'_θ, respectively) are initially equal. During the elastic phase of expansion, the radial displacement, takes the form

$$u = A \cdot r + B/r \qquad (1)$$

in which the 'B' term is that for an infinite boundary and the 'A' is a uniform tension correction to bring the outer boundary back down to the initial stress value.

For plane-strain conditions ($\varepsilon_z = 0$), the stress increments are

$$\Delta\sigma'_r = -\left[\frac{E}{(1+\nu)\ (1-2\nu)}\right]\left[A - \frac{B}{r^2}(1-2\nu)\right] \qquad (2)$$

$$\Delta\sigma'_\theta = -\left[\frac{E}{(1+\nu)\ (1-2\nu)}\right]\left[A + \frac{B}{r^2}(1-2\nu)\right] \qquad (3)$$

These elastic stress increments can be solved by considering the following boundary conditions:

(1) for a constant lateral boundary stress at radius 'b', $\Delta\sigma'_{r\ (r=b)} = 0$

(2) For a Mohr-Coulomb material, as the cavity starts to expand, σ'_r increases and σ'_θ decreases until the soil at the cavity wall yields at a stress obliquity $N_\phi' = \sigma'_r/\sigma'_\theta$.

Then, from equation (1),

$$A = B\,(1-2\nu)/b^2 \tag{4}$$

$$\Delta\sigma'_r = 2GB\left(\frac{1}{r^2} - \frac{1}{b^2}\right) \tag{5}$$

$$\Delta\sigma'_\theta = -\,2GB\left(\frac{1}{r^2} + \frac{1}{b^2}\right) \tag{6}$$

But since $\varepsilon_r = du/dr$ and $\varepsilon_\theta = u/r$, then from Eqs. (1) and (4)

$$\varepsilon_r = -\,B\left(\frac{1}{r^2} - \frac{(1-2\nu)}{b^2}\right) \tag{7}$$

$$\varepsilon_\theta = B\left(\frac{1}{r^2} + \frac{(1-2\nu)}{b^2}\right) \tag{8}$$

The gradient of the pressure-expansion curve during the purely elastic phase is

$$\frac{dp}{d\varepsilon} = 2G\,\frac{1-(a/b)^2}{1+(a/b)^2\,(1-2\nu)} \tag{9}$$

As $b \to \infty$, this expression reduces to 2G which is equivalent to the expression relating Young's modulus and cavity strains derived by Gibson and Anderson (1961) for the pressuremeter test.

The stresses at the cavity wall (r=a) will be

$$\sigma'_r = P_o + 2\,G\,B\left(\frac{1}{a^2} - \frac{1}{b^2}\right) \tag{10}$$

$$\sigma'_\theta = P_o - 2\,G\,B\left(\frac{1}{a^2} + \frac{1}{b^2}\right) \tag{11}$$

The equations derived so far related to the elastic behaviour of the material before yielding starts. By applying the second boundary condition, yielding begins at the cavity wall under the stress obliquity $N_\phi' = \sigma'_r/\sigma'_\theta$ (assuming Mohr-Coulomb failure). Then at the cavity wall

$$\left(\frac{\sigma'_r}{\sigma'_\theta}\right)_{r=a} = \frac{1 + \sin\phi'}{1 - \sin\phi'} = \frac{P_o + 2GB\,(1/a^2 - 1/b^2)}{P_o - 2GB\,(1/a^2 + 1/b^2)} \qquad (12)$$

From this a value of B can be determined as

$$B = \frac{P_o \sin\phi'}{2G\,(1/a^2 + \sin\phi'/b^2)} \qquad (13)$$

Therefore, when failure starts, the radial and circumferential stresses and strains at the cavity wall are

$$\sigma'_{r\,(\text{at } R=a)} = \frac{P_o\,(1 + \sin\phi')}{1 + (a/b)^2 \cdot \sin\phi'} \qquad (14)$$

$$\sigma'_{\theta\,(\text{at } R=a)} = \frac{P_o\,(1 - \sin\phi')}{1 + (a/b)^2 \cdot \sin\phi'} \qquad (15)$$

$$\varepsilon_{r\,(\text{at } R=a)} = -\frac{P_o}{2G}\,\frac{1 - (a/b)^2(1-2\nu)}{1 + (a/b)^2 \cdot \sin\phi'} \cdot \sin\phi' \qquad (16)$$

$$\varepsilon_{\theta\,(\text{at } R=a)} = \frac{P_o}{2G}\,\frac{1 + (a/b)^2(1-2\nu)}{1 + (a/b)^2 \cdot \sin\phi'} \cdot \sin\phi' \qquad (17)$$

When the plasticity has reached as far as radius R, then Eqns. (14) to (17) will still apply at the interface. Hence

$$\sigma'_r(R) = \frac{P_o\,(1 + \sin\phi')}{1 + (R/b)^2 \cdot \sin\phi'} \qquad (18)$$

$$\varepsilon_\theta(R) = \frac{P_o \sin\phi'}{2G}\left(\frac{1 + (R/b)^2(1-2\nu)}{1 + (R/b)^2 \cdot \sin\phi'}\right) \tag{19}$$

Eqns. (18) and (19) show that σ'_R (= $\sigma'_r(R)$) and $\varepsilon_\theta(R)$ are both functions of the outside diameter 'b'. However, when the infinite lateral boundary condition is imposed (as in field tests), then $b \to \infty$ and P_o is replaced by the horizontal stress, σ'_h. The stress and strain values at the interface become constant quantities given by

$$\sigma'_R = \sigma'_h (1 + \sin\phi') \tag{20}$$

$$\varepsilon_\theta(R) = \sigma'_h \cdot \sin\phi'/2G \tag{21}$$

The stresses within the failed zone can be obtained from the equilibrium equation as follows:

$$\frac{d\sigma'_r}{dr} + \frac{\sigma'_r - \sigma'_\theta}{r} = 0 \tag{22}$$

Replacing σ'_θ from the stress - obliquity relationship gives the following relationship for the yielded zone:

$$-\frac{d\sigma'_r}{dr} = \frac{N_{\phi'} - 1}{N_{\phi'}} \cdot \frac{\sigma'_r}{r} \tag{23}$$

Integrating this equation (on the assumption that ϕ' is constant) and using the boundary condition at the elastic-plastic interface (r = R) with radial stress σ'_R would give

$$\ln\left(\frac{\sigma'_r}{\sigma'_R}\right) = \frac{N_{\phi'} - 1}{N_{\phi'}} \ln\frac{R}{r} \tag{24}$$

Or

$$\sigma'_r = \sigma'_R \left(\frac{R}{r}\right)^{(N_{\phi'} - 1)/N_{\phi'}} \tag{25}$$

By replacing σ'_R from Eqn. (20) in Eqn. (25) for an infinite case, the cavity pressure, P, would be obtained as

$$P = \sigma'_h(1 + \sin\phi')\left(\frac{R}{r}\right)^{(N_\phi' - 1)/N_\phi'} \qquad (26)$$

Hughes et al. (1977) used infinite field conditions [Eqns. (20) and (21)] to show that a linear relationship between in-situ expansion pressure and cavity strain can be calculated as follows:

If they assumed that the sand in the yielded zone was dilating at a constant rate, then the cumulative volumetric strain, $\Sigma\varepsilon_v$, can be related to the cumulative shear strain, $\Sigma\varepsilon_\gamma$, through the dilation angle, ψ, given by

$$\Sigma\varepsilon_v = \Sigma\varepsilon_\gamma \sin\psi \qquad (27)$$

(This will have assumed that elastic strains are negligible).

During plane-strain expansion, $\varepsilon_z = 0$; then $\varepsilon_v = \varepsilon_r + \varepsilon_\theta$ and $\Sigma\gamma = \varepsilon_r - \varepsilon_\theta$ in which $\varepsilon_r = du/dr$ and $\varepsilon_\theta = u/r$ (u is the radial displacement). Putting these quantities into Eq. (27) gave

$$\frac{du}{dr}(1 - \sin\psi) = -\frac{u}{r}(1 + \sin\psi) \qquad (28)$$

Defining a strain obliquity as $N_\psi = \dfrac{1 + \sin\psi}{1 - \sin\psi}$

(and still ignoring elastic strains), then Eqn. (28) can be expressed as

$$N_\psi \cdot \frac{du}{dr} = -\frac{u}{r} \qquad (29)$$

Integration of Eqn. (29) and application of the boundary conditions in the plastic zone $a \leq r \leq R$, gives

$$N_\psi \ln \frac{u_a}{u_R} = \ln \frac{R}{a} \tag{30}$$

This equation can be re-arranged to convert the displacements into their equivalent circumferential strain values:

$$\ln \frac{\varepsilon_c}{\varepsilon_R} = \frac{1 + N_\psi}{N_\psi} \ln \frac{R}{a} \tag{31}$$

where $\varepsilon_c = u_a/a$ = cavity strain and $\varepsilon_\theta(R) = u_R/R$ = circumferential strain at the interface.

Re-writing Eqn. (24) for r = a (at the cavity wall) and replacing σ_a by P (the expansion pressure) and then combining with Eqn. (31) to eliminate R/a gives

$$\log P = \frac{N_\psi (N_{\phi'} - 1)}{N_{\phi'}(N_\psi + 1)} \ln \varepsilon_c + \ln \sigma'_R - \frac{N_\psi (N_{\phi'} - 1)}{N_{\phi'}(N_\psi + 1)} \log \varepsilon_\theta(R) \tag{32}$$

Under in-situ conditions with the last two terms constant, Eqn. (32) shows that the cavity pressure is related linearly to the cavity strain on a double logarithmic basis. Therefore, a plot of log P against log ε_c has a slope, S, given by

$$S = \frac{N_\psi (N_{\phi'} - 1)}{N_{\phi'}(N_\psi + 1)} = \frac{(1 + \sin\psi)\sin\phi'}{1 + \sin\phi'} \tag{33}$$

When a typical medium dense or dense sand is sheared, it does not actually deform at constant angle of friction, but instead shows a more

or less gentle peak (ϕ'_p) with a subsequent drop towards a constant volume or critical state value (ϕ'_{cv}) [Fig. A2.1a]. This stress strain response is accompanied by volume changes in the sand [Fig. A2.1b].

Sinψ and **sinϕ'** may be regarded as related by the following stress-dilatancy relationship of Rowe (1971)

$$\frac{1 + \sin\phi'}{1 - \sin\phi'} = N_{\phi'_{cv}} \cdot \frac{1 + \sin\psi}{1 - \sin\psi} \qquad (34)$$

where

$$N_{\phi'_{cv}} = \frac{1 + \sin \phi'_{cv}}{1 - \sin \phi'_{cv}}$$

Combining Eqs. (33) and (34) gives

$$\sin\phi' = \frac{(N_{\phi'_{cv}} + 1)\ S}{(N_{\phi'_{cv}} - 1)\ S + 2} \qquad (35)$$

and

$$\sin\psi = \frac{2\ N_{\phi'_{cv}} \cdot S - (N_{\phi'_{cv}} - 1)}{N_{\phi'_{cv}}} \qquad (36)$$

Eqs. (35) and (36) have been plotted in Fig. A2.2 (data from Mair and Wood, 1987) which relates various parameters. Using this figure requires a value to be chosen for ϕ'_{cv}. Although values of ϕ'_{cv} should ideally be determined from plane strain tests, results from drained triaxial tests are usually more readily available. These are likely to give lower values of ϕ'_{cv}, which result in lower values of ϕ' and higher values of ψ being derived (Mair and Wood, 1987). In the absence of test data, approximate generally accepted values of ϕ'_{cv} may be taken. The range $30 < \phi'_{cv} < 35$ covers most quartz sands. The above authors believe that micaceous sands and feldspar sands will probably produce higher values.

The above figure shows that an uncertainty of 5° in ϕ'_{cv} corresponds to an uncertainty of about 2.5° in ϕ'. As ϕ'_{cv} is not a function of initial density, disturbed samples can be obtained from the field and tested in the laboratory using, say, the direct shear box test to obtain ψ'_{cv} for the particular sand (Fahey and Randolph, 1984). Direct shear-box tests on Hokksund sand gave a value of $\phi'_{cv} = 36°$.

Hence, the pressuremeter measurements of cavity pressure and strain up to a point sufficient to establish a constant slope to the logP-logε_c plot allow values of ϕ' and ψ to be derived for a value of ϕ'_{cv} for the particular sand.

Actually, the N_ψ value could more strictly have been defined in terms of plastic only components of strain and the appropriate plastic cavity strains used in the log plot.

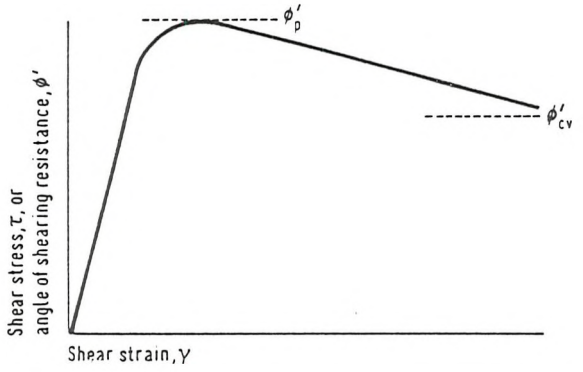

(a) Peak angle of friction, ϕ'_p, and constant volume angle of friction, ϕ'_{cv}

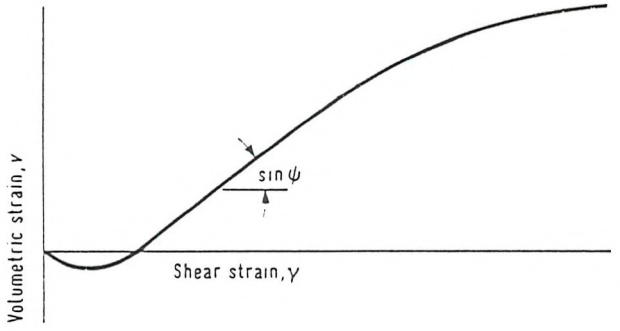

(b) Associated volumetric strains and angle of dilation, ψ

Fig. A.2.1. Typical shear stress - shear strain and dilatancy response of dense or medium-dense sand

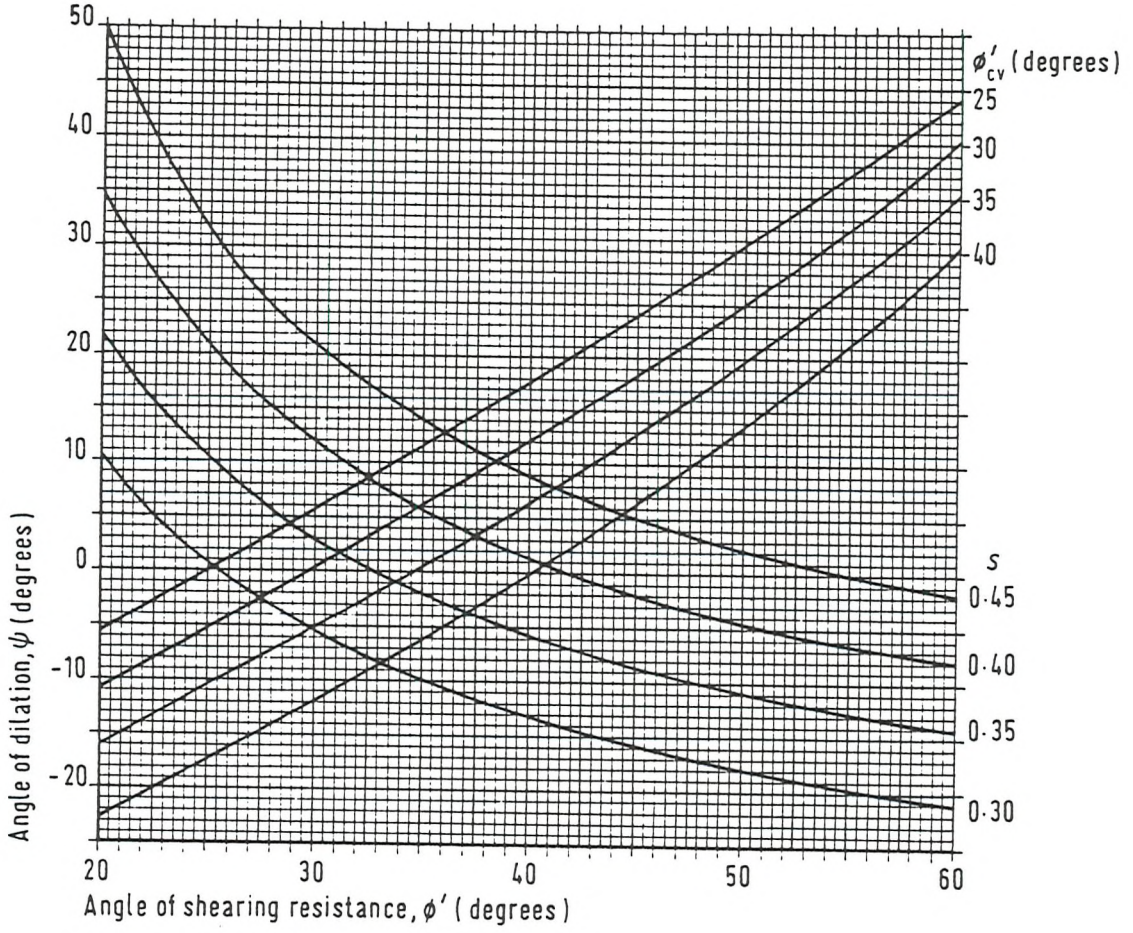

Fig. A.2.2. Curves for pressuremeter tests in sand, relating various parameters (after Mair and Wood, 1987)

APPENDIX III

Strain Gauge Installations

Any standard strain gauging of a surface requires specific procedures and techniques which constitute a carefully developed and thoroughly proven system. Such a task would include the following procedures in the order of application:

- surface preparation for strain gauge bonding
- strain gauge installations
- strain gauge soldering
- strain gauge clamping
- final protective coating

These procedures are discussed in detail in the following sections. These techniques were recommended by Micro-Measurement Division of the Measurement Group, Inc., represented by Welwyn Strain Measurement, U.K.

1. Surface Preparation for Strain Gauge Bonding

The purpose of surface preparation was to develop a chemically clean surface having a roughness appropriate to the gauge installation requirements, a surface alkalinity corresponding to a pH of 7 or so, and visible gauge layout lines for locating and orienting the strain gauge. Fundamental to the surface preparation is an understanding of cleanliness, and of contamination. It was important to guard against recontamination of a once cleaned surface.

1.1. Solvent Degreasing

Degreasing was necessary to remove oils, greases, and any soluble chemical residues from the surface. The inner wall of the chamber was first washed very thoroughly with soap and hot water to obtain an all around clean surface. Because of very large surface area, the whole surface could not have been degreased with a chemical degreaser, but, instead, an area covering 4 to 6 inches on all sides of the gauge area was cleaned. This minimised the chance of recontamination in subsequent operations, and provided an area adequately large for applying protective coatings in the final stage of gauge installations.

1.2. Surface Abrading

In preparation for gauge installation the surface was abraded to remove any loosely bonded adherents (scale, rust, paint, galvanised coating, oxides, etc.), and to develop a surface texture suitable for bonding. Being a relatively coarse surface, it was necessary to start with a disc grinder (sander). Through a series of abrasion with finer grit flapper discs, the surface was further smoothed. The final finish was obtained using silicone-carbide paper of 600 grit under wet conditions. Wet abrasion was carried out using a special conditioning material called M-Prep Conditioner A which was compatible with the steel of the chamber wall. This conditioner is a mildly acidic solution which generally accelerates the cleaning process.

1.3. Gauge - Location Layout Lines

For accurately locating and orienting a strain gauge, the test surface was first marked with a pair of crossed referance lines at the point where the strain measurement was to be made. The lines were made perpendicular to one another, with one line oriented in the direction of strain measurement. The reference or layout lines were made using a 4H drafting pencil. Such lines were, in fact, applied following the abrading operation and before final cleaning. All residue from the marking operation was removed by scrubbing with Conditioner A as

described in the following section.

1.4. Surface Conditioning

After the layout lines were marked, Conditioner A was applied repeatedly, and the surface scrubbed with cotton-tipped applicators until a clean tip was no longer discoloured by the scrubbing. During this process, the surface was kept constantly wet with the conditioner until the cleaning was completed. When clean, the surface was dried by wiping the cleaned area with a single slow stroke of a gauze sponge, thus never allowing the cleaning solution to dry on the surface.

1.5. Neutralising

The final step in surface preparation was to bring the surface condition back to an optimum alkalinity of 7.0 to 7.5 pH, which is suitable for all strain gauge adhesive systems. This was done by applying a neutralising agent called M-Prep Neutraliser 5 liberally to the cleaned surface, and cleaning the surface with a clean cotton-tipped applicator. Then the surface was dried with a gauge sponge as before.

2. Strain Gauge Installations

The installation was done using an adhesive called Resin AE10 adhesive which is a high performance 100% solid epoxy, formulated specially for bonding strain gauges. This resin comes with a curing agent both of which are mixed thoroughly prior to application.

The Gauge was first removed from the acetate envelope and then placed on a chemically clean glass plate with the bonding side of the gauge down. Then a solder terminal was positioned adjacent to the gauge using a clear cellophane tape. Holding the tape in position at a shallow angle, the gauge/tape assembly was wiped onto the surface. One end of the tape was lifted at a shallow angle to the surface with the bonding side exposed. Both surfaces were applied a thin coating of the

adhesive after which the tape was wiped over the chamber surface. A piece of silicone gum pad and a backup plate were then placed over the gauge installation. This allowed the clamping force to be exerted evenly over the gauge.

Since it was not possible to clamp a single installation locally, the series of 11 gauges in each column were placed together and then all clamped simultaneously using a specially made clamping frame (Fig. III. 2). The clamping pressure was obtained using sprung bolts which pressed a block of wood over the gum. The clamping frame was itself clamped at both ends to the two extreme ends of the chamber. To achieve proper curing and performance, the clamp was left on the gauges over night. Once the clamps were removed, the gauges were ready for soldering.

3. Strain Gauge Soldering

The most common method of making electrical connections in strain gauge circuits is by means of soft solder in wire form.

Although soldering is considered a simple operation, it was necessary to do it with appropriate tools and techniques to assure accurate strain measurements. One such tool was a temperature or power controlled soldering station that provided low voltage and adjustable temperature to the soldering iron tip. The solder used was of the type with a core of activated rosin flux which made soldering much more convenient.

3.1. Tinning Solder Tabs and Bondable Terminals

All strain gauge solder tabs, terminals, and leadwires were properly tinned before making soldered connections. This helped insure active surface wetting and good heat transfer during the soldering operation.

Before tinning the solder tabs on open-face strain gauges, the

entire measuring grid and the upper portion of the solder tabs were protected with drafting tape. This not only shielded the grid from soldering flux and inadvertent solder splash, but also restricted the flow of solder on the tabs.

The tinning procedure consisted of first cleaning and reapplying a small amount of solder to the hot soldering iron tip. Then a drop of flux was applied to the tab or terminal. Leadwire ends were stripped of insulation before tinning. Then some solder was melted on the hot tip to form a hemisphere of molten solder twice the diameter of the wire to be tinned. Leadwires were then firmly anchored to the surface with drafting tape routing to the terminal strip before soldering was made. The tinned leadwire ends were bent slightly to form a loop, taping the wires firmly over the connection area with drafting tape. Using fresh solder each time after cleaning the tip insured a good soldering operation with little traces of residual flux around the joints. All the tapes were removed using a solvent once there was no trace of residual flux around the joints after cleaning.

APPENDIX IV

THE EFFECTS OF OUT-OF-ROUNDNESS OF THE CHAMBER ON THE MEASURED STRESSES

During both the K_o consolidation and the penetration phases of different tests it was noticed that the four columns of strain gauges seemed to exhibit unequal behaviour: two opposite columns seemed to show greater circumferential strains than the other pair, which in some cases appeared to show very little movement or even to experience compressive strains during both loading and testing stages. This led the author to believe that the inner-shell of the chamber could go slightly out of shape and become elliptical. Hence, this deformation and its effects on the soil stresses are studied here. The phenomenon seemed to vary from one test to another and may have been due to slight density variations in the sample as a result, perhaps of uneven pluviation.

If we assume that deformation from a vertical cylindrical shape is a result of a uniformly distributed lateral load, then we may follow Smolira (1955) and obtain a maximum B.M. at both crown and haunches (in terms of conventional loading on a pipe semi-circle) of $\omega R^2/4$. The corresponding deflections are also obtained as $\omega R^4/12EI$.

The average differential strain between adjacent columns of strain gauges on the inner chamber shell was 7.5 microstrain and this can be regarded as distributed equally between the positive and negative B.M. positions and would correspond to deflections of $\pm$ 0.16 mm under a differential load of approximately 50 pa, i.e., 1 % of the initial lateral loading due to the self-weight of the sand or 0.1 % of the lateral loading (about 50 kpa) at the end of K_o consolidation. These values are well within the ranges expected of experimental variations

and could as well have been caused by a reduction of out-of-roundness of the initial shape of the cylinder as the K_o loading was applied. (The 'roundness' of the chamber was not checked to this level of accuracy).

Although in these calculations the effect of the stiff 'ends' of the cylinder has been ignored as has the posibility of the strain gauge columns not being at the position of maximum bending moment, it is clear that the differential strain gauge values are consistent with normal operations and, further, that their absolute values (as distinct from relative values in the same column) are subject to errors of the order of the readings themselves.

APPENDIX V

Evaluation of the Elastic Parameters

The analysis of the expanding cylinder test results together with the developed transversely isotropic model relies on the five elastic constants. It will be reported in Chapter 8 that G′ can be written as a function of the other four parameters. To obtain these four parameters, it is necessary to use special laboratory tests together with the theoretical relationships that are discussed here.

The stress-strain relationships for a transversely isotropic elastic material can be written as

$$\delta\varepsilon_r = \frac{1}{E}\left(\delta\sigma'_r - \nu\delta\sigma'_\theta\right) - \frac{\nu'\delta\sigma'_z}{E'} \tag{1a}$$

$$\delta\varepsilon_\theta = \frac{1}{E}\left(\delta\sigma'_\theta - \nu\delta\sigma'_r\right) - \frac{\nu'\delta\sigma'_z}{E'} \tag{1b}$$

$$\delta\varepsilon_z = \frac{1}{E'}\left(\delta\sigma'_z - \nu'\left(\delta\sigma'_\theta + \delta\sigma'_r\right)\right) \tag{1c}$$

By setting Eqn. (1a) equal to zero for K_o consolidation and rebound, and noting that $\delta\sigma_r$ would be equal to $\delta\sigma_\theta$, K_{oe} (the slope of the tangent to the unloading curve of an overconsolidated K_o test at the desired stress level) can be obtained as

$$K_{oe} = \left.\frac{\delta\sigma_r}{\delta\sigma_z}\right|_{\varepsilon_r = 0} = \frac{\nu' E}{(1-\nu)E'} = \frac{\nu'}{1-\nu}\,\rho \tag{2}$$

where $\rho = E/E'$ and ν and ν' are the Poisson's ratios in rθ and rz planes, respectively. Then by definition

$$\delta K_o = \frac{\sigma_r + \delta\sigma_r}{\sigma_z + \delta\sigma_z} - \frac{\sigma_r}{\sigma_z} \tag{3}$$

from which $K_{oe} = \dfrac{\delta\sigma_r}{\delta\sigma_z}$ needs to be deduced.

Combining Eqns. (1c) and (2) will give

$$\delta\varepsilon_z = \frac{1}{E'}(\delta\sigma_z - 2\nu'\delta\sigma_r) = \frac{\delta\sigma_z}{E'}(1 - 2\nu' K_{oe}) \tag{4}$$

As a perturbation during K_o consolidation, it is possible to hold ε_z constant and change σ_r and ε_r. This will also cause a change in σ_z [Test SU73]. Then by setting Eqn. (1c) equal to zero, the value of ν' can be obtained from

$$\delta\sigma_z = 2\nu'\delta\sigma_r \tag{5}$$

The constrained modulus, M, can be used to find the elasticity modulus in the rz plane, E', as a function of ν'. Since $M = \delta\sigma_z/\delta\varepsilon_z$ then Eqn. (4) becomes

$$M = \frac{\delta\sigma_z}{\delta\varepsilon_z} = \frac{E'(1 - \nu)}{1 - \nu - 2\rho\nu'^2} \tag{6}$$

From Eqn. (2),

$$\rho\nu' = K_{oe}(1 - \nu) \tag{7}$$

Combining Eqns. (6) and (7) will give

$$E' = M(1 - 2\nu' K_{oe}) \tag{8}$$

The plane-strain elasticity modulus, E, is related to the shear modulus in the same plane ,G, by

$$E = 2G(1 + \nu) = \rho E' \tag{9}$$

The shear modulus G can be obtained from the unload-reload loop of the first stage of the expanding cylinder tests. Solving for ρ in Eqns. (2) and (9) gives

$$\nu = \frac{E'K_{oe} - 2G\nu'}{E'K_{oe} + 2G\nu'} \tag{10}$$

APPENDIX VI

Axial Cylindrical Cavity Expansion in a Transversely-isotropic Elastic Medium

The stress-strain equations for a transversely-isotropic material can be written as follows:

$$\varepsilon_r = \frac{1}{E}\left(\sigma_r - \nu\sigma_\theta\right) - \frac{\nu'}{E'}\sigma_z \tag{1}$$

$$\varepsilon_\theta = \frac{1}{E}\left(\sigma_\theta - \nu\sigma_r\right) - \frac{\nu'}{E'}\sigma_z \tag{2}$$

$$\varepsilon_z = \frac{1}{E'}\left(\sigma_z - \nu'(\sigma_r + \sigma_\theta)\right) \tag{3}$$

For the plane strain condition, $\varepsilon_z = 0$ and, from Eqn. (3),

$$\sigma_z = \nu'(\sigma_r + \sigma_\theta) \tag{4}$$

The radial stress, as a function of the two strains, is then:

$$\sigma_r = C_{11}\varepsilon_r + C_{12}\varepsilon_\theta \tag{5}$$

where

$$C_{11} = \frac{E(1 - \rho\nu'^2)}{(1 + \nu)(1 - \nu - 2\rho\nu'^2)} \tag{6}$$

$$C_{12} = \frac{E(\nu + \rho\nu'^2)}{(1 + \nu)(1 - \nu - 2\rho\nu'^2)} \tag{7}$$

and $\rho = E/E'$

From the definitions of the radial and circumferential strains,

$$\varepsilon_r = \frac{du}{dr} \qquad \text{and} \qquad \varepsilon_\theta = \frac{u}{r}$$

the general solution for the displacement in plane-strain can be written as

$$u(r) = A \cdot r + \frac{B}{r} \tag{8}$$

Then the strains will become:

$$\varepsilon_r = A - \frac{B}{r^2} \tag{9}$$

$$\varepsilon_\theta = A + \frac{B}{r^2} \tag{10}$$

Replacing these for radial and circumferential strains in Eqn. (5) gives:

$$\sigma_r = A(C_{11} + C_{12}) - \frac{B}{r^2}(C_{11} - C_{12}) \tag{11}$$

To solve for Constants A and B in this equation, it is necessary to apply the following boundary conditions:

(i) at $r = a$, $\sigma_r = P_i$
and (ii) at $r = b$, $\sigma_r = 0$ [for BC1 boundaries],

where a and b are the internal and external radii.

Then from Eqn. (11)

$$A = \frac{a^2 P_i}{(a^2 - b^2)(C_{11} + C_{12})}$$

and

$$B = \frac{a^2 b^2 P_i}{(a^2 - b^2)C_{66}}$$

Substituting for A and B in Eqn. (11) gives the radial stress as:

$$\sigma_r = \frac{a^2 P_i}{a^2 - b^2}\left(1 - \frac{b^2}{r^2}\right) \tag{12}$$

As $b \to \infty$, the stress becomes

$$\sigma_r = \frac{a^2}{r^2} P_i \tag{13}$$

and the σ_r at b (for the infinite boundary case):

$$\sigma_r = \frac{a^2}{b^2} P_i \tag{14}$$

The radial displacement can also be obtained by substituting for A and B in Eqn. (8) to get

$$u(r) = \frac{a^2 P_i}{(a^2 - b^2)}\left(\frac{r}{(C_{11} + C_{12})} + \frac{b^2}{C_{66} \cdot r}\right) \tag{15}$$

However, when $b \to \infty$, this equation simplifies to

$$u(r) = -\frac{a^2 P_i}{2Gr} \tag{16}$$

and, for the displacement at b for the infinite boundary case:

$$u(b) = -\frac{a^2 P_i}{2Gb} \tag{17}$$

Eqns. (12) and (13) are the Lame' 2-D stress solutions for an isotropic material and the infinite boundary displacement solution

[Eqn. (16)] is also that of the equivalent Lame' using the transverse-isotropic G value.